Università degli Studi della Tuscia di Viterbo
Dipartimento di Economia, Ingegneria, Società e Impresa (DEIM)

Corso di Dottorato di Ricerca in
Engineering for Energy and Environment - XXXVI ciclo

Energy load on tokamak plasma-facing components and its dependence on plasma regimes

s.s.d. FIS/03

Tesi di dottorato di:
Dott. Andreas Redl

Coordinatore del corso
Prof. Andrea Facci

Tutore
Prof. Giuseppe Calabrò

Co-tutore
Dott. Thomas Eich

Dott. Nicola Vianello

A.A. 2023/24

Das Plasma gegen die Wand fahren.

Dr. Michael Faitsch

Contents

Estratto

Il concetto di fusione nucleare è visto come una possibile fonte di energia a bassa emissione di CO_2, che potrebbe un giorno sostituire la fissione nucleare e i combustibili fossili. Una sfida fondamentale per la realizzazione di un possibile reattore a fusione commerciale è la corretta gestione dei carichi termici sui componenti esposti al plasma.
Questa tesi presenta un'analisi dei carichi energetici sui componenti del deviatore e del non deviatore nel Tokamak di aggiornamento ASDEX Upgrade (Garching, Germania). L'impatto dell'aumento del trasporto dei filamenti, che può dominare il trasporto convettivo radiale nello strato di raschiamento (SOL) verso la prima parete, è studiato utilizzando plasmi H-mode dedicati con un equilibrio magnetico caratterizzato da un'alta triangolarità superiore δ_u e un'alta elongazione κ. Il database presenta una variazione del fattore di sicurezza q cambiando il campo magnetico toroidale B_{tor} e un'ampia copertura nello spazio operativo di densità cambiando il livello di alimentazione del feed-forward flattop in base ai colpi. Sono stati acquisiti modi H a bassa densità associati a modi localizzati ai bordi (ELM) di tipo I e modi H ad alta densità associati a un maggiore trasporto convettivo radiale. Quest'ultimo scenario è noto anche come regime di scarico quasi-continuo (QCE). Sono incluse un'analisi delle proprietà dei filamenti e una stima dell'erosione delle prime componenti della parete.
Come prerequisito per una scalatura affidabile dei carichi energetici in ASDEX Upgrade, il bilancio energetico globale è stato stabilito utilizzando la calorimetria dell'acqua di raffreddamento rivista. Oltre alla calorimetria rivista, per ottenere un bilancio energetico globale rappresentativo è necessario considerare i contributi della radiazione del plasma e delle perdite di iniezione del fascio neutro. Sulla base delle nuove conoscenze, il compito di ottenere un bilancio energetico globale ragionevole è stato ripetuto al Tokamak JET (Culham, Regno Unito).
Gli esperimenti hanno rivelato che i carichi energetici normalizzati dei componenti del deviatore e del non deviatore sono correlati in modo lineare con il parametro di controllo della turbolenza α_t che definisce la forza del motore di interscambio. La transizione da un regime QCE ad alta densità a uno scenario ELMy H-mode di tipo I presenta un andamento lineare coerente. Una generalizzazione della scala ottenuta è stata realizzata estendendo il database con scariche di aggiornamento ASDEX Upgrade con diverse caratteristiche del plasma.
Contemporaneamente, sono stati osservati cambiamenti sostanziali dei profili SOL a monte e a valle. L'ampiezza del flusso di calore nella SOL subisce un significativo allargamento,

riducendo il picco del flusso di calore e aumentando l'area su cui si deposita il flusso di calore parallelo. Inoltre, è stata dimostrata una riduzione del trasporto conduttivo parallelo mediante misure con termocoppia, anche se non del tutto coerente con informazioni simili ottenute da sonde di Langmuir montate a parete. Le misure della pressione neutra e della densità di flusso neutro nella camera principale indicano un andamento lineare con α_{t}, mentre per le misure nel divertore è necessaria una diversa dipendenza da $q_{\mathrm{cyl}}\ B_{\mathrm{tor}}$. Allo stesso tempo, l'ampiezza della spalla di densità valutata da un qualificatore di densità SOL si satura quando α_{t} supera ≈ 0.55 all'interno di questo database. La lunghezza di decadimento della densità di e-folding λ_{n} che descrive il comportamento della densità nello strato vicino al raschiamento rivela una tendenza simile.
L'analisi delle proprietà dei filamenti, misurate sfruttando teste di sonda dedicate in prossimità della prima parete, mostra un andamento lineare comparabile del contributo convettivo dei filamenti ai flussi di calore e di particelle con l'aumentare di α_{t}. Allo stesso tempo, è stato identificato che la causa dell'aumento del trasporto filamentoso in modalità H per gli scenari QCE è un aumento del flusso di particelle, causato principalmente da un aumento della densità dei filamenti e della frazione di impaccamento. È degno di nota il fatto che la temperatura del filamento per gli ioni e gli elettroni rimanga costantemente alta, senza variazioni sostanziali, ogni volta che si raggiunge il regime di alta densità. Un bilancio di potenza basato su misure di sonda e calorimetria suggerisce che il contributo del flusso di calore del filamento rimane costante, per lo più al di sotto del 25 %, per l'intero database.
La stima dell'erosione grossolana sulla prima parete indica che l'erosione è dovuta ai contributi di fondo e non ai filamenti. Un'erosione significativa è causata solo in presenza di impurità nel far-SOL. Inoltre, l'erosione lorda sembra saturare quando α_{t} supera ≈ 0.55 in questo database.

Abstract

The concept of nuclear fusion is seen as a possible low CO_2 source for power generation which could one day replace nuclear fission power and fossil fuels. A key challenge in realizing a possible commercial fusion reactor is the proper handling of heat loads on plasma-facing components.

This thesis presents an analysis of the energy loads on divertor and non-divertor components in the ASDEX Upgrade Tokamak (Garching, Germany). The impact of enhanced filament transport, which can dominate the radial convective transport in the scrape-off layer (SOL) to the first wall, is investigated using dedicated H-mode plasmas with a magnetic equilibrium characterized by a high upper triangularity δ_u and high elongation κ. The database features a variation in the safety factor q by changing the toroidal magnetic field B_{tor} and a large coverage in the density operational space by changing the feed-forward flattop fuelling level on a shot-to-shot basis. Low density H-modes associated with type-I edge localised modes (ELMs) and high density H-modes associated with an increased radial convective transport have been acquired. The latter scenario is also known as quasi-continuous exhaust (QCE) regime.

As a prerequisite for trustworthy energy load scalings in ASDEX Upgrade, the global energy balance has been established using the revised cooling water calorimetry. In addition to the revised calorimetry, contributions from plasma radiation and from neutral beam injection losses need to be considered to achieve a representative global energy balance. Based on the novel understandings, the task in achieving a reasonable global energy balance has been repeated at the JET Tokamak (Culham, United Kingdom).

The experiments have revealed that the normalized energy loads of divertor and non-divertor components correlate linearly with the turbulence control parameter α_t defining the strength of interchange drive. The transition from a high-density QCE regime to a Type-I ELMy H-mode scenario exhibits a consistent linear trend. A generalization of the achieved scaling has been realized by extending the database with ASDEX Upgrade discharges with different plasma characteristics.

Simultaneously, substantial changes of up- and downstream SOL profiles have been observed. The width of the heat flux in the SOL undergoes a significant broadening reducing its peak heat flux and increasing the area on which the parallel heat flux is deposited. Furthermore, a reduction of the parallel conductive transport is proven by means of thermocouple measurements, although not fully consistent with similar information obtained from wall mounted Langmuir Probes. The neutral pressure and neutral flux density measure-

ments in the main chamber indicate a linear trend with α_t, whereas for the measurements in the divertor a different dependence on q_{cyl}/B_{tor} is necessary. At the same time, the density shoulder amplitude assessed by a SOL density qualifier saturates when α_t exceeds ≈ 0.55 within this database. The e-folding density decay length λ_n describing the density behaviour in the near-SOL reveals a similar trend.
An analysis of filament properties measured by exploiting dedicated probe-heads near the first wall show a comparable linear trend of filamentary convective contribution to heat and particle fluxes with α_t. At the same time, it has been identified that the cause of the enhanced filamentary transport in H-mode for QCE scenarios is an increase in particle flux, primarily caused by an increase of filament density and the packing fraction. It is noteworthy that the filament temperature for ions and electrons remain consistently high without substantial variation whenever the high density regime has been achieved. A power balance based on probe and calorimetry measurements suggests that the filament heat flux contribution remains constant, mostly below 25 %, throughout the entire database.
The estimation of the gross erosion on the first wall indicates that the erosion is carried by the background contributions and not by filaments. Significant erosion is caused only in the presence of impurities in the far-SOL. Furthermore, the gross erosion appears to saturate when α_t exceeds ≈ 0.55 within this database.

Chapter 1

Why do we need fusion power plants and what are the challenges?

1.1 Thermonuclear Fusion

In times, in which the question of environmentally friendly energy supply has not yet been conclusively clarified, the search for alternative ways of generating energy is inevitable. Until today, and for the foreseeable future without much change, a considerable part of our energy is covered by burning of limited fossil resources (oil, natural gas, coal). In the last 40 years, the worldwide energy demand has more than doubled, with the same share of fossil resources for energy production [bpb23], and will continue to increase due to the rising industrialization of so-called newly industrialized countries and third world countries. This is associated with a continuous increase in emission of so-called greenhouse gases, mainly CO_2. In addition to the climatic changes and damage caused by the increased fraction of greenhouse gases in the atmosphere, the limited energy resources, colliding with the increasing global energy demand, are among the greatest challenges since human recollection. One promising candidate, which could contribute to solve the future human energy demand, is nuclear fusion.

Nuclear fusion is the physical process in which lighter nuclei fuse into a heavier one by releasing energy. It thus corresponds to the reverse process of induced nuclear fission in which a heavy nucleus is split into lighter nuclei. The approach of fission has already been used for many decades in research, in commercial power generation as well as for military atomic weapons.

The amount of energy released per fission is about six to seven orders of magnitude greater than in chemical reactions such as burning of fossil fuels, but nuclear fission also has its risks. Although no CO_2 is generated during power generation, the fuel rods are problematic to handle. These rods consist of highly radioactive uranium, which causes serious damage to the health of living organisms. Furthermore, the nuclear waste produced by fission reactions is also still highly radioactive making storage extremely difficult. To date, there is no suitable concept for the final storage of nuclear waste.

Nuclear fusion would have the advantage that no long-lived radioactive end products would be generated and the fusion reaction would be interrupted by slightest changes in its boundary conditions. The first proof of nuclear fusion was provided by Ernest Rutherford in 1919 [Rut19]. In 1920 Arthur Eddington was able to use this process to conclusively explain the energy production of the sun [Edd20]. Nuclear fission was experimentally proven in 1938 by Otto Hahn [HS39] and theoretically described a year later by Lise Meitner [MF39].
The reason, why these nuclear reactions of fusion and fission are possible at all, can be explained by the *binding energy* released per nucleon. Protons and neutrons that are bound (forming an atomic nucleus) are in a more energetically favourable state than free ones. If the binding energy per nucleon of the resulting nucleus is greater than of the original

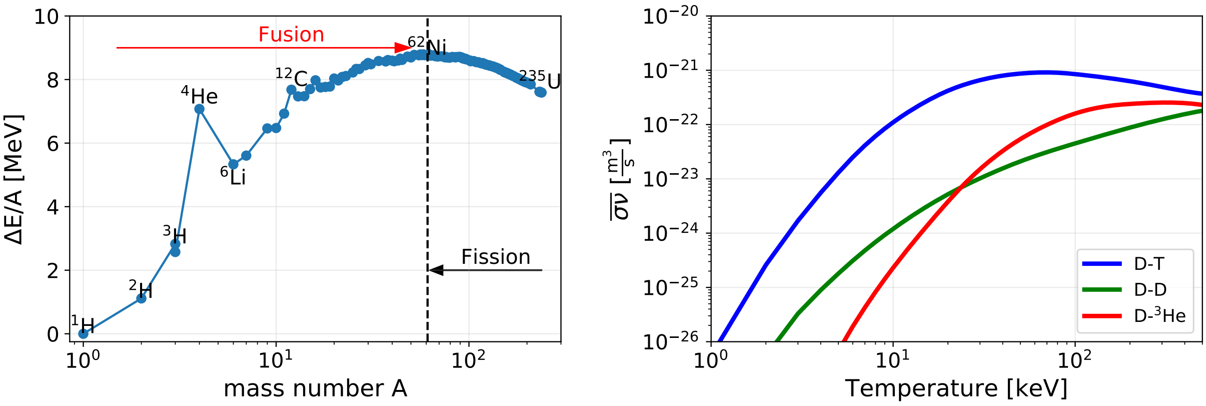

Figure 1.1: Left plot: binding energy per nucleon as a function of the atomic mass number A [GGGH11]. Right plot: reaction rates for possible fusion reactions in dependence on temperature [MTI74].

ones, energy is released. Fig. 1.1 (left plot) shows the dependence of the binding energy per nucleon. As seen the curve has a broad maximum around an atomic mass number of about 60. The element with the highest releasing binding energy per nucleon is ^{62}Ni and is a characteristic separator that divides the graph into two areas: the side to the left of the maximum characterizes the energy surplus in fusion processes, the side to the right of the maximum describes the case for fission processes. It can easily be seen that nuclear fusion releases much more energy per nucleon than nuclear fission. The highest energy gain could be achieved with the fusion of hydrogen to helium:

$$\mathrm{H} + \mathrm{H} \longrightarrow \mathrm{D} + \nu_e + \mathrm{e}^+ + 0.42\ \mathrm{MeV} \tag{1.1}$$
$$\mathrm{H} + \mathrm{D} \longrightarrow {}^3_2\mathrm{He} + \gamma + 5.49\ \mathrm{MeV} \tag{1.2}$$
$${}^3_2\mathrm{He} + {}^3_2\mathrm{He} \longrightarrow {}^4_2\mathrm{He} + 2\mathrm{p} + 12.9\ \mathrm{MeV} \tag{1.3}$$

This reaction chain dominates the energy production processes in the sun, where the temperature of the solar center is less than 1 keV. Four protons fuse to form a helium core and release in sum 26.7 MeV of energy in the form of radiation and kinetic energy. However, this reaction, also known as *proton-proton* chain, is unsuitable for nuclear fusion processes on earth, because the reaction rates of the weak interaction involved in this chain are marginal. Instead, reactions which exploit isotopes of hydrogen and helium could be exploited:

$$\mathrm{D} + \mathrm{D} \longrightarrow ^3_2\mathrm{He} + \mathrm{n} + 3.27\ \mathrm{MeV} \tag{1.4}$$

$$^3_2\mathrm{He} + \mathrm{D} \longrightarrow ^4_2\mathrm{He} + \mathrm{p} + 18.4\ \mathrm{MeV} \tag{1.5}$$

$$\mathrm{D} + \mathrm{T} \longrightarrow ^4_2\mathrm{He} + \mathrm{n} + 17.6\ \mathrm{MeV} \tag{1.6}$$

The quantity *reaction rates* $\langle \sigma_{\mathrm{Fus}} u \rangle$ is suitable to identify the reaction with the most realistic feasibility and can be defined by the following integral [Str18]:

$$\langle \sigma_{\mathrm{Fus}} u \rangle = \frac{4}{\sqrt{2\mu_{\mathrm{r}} \pi T^3}} \int dE_{\mathrm{r}} E_{\mathrm{r}} \sigma_{\mathrm{Fus}}(E_{\mathrm{r}}) e^{-E_{\mathrm{r}}/k_B T}, \tag{1.7}$$

where μ_{r} denotes the reduced mass, E_{r} the relative energy between the fusion partner, k_{B} the Boltzmann constant, T the temperature and σ_{Fus} the fusion cross-section. Fig. 1.1 (right plot) shows the reaction rates of potential fusion reactions against temperature, in keV.[1] It is easy to see that the reaction with deuterium and tritium has the greatest potential. It has the highest the reaction rate at the lowest temperature among all possible reactions and a broad maximum around 50 keV.

Deuterium is present at 0.0156 % of all naturally occurring hydrogen compounds and could be obtained from seawater. However, tritium is radioactive and does not occur in nature because of its half-life of 12.3 years. Instead, it could be bred from lithium using fusion neutrons, as suggested in Equ. (1.8) and (1.9):

$$\mathrm{n} + ^6_3\mathrm{Li} \longrightarrow ^4_2\mathrm{He} + \mathrm{T} + 4.800\ \mathrm{MeV} \tag{1.8}$$

$$\mathrm{n} + ^7_3\mathrm{Li} \longrightarrow ^4_2\mathrm{He} + \mathrm{T} + \mathrm{n} - 2.466\ \mathrm{MeV} \tag{1.9}$$

Equ. (1.8) is exothermic and Equ. (1.9) is endothermic. Despite the different energy balance, both lithium isotopes can be used as starting materials for the breeding process. Both isotopes produce the required tritium as an end product and $^7_3$ Li could be considered as a neutron multiplier in future fusion scenarios. An isotopic separation is therefore not necessarily needed. The worldwide lithium resources should be sufficient to cover the demand for a long time despite the increasing fraction of alternative considerations in energy generation and the associated storage problems. To achieve the desired fusion of deuterium and tritium by overcoming the Coulomb potential, temperatures above 10 keV, about 100 million Kelvin, are required. In this temperature range, deuterium and tritium are fully ionized and form a plasma. Overall, the total plasma remains still quasi-neutral ($n_{\mathrm{e}} = Z_{\mathrm{i}} n_{\mathrm{i}}$).

Simply increasing the temperature is not sufficient to achieve the boundaries for earth-bound nuclear fusion. Further boundary conditions have to be taken into account in order

[1] In plasma physics, the temperature is defined in eV. 1 eV corresponds to 11605 K.

to achieve plasma parameters in which the fusion process takes place in a self-sustaining manner. By assuming a pure plasma consisting of equal fractions of deuterium and tritium (each $\frac{\bar{n}}{2}$)[2] the internal energy balance can be expressed as [Str18]:

$$\left(\frac{\bar{n}}{2}\right)^2 \langle \sigma_{\mathrm{Fus}} u \rangle E_\alpha \geq \frac{3\bar{n}\bar{T}}{\tau_{\mathrm{E}}} + c_{\mathrm{Br}} Z_{\mathrm{eff}} \bar{n}^2 \sqrt{\bar{T}}, \tag{1.10}$$

where the term on the left side describes the generation of heating power density by α-particles with an energy $E_\alpha = 3.52$ MeV produced in fusion processes and the previously discussed reaction rate $\langle \sigma_{\mathrm{Fus}} u \rangle$. The first term on the right side describes the losses due to transport processes. The stored energy within a pure plasma can be estimated by a volume integral over the energy contributions of participated electron and ions:

$$W = W_{\mathrm{e}} + W_{\mathrm{i}} = \int_V dV \frac{3}{2}(n_{\mathrm{e}} T_{\mathrm{e}} + n_{\mathrm{i}} T_{\mathrm{i}}) \approx 3V\bar{n}\bar{T}, \tag{1.11}$$

and $\tau_{\mathrm{E}} = \frac{W}{P_{\mathrm{loss}}}$ is the energy confinement time. The second term describes the bremsstrahlung losses, which are relevant for temperatures above 10 keV. For this contribution, a small fraction of impurities has to be supposed. Bremsstrahlung is generated by the deceleration of electrons through coulomb collisions with charged particles. The conservation of energy is guaranteed by the emission of radiation. The value of c_{Br} is $1.04 \cdot 10^{-19} \mathrm{m}^3 \sqrt{\mathrm{eV}}/\mathrm{s}$. Z_{eff} is the effective charge number and is defined as:

$$Z_{\mathrm{eff}} = \frac{\sum_{\mathrm{i}} n_{\mathrm{i}} {Z_{\mathrm{i}}}^2}{n_{\mathrm{e}}}, \tag{1.12}$$

where the sum considers all ion species. If the energy balance in Equ. 1.10 satisfies the inequality, the plasma can burn in a self-sustaining manner. From this equation an ignition condition for the plasma, known as Lawson criterion (or triple product) [Law57], can be derived [Str18]:

$$\bar{n}\bar{T}\tau_{\mathrm{E}} > \frac{12\bar{T}^2}{E_\alpha \langle \sigma_{\mathrm{Fus}} v \rangle - 4 c_{\mathrm{Br}} Z_{\mathrm{eff}} \sqrt{\bar{T}}} \tag{1.13}$$

Fig 1.2 shows the progress in reaching the ignition condition. Above the threshold given by Equ. (1.13), the plasma ignites and burns in a self-sustaining manner. Starting from the first Soviet tokamaks (T3,..) up to the first Western fusion experiments, a continuous improvement of the triple product can be seen in the progressing state of research.

In order to assess how close the plasma is to the ignition condition, the quantity Q is introduced. This parameter is defined as the ratio between the heating power produced by the fusion reactions P_{fus} and the applied external heating power P_{ext}:

$$Q = \frac{P_{\mathrm{Fus}}}{P_{\mathrm{ext}}} \tag{1.14}$$

[2]the crossbar denotes the mean value over the plasma volume

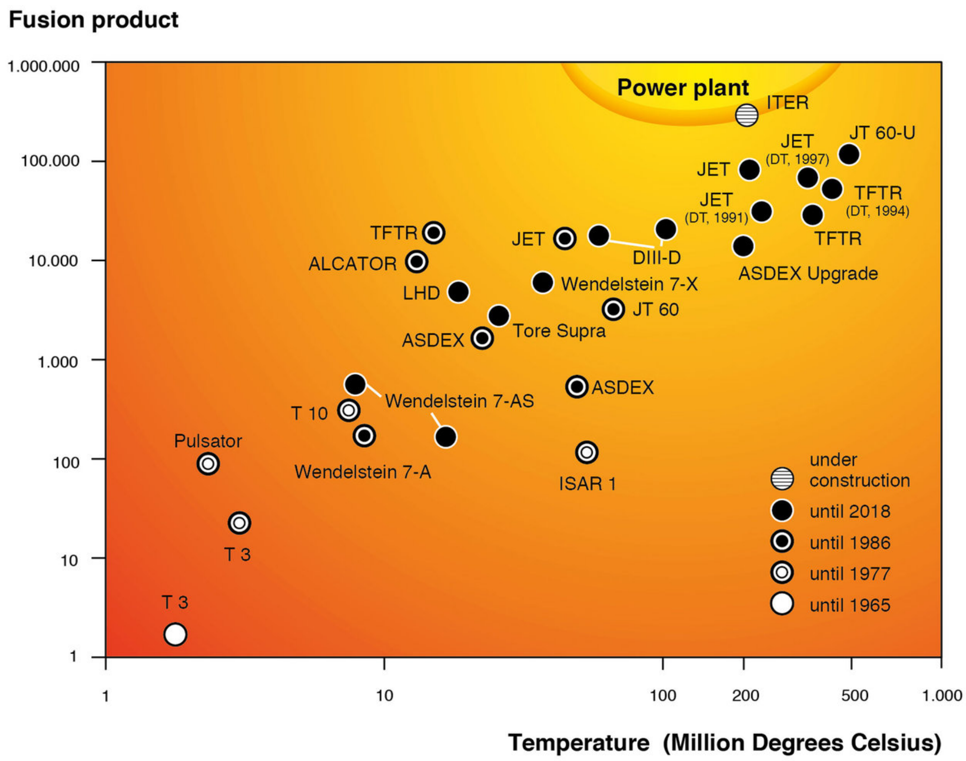

Figure 1.2: Evolution of the triple product for different fusion experiments against temperature [IPP23b].

If $Q = 1$, the same amount of power is generated as is injected by the external heating systems. If the ignition condition is reached, $Q \rightarrow \infty$. Previous fusion experiments have always delivered a value smaller than 1. The experiment ITER [Big19], a project supervised by 35 states currently under construction in Cadarache (France), would be the first magnetically confining fusion experiment which would overcome the break-even point ($Q > 1$). In optimized scenarios, ITER should achieve $Q \approx 10$.

1.2 The tokamak, a magnetic confinement device

As already discussed, high temperatures are required in order to create the conditions for fusion reactions. However, no material is known which could withstand these high thermal heat loads in steady state. Therefore, the plasma has to be confined in a different manner. A promising approach is to magnetically confine the plasma by exploiting the controllable interaction of charged particles with magnetic fields. To avoid large end losses, the plasma chamber is bent into a torus. The toroidal confinement is provided by a set of toroidal field coils arranged equidistantly along the torus (blue field coils in Fig. 1.3). Since the toroidal coils are arranged closer on the inner side of the torus (high field side (HFS) than

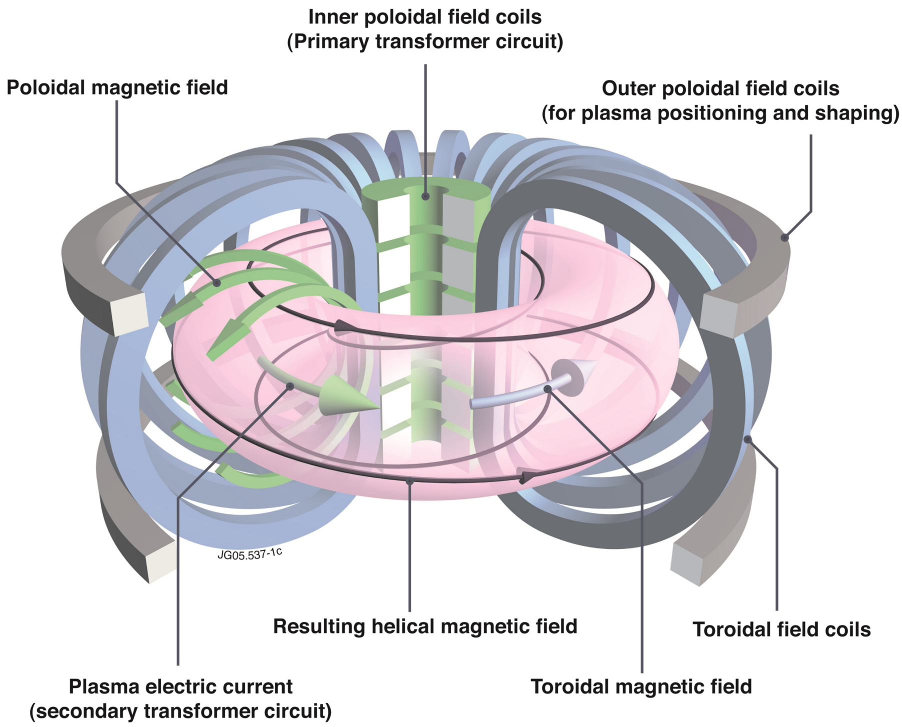

Figure 1.3: Sketch of a tokamak. The poloidal field coils are indicated in grey, the toroidal field coils in blue and the central solenoid in green [PBP06].

the outer side (low field side (LFS)), it leads to a radial gradient in the toroidal magnetic field B_{tor} which decreases with increasing radius:

$$B_{\text{tor}} \propto \frac{1}{R}, \tag{1.15}$$

where R denotes a radial coordinate along the major radius. As a consequence, a charge-dependent drift arises:

$$v_{\text{mag}} = \left(\frac{mv_\perp^2}{2q} + \frac{mv_\parallel^2}{q} \right) \frac{\boldsymbol{B} \times \nabla B}{B^3}, \tag{1.16}$$

where m denotes the particle mass, q the electric charge and $v_{\perp(\parallel)}$ the velocity perpendicular (parallel) to the magnetic field B. The term depending on $v_\perp$ is derived from the magnetic moment:

$$\mu = \frac{mv_\perp^2}{2B}, \tag{1.17}$$

whereas the term following $v_\parallel$ is caused by the curvature of the magnetic field, which can be expressed as:

$$\nabla B = -\frac{\boldsymbol{R}}{|R|^2} B, \tag{1.18}$$

following the definition of B introduced in Equ. (1.15). The inhomogeneous magnetic field leads to a charge-dependent drift causing a spatial separation of electrons and ions producing an additional electric field $\boldsymbol{E}$. This additional electric field leads to a charge-independent, global drift forcing the plasma towards the first wall. This additional drift can be expressed as:

$$v_{\mathrm{E\times B}} = \frac{\boldsymbol{E}\times\boldsymbol{B}}{B^2}. \tag{1.19}$$

The plasma is therefore unstable and reduces the required confinement times. To avoid the arising charge separation, an additional poloidal magnetic field B_{pol} is superposed, which leads to a twisting of the toroidal field lines towards helical ones, as seen in Fig. 1.3. In tokamaks (the tokamak concept was invented by Igor Tamm and Andrei Sakharov, two Soviet physicists, in the 1950s [Sak58]), this additional poloidal magnetic field is realized by the toroidal plasma current I_{p}. This current is produced by a transformer coil in the center of the torus as illustrated in Fig. 1.3 (green solenoid). The conductive plasma inside

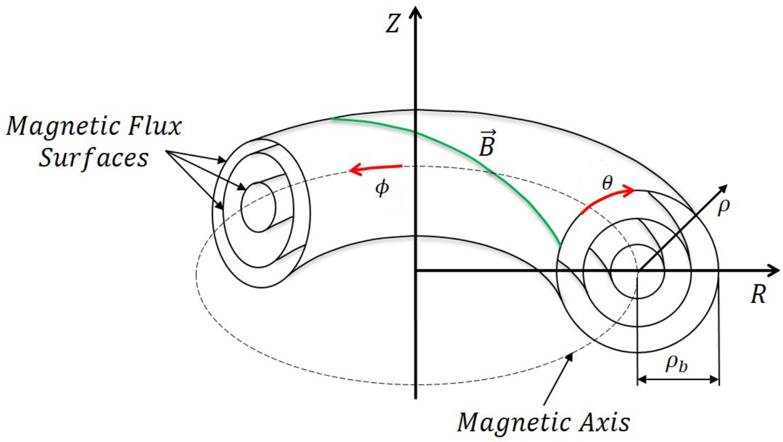

Figure 1.4: schematic illustration of a circular shaped tokamak plasma [BWS+15].

the torus acts as a second transformer coil in which the transformer current is induced and creates a magnetic field in the poloidal direction due to Ampere's law. In addition, the induced plasma current heats the enclosed plasma. This kind of plasma heating is called *ohmic heating*. Additional poloidal field coils (highlighted in grey in Fig. 1.3) are used for the positioning and shaping of the plasma.
To describe to this variation of the superposed magnetic field lines on a flux surface, the safety factor q is introduced:

$$q = \frac{r\cdot B_{\mathrm{tor}}}{R\cdot B_{\mathrm{pol}}}, \tag{1.20}$$

where r is the minor radius of a magnetic flux surface and R the major radius of a magnetic flux surface. The safety factor can simply be expressed as the *twisting* of the poloidal magnetic field along a full toroidal winding.

1.2.1 Plasma coordinates

A plasma can be described by a cartesian-cylindrical coordinate system, where ϕ describes the angle in toroidal direction, θ the angle in poloidal direction and ρ the normalized radius (see Fig. 1.4). The quantity ρ is based on the magnetic fluxes and can be expressed in terms of the toroidal and poloidal contribution. For an ideal magnetohydrodynamic

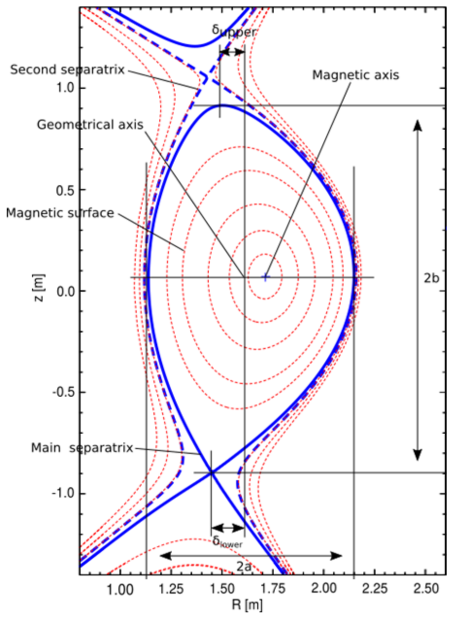

Figure 1.5: Magnetic equilibrium of AUG discharge #39231 at t = 4.0 s in CDN-configuration. Several geometrical quantities required for the characterization of the magnetic equilibrium are indicated. The solid blue line illustrates the primary separatrix aligned with the lower X-point.

(MHD) equilibrium, the single fluid force balance can be written as:

$$\boldsymbol{j} \times \boldsymbol{B} = \nabla p, \tag{1.21}$$

where $\boldsymbol{j}$ is the plasma current density, $\boldsymbol{B}$ is the total magnetic field on a given magnetic flux surface, and ∇p is the pressure gradient. From this equation, one can deduce that the pressure gradient ($\boldsymbol{B} \cdot \nabla p = 0$) as well as the current density ($\nabla \cdot \boldsymbol{j} = 0$) is constant on each flux surface. As the parallel heat conduction is much larger than the perpendicular, it is justified to suppose that not only the pressure, but also the density and temperature are constant on flux surfaces. These flux surfaces can be used to determine a suitable coordinate system. One needs the poloidal flux surface Ψ_{pol} of a certain radial position, $\Psi_{\text{separatrix}}$ of the separatrix, also called the last closed magnetic flux surface (LCFS), and Ψ_{axis} of the magnetic axis:

$$\rho_{\text{pol (tor)}} = \sqrt{\frac{\Psi_{\text{pol}} - \Psi_{\text{axis}}}{\Psi_{\text{separatrix}} - \Psi_{\text{axis}}}}, \text{ with } \Psi_{\text{pol}} = \int \boldsymbol{B}_{\text{pol (tor)}} \cdot d\boldsymbol{S} \tag{1.22}$$

1.2.2 Plasma shaping

To characterize the reconstructed magnetic equilibrium, several geometric quantities, which are based on the magnetic equilibrium, are commonly used. Over the years, various plasma shapes have been explored, starting from circular shaped plasmas constrained by (toroidal/poloidal) limiter tiles over to diverted shaped plasmas with single or multiple X-points in order to minimize the contact between the plasma within the LCFS or separatrix and the plasma-facing components (PFCs). Plasmas with a X-point close to the lower divertor are called lower single-null (LSN) configuration. It is also possible to realize diverted plasmas with a X-point close to the upper divertor, which is called upper-single null (USN) configuration. Diverted plasmas with two X-points and two separatrices at the same time are called double-null (DN) configuration. Diverted plasmas which are close to the DN-configuration are referred here as close to double-null (CDN) configuration. Fig. 1.5 visualizes the magnetic equilibrium of ASDEX Upgrade (AUG) discharge #39231 at t = 4.0 s in a CDN-configuration. Subsequently, a set of these geometric quantities [Sau16] are listed:

$$R_{\text{geo}} = \frac{R_{\text{max}} + R_{\text{min}}}{2}, \tag{1.23}$$

$$a = \frac{R_{\text{max}} - R_{\text{min}}}{2}, \tag{1.24}$$

$$\kappa = \frac{z_{\text{max}} - z_{\text{min}}}{R_{\text{max}} - R_{\text{min}}} = \frac{b}{a}, \tag{1.25}$$

$$\delta_{\text{u}} = \frac{R_{\text{geo}} - R(z = z_{\text{max}})}{a}, \tag{1.26}$$

$$\delta_{\text{l}} = \frac{R_{\text{geo}} - R(z = z_{\text{min}})}{a}, \tag{1.27}$$

$$\delta = \frac{\delta_{\text{lower}} + \delta_{\text{upper}}}{2} \tag{1.28}$$

where R_{max}, R_{min}, $R(z = z_{\text{min}})$ and $R(z = z_{\text{max}})$ are the radius of outer, inner, upper and lower most points of the separatrix for diverted plasmas, whereas z_{min}, z_{max} are the vertical coordinate at the lower, upper most point of the separatrix. R_{geo} is the geometrical major radius, a is the minor radius, κ is the elongation and $\delta_{\text{u/l}}$ the upper/lower triangularity. Of interest is also the position of the separatrix R_{LCFS} at $z = 0.0$ m. This area is called outer midplane (OMP), where the phrase *outer* refers to its position on the LFS.

1.3 The H-mode, the foreseen regime for ITER and future fusion reactors

In 1982, it has been observed in the ASDEX (***A****xial****S****ymmetrisches* ***D****ivertor-****EX****periment*) tokamak [WBB+82] that above a certain heating threshold, the confinement of a plasma rises strongly (by a factor of ~ 2) forming an edge transport barrier (ETB) close to the plasma edge [WBB+85]. The ETB suppresses turbulent transport leading to a so-called *pedestal* with steep density and temperature gradients and improves significantly the global plasma performance. Such a regime is called *high confinement mode* (H-mode) [WFG+84] in contrast to a *low confinement mode* (L-mode) which labels discharges below the L-H threshold. The difference in the pressure profile between a L- and a H-mode is illustrated in Fig. 1.6 (left). The pedestal position itself is normally associated with the position of the maximum gradient in this region. Due to its promising confinement, H-mode plasma scenarios are the foreseen scenarios for ITER [IToCM+99] and also for future fusion devices [FKW+14].

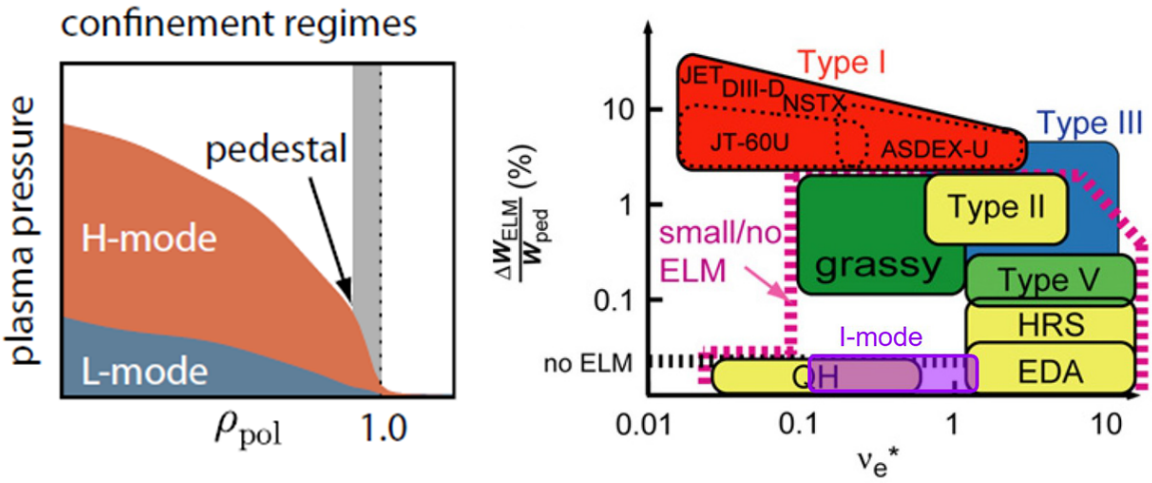

Figure 1.6: Left: Illustration of the difference between a L- and a H-mode based on their pressure profiles plotted against ρ_{pol}. The location of the pedestal region is highlighted in grey. The separatrix position is added as vertical black dashed line. Taken from Ref. [Gri18] and adapted. Right: Sketch illustrating the variety of ELM and no/small ELM scenarios [Vie18].

However, the presence of the steep gradients combined with high edge current densities triggers periodically occurring MHD instabilities. Such MHD instabilities are called *edge localised modes* (ELMs) [KBB+84]. With every ELM, the pedestal temperature and density collapse and ejects high energetic particles from the pedestal into the scrape-off layer (SOL), which reaches divertor and limiter components. The SOL denotes the area outside the LCFS in which the magnetic field lines are not closed. The magnetic topology forces the open field lines (and therefore any charged particles in the SOL) to the divertor plates which are designed to withstand high heat loads. After each ELM, the pedestal is recovered.
Since the exploration of the H-mode scenario, a zoo of H-mode scenarios with various kinds of ELMs have been discovered and investigated. A full classification for all reported type of ELMs is not possible and will be always incomplete. In Ref. [Zoh96], a classification for most common ELM-types has been suggested:

- **Type I**: Discovered together with the H-mode at ASDEX. The ELM-frequency f_{ELM}

increases with the heating power [Zoh96, GML+88]. Relative energy losses are reported to be up to 20 %. The ELM-evolution, also called *ELM-cycle*, can be well described by an ideal MHD-model based on the coupled peeling-ballooning boundaries [Con98, SWF+02]. However, this type of ELMs have to be avoided in future reactors. Various techniques have been suggested and experimentally tested [LCE+04, DML+03, dlLCR+15, NPSC+15, SKB+18] in order to suppress or mitigate large Type-I ELMs.

- **Type II**: Such ELMs are observed in plasmas with high κ, high δ_u and high separatrix density $n_\mathrm{e,sep}$ independent on the heating power [OA90, OCL+90]. They have been explored on several devices [SLS+05a, SLS+05b, KOS+09, WBB+11]. Such ELMs occur more frequently and with less amplitude than Type-I ELMs. Therefore, they are also called grassy or small ELMs. The relative energy loss is below 5 %.

- **Type III**: In contrast to Type-I ELMs, its f_ELM follows inversely the heating power [Zoh96]. They are normally observed close to the L-H threshold [KGM+98]. At AUG, such ELMS are also observed in the so-called I-phase [BCC+16] or in high-radiative scenarios at high density [BWH+17].

- **ELM-free H-modes**: It must be mentioned that also some H-mode scenarios have been reported in which larger ELMs are *naturally* absent. However, they have not been achieved in a large number of devices and less understood than the other ELM-types. A promising candidate out of these naturally ELM-free H-modes is the so-called enhanced D_α, dubbed EDA, regime which was originally discovered at Alcator C-mod [GBB+00] and has recently been explored at AUG [GSH+20]. Its main characteristic is the presence of a strong edge localised *quasi-coherent mode* (QCM).

An ELM-quantity, which is of relevance for the power exhaust task, is the so-called *relative ELM loss* [LSS+03]. It simply describes the energy ΔW_ELM lost due to a single ELM event and normalised by a reference plasma energy expression, which is usually the pedestal energy before an ELM crash $W_\mathrm{pre-ELM}$. For the determination of both quantities, the expression introduced in Equ. (1.11) can be used. By replacing n_e, T_e and T_i in Equ. (1.11) by the corresponding values from the pedestal close to an ELM event and integrating over the pedestal volume [LSS+03], one obtains $W_\mathrm{pre-ELM}$. To determine $W_\mathrm{post-ELM}$, the calculation has to be repeated with values acquired shortly after an ELM event. The difference between $W_\mathrm{pre-ELM}$ and $W_\mathrm{post-ELM}$ yields ΔW_ELM. The common parameter to assess the ELM-induced losses is the neoclassical pedestal collisionality ν_e^*, which can be expressed as [SALL99]:

$$\nu_\mathrm{e}^* = 6.9 \cdot 10^{-18} \frac{R q_{95} n_\mathrm{e} Z_\mathrm{eff} \ln \Lambda_\mathrm{e}}{\epsilon^{3/2} T_\mathrm{e}^2}, \tag{1.29}$$

where q_{95} denotes the safety factor q at ρ_pol=0.95, $\ln \Lambda_\mathrm{e}$ the Coulomb logarithm and ϵ the inverse aspect ratio.

Typically, the different ELM-types have been classified using ΔW_ELM and ν_e^* from different devices. Fig. 1.6 (right) illustrates the classification for various type of ELMs by its ΔW_ELM

plotted against the pedestal collisionality ν_e^*. It can be clearly seen that with decreasing ν_e^*, ΔW_{ELM} increases continuously for Type-I ELMs. As the foreseen H-mode scenario for ITER will operate at $\nu_e^* < 1$, ΔW_{ELM} will become critical for the lifetime of divertor and non-divertor components leading to an inevitable challenges for the power exhaust task.

1.4 How to deal with the power exhaust?

In order to generate fusion power in future fusion reactors, the triple product as introduced in Equ. (1.13) must be fulfilled. However, it has been realized that the variation of the three input parameters is experimentally constrained.
The maximum plasma temperature is limited by an optimal value in the reaction rates for the D-T reaction as shown in Fig. 1.1 (right). At the same time, the maximum achievable density is limited by an empirically deduced density limit. This density limit is called *Greenwald density limit* n_{GW} [Gre02] and is defined as:

$$n_{\mathrm{GW}} = I_{\mathrm{p}}/(\pi a^2). \tag{1.30}$$

As a last option, τ_{E} can be adjusted to optimize the triple product. τ_{E} depends on the choice of the operational regime (L-mode, H-mode,...). Assuming an H-mode scenario, τ_{E} can be expressed by a regression formula [IToCM+99] which considers only engineering parameters:

$$\tau_{\mathrm{E}} = 0.0562 \cdot I_{\mathrm{p}}^{0.93} \cdot B_{\mathrm{tor}}^{0.15} \cdot P^{-0.69} \cdot n^{0.41} \cdot M^{0.19} \cdot R^{1.97} \cdot \epsilon^{0.58} \cdot \kappa^{0.78}, \tag{1.31}$$

where P denotes the absorbed power, n the line-averaged density and M the hydrogen isotope mass. From Equ. (1.31), one can conclude that τ_{E} correlates strongly with the main radius R which makes it the easiest and most promising way to increase τ_{E}. Although increasing R has a positive effect on τ_{E}, it also has a negative effect on the power exhaust task. With increasing machine size, the power exhaust of a machine becomes more and more challenging. The fusion power generated by α-heating, the foreseen dominating heating channel in future fusion reactors, scales with R^3 [Zoh10]. Simultaneously, A_{Div}, the area on which the power crossing the separatrix is exhausted, scales linearly with R:

$$A_{\mathrm{Div}} = 2\pi R_{\mathrm{div}} f_{\mathrm{tor}} \lambda_{\mathrm{int}}, \tag{1.32}$$

where R_{div} is the major radius at the divertor, f_{tor} the toroidal wetted fraction and λ_{int} the poloidal extent of the wetted area along the divertor target. f_{tor} denotes the toroidal wetted fraction caused by the tile edge shadowing. At AUG, it is about 80 % [SEF+16]. The first two quantities are engineering parameters, whereas the latter one is a pure physical one. To keep the divertor peak heat fluxes below the material limits, λ_{int} should scale quadratically with R. λ_{int} can be expressed by a simple formula [MEG+12]:

$$\lambda_{\mathrm{int}} \approx \lambda_{\mathrm{q}} + 1.64 \cdot S, \tag{1.33}$$

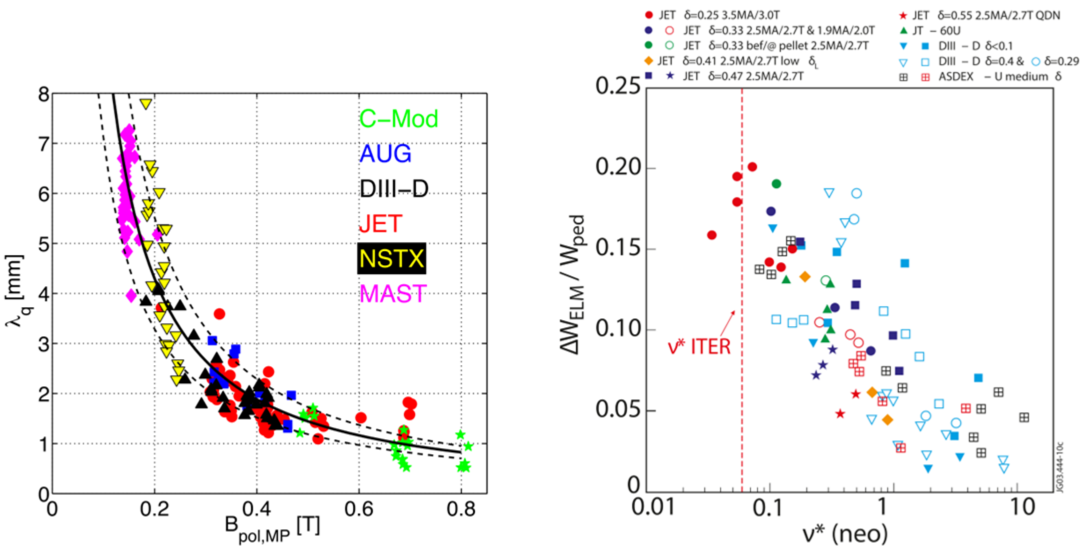

Figure 1.7: Left: Scaling of λ_q using $B_{\rm pol,OMP}$ [ELP+13]. Right: Relative ELM energy loss $\Delta W_{\rm ELM}/W_{\rm ped}$ for Type-I ELMs plotted against pedestal collisionality ν_e^* for different devices [LSS+03].

where λ_q denotes the power-fall length in the SOL and S the divertor broadening describing the decay length of the parallel heat flux into the private flux region [ESS+11, ELP+13]. For a LSN configuration, the private flux region is denoted as the area below the X-point and between the inner and outer strikeline. Both quantities can be derived by means of Infrared (IR) measurements from the divertor tiles by applying the Eich-fit [ESS+11]:

$$q(s) = \frac{q_0}{2} \exp\left(\left(\frac{S}{2\lambda_q}\right)^2 - \frac{s}{\lambda_q f_x}\right) \cdot \mathrm{erfc}\left(\frac{S}{2\lambda_q} - \frac{s}{S f_x}\right), \tag{1.34}$$

where q_0 denotes the peak heat flux at the divertor entrance, s the target location relative to the strikeline position and f_x the poloidal flux expansion [LBC+99] which takes into account the poloidal variation between the flux surface from the outer divertor target to outer midplane. S is defined for the target location range $s < 0$, whereas λ_q is defined for the target location range $s > 0$.
There are no empirical multi-machine scalings for S yet. For λ_q, a ITPA multi-machine based scaling has been provided for the Inter-ELM λ_q in attached conditions [ELP+13]. This scaling reports on a inverse correlation of λ_q with the poloidal magnetic field from the OMP $B_{\rm pol,OMP}$. The regression formula yields:

$$\lambda_{\rm q,scal} = (0.63 \pm 0.08) \cdot B_{\rm pol,OMP}^{-1.19\pm0.08} \tag{1.35}$$

The scaling is illustrated in Fig. 1.7 (left). Equ. (1.35) predicts a λ_q for steady-state heat loads of about 1 mm for the foreseen ITER operational conditions leading to insurmountable challenges for the divertor PFC target materials, whose heat load limit is envisaged to be 10 MW/m^2 [VKR$^+$21]. Next to steady-heat loads, one has to take also into account transient heat loads caused by the periodically occurring Type-I ELMs, which expel a large amount of high energetic particles into the SOL reaching divertor and non-divertor PFCs. In current devices, like JET and AUG, these additional heat loads are well below the material limits of divertor and non-divertor PFCs. However, following the trend as reported in Ref. [LSS$^+$03] and illustrated in Fig. 1.7 (right), the predicted relative ELM loss will be up to 20 % for the foreseen ITER pedestal collisionality. This will exceed the divertor heat load limit of about 10 MW/m^2 and in particular of non-divertor PFCs, whose heat load limit for steady-state conditions is about 2 MW/m^2. For ITER, such transient events must be suppressed or mitigated and in any future reactors totally avoided [FLS03, LHF$^+$14, EAH$^+$07, FBB$^+$19], otherwise the lifetime of the divertor and non-divertor PFCs will be significantly reduced.

1.5 The renaissance of the Type-II ELMy H-mode as solution for the power exhaust in ITER?

Several scenarios which attempt to handle the power exhaust challenge by exploiting different approaches are under investigation. An already abandoned scenario which has experienced a renaissance and has attracted great interest in recent years [HFR$^+$22, HWD$^+$18, Gri18, FEH$^+$21] is the Type-II ELMy H-mode. As a sign of a new beginning, this H-mode scenario has been renamed into *quasi-continuous-exhaust* (QCE) [FEH$^+$21] regime to reflect the new understanding in its physics.

This revived scenario combines high plasma core density $n_{\mathrm{e,core}}$ (close to 1.0 n_{GW}) and high separatrix density $n_{\mathrm{e,sep}}$ (up to 0.7 n_{GW} reached as well with pellet fuelling [FEH$^+$23]) at high upper triangularity δ_{u} in CDN-shaping. Beside the relevance of high $n_{\mathrm{e,sep}}$ in order to achieve both, high volumetric radiation losses in the SOL [GRS17] and a high neutral recycling state and divertor detachment [KPP$^+$13], high separatrix density plays a key role in the mechanism [HWD$^+$18, LEH$^+$19, WBB$^+$11, SLS$^+$05b] according to which Type-I ELMs are replaced by smaller, high frequency, incoherent filamentary[3] ELMs or bursts [Gri18, FEH$^+$21, VWD$^+$21].

As known from previous work in AUG at high $n_{\mathrm{e,sep}}$ [SWE$^+$15], a broadening of the e-folding temperature and density decay lengths λ_{n} and λ_{t} in the near-SOL is also observed in the QCE regime together with the formation of a density shoulder, which is associated with an enhancement of filamentary activities in the far-SOL [FEH$^+$21, VWD$^+$21, SVT$^+$22, CAB$^+$18]. As the width of the power-fall-off length in the SOL λ_{q} [ESS$^+$11] strongly correlates with the electron temperature decay length λ_{t} [SWE$^+$15], a broadening of λ_{q} at the main target together with a reduction of the the peak heat flux is also observed [FEH$^+$21].

[3]Filaments are described as objects which are elongated along the magnetic field lines and have a higher density than the background plasma in the SOL. Filaments cause a radially outward directed convective transport due to a self-generated ExB-drift in the SOL, which can significantly contribute to heat and particle fluxes to non-divertor PFCs [DMZ11].

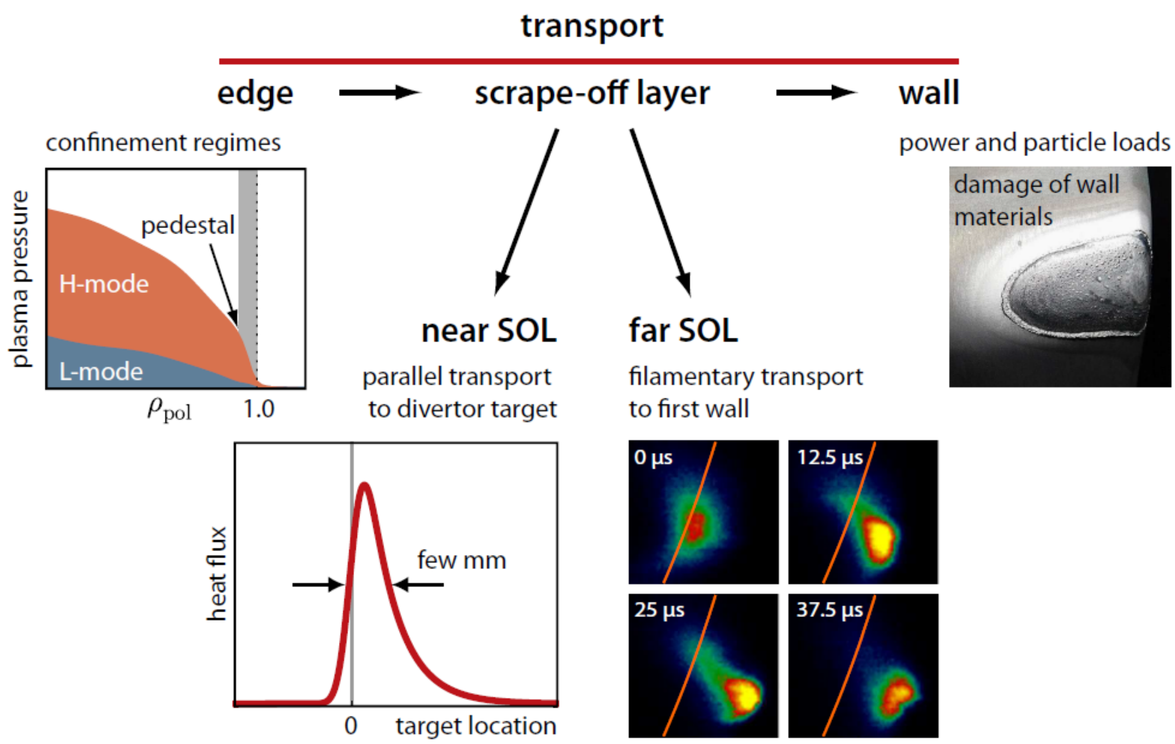

Figure 1.8: Sketch of transport processes starting at the plasma edge, covering the SOL and ending at the first wall. The transport in the SOL is characterized by its plasma conditions at the plasma edge, the conductive transport by the effective power fall of length in the near-SOL and the heat flux in the far-SOL by turbulent filaments. All these transport channels can lead to high heat loads on non-divertor components, like the first wall, as illustrated by a molten tungsten surface [Gri18].

So far, linear ballooning stability calculations realized with the code HELENA [HGK91, RDW+22] and non-linear, resistive, magnetohydrodynamic calculations realized with the code JOREK [CHH+22] suggest that the QCE regime profits from modes around the separatrix [HWD+18, LEH+19, Gri18] making this region ideally ballooning unstable and triggering more frequently filaments [DMZ11, Sco97] into the SOL. Such filaments are linked to the normalised pressure gradient, which is close to the critical value of ideal ballooning modes without reaching the peeling-ballooning boundary [HWD+18]. This might also be linked to fluctuative modes, which are located close to the separatrix, and have been observed with the thermal helium beam [Gri18] and with Doppler reflectometry [WBB+11]. The QCE scenario combines features that could be of interest for ITER or future fusion reactors. To date, however, the full extent of the enhanced filamentary transport is not yet known, which may lead to new challenges for the PFC material of non-divertor components, in particular for the first wall PFCs [WAA+17, BMC+15, DLA+17]. Fig. 1.8 illustrates this challenging interplay. The enhancement of filamentary activities around

the midplane [FEH+21, Gri18, VWD+21, SVT+22, WLC+18, SSC+22, DMZ11, CAB+18, VCT+20] causes a new convectively driven power loss channel directed radially to the first wall. This is linked to an increased energy deposition outside the divertor and has been intensively investigated over the last years in L- and H-modes in various devices [FEH+21, GWC+18, SSC+22, CAB+18].
However, the measurement of energy loads on non-divertor components requires dedicated diagnostics and is generally challenging. Most studies published so far lack of robust measurements of non-divertor energy loads. Over the last 30 years, several attempts have been reported in which the AUG IR thermography [HER+04, FEH+05], the AUG bolometry [BEK+15], the AUG cooling water calorimetry [RV94] and the JET thermocouples [MBD+17, MEF+01] have been exploited to measure non-divertor energy loads achieving a proper energy/power balance. However, the results of most studies are inconclusive, regardless of whether they were performed in a carbon, a full tungsten, or an ITER-like wall (ILW) device. To date, there is no in-depth analysis of the consequences of convective transport in terms of the power exhaust for the QCE scenario, which is of great relevance to become interesting for ITER. It is of utmost importance to investigate the link between convective transport processes in the SOL and their contributions to the heat flux reaching non-divertor PFCs.

1.6 Scope of this thesis

This thesis aims at assessing the consequences of an enhanced filamentary transport in H-mode discharges in AUG with respect to the power exhaust challenge. An enhanced filamentary transport is associated, inter alia, with an increased energy deposition on non-divertor components, mainly the first wall, which has to be investigated and understood for future magnetic confinement devices in order to avoid new challenges. As it has already been pointed out, the QCE scenario has many promising properties making it a reasonable choice for ITER and/or DEMO. However, this can be negated by disadvantageous properties in the area of power exhaust. The key questions faced in this thesis are therefore:

- Are we able to set up a reasonable global energy balance of a large, representative database?
- Are we able to resolve the radial convective filamentary energy transport to the first wall exploiting calorimetry and probe measurements?
- Is a radially directed enhanced filamentary energy transport connected with a redistribution of energy loads on the PFCs?
- Is there a parameter, most likely defined around the separatrix, which properly describes the evolution of SOL properties?

In **chapter 2**, both experiments, the AUG and JET tokamak, considered in this thesis are introduced. Furthermore, an overview of the commonly available diagnostics for both experiments is provided. The chapter is concluded with a short introduction in the theory of the separatrix operational space, which attempts to properly describe the global plasma performance by a set of dimensionless quantities deduced from separatrix quantities.

In **chapter 3**, the technical effort in revising the AUG calorimetry systems is firstly summarized. Steps to optimize the evaluation of the data and the values obtained are addressed. The revised evaluation methodology of both calorimetric diagnostics, the cooling water calorimetry and the wall thermometry, are discussed.

In **chapter 4**, a novel attempt in setting up the global energy balance in AUG is reported. A reasonable energy balance equation is defined. Each output contribution and its determination scheme is presented. Sources of uncertainties in the AUG global energy balance and possible improvements are discussed. Furthermore, a novel attempt in setting up the global energy balance in JET is also addressed. The chapter is concluded with an implication for empirical scalings.

Chapter 5 is divided into four parts: Firstly, the dedicated configuration of the discharges, which is necessary for this study, is discussed. The consideration of calorimetric diagnostics leads to peculiar requirements. Subsequently, the evolution of calorimetric measurements is associated with appropriate quantities. This also serves to assess the AUG operational space covered within this database. Based on this, the obtained correlations are linked to up- and downstream SOL profiles. Subsequently, dedicated probe measurements are discussed, which were performed close to the limiter. These allow a determination of the filamentary contribution to the convective transport. An estimation of the gross erosion on the first wall is addressed.

In **chapter 6**, the results of this thesis are summarized and an outlook discussing possible future studies is added.

Chapter 2

What do we need to describe a plasma?

In this chapter, an overview is given of the two fusion experiments with their properties and capabilities on which the results of this thesis have been carried out. Firstly, the ASDEX Upgrade (AUG) tokamak is introduced followed by an overview of the commonly available diagnostics, which are demanded for this thesis. Afterwards, the ***J****oint tokamak* ***E****uropean* ***T****orus* (JET) tokamak and its considered diagnostics are introduced. This chapter is concluded with a short introduction into the theory of the **SEP**aratrix **O**perational **S**pace (SepOS).

2.1 The AUG tokamak and its operational capabilities

AUG is the successor of the ASDEX tokamak, a fusion experiment which was successfully operated by the Max Planck Institute for Plasma Physics in Garching from 1980 to 1990. The special feature of ASDEX was the innovative use of the divertor, a special magnetic field topology, which on the one hand reduces significantly the contact of the enclosed plasma with the vacuum chamber and on the other hand enables efficient pumping of ash particles at the divertor plates due to the adapted magnetic field topology. This concept has proven successful and has been retrofitted in experiments such as JET and is intended for ITER.

AUG is a medium-sized tokamak in Germany, which has been operated by the Max Planck Institute for Plasma Physics in Garching since its commissioning in 1992. A sketch of this experiment is given in Fig. 2.1. Due to its construction, its divertor geometry and the special feature of a plasma chamber fully covered with tungsten (first demonstration of plasma operation with a full tungsten wall [NBB+07]), this fusion experiment is well suited to study reactor-relevant scenarios for the next tokamak generation, such as ITER. For its tasks, AUG is well equipped with a large number of heating methods (ohmic heating, neutral beam injection, electron and ion cyclotron resonance heating) and diagnostics covering

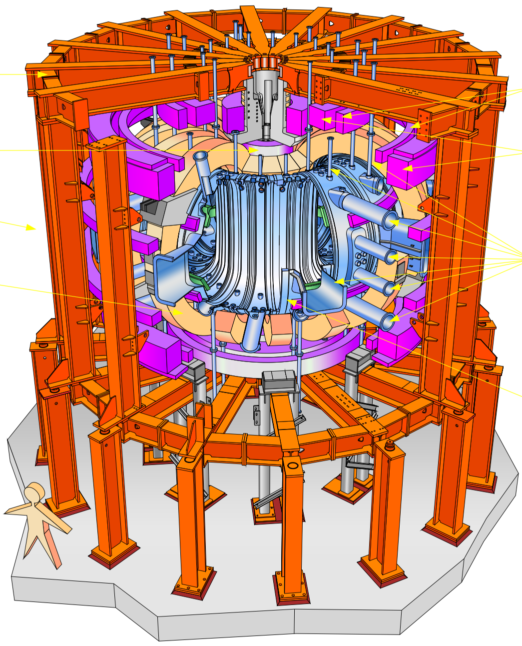

Figure 2.1: schematic illustration of the AUG tokamak [IPP23a].

key areas in the plasma core, edge and in the SOL. Important engineering parameters are summarized in Table 2.1. AUG has 16 toroidal magnetic field coils (light orange coloured coils in Fig. 2.1) generating the toroidal magnetic field. The poloidal part of the magnetic field is realized by means of a solenoid installed in the center of the vacuum chamber. In addition, there are further vertical field coils (purple coloured coils in Fig. 2.1) which are used for the positioning and shaping of the plasma.

major plasma radius R	1.65 m
minor plasma radius r	0.5 m
toroidal magnetic field $\lvert B_{\mathrm{tor}}\rvert$	1 to 3 T
plasma current $\lvert I_{\mathrm{p}}\rvert$	0.4 to 1.2 MA
heating power	up to 33 MW
plasma volume	14 m^3
plasma mass	3 mg
main plasma fuel	D, H, He

Table 2.1: Main parameters of the AUG tokamak

2.1.1 Reconstruction of the magnetic equilibrium

As the plasma density and temperature are commonly assumed to be approximately constant on each flux surface, the proper reconstruction of the magnetic equilibrium plays a key role. In order to obtain the the poloidal flux function $\psi(R, z)$, the Grad-Shafranov equation needs to be solved [GR58, Sha66]. The Grad-Shafranov equation is a partial differential equation which connects the poloidal magnetic flux with the current distribution in the plasma. At AUG, the code CLISTE [SML+00, MMS99] is used to solve the Grad-Shafranov equation with a linear combination of spline functions representing the current density. To match the magnetic measurements of the pick-up coils, which are shown as black markers in Fig. 2.3 (left), the coefficients of the spline functions are iteratively adjusted. These coils are placed around the entire vessel to measure the time derivative of the magnetic field and, by integrating the coil signals over time, the magnetic field at each coil position.

2.1.2 Internal and external heating methods

Ohmic Heating

In order to heat a magnetised plasma and to reach the conditions for fusion, several heating methods are utilized. An intrinsic heating method is the ohmic heating (OH). The toroidal current, which is generated through the central solenoid and required to produce the poloidal magnetic field contribution B_{pol}, heats the plasma through its resistivity [Spi51] well approximated by the so-called *Spitzer-conductivity.* This quantity can be expressed as [Str18, Spi51]:

$$\sigma_{\mathrm{Spitzer}} \approx \frac{(4\pi\epsilon_0)^2 (k_{\mathrm{B}} T_{\mathrm{e}})^{3/2}}{\pi Z_{\mathrm{i}} e^2 m_{\mathrm{e}}^{1/2} \ln \Lambda_{\mathrm{e}}} \tag{2.1}$$

where ϵ_0 denotes the vacuum permittivity and Z_{i} the ion charge. According to Equ.(2.1), this heating method is efficient at low temperatures, but its efficiency decreases, since $\sigma_{\mathrm{Spitzer}}$ scales with $T_{\mathrm{e}}{}^{-3/2}$. Further external heating methods are required. The most common ones present at any today's magnetic confinement devices are the neutral beam injection heating method and the electron/ion cyclotron resonance heating methods. Both are briefly described in the next sections.

Neutral Beam Injection Heating

The neutral beam injection (NBI) heating method heats the plasma by injecting fast neutral particles into the plasma. The entire heating mechanism can be described as follows: Ions are generated in a low temperature plasma, extracted and accelerated through an electric field with high voltages. The accelerated ions are neutralised via charge-exchange through a neutral gas cloud. Remaining ions are removed by a perpendicular magnetic field by deflections into an ion dump before reaching the plasma. The fast particles entering the

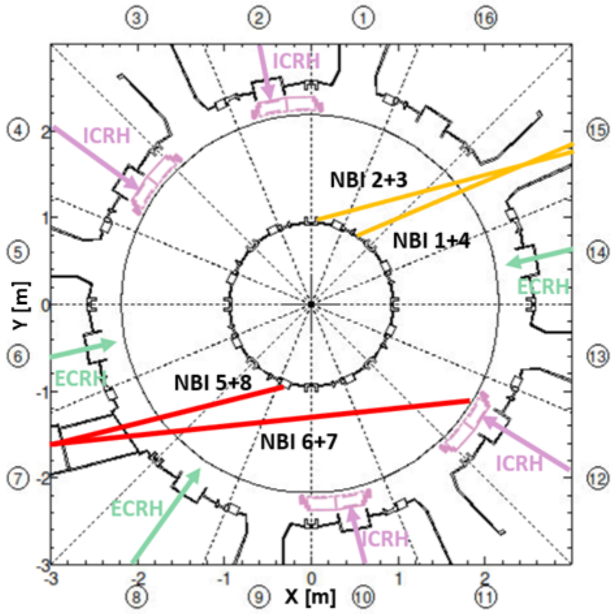

Figure 2.2: Toroidal overview of the AUG vessel indicating the position of the different available heating sources. Figure is motivated by Ref. [Leb18] and adjusted.

plasma transfer energy to the plasma via collisions, and once ionized are then confined by the existing magnetic field. Deuterium is typically used as ion source at AUG. As seen in Fig. 2.2, the NBI system of the AUG tokamak consists of 2 boxes installed in segment 15 (Box I) and segment 7 (Box II) with 4 beams, respectively. Each beam injects the particles with a total power of 2.5 MW. The beam sources labelled 1-4 installed in Box II have a full injection energy of 93 keV, the beam sources labelled 5-8 installed in Box I have a maximum injection energy of 60 keV.

Electron/Ion Cyclotron Resonance Heating

Next to injecting fast neutral particles, a plasma can be heated through electromagnetic waves injected into the plasma at the gyro-frequency or harmonics of the charged particles. The gyro-frequency is defined as:

$$\omega_c = \frac{ZeB}{m}, \tag{2.2}$$

where Ze is the charge number, B the magnetic field strength at the location of power deposition and m the mass of the charged particle. In fusion experiments, the wave heating of electrons is executed in GHz range and for ions in the MHz range. The frequency of the injected waves must fulfil the conditions for the wave given by the plasma dispersion relation to exist, to propagate through the plasma and to deposit its energy in a layer that corresponds to a plasma resonance. In case of the electron cyclotron resonance heating

(ECRH), the maser effect is exploited which allows to direct the radiation through mirrors into the plasma and to place the most components of the heating system outside the torus. Two different wave polarisations can be used, O-mode ($\boldsymbol{E} \parallel \boldsymbol{B}$) or X-mode ($\boldsymbol{E} \perp \boldsymbol{B}$). The AUG ECRH system consists of eight gyrotrons, for which each gyrotron can deliver 0.8 MW. Every gyrotron can emit waves at 140 GHz for standard operation at B_{tor} = - 2.5 T and waves at 105 GHz for plasma discharges at lower B_{tor} = - 1.8 T [SLL+03]. ECRH is beneficial to prevent the accumulation of (heavy) impurities such as tungsten in the plasma core, which reduces the plasma confinement due to increased radiation losses and can cause a plasma disruption.
The wavelength of the ion cyclotron resonance heating (ICRH) is in the order of meters, since the electron mass differs from the ion mass by a factor of $\sim 10^3$. In order to obtain best coupling with the plasma, the antenna size has to be on the same magnitude as the wavelength. Consequently, large antennas are installed into the vessel structure. Each antenna is equipped with a shielding, called *Faraday screen*, to avoid oscillations of ions in front of the antennas caused by local electric fields. The ICRH provides different absorption schemes in which resonant ions transfer mainly their energy to the bulk ions or to the electrons. The AUG ICRH system operate with four antennas that provide up to 6 MW at frequencies normally at 30 or 36 MHz. The positions of the ECRH and ICRH antennas in AUG are indicated in Fig 2.2.

2.2 An overview of exploited AUG diagnostics

For appropriate conclusions, accurate and reliable measurements of any quantity are decisive. The AUG tokamak provides a large amount of unique diagnostics. All commonly available diagnostics demanded for this thesis are briefly introduced in the subsequent section.

Foil Bolometry

In tokamaks, bolometers are used to measure the spectrally integrated radiation along each line of sight (LOS). By covering the vessel with a close-meshed LOS distribution the total plasma radiation can be determined. Foil bolometers utilize a thin foil of inert metal (e.g. gold) covering a meander structure, which is heated up by the radiation. The radiated power can be calculated from the resistance, which is sensitive to the changing foil temperature by a Wheatstone bridge. The radiative power can thus be determined by the following relation [GMS02]:

$$P_{\text{rad}} = C_1 \frac{dU}{dt} + C_2 \frac{dU}{\tau_{\text{c}}}, \tag{2.3}$$

where P_{rad} denotes the power deposited on the foil, U the voltage along the Wheatstone bridge and τ_{c} the cooling time constant of the foil. $C_{1,2}$ are calibration factors that summarize the heat capacity, the resistance and the electronic circuit [Ber13]. The AUG foil bolometry system consists of 128 LOS [DBP+21] (red lines in Fig. 2.3 (left)), and has a data acquisition rate of 1 kHz. A novel scheme (BPT) [DBP+21] allows an accurate estimation of the totally radiated power. With the aid of tomographic reconstructions [FMH+94], a 2D-radiation distribution can be obtained.

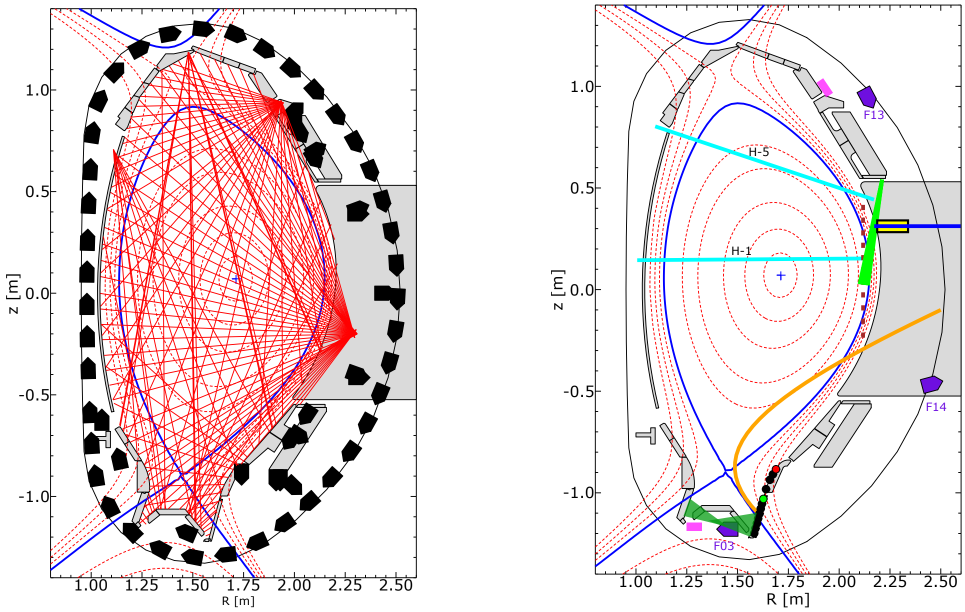

Figure 2.3: Left: Poloidal cross-section of AUG visualizing the distribution of foil bolometer LOS (red) and of magnetic pick-up coils (black). Right: Poloidal cross-section of AUG visualizing LOS of H-1 and H-5 interferometry (cyan), edge TS (brown), CXRS (green), IR (orange), MEM (blue) covering the LOS of the LIB, RFA2 (yellow with black contour), the distribution of the LPs (black, green and red) at the outer target, the baratrons (purple rectangles), the manometers (dark blue) and the D_α-LOS in the divertor (dark green triangles).

Laser interferometry

By passing through the plasma an electromagnetic wave with a wavelength λ_0 reveals a phase shift by a certain angle ϕ, which depends on the local electron density $n_e(l)$:

$$\phi = \frac{\lambda_0 e^2}{4\pi\epsilon_0 m_e c^2} \int n_e \mathrm{d}l, \tag{2.4}$$

where l is the path of the wave through the plasma and c the speed of light. Laser interferometry measures the line-integrated density of n_e and with a LOS mesh, the entire n_e-profile can be determined. At AUG, a deuterium cyanide laser (DCN) system equipped with a laser working at a wavelength of 195 μm is installed. Fig. 2.3 (left) shows the two relevant lines of sights H-1 corresponding to the core density and H-5 corresponding to the edge density. At the inner heat shield, a mirror is installed to reflect the injected electromagnetic waves. The phase shift ϕ is measured with a Mach-Zehnder interferometer. A phase shift of 2π measured with the interferometer refers to a line-integrated density of 5.3×10^{18} electrons/m^2 [MSE+10].

Lithium beam emission spectroscopy

The Lithium-beam emission (LIB) spectroscopy at AUG [WAW+93, FBB+99] measures the spectral radiance of the Li I(2s-2p) state transition from Li atoms injected into the plasma with an energy between 30 and 80 keV. The neutral Li atoms are excited and de-excited by collisions with the plasma particles. Ionisations through collisions and charge-exchange processes can also occur. As these processes depend all on n_e, a system of coupled linear equations are used to reconstruct n_e [FWStAUT08]:

$$\frac{dN_\mathrm{i}}{dl} = \sum_\mathrm{j} [n_\mathrm{e}(l) a_\mathrm{ij}(T_\mathrm{e}(z)) + b_\mathrm{ij}] N_\mathrm{j}(z), \tag{2.5}$$

$$N_\mathrm{i}(l = 0) = \delta_\mathrm{ij}, \tag{2.6}$$

where l is the coordinate along the lithium beam with l=0 representing the entrance of the beam to the plasma), N_i is the population state of the i-th energy level, a_ij is the rate coefficient for the transition $i \rightarrow j$ through collisions and the b_ij is the Einstein coefficient for spontaneous emission. The temporal resolution available at AUG, is 200 kHz [WWF+12].

Thomson scattering

The Thomson scattering (TS) diagnostic measures simultaneously n_e and T_e. The approach is based on the incoherent scattering of laser light on plasma electrons. Electromagnetic waves accelerate charged particles emitting radiation isotropically and scattering the incident wave. In magnetized plasma, only the scattering of electrons is considered. The Doppler width of the scattered incident wave provides information about T_e and the intensity about n_e. At AUG [KM11], two vertical TS systems are installed, one for the plasma core and one for the plasma edge. The latter is relevant for this thesis. The edge system consists of 4 lasers. The scattered incident waves are collected with 26 polychromators. The TS system provides a temporal resolution of 8 and 3 ms for n_e and T_e-measurements. The edge system covers a scattering volume of $\sim$ 3 mm^3. Fig. 2.3 (right) visualizes the LOS of the edge TS.

IR thermography

The IR thermography is a common tool to study heat fluxes on various plasma-facing components (PFCs). AUG is equipped with several IR cameras [SFH+15]. In this work, the IR camera, which observes heat fluxes on the divertor main target, is used. The photon flux Γ_λ is measured at a certain wavelength λ by the camera detector. According to Planck's law, the photon flux is related to the target surface temperature:

$$\Gamma_\lambda(T) = c_0 \epsilon \frac{2\pi c}{\lambda^4} \frac{1}{\exp(\frac{hc}{\lambda k_\mathrm{B} T}) - 1}, \tag{2.7}$$

where ϵ is the surface emissivity and h the Planck's constant. The quantity c_0 contains information of calibration, spectral bandwidth and the viewing angle of the camera. Supposing invertibility of Equ. (2.7), one can obtain an expression for the surface temperature T_surf depending on the measured Γ_λ. With the temporal evolution of the surface temperature the target heat flux can be calculated by solving the heat diffusion equation

$$\rho c_\mathrm{p} \frac{\partial T}{\partial t} = \nabla \cdot \boldsymbol{q}, \quad \text{with} \quad \boldsymbol{q} = \kappa \nabla T, \tag{2.8}$$

where ρ is mass density, c_p the specific heat capacity of the target and κ the heat conductivity of the target. At AUG, Equ. (2.8) is numerically solved using the implicit version [NvTSF18] of THEODOR [HJG+95]. The present system observing the divertor main target provides a spatial resolution of 0.6 mm and a temporal resolution of $\sim$ 0.5 ms. Applying the Eich-fit (1.34), allows to determine several key quantities assessing the target heat fluxes. Any deduced quantities are remapped to the OMP by exploiting the flux expansion f_x [LBC+99].

Langmuir probes

Langmuir probes (LPs) [Hut02] measure the current-voltage (I-V) characteristics of the plasma sheath with one or multiple protruding electrodes. The I-V characteristic is caused by the plasma particle fluxes and the electron temperature at the sheath entrance. Close to the wall, where the plasma gets in contact with the target, the so-called electrostatic sheath is generated. The electrons have much a higher mobility than ions, so that a negatively charged cloud is quickly established in front of the target. The potential difference caused by the sheath between the plasma and the target is called the plasma potential. Using sheath theory, several plasma parameters, like the electron or ion temperature $T_\mathrm{e/i}$, the electron density n_e and the heat flux $q_\perp$, can be simply obtained by fitting a theoretically derived I-V curve to the measured one. At AUG, so-called triple Langmuir probes [WC96] consisting of three electrodes are currently installed in the lower divertor and strongly simplify the analysis of the desired quantities. The poloidal resolution of the Langmuir probes on the divertor main target is 2–3 cm with an extension of 5 mm of the collectors. The distributions of the Langmuir probes at the outer target, which are mainly used on this study, are visualized in Fig. 2.3 (right).

Divertor shunt currents

So-called (thermo-)electric currents arise, if the plasma temperature in front of two ground tiles connected by a field line is different and consequently the floating potentials are also different. The (thermo-)electric currents compensate this arising potential difference.

These SOL currents [KCP+01a] are measured at multiple toroidal and poloidal locations in AUG by shunt resistors which are installed in the inner and outer divertor tiles. The currents of different poloidal locations, which are sensitive to ELMs, are added up to estimate the total current. The divertor shunt current is the main ELM monitoring signal for analysis work at AUG and is used for ELM-filtering aspects in this work.

D_α-radiation

Photo-diodes with a D_α filter are commonly used to measure the deuterium α spectral line. The measurements monitor the interaction of the plasma with neutral particles at several locations, mainly the plasma edge and SOL [LKG+17]. The light intensity depends on the electron temperature and density. ELMs are normally observed by the D_α-emission around the divertor target plates. The D_α-radiation is a further ELM monitoring signal for analysis work at AUG and also used for ELM-filtering aspects in this work. For this study, only the divertor measurements are considered. The LOS of D_α-measurements are indicated by the dark green triangles in Fig. 2.3 (right).

Charge-exchange recombination spectroscopy

To measure the ion temperature in plasmas, the charge-exchange recombination processes of impurities present in the plasma are used [VPC+13]. This is possible, since impurities are also subjects to ionization, recombination and emission of characteristic line. Common impurities at AUG are typically carbon, boron, nitrogen and helium, and can receive an electron via charge-exchange processes from neutral deuterium injected by a NBI beam. Assuming that the ionized impurity keep the bulk impurity energy and velocity, one can determine the temperature from the Doppler-broadening of the line radiation originating from those impurities. Since the thermalization time scales between impurity and main ions in AUG are shorter than those of the transport, it can be assumed that the temperature of the impurities is equal to the temperature of the main ions. The LOS of the toroidal edge charge-exchange recombination spectroscopy (CXRS) system are shown in Fig. 2.3 (right). Gaussian process fitting schemes [RN10, CGH+17] can be applied to combine the various CXRS diagnostics to provide the most likely profile for each quantity from IDI (Integrated Data analysis for Ion profiles) [FGI+20].

Baratron

The AUG tokamak is equipped with an extensive mass spectrometer system [RDM+19, NRSStAUT12] consisting of mass analyzers, capacitance gauges, ionization gauges and a pumping system, which allows measurements inter alia, of the neutral pressure p_n at different poloidal and toroidal positions. The pressure in the residual gas analyzer (RGA) is betwen 10^{-5} Pa and 10^{-1} Pa during discharges. p_n is seen as an engineering parameter, which depends on the fuelling level and the pumping speed. The measurements are calibrated to represent the neutral pressure at the port entrance and is a proxy for the neutral fluxes. In Fig. 2.3 (right), the purple rectangles illustrate the positions of the pressure gauges, also called baratron, in AUG, which are used for this study. One pressure gauge is installed in the roof baffle close to the inner divertor and one is located between the upper outer divertor and the passive stabilization loop (PSL) at the low field side.

Manometer

In order to measure properly the neutral flux density at various positions inside the vessel, linear hot cathode ionization manometers are considered. A hot cathode emits electrons which are then accelerated in an electric field in order to ionize neutral gas particles. An additional electrode collects the ionized gas particles. The ion and electron currents collected with the electrode allows to determine the neutral flux density. AUG is equipped with several manometers [HB98] at different poloidal and toroidal positions. The ones used in this study are indicated in Fig. 2.3 (right) as dark blue markers. F03 denotes the manometer operating in the roof baffle, F13 the one operating close to the upper divertor and F14 the one measuring the main chamber neutral flux density.

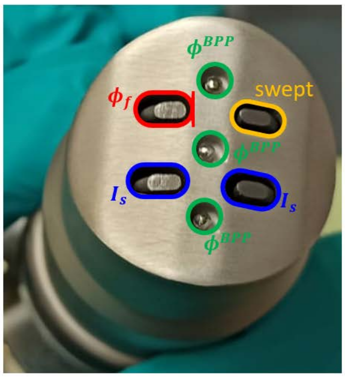

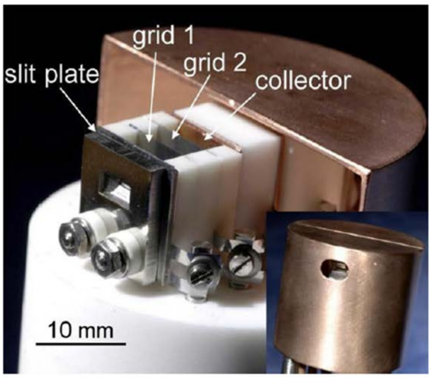

Figure 2.4: Left: Tip of the BPP head visualizing the probe distribution of the 3 BPPs (green) and the 4 LPs (blue, red and yellow). Taken from Ref. [GAK+22] and adapted. Right: Close-up of the RFA2 probe head showing the slit plate, grids, and collector. The insert in the right corner shows the RFA2 head with its housing. Taken from Ref. [KACC+12] and adapted.

Introduction of dedicated probe-heads

Both probe-heads are separately discussed in order to ensure a complete picture of their capabilities and evaluation methodology.

- **Ball-pen probe head**
  The Ball-pen probe head (BPP) is a probe-head recently available at AUG and is equipped with 3 ball-pen probe pins (BPPs) [AKP+08, AMS+16] and 4 Langmuir probes (LPs). The spatial probe tip distribution is shown in Fig. 2.4 (left). The

3 probes indicated in green are the BPPs on floating configuration ϕ^{BPP}, the blue indicated LPs measuring the ion saturation current I_{sat}, the red one the floating potential ϕ_{f} and the orange one indicated by *swept* the electron temperature T_{e}, ϕ_{f} and I_{sat}. The offset of each signal is subtracted by a running median filter. The BPP-head operates with an acquisition frequency of 2 MHz. This probe-head is mounted on the midplane manipulator (MEM) and executes several plunges within a single discharge. Each plunge lasts about 200 ms. The MEM operates about 35 cm above the midplane. The measurements of the BPP-head were taken about 1 cm in front of the limiter to ensure a safe operation for both, the diagnostic and the overall plasma. The detection of filaments follows the mostly commonly accepted approaches [TBM+18, GAK+22, DMZ11]. The analysis shown here uses a modified threshold

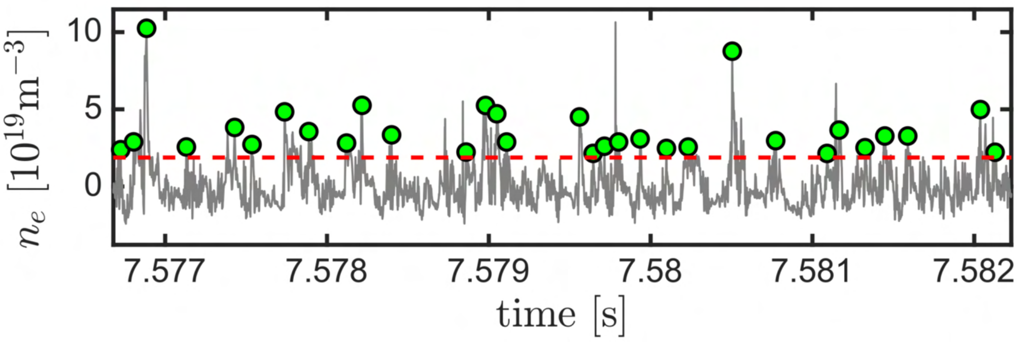

Figure 2.5: Time-trace of the density of a single plunge to illustrate the signal peaks as filaments detection criterion. The horizontal red dashed line represents the threshold criterion according to Equ. (2.9). The green markers indicate the peaks which are identified as filaments.

criterion in the density amplitude. The fundamental criterion being detected as filament is as follows:

$$I_{\mathrm{sat}}^{\mathrm{pk}} > 1.5\sigma + \langle I_{\mathrm{sat}} \rangle, \tag{2.9}$$

where $I_{\mathrm{sat}}^{\mathrm{pk}}$ denotes the amplitude peak, σ the standard deviation and $\langle I_{\mathrm{sat}} \rangle$ the mean value of the time interval chosen for the evaluation. Not all peaks above the threshold criterion are identified as filaments. Next to the threshold criterion (Equ. (2.9)), a filament must additionally fulfill a minimum peak width ($\omega_{\mathrm{sat}}^{\mathrm{pk}} = 5\mu s$), a peak distance ($d_{\mathrm{sat}}^{\mathrm{pk}} = 100\mu s$) and a correlation criterion as introduced in Ref. [TBPG07]. In Fig. 2.5, the red dashed horizontal line denotes the threshold criterion as defined in Equ. (2.9). The green markers denote peaks detected to be filaments.
For each identified filaments, several quantities can be derived. Fig. 2.6 (left) illustrates the density n_{e}, radial velocity v_{r} and electron temperature T_{e} derived from conditional average sampling utilizing the identified peaks in ion saturation current associated with filaments. T_{e} can be derived from:

$$T_{\mathrm{e}} = \frac{\phi^{\mathrm{BPP}} - \phi_{\mathrm{f}}}{\alpha^{\mathrm{LP}} - \alpha^{\mathrm{BPP}}}, \tag{2.10}$$

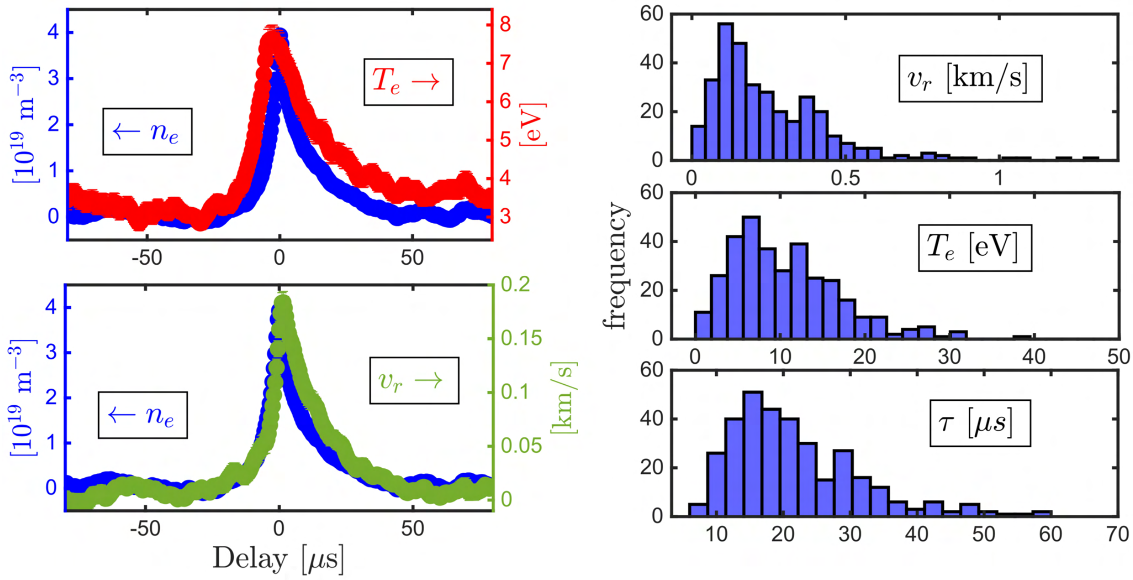

Figure 2.6: Left: Identified peaks and the derived quantities filament density n_e, filament radial velocity v_r and filament electron temperature T_e following the condition Equ. (2.9) and conditional averaged. Right: Histogram distribution of v_r, T_e and the filament correlation time τ of all detected filaments of a single plunge.

where α^{LP} and α^{BPP} denote the LP and BPP coefficients [GAK+22]. For α^{LP} an analytical formula is given [Sta00], whereas α^{BPP} must be experimentally determined [GAK+22]. The quantity v_r, which is caused by the ExB-drift of filaments [TBM+18], can be expressed by:

$$v_r = \frac{\Delta\phi^{BPP}}{d \cdot B}, \tag{2.11}$$

where $\Delta\phi^{BPP}$ denotes the potential fluctuation difference between two BPP, d the distance between these two BPPs and B the magnetic field strength at the tip. Since the LPs acts as a Mach probe, the parallel Mach number $M_\parallel$ [Hut02] is given by the expression:

$$M_\parallel = \frac{v_\parallel}{c_s} \approx 0.44 \log\left(\frac{j_{sat,up}}{j_{sat,down}}\right), \tag{2.12}$$

where $j_{sat,i}$ denotes I_{sat} of the respective LP divided by the probe surface area A_{LP}. n_e determined from a Mach probe can be expressed by [Hut02]:

$$n_e \approx \frac{1}{2ec_s}\left(\frac{j_{sat,up}}{\gamma^{up}} + \frac{j_{sat,down}}{\gamma^{down}}\right), \tag{2.13}$$

where $c_s \approx \sqrt{(T_i + T_e)/m_i}$ denotes the sound speed and γ^{down} is defined as [Hut02]:

$$\gamma^{down}(M_\parallel) = e^{(-1-1.1\cdot M_\parallel)} \tag{2.14}$$

Based on that, γ^{up} is defined as:

$$\gamma^{\mathrm{up}}(\mathrm{M}_{\parallel}) = \gamma^{\mathrm{down}}(-\mathrm{M}_{\parallel}) \tag{2.15}$$

The filament correlation time τ is based on the double *Full Width at Half Maximum* (FWHM) of an exponential decay function fitted to the peak profile. Multiplying the τ with the filament detection frequency ν_{detect} provides the so-called packing fraction f_{PF} [CAB+18]. As a last quantity, one can define the particle flux Γ_{r}, which is defined as:

$$\Gamma_{\mathrm{r}} = f_{\mathrm{PF}} n_{\mathrm{e}} v_{\mathrm{r}}. \tag{2.16}$$

For each plunge, all detected filaments are collected in order to derive the quantities as introduced above. For each quantity and plunge a histogram distribution can be provided. The filamentary quantities are obtained from their respective distributions. The background quantities are defined as the mean value of each plunge.

- **Retarding field analyzer #2**
  The AUG tokamak is equipped with an additional retarding-field-analyzer, dubbed RFA2 [ODB+20], which operates at the same poloidal position as the MEM, but at a toroidal different position as the MEM. The setup of the RFA2 probe-head follow common designs and can be found in Refs. [BLOW13, DRXH09]. The RFA2 provides $T_{\mathrm{i,RFA2}}$-measurements of the intermittent/turbulent nature of the far-SOL at the limiter surface. The RFA2 sweeps with up to 10 kHz its current–voltage (I–V) characteristics. The RFA2 evaluation scheme exploits a novel probabilistic

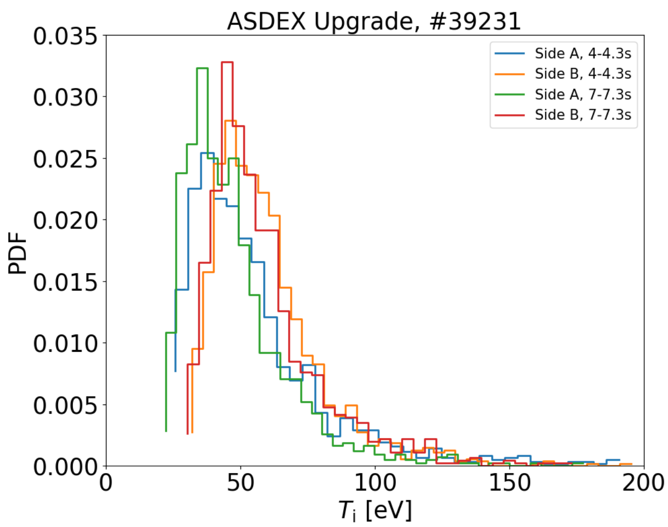

Figure 2.7: T_{i}-PDF measured close to the limiter surface by the RFA2. Two plunges were performed lasting 200 ms. Side A and B denotes the two grids as shown in Fig. 2.4 (right). For each plunge, the average of side A and B is taken and afterwards the mean value of both plunges is taken for further processing.

approach in order to determine $T_{\mathrm{i,RFA2}}$. A detailed description of the full probabilistic approach is provided in Ref. [ODB+20]. In the presented study, the RFA2 sweeps its current–voltage characteristics with 5 kHz. The choice of 5 kHz is a compromise due to the use NBI and short plunge durations. The obtained probability distributions function (PDF) of both grids (side A and B) are averaged (firstly side A and B of each plunge and then the plunges of a single discharge) and results in the $T_{\mathrm{i,RFA2}}$-representation. A profile of the $T_{\mathrm{i,RFA2}}$-PDF is illustrated in Fig. 2.7. Because of its field-alignment, the RFA2 actually provides $T_{\mathrm{i},\parallel}$ and not $T_{\mathrm{i},\perp}$, which would be actually demanded for the characterization of the radial transport. Due to the large distance from the separatrix, it is reasonable to assume that all degrees of freedom of the $T_{\mathrm{i,RFA2}}$-distribution in filaments as well as in the background plasma are evenly distributed. Therefore, it is assumed $T_{\mathrm{i},\perp}= T_{\mathrm{i},\parallel}$ in this analysis, which is covered by previous AUG high-density L-modes studies [CAB+18]. Due to choice of 5 KHz sweeping frequency, the provided $T_{\mathrm{i,RFA2}}$-values do not resolve the fluctuations associated with filaments and they can only be considered as a lower limit for $T_{\mathrm{i,fil}}$. Nevertheless, important conclusions can still be drawn from the evolution of $T_{\mathrm{i,RFA2}}$ throughout the conducted fuelling scans.

2.3 The JET tokamak and its operational capabilities

The JET tokamak is currently the largest operating tokamak, located in Culham, United Kingdom, and is operated by the Culham Center for Fusion Energy (CCFE) until December 2023. The JET tokamak is currently the only tokamak in the world which is able to perform D-T plasmas. JET was commissioned as a limiter tokamak in 1983 and upgraded to a divertor tokamak in 1993. Between 2009 and 2011 the original carbon fibre reinforced composites (CFC) PFCs were replaced by an ITER-like design (JET-ILW) using beryllium tiles in the main chamber and tungsten tiles in the divertor. The plasma can be heated by several (external) heating methods using OH, NBI with up to 32 MW and ICRH with up to 10 MW. In sum JET plasmas can be externally heated with up to 42 MW.

major plasma radius R	3.2 m
minor plasma radius r	1.0 m
toroidal magnetic field $\lvert B_{\mathrm{tor}}\rvert$	up to 4 T
plasma current $\lvert I_{\mathrm{p}}\rvert$	up to 3.5 MA
heating power	up to 42 MW
plasma volume	80 m^3
main plasma fuel	D, H, He, T, DT

Table 2.2: Main parameters of the JET tokamak

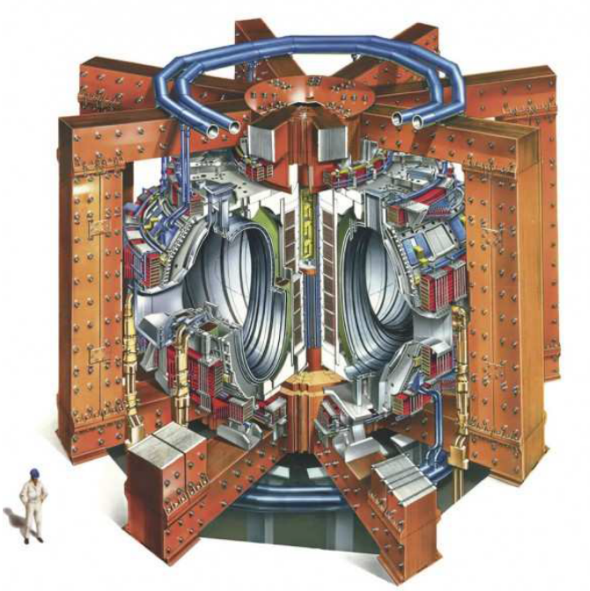

Figure 2.8: schematic illustration of the JET tokamak [EUR23].

2.4 An overview of exploited JET diagnostics

2.4.1 Bolometry

At JET, two main-vessel bolometric cameras (KB5V and KB5H) are installed with a horizontal and a vertical LOS distribution with 24 chords for each camera. This system covers a high energy range (up to 8 keV) together with high sensitivity ($\sim$ 6.2 V/W) and high temporal resolution ($\sim$ 2 ms). The divertor region is equipped with three additional bolometer cameras (KB3) with 12 LOS in total. Both systems (KB3 and KB) combined enable measurements with a sufficient spatial resolution to clearly determine the divertor and main chamber radiation. Fig. 2.9 (left) provides the LOS distribution of the JET bolometric system [HMA+07].

2.4.2 Calorimetry

To measure reliably energy loads on any PFCs, the JET tokamak is extensively equipped with thermocouples covering the entire divertor, the inner/outer guard limiters and the upper dump plates. The tiles in JET are inertially cooled and thermally insulated from the support structure. As a consequence, the JET tiles require long times to cool down in order to be in internal thermal equilibrium. This is fulfilled $\sim$ 500 s after each discharge. Therefore, cooling by radiation is the dominating energy loss channel for all tiles. To extrapolate the decay profile, the function of radiation cooling must be fitted to the experimental profiles [MEF+01]:

$$\frac{dT_{\mathrm{TC}}}{dt} = a(T_0^4 - T_{\mathrm{TC}}^4), \tag{2.17}$$

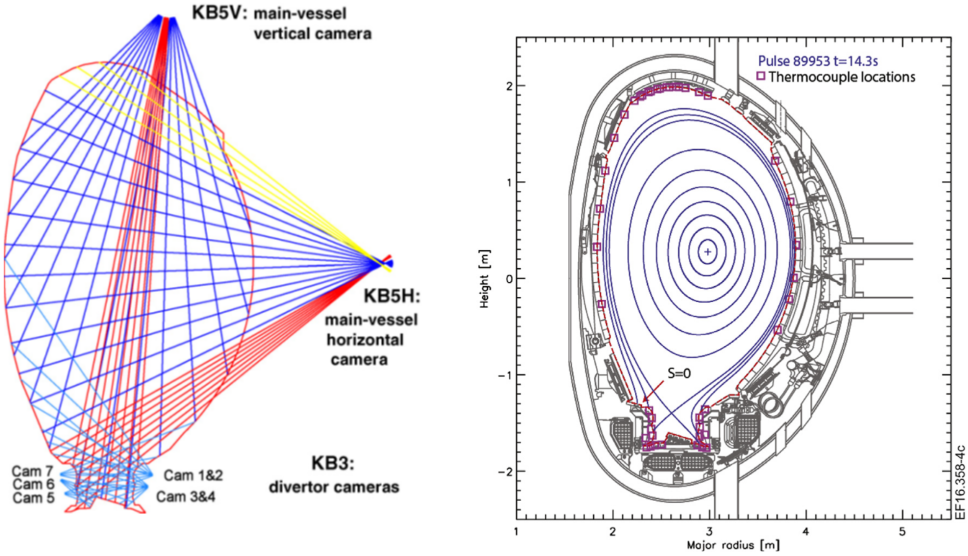

Figure 2.9: Left: LOS distribution of the JET bolometry consisting of the bolometry cameras KB5 and KB3 [HMA+07]. Right: Distribution of the thermocouples in JET [MBD+17].

where T_{TC} is the thermocouple temperature in K, T_0 the temperature of the radiation sink and a is a constant. a and T_0 are determined from the fitting procedure.
With the fit function and the tile mass m_{tile}, the tile-resolved stored energy Q can be determined:

$$E_{\mathrm{tile}} = m_{\mathrm{tile}} \int c_{\mathrm{p}}(T) dT, \tag{2.18}$$

where c_{p} denotes the heat capacity of the tile material (values can be found in Ref. [MBD+17]). Fig. 2.9 (right) illustrates the thermocouple distribution in JET.

2.5 The SepOS-theory, a novel theory to describe the plasma performance

For the characterisation of the SOL turbulent transport, not only high-performance diagnostics are desirable, but also a consistent theory, which is able to properly describe the plasma performance. Over the last years, a novel theoretical framework has been developed attempting to properly describe the widening of the SOL decay lengths by a set of dimensionless parameters. The SepOS-theory, first introduced in Refs. [RDZ98, Sco05a, Sco07] and revived and unified in Refs. [EMG+20, EMtAUt21, EAH+07], is based on the complex Drift-Alfven (DALF) model [Sco98a, RDZ98, Sco05b] and attempts to best describe DALF turbulence and therefore also interchange and MHD instabilities by exploiting separatrix conditions.

It is a concept which seems to be able to properly qualify the power exhaust capabilities of a plasma scenario in terms of ideal ballooning stability and the nature of turbulence. In Ref. [EMG+20] for low-δ discharges and in Ref. [FEH+23] for high-δ discharges, it has been experimentally proven in AUG that the operational window and limits of L- and H-mode discharges correlate well with the separatrix properties.
In this section, the methodology to determine robustly values close at the separatrix is first introduced. Subsequently, the novel turbulence control parameter α_t is introduced in Refs. [EMG+20, EMtAUt21], describing turbulence at the separatrix as well as the boundaries of H-modes in the $n_{e,sep}$-$T_{e,sep}$ plot.

2.5.1 Methodology

To determine robustly the separatrix quantities in a standardised scheme, the framework as introduced in Refs. [SWE+15] is used, exploiting the AUG edge TS. The edge TS data are ELM-filtered and need to be averaged in 300 ms intervals in order to obtain usable TS profiles, particularly for the inter-ELM profiles of Type-I ELMy H-modes. Due to the vertical LOS distribution, the TS profiles have to be remapped exploiting the reconstructed magnetic equilibrium.
To determine the separatrix position, which is challenging due to the presence of steep gradients between pedestal and separatrix, the power balance ansatz described below is applied assuming Spitzer-Härm electron heat conduction to be the dominating parallel transport mechanism in the SOL, which sets the electron temperature at the separatrix. To calculate this value, the so-called *Two-Point-Model*, introduced in Ref. [Sta00], is exploited. The parallel heat flux can be expressed by:

$$q_{\parallel} = -\kappa_0 T_e^{\frac{5}{2}} \frac{dT_e}{ds_{\parallel}}, \tag{2.19}$$

where $s_{\parallel}$ is the parallel coordinate along the field lines and κ_0 the Spitzer-Härm thermal heat conductivity. The latter quantity can be written as:

$$\kappa_0 = 60 \frac{\sqrt{2\pi}\epsilon_0^2}{e^4 \sqrt{m} Z_{\rm eff} \ln \Lambda_e}, \tag{2.20}$$

where ϵ_0 is the electric constant. For AUG, typical values of κ_0 (considering $Z_{\rm eff} \sim 2$ in the SOL) are $\sim 2000\ \frac{\rm W}{\rm eV^{7/2} m}$ [KCP+01b]. Assuming that the power crossing the separatrix P_{sep} ($P_{sep} = P_{heating,tot} - P_{radiation,core}$) is transferred uniformly into the SOL along the connection length L (from the OMP down to the outer target) leads to the expression:

$$\frac{dq_{\parallel}}{ds_{\parallel}} = \frac{P_{Sep}}{A_{SOL} L}, \tag{2.21}$$

where A_{SOL} is the SOL cross-sectional area perpendicular to the magnetic field. Integrating twice along $s_{\parallel}$ from the target ($s = 0$) to the outer divertor target ($s = L$) yields:

$$T_u = \left(T_t^{7/2} + \frac{7}{4} \frac{P_{sep} L}{A_{SOL} \kappa_0} \right)^{2/7} \approx \left(\frac{7}{4} \frac{P_{sep} L}{A_{SOL} \kappa_0} \right)^{2/7}, \tag{2.22}$$

where in the last step the target temperature T_t is neglected, since the upstream temperature T_u normally fulfils in H-modes the condition $T_u \gg T_t$. The expressions L and A_{SOL}, can be further simplified [EGK+18]:

$$L = \pi q_{cyl} R, \quad A_{SOL} = 4\pi R \langle \lambda_q \rangle \cdot \frac{B_{pol}}{B_{tor}}, \tag{2.23}$$

where $\langle \lambda_q \rangle$ the poloidally averaged power fall-off decay length [ELP+13] and q_{cyl} the cylindrical safety factor. The latter two quantities are defined as [EMG+20]:

$$q_{cyl} = \frac{B_{tor}}{B_{pol}} \frac{a}{R} \hat{\kappa}, \tag{2.24}$$

$$\text{with } B_{pol} = \frac{\mu_0 I_p}{2\pi a \hat{\kappa}} \tag{2.25}$$

$$\text{and } \hat{\kappa} = \sqrt{\frac{1 + \kappa^2 (1 + 2\delta^2 - 1.2\delta^3)}{2}}, \tag{2.26}$$

where μ_0 is the vacuum permeability. All these quantities can be inserted into Equ. (2.22) leading to the expression:

$$T_{e,sep} \approx \left(\frac{7 P_{sep} q_{cyl}^2 R}{16 \kappa_0 \hat{\kappa} a \langle \lambda_q \rangle} \right)^{\frac{2}{7}}. \tag{2.27}$$

As last step, T_u is relabelled to $T_{e,sep}$ to be clearly termed as separatrix electron temperature. Applying a diffusive ansatz for the parallel transport in the SOL, T_e and q can be expressed in terms of exponential decay functions:

$$T_e(s) = T_{e,sep} \cdot \exp\left(-\frac{s}{\lambda_t \cdot f_x} \right), \tag{2.28}$$

$$q_{\parallel}(s) = q_{\parallel,0} \cdot \exp\left(-\frac{s}{\lambda_q \cdot f_x} \right), \tag{2.29}$$

where $s = 0$ denotes the position at the separatrix and $s > 0$ the SOL region. $s < 0$, covering the area in the private flux region, is excluded. Inserting these two equations into Equ. (2.27), one yields the ratio:

$$\frac{\lambda_t}{\lambda_q} = \frac{7}{2} \tag{2.30}$$

To obtain this ratio, the relation $q_{\parallel} = P_{Sep}/A_{SOL}$ has to be inserted into Equ. (2.19)). This correlation between heat flux and temperature decay length has been proven experimentally to be in good agreement for AUG plasmas in Ref. [SWE+15].
An iterative numerical scheme solves Equ. (2.27) searching for the position in the TS electron temperature profiles where the calculated and the measured $T_{e,sep}$ matches within 2 %. The corresponding values of n_e, T_e and electron pressure p_e, with their respective e-folding decay lengths, correspond to ρ_{pol}=0.999 [EMG+20].

2.5.2 Introduction of the turbulence control parameter α_{t} deduced from the DALF model

In the original works [Sco98a, Sco98b, Sco05b, RDZ98], two dimensionless parameters were identified to properly describe the relative strength of the turbulent transport mechanisms. The theory suggests to describe the highly complex phenomena of plasma edge turbulence by a set of parameters connecting them with the broadening of the near SOL decay lengths (λ_{n}, λ_{t} and the pressure decay length λ_{p}). In Ref. [RDZ98], two key parameters were identified which control the plasma edge turbulence. One is the ideal MHD ballooning parameter α_{MHD}:

$$\alpha_{\mathrm{MHD}} = R q_{\mathrm{cyl}}^2 \frac{\beta}{\lambda_{\mathrm{p}}}, \tag{2.31}$$

$$\text{with } \beta = \frac{4\mu_0 p_{\mathrm{e}}}{B_{\mathrm{tot}}^2}. \tag{2.32}$$

Furthermore, the diamagnetic parameter α_{d}, controlling the impact of drift-wave dynamics on the interchange instability has been introduced:

$$\alpha_{\mathrm{d}} = \sqrt{\frac{(m_{\mathrm{i}}/m_{\mathrm{e}})c_{\mathrm{s}}}{0.51\nu_{\mathrm{ei}}(2\pi q_{\mathrm{cyl}})^2 R}} \left(\frac{R}{\lambda_{\mathrm{p}}}\right)^{\frac{1}{4}}, \tag{2.33}$$

where ν_{ei} denotes the electron-ion Braginskii collision frequency [Bra65]. In Refs. [Sco05a, Sco07], the same phenomena is described from a different point of view by considering the impact of the interchange effect on drift-wave turbulence controlled by the so-called resistive ballooning parameter $C\omega_{\mathrm{B}}$. ω_{B} describes the strength of the curvature drive and therefore the strength of the interchange turbulence. This quantity is defined as:

$$\omega_{\mathrm{B}} = \frac{2\lambda_{\mathrm{p}}}{R}\left(1 + \frac{1}{\bar{Z}}\right), \tag{2.34}$$

where $\bar{Z} = n_{\mathrm{e}}/\sum_{\mathrm{j}} n_{\mathrm{j}}$ denotes the average ion charge. The thermal diffusivities, $\chi_{\mathrm{e,i}}$ follow linearly the normalised collisionality $\chi_{\mathrm{e,i}} \sim C \cdot \chi_{\mathrm{GB}}$ with χ_{GB} the gyro-Bohm diffusivity [Sco02]. Therefore, the transport seems to be partially controlled by the normalized collisionality C:

$$C = 0.51\nu_{\mathrm{ei}} \frac{\lambda_{\mathrm{p}}}{c_{\mathrm{s}}} \frac{m_{\mathrm{e}}}{M_{\mathrm{i}}} \left(\frac{q_{\mathrm{cyl}} R}{\lambda_{\mathrm{p}}}\right)^2. \tag{2.35}$$

where $(\hat{q}_{\mathrm{cyl}} R/\lambda_{\mathrm{p}})$ denotes the ratio of the parallel to the perpendicular scale lengths controlling the adiabaticity of the electrons and $\lambda_{\mathrm{p}}/c_{\mathrm{s}}$, which is required due to time normalization. $M_{\mathrm{i}} = \bar{M}/\bar{Z}$ denotes the characteristic ion mass, where $\bar{M} = \sum_{\mathrm{j}} n_{\mathrm{j}} M_{\mathrm{j}}/\sum_{\mathrm{j}} n_{\mathrm{j}}$ denotes the average ion mass with M_{j} the mass of the different ion species and n_{j} the density of the different ion species. In Ref. [EMG+20], geometrical effects of the non-circularity of the separatrix are taken into account by $\hat{\kappa}$ (introduced in Equ. (2.26)) and corrections for impure plasmas by $\bar{M}$.

Simulations have proven that $C\omega_{\mathrm{B}}$, like α_{d}, seems to be able to control the relative strength of interchange and drift-wave turbulence by determining the cross-phase between pressure and potential perturbations [Sco02, EMG+20]. It is indicated that the transition to the ideal ballooning regime requires a critical, sharp value in α_{MHD}, whereas the transition to interchange turbulence (*resistive ballooning turbulence*) is rather continuous and smooth [Sco02]. Based on that, the novel turbulence control parameter α_{t} defined in Ref. [EMG+20] has been introduced:

$$\alpha_t = C\omega_{\mathrm{B}} = q_{\mathrm{cyl}}^2 R \sqrt{\frac{m_{\mathrm{e}}}{\bar{M}}} \frac{1.02\sqrt{2}e^4 \ln(\Lambda) n_{\mathrm{e}}}{12\pi^{3/2}\epsilon_0^2 T_{\mathrm{e}}^2} \cdot \sqrt{\bar{Z}}(1 + 1/\bar{Z}) \cdot Z_{\mathrm{eff}} f_{Z_{\mathrm{eff}}}, \tag{2.36}$$

where $f_{Z_{\mathrm{eff}}}$ denotes a correction function considering the modifications in the numerical factor in the Braginskii electron resistivity for single-charges ion species for $Z_{\mathrm{eff}} > 1$ [EMG+20]. For the study presented in this thesis, a simplified formula, which is only valid for AUG

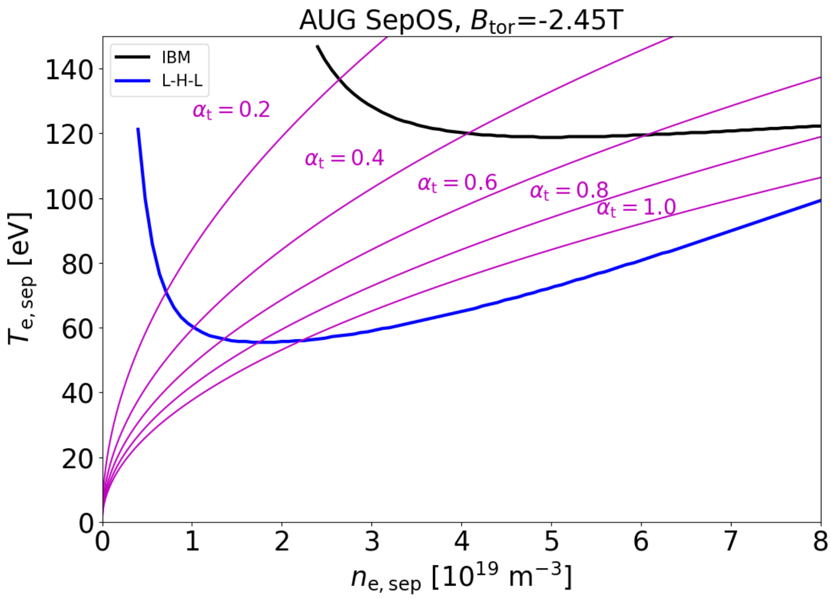

Figure 2.10: AUG separatrix operational space in edge density $n_{\mathrm{e,sep}}$ and $T_{\mathrm{e,sep}}$ with B_{tor}=-2.45 T and I_{p}=0.8 MA at $\delta_{\mathrm{u}} \approx 0.28$ and $\kappa \approx 1.7$. Z_{eff} is set to 1.24. The L-H-L transition boundary (blue) and ideal ballooning limit boundary (black) are indicated narrowing the accessible operational window for H-modes in the $n_{\mathrm{e,sep}} - T_{\mathrm{e,sep}}$ plot. Isobars of α_{t} (purple) at [0.2, 0.4, 0.6, 0.8, 1.0] are added.

conditions, can be used [EMtAUt21]:

$$\alpha_{\mathrm{t}} \approx 3.0 \cdot 10^{-18} q_{\mathrm{cyl}}^2 \frac{n_{\mathrm{e}}}{T_{\mathrm{e}}^2} Z_{\mathrm{eff}} \tag{2.37}$$

α_{t} seems to regulate the strength of the resistive-interchange turbulence relative to drift-wave transport by setting the phase shift between the potential and electron pressure

fluctuations [EMG+20]. According to Ref. [EMtAUt21], several boundaries constrain the operational space of a tokamak (Greenwald density limit, accessibility of high confinement, H-mode and loss of high confinement and technical feasibility due to power exhaust requirements). In Ref. [EMG+20], three boundaries are introduced; two of them are relevant for this thesis: the ideal ballooning mode limit, which describes the boundary for the maximum achievable pressure gradient and the L-H-L transition boundary (Equ. 8 in Ref. [EMG+20]), which describes the boundary for the minimum separatrix temperature required to enter the high confinement mode. Both boundaries are outlined in Fig. (2.10) for an AUG plasma with B_{tor}=-2.45 T and I_{p}=0.8 MA at $\delta_{\mathrm{u}} \approx 0.28$ and $\kappa \approx 1.7$. Z_{eff} is set to 1.24. Additionally, the isobars of α_{t} covering the entire H-mode operational window narrowed by the two boundary lines are added. In Ref. [FEH+23], it has been shown that these boundaries seem to be also valid for high-δ plasmas.
Most of the separatrix operational space is in the drift-wave regime ($\alpha_{\mathrm{t}} < 1$), particularly any H-mode discharges are in this regime. Following Refs. [RDZ98, Sco05a] the interchange regime becomes dominant for ($\alpha_{\mathrm{t}} > 1$) yielding an H-Mode operational limit in the region of $\alpha_{\mathrm{t}} \sim 1$. In Ref. [FEH+23], it has been shown that for high-δ H-mode plasmas, α_{t} can exceed 1 and the H-mode plasma is still preserved, leading to a new, so far unknown, upper limit for α_{t}.
As highlighted in Refs. [EMG+20, FEH+23], α_{t} is strongly linked to the normalised edge collisionality ν_{ei}, which is a common parameter to describe filamentary properties [VCT+20, CAB+18] and already shown to be of interest in Refs. [SVT+22, REV+23]:

$$\alpha_{\mathrm{t}} \propto q_{\mathrm{cyl}} \nu_{\mathrm{ei}}^{*}, \quad \text{with} \quad \nu_{\mathrm{ei}}^{*} = \frac{\pi q_{\mathrm{cyl}} R n_{\mathrm{e}} Z_{\mathrm{eff}}}{10^{16} T_{\mathrm{e}}^{2}}, \tag{2.38}$$

where α_{t} reveals a stronger dependence on q_{cyl} than ν_{ei}^{*}.

Chapter 3

Introduction of the recommissioned calorimetry diagnostics of AUG

This chapter introduces two calorimetric diagnostics, the cooling water calorimetry, dubbed KWK, and the wall thermometry, which are key diagnostics for this study. These two diagnostics have been revised and recommissioned as part of this thesis. Before both diagnostics are introduced, a short section summarizes the effort in updating and optimizing the data acquisition. Excerpts of this chapter are taken from Refs. [HRR$^+$23, RHE$^+$23a].

3.1 Hardware update of the entire data acquisition as requirement for the revision of the AUG calorimetry diagnostics

With the construction of the AUG tokamak in the early 1990s, an extensive cooling system was installed that encompasses the entire vessel and allows the cooling water temperature to be measured separately for all 16 segments of the vacuum vessel. This cooling system has been exploited to set up the cooling water calorimetry, which will be introduced later. However, this 1st generation setup suffered from several drawbacks including limited data acquisition time, noisy signals which limited the accuracy of the measurements, and maintenance effort [HRR$^+$23, RHE$^+$23a]. It was therefore abandoned in 2006 after AUG discharge #20739.
During the last years, the use of W PFCs and the development of novel plasma scenarios have renewed the importance of calorimetric measurements. To overcome the disadvantages of the old KWK, the signal acquisition, which was originally self-made, has been entirely revamped using standardized industrial components keeping the maintenance effort at a low level. The use of standardized industrial components also provides Windows programs, automatically updated and maintained by the manufacturer, for flexible interaction with the system and easy extraction of profiles, which are required for the evaluation of the calorimetric diagnostics. This modernization allows the performance of the system

to be increased, which is now able to resolve the temperature with an uncertainty of ± 0.03 K and a time resolution of 1 s for the KWK. In the case of the AUG wall thermometry, the resolution of the thermocouples have been improved to 0.5 K with a time resolution of 1 s.

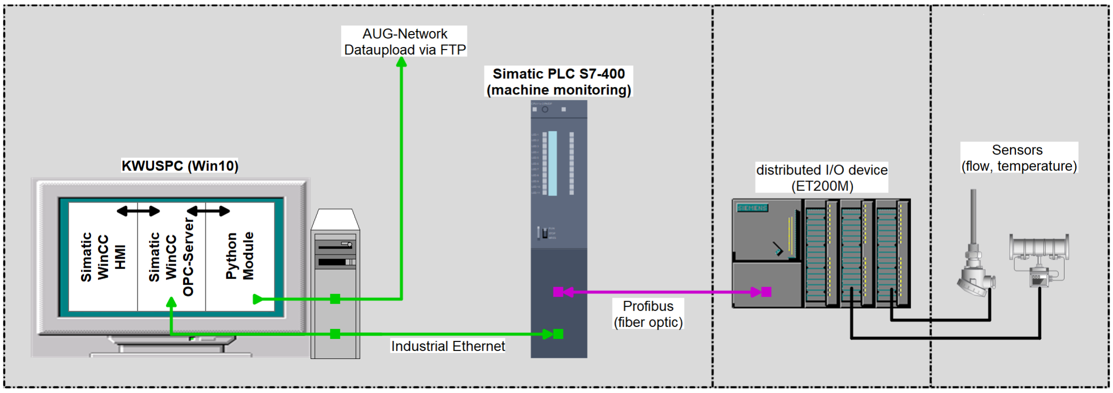

Figure 3.1: Simplified sketch of the data acquisition procedure [HRR+23].

Fig. 3.1 provides a simplified overview of the setup for the optimized data acquisition [HRR+23], which has been finished during the campaign 2020/2021. One Siemens ET200M [Sie21a], a modular periphery device, is used for each octant (a unit consisting of two segments; the AUG vessel is toroidally divided into 16 units of equal size). All Platinum resistor thermometers PT-100 of an octant are connected to the ET200M via copper cables. This modular periphery device is connected via fiber optics with a Simatic Controller, model S7-400 414-3 [Sie21b]. Visualization of the acquired data is carried out via the Simatic WinCC program. Access to the data provided by the Simatic S7-400 CPU is enabled via an Industrial Ethernet connection. In addition, a Python script runs on the PC with the Simatic WinCC program which aggregates the data for both diagnostics from the OPC server following the trigger marks of the AUG discharge operation. The data is captured between the trigger signal *DV1* (10 s before an AUG discharge starts) until the trigger signal *TS0* ($\sim$ 30 s before the subsequent discharge) of the following discharge. The recorded temperature data with a temporal resolution with 1 s are therefore not of equal length. The minimum length is 600 s, which corresponds to the minimum break between two experiments at AUG, up to a restricted length of 3600 s. When the trigger *TS0* occurs, the file is saved locally on the PC and additionally automatically uploaded to the andrew file system (AFS) data storage system [BBB+99, BBB+14] via a File Transfer Protocol (FTP) connection for further processing. On the AFS data storage system, this file is written into a standardized shotfile for AUG visualization tools [BBB+99, BBB+14] using another Python routine. The improvement made with these efforts is illustrated in Fig. 3.2 comparing dedicated time traces of cooling water temperatures.

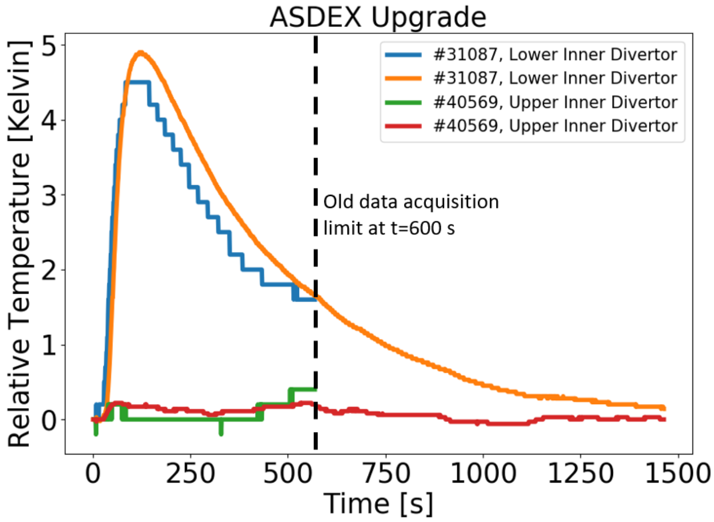

Figure 3.2: Curve comparison from lower and upper inner divertor in segment 1. The blue and green curves show the trace from data acquired with the old data acquisition system, which is limited to max. 600 s length and the orange and red curves show the data acquired with the new system. Plasma discharges with similar parameters are compared.

3.2 The AUG cooling water calorimetry

At the time of its construction, an extensive cooling water system covering the AUG tokamak has been installed to ensure the proper cooling of all PFCs as well of the supporting structures. Each of the 16 toroidal segments constituting the vessel shares a cooling circuit with an adjacent segment to cool the in-vessel components. In this system specific in-vessel components are assigned to a single cooling unit. Fig. 3.3 (left) provides an overview of the installed cooling units denoted with colored areas, which encompass these areas completely, in the toroidal direction. Each segment is equipped with five cooling units covering respectively the upper (inner/outer) divertor, the lower (inner/outer) divertor and the heat shield resulting a total of 80 cooling units. The roof baffle is aligned to the cooling unit *Lower Inner Divertor* due to changes in the divertor geometry since the 1^{st} generation setup. The cooling units indicated in black in Fig. 3.3 (left) are installed in specific segments. All PFCs of each ICRH antenna are connected to the cooling system, are assigned to one cooling unit and are individually resolved. The ICRH antennas are installed in segments 2, 4, 10 and 12 and define the main midplane limiter of the divertor tokamak. The additional auxiliary limiters are installed in segments 6, 8, 14 and 16. One auxiliary limiter is installed on each side of the NBI duct and represents one cooling unit. Each auxiliary limiter is located radially slightly behind the main limiter in order to reduce energy loads on diagnostics. In total, 88 cooling units are available, which cover almost entirely the vessel in the poloidal and toroidal directions. Additionally, the tiles covering the PSL are highlighted in yellow. Due to the huge thermal capacity of the Copper PSL structure [VSE$^+$13], this part of the in-vessel components cannot be used for calorimetric

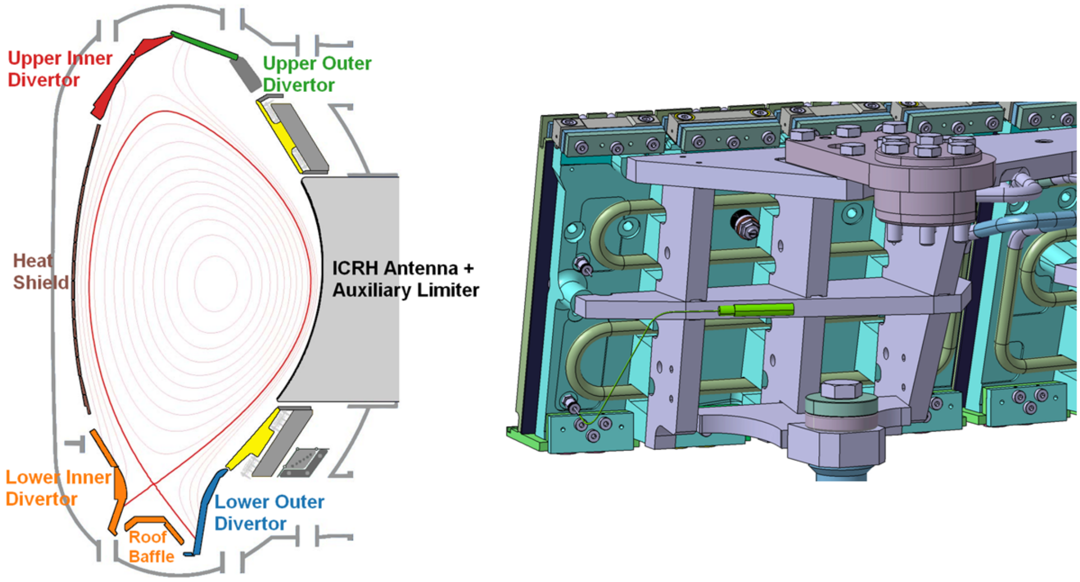

Figure 3.3: Left: Poloidal cross-section of AUG showing all installed cooling units. The cooling units highlighted by colored areas are installed in all 16 segments. The roof baffle is assigned to the cooling unit *Lower Inner Divertor*. The cooling units marked in black are installed in specific segments: the auxiliary limiters are installed in segments 6, 8, 14 and 16. The ICRH antennas are installed in segments 2, 4, 10 and 12. The tiles covering the PSL are highlighted in yellow. Right: CAD drawing of the backside of a part of the cooling unit *Lower Outer Divertor* of a single segment.

studies.
Fig. 3.3 (right) shows a computer-aided design (CAD) drawing of the rear side of parts of the cooling unit *Lower Outer Divertor* of a single segment illustrating the setup of the AUG cooling system. The full tungsten tiles are mounted on the front of the support structure by clamps at the top and bottom of the tile. Papyex furnished with graphite (Mersen) is placed between the tiles and the support structure in order to ensure contact between tiles and the support structure and to reduce the thermal resistance. The cooling water tubes (green) brazed on the rear side of the support structure are installed to transport the deposited energy in the tiles by the cooling water out of the vessel.
Each segment has its own branch of the cooling circuit which supplies the colored cooling units in Fig. 3.3 and the cooling units of the auxiliary limiter in the respective segments. The inlet cooling tube is divided among the individual cooling units of the segment, which is illustrated in Fig. 3.4 (left), and merged after leaving the tokamak vessel. Platinum resistor thermometers PT-100 are installed in both the inlet cooling tube (before branching) and outlet cooling tubes of the cooling units (after leaving the vessel) in order to measure the cooling water temperature. These thermometers are installed as close as possible to the experiment in order to minimize energy losses in the cooling water due to thermal

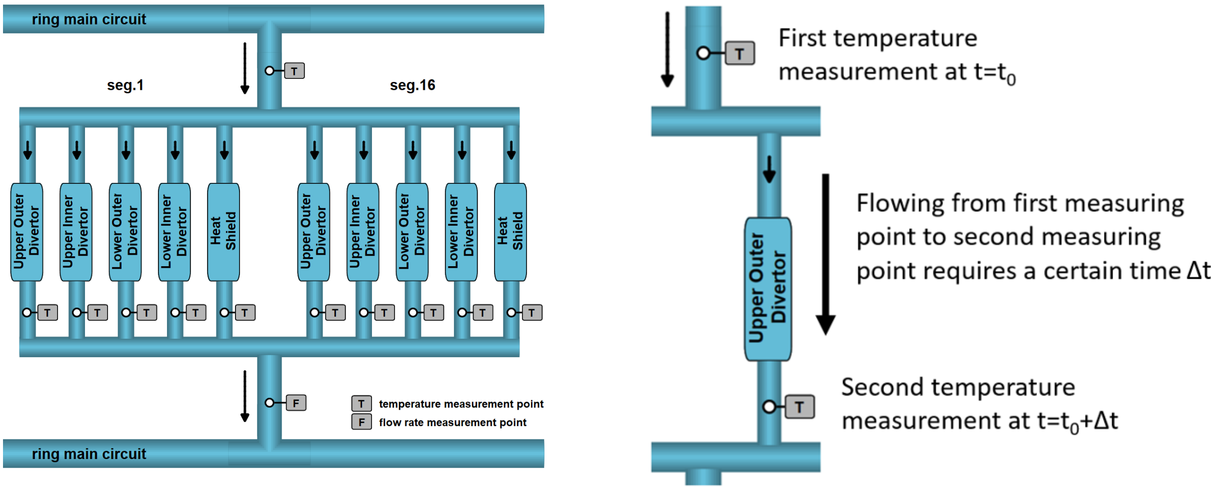

Figure 3.4: Left: Simplified illustration of the cooling circuit of two segments (here segments 1 and 16). From the ring main circuit, the inlet cooling water temperature is measured before the cooling water is distributed to the individual cooling units of each segment. After leaving the vessel, the temperature of the outlet cooling water of the respective cooling units is measured. After merging the individual cooling tubes, the flow rate of the segment is measured. Right: Close-up of the cooling water circuit of the cooling unit *Upper Outer Divertor* to illustrate the required shift in the temperature profile between inlet and outlet cooling water temperature measurements.

transfer through the tubes to the environment (even though the tubes are thermally insulated outside the vessel). The cooling units of the ICRH antennas have their own cooling circuits in the respective segments. The setup is equipped with single flow rate meters and differential pressure transmitters in order to measure the flow rate of the outlet cooling water of each octant and the cooling circuits of the ICRH antenna.

3.2.1 The underlying theory for the calorimetric evaluation of the cooling water system

To calculate the energy deposition per cooling unit Q, the formula as given in Refs. [RV94, RV92] has to be solved:

$$Q = m \int_{t_1}^{t_2} \Delta T c_{\mathrm{p}} dt \tag{3.1}$$

To solve this integral several experimental inputs are needed:

- the heat capacity of the cooling water c_{p}, here 4184 $\frac{\mathrm{J}}{\mathrm{kg \cdot K}}$.
- the flow rate m for each cooling unit. At AUG, active flow rate measurements are not available for individual cooling units and must be measured manually. For this purpose, a portable ultrasonic flow-meter, KATflow 200, is used.

- the relative temperature ΔT, which is the difference between the inlet and outlet cooling water temperature.
- the time interval $[t_1, t_2]$, which has to cover the full excursion in the relative temperature profile ΔT.

The flow rates used for the AUG campaigns 2020/21 and 2021/2022 for all cooling units can be found in Ref. [RHE+23b]. The DivIIo-Upgrade [HTZ+19] will not affect the flow rate values. The flow rates of the cooling units in segments 2 and 10 cannot be measured anymore, since the respective cooling tubes are blocked by various installations. In order to achieve usable flow rates for segments 2 and 10 the relative branchings of comparable segments are used and multiplied by the flow rate of the inlet cooling water of segments 2 and 10.
Since the discharge duration is short (max. 10 s), which is much smaller than the heat conduction time for the in-vessel components, no real-time data is available. Measuring the temperature signals during the cooling-down phase, allows only time-integrated results representing the entire discharge.
For the proper determination of the time variation of the relative temperature ΔT, several adjustments have to be taken into account:

- All PT-100 signals of a segment have to be calibrated to a reference signal. A PT-100 measures absolutely the cooling water temperature, but small offsets are unavoidable and can prevent the evaluation, particularly for cooling units with a small ΔT. Fig. 3.5 (upper) shows the raw data from of segment 1 without any adjustments for AUG discharge #39649. If both, the cooling water and cooling units are in thermal equilibrium, the difference in the temperatures represents the offset by which the signal must be corrected. Fig. 3.6 (left) illustrates the temperature of the equilibriated cooling unit in segment 1. The outlet cooling water data are shifted to the inlet one of the respective segment. Fig. 3.6 (right) presents the corrective shift for segment 1 and Fig. 3.5 (middle) illustrates the cooling water temperature data corrected by the offset shift on the outlet temperature data. This corrective offset must be experimentally determined every few weeks.
- The cooling water requires a certain time Δt in order to flow from the inlet to the outlet measuring point requiring, a shift by Δt for the relative temperature rise. Fig. 3.4 illustrates the cause of the correction. This time correction Δt can be obtained by using the flow rate of the respective cooling unit, the tube diameter d and the distance between the two measuring points l. The first two parameters are well known, but the latter is not. Therefore, the inlet temperature data are manually shifted in time to the outlet temperature data according to characteristics in the inlet and outlet temperature data. Fig. 3.5 (lower) illustrates the offset and time corrected data finally usable to determine the energy deposited in each cooling unit. Using the obtained time correction values, the distance between the two measuring points can also be estimated. The distances obtained are reasonable and vary between 15 and

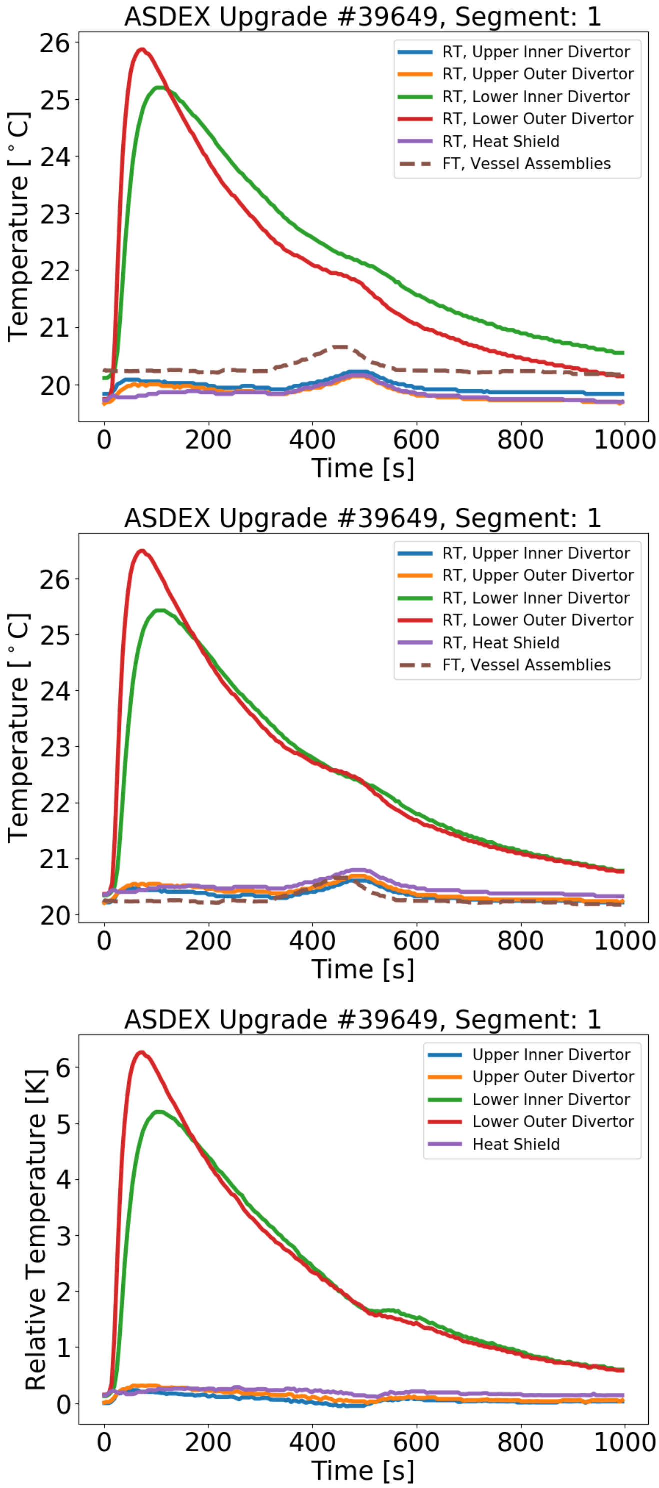

Figure 3.5: Upper: Raw data from segment 1 of the return temperatures (RT) and flow temperature (FT) of AUG discharge #39649. Middle: Offset as defined in Fig. 3.6 (right) applied on all RT signals. Lower: Δt-corrected and FT-subtracted relative temperatures of RT signals.

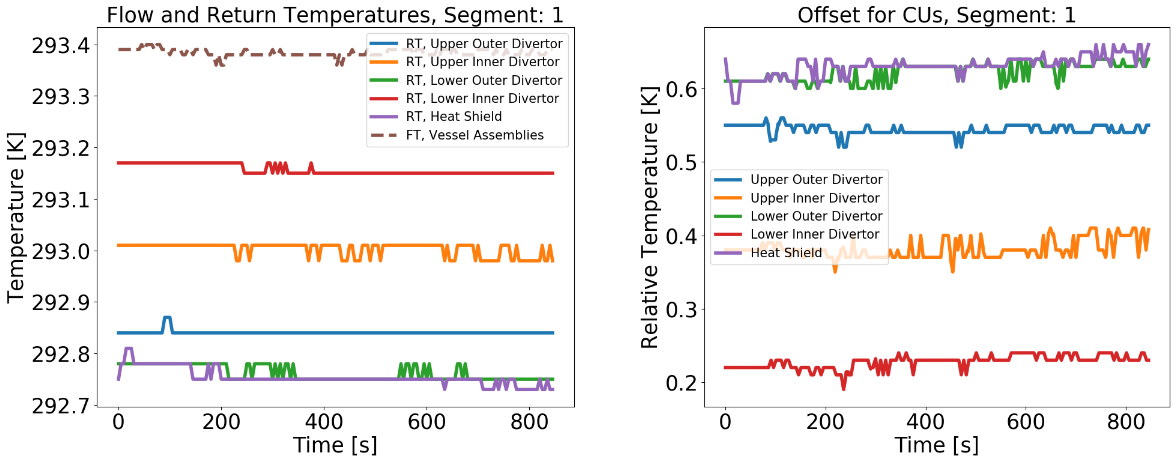

Figure 3.6: Left: Raw data of the equilibriated cooling units in order to correct the offset between flow and return temperature profiles. Right: Offsets obtained by subtracting return temperature data from the flow temperature data.

25 m depending on the cooling unit. The obtained results can be found in Ref. [RHE+23b].

For the proper determination of the relative temperature ΔT, the chosen time interval $[t_1, t_2]$ must cover the full rise in ΔT in order to calculate correctly the energy deposition in each cooling unit. The temperature signals may not cover the full cooling down phase. Fig. 3.7 shows an example of a not fully acquired decay curve. The red and green curves represent the original ΔT data. The evaluation routine identifies the peak of the relative temperature ΔT and separates it into two curves at a time point 75 s after the identified peak. The red curve in Fig. 3.7 represents the part of the profile until the separation and is simply numerically integrated. The green curve in Fig. 3.7 represents the profile after the separation and is used as fit reference for a double exponential fit defined as:

$$\Delta T(t) = T_0 \cdot (\mathrm{e}^{-\kappa_{\text{cooling down, 1}} \cdot (t - t_{\text{start}})} + \mathrm{e}^{-\kappa_{\text{cooling down, 2}} \cdot (t - t_{\text{start}})}), \tag{3.2}$$

where T_0, $\kappa_{\text{cooling down, 1}}$ and $\kappa_{\text{cooling down, 2}}$ have to be fitted. In case of the heat shield, a simpler fit function with just one exponential decay function is used. The parameter t_{start} represents the time at the starting point for the fit, T_0 the initial relative cooling water temperature at time t_{start} and $\kappa_{\text{cooling down, 1/2}}$ cooling down coefficients. The limit of Equ. (3.2) is set to 0. The two cooling down coefficients, which are required to best match the experimental data may be related to short term and long-term cooling down behaviour between the PFCs and their connected cooling structure. The fit representing the decay curve is extrapolated until it reaches the initial temperature before the temperature rise. The orange curve in Fig. 3.7 represents such an extrapolated fit curve. The sum of the integrated red curve and the orange curve yields the full energy deposited in a cooling unit.

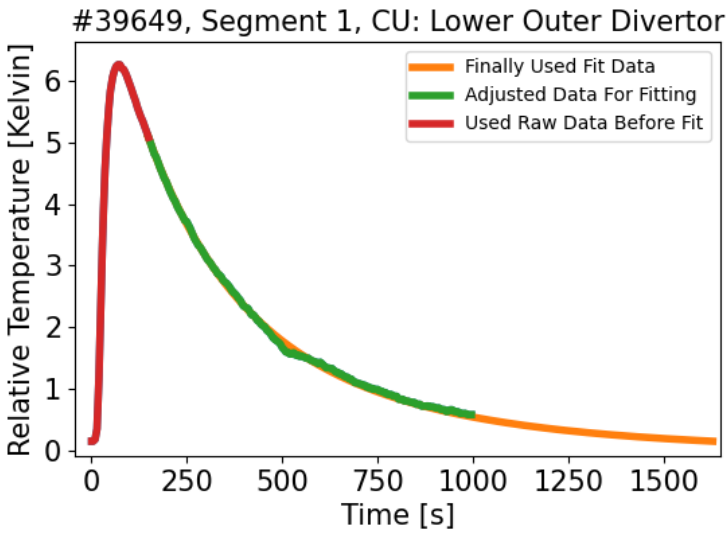

Figure 3.7: Plot of the ΔT-profile for the cooling unit in the lower outer divertor in segment 1 for AUG discharge #39649. The green and red curves yield the original ΔT. The orange curve represents the extrapolated fit function (according to Equ. (3.2)) providing the full decay singal required for the calculation of the deposited energy in this cooling unit.

An overall error associated with the evaluation can be estimated and is based on two uncertainties:

- the uncertainty in the measured flow rate; according to the manual ± 3 %
- the uncertainty in the acquired cooling water temperature profiles, here ± 0.03 K

The uncertainty of the flow rate meter is multiplied by 2 (meaning ± 6 %) in order to take into account that the required setup of the portable ultrasonic flow rate meter to measure the flow rate cannot be realized properly for all cooling tubes close to the AUG vessel due to the pipeline routing, leading to a larger uncertainty than provided by the manufacturer. Since several mathematical operations are required to obtain the required ΔT-profile for Equ. (3.1), the overall uncertainty from this source is ± 0.12 K (for each mathematical operation the resolution uncertainty of ± 0.03 K is added). Both uncertainties are used as additional fit parameters in the fit routine for Equ. (3.2). The upper/lower error for all cooling units is the sum of the respective upper/lower error of each cooling unit yielding an estimated overall error of ± 6-7 %.

3.2.2 First results of the energy distribution in AUG

The AUG campaigns 2020/2021 and 2021/2022 are the first campaigns in which measurements of the revised cooling water calorimetry have been acquired and evaluated. To illustrate the capabilities of the new calorimetric diagnostic, the time traces of main plasma parameters, the equilibrium and the energy distributions of three different discharge scenarios are discussed (overviews provided in Fig. 3.8 and in Table 3.1). The plots of the first column show the time traces of specific plasma parameters, the middle column the equilibrium at time = 4.0 s and the third column the energy distribution obtained with the revised calorimetry.

The energy distribution of a ***Quasi-Continuous-Exhaust*** discharge

The upper row illustrates the properties and results of a typical QCE discharge. The key properties of such a scenario are operation at a high δ_{upper}, leading to a CDN-shaping (the middle plot visualizes this equilibrium), high core and separatrix density $n_{\mathrm{e,core/sep}}$ (see plot c) and the absence of Type-I ELMs associated with an enhanced filamentary transport in the far-SOL, which dominates the radial transport at the midplane [FEH$^+$21, VCT$^+$20]. These properties are consistent with the observations made with the cooling water calorimetry. The energy found on the lower inner divertor (orange bars) is lower compared to the one found on the lower outer divertor (blue bars). These conditions are compatible with a (partial) detachment of the inner divertor. The cooling unit *Lower Inner Divertor* consists of the PFCs of the lower inner divertor *and* roof baffle. The energy found on the lower inner divertor is expected to be significantly lower than given by the calorimetric value. At the same time, high energy load depositions can be found at the first wall (ICRH antennas and auxiliary limiters, purple bars) and the upper outer divertor (green bars), which confirms the presence of a significant radial heat transport likely caused by enhanced filamentary transport. These observations confirm previous studies in L- and H-modes [CAB$^+$18, BMC$^+$15, FEH$^+$21, VCT$^+$20].

The energy distribution of an ***Advanced Tokamak*** discharge

The middle row represents the properties and energy distribution of an *Advanced Tokamak* (AT) discharge [BFF$^+$17]. Such scenarios typically require a low separatrix density $n_{\mathrm{e,sep}}$ to maximize the current drive efficiency of ECRH and NBI and to minimize the dependence on I_{p}, combined with a high fraction of bootstrap current j_{BS} for non-inductively driven H-modes [BFF$^+$17]. Due to the lower $n_{\mathrm{e,sep}}$, the lower inner divertor is attached. A significant fraction of energy loads can be measured by the calorimetry at the inner lower divertor, confirming this property. The calorimetric measurements confirm that the energy loads on the first wall are low even in the presence of Type-I ELMs (compared to the totally calorimetric acquired energy loads). This observation indicates that the ratio between parallel and radial transport is different with respect to the previous scenario with more energy deposited into the inner/outer divertor and less energy deposited at the first wall.

The Energy distribution of a ***Compact Radiative Divertor*** discharge

The lower row shows the properties and energy distribution of a *Compact Radiative Divertor* (CRD) scenario [LBB$^+$23] in USN-configuration. This scenario is an alternative power

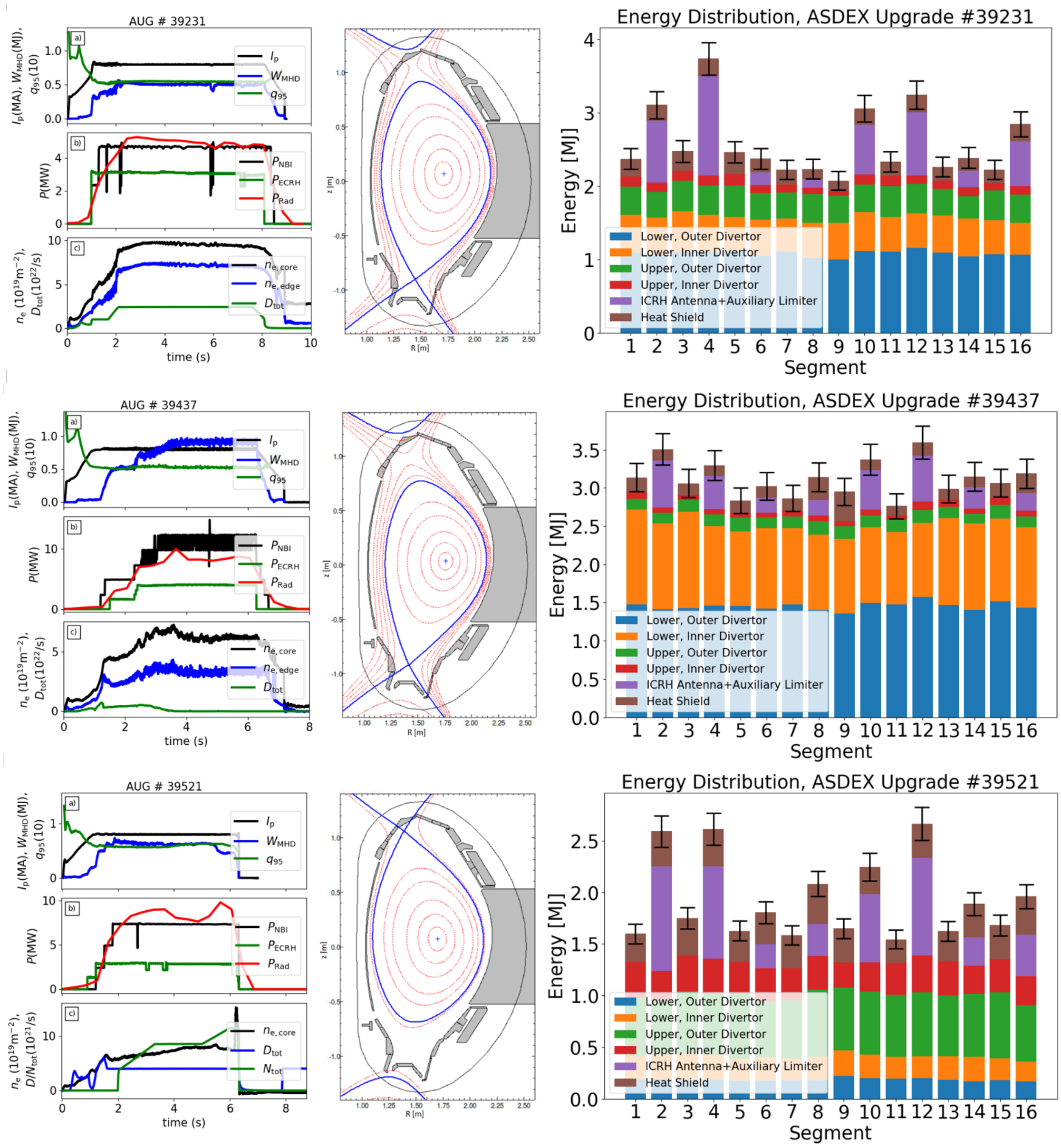

Figure 3.8: Overview of time traces of main plasma parameters, equilibrium at t = 4.0 s and the energy distribution calculated with the cooling water calorimetry for three different scenarios: upper row a QCE discharge (for more information concerning this discharge, see Ref. [REV+23]), middle an AT discharge [BFF+17] and lower a USN discharge in the compact radiative divertor configuration (see Ref. [LBB+23]). For this last discharge, the edge density $n_{\mathrm{e,edge}}$ measured with the interferometer is not available. Instead, the nitrogen seeding rate N_{tot} is plotted. It must be emphasized that the scaling of the y-axis for each of the energy distributions is different.

Shotnumber	E_{OH}	E_{NBI}	E_{ECRH}	$E_{\mathrm{Calorimetry}}$
#39231	2.8 MJ	31.0 MJ	21.9 MJ	41.5 MJ
#39521	2.3 MJ	31.6 MJ	14.9 MJ	28.9 MJ
#39437	4.1 MJ	43.6 MJ	17.0 MJ	49.9 MJ

Table 3.1: Overview of the injected and measured energies acquired by the revamped cooling water calorimetry

exhaust solution for ITER and DEMO with shallow field line incidence angles at reasonably high power and promising confinement [LBB+23]. The key channel of power losses in such scenarios is radiation (radiative losses above 90 % can be achieved by developing a X-point radiator [BJS+21]). Even for such a dedicated discharge with dominating radiative fraction, the calorimetry can resolve a reasonable distribution. A significant fraction of the injected energy goes to the upper divertor, consistent with the fact that the configuration is in USN. The energy deposition in the upper divertor is concentrated on the upper outer divertor consistent with the strikeline and X-point configuration (see the corresponding equilibrium) in this dedicated scenario. Strong radiative losses can cause significant energy loads on any PFCs, which are properly acquired by the revamped calorimetry. The calorimetry cannot discriminate between particle and radiation caused energy loads.

3.3 The AUG wall thermometry

The AUG tokamak is equipped with an extensive wall thermometry system consisting of 94 thermocouples (TCs) covering poloidally important areas of in-vessel components. The thermocouples are NiAl-NiCr type K thermocouples. This extensive system covers mainly the lower (segments 4, 8, 10 and 13) and upper divertor (segments 4 and 13) increasing the spatial resolution to tile-resolved calorimetric measurements. Fig. 3.9 (left) illustrates their poloidal coverage in the upper/lower divertor. Next to the upper/lower divertor, thermocouples are additionally installed in tiles of the heat shield, where the NBI shine through can reach the inner columns, Fig. 3.10 (right plot) gives an overview of their location in each segment. The ICRH antennas (segments 2 and 10) and the auxiliary limiters are also equipped with thermocouples, Fig. 3.10 (right left and centre) gives an overview of their location in the respective segment. Additionally, single tiles of the lower PSL are equipped with thermocouples (green markers in Fig. 3.9 (left)). During the DivIIo-Upgrade [HTZ+19], tiles of the upper PSL (red markers in Fig. 3.9 (left)) will be equipped with thermocouples for tile-resolved calorimetric measurements.
In the AUG tokamak, one tile of each row of a segment with thermocouples is equipped with one thermocouple, except for the divertor target tiles. In this case, two thermocouples are installed in one tile. For the calorimetric evaluation, the mean value of these two profiles is used, as suggested in Ref. [MBD+17]. Fig. 3.9 (right) illustrates the position of thermocouples for such a divertor target tile. For each thermocouple there is a small drill hole which is large enough to accommodate the thermocouple probe-head. This installation

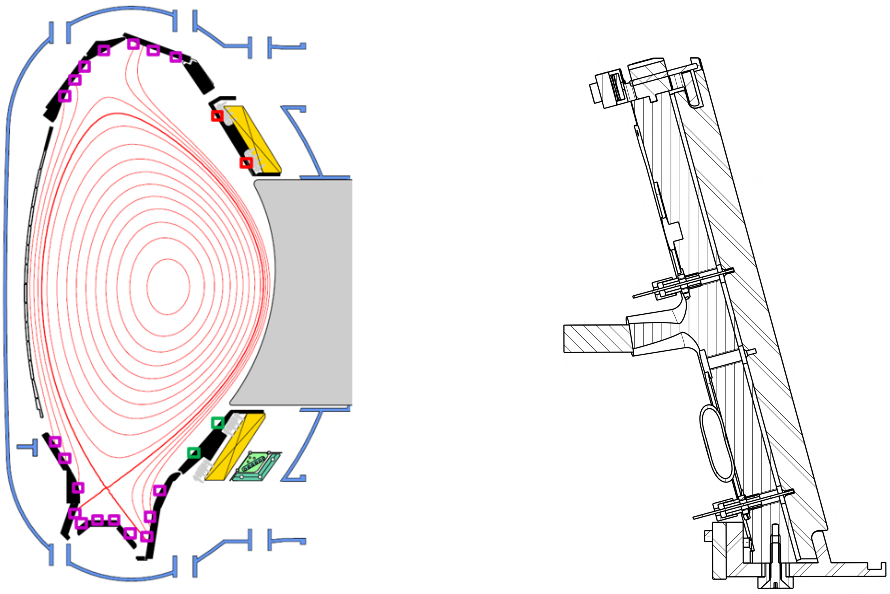

Figure 3.9: Left: Poloidal cross-section of AUG showing tiles equipped with thermocouples. Each square marker represents one thermocouple. Purple markers represent thermocouple installed in the lower/upper divertor, green markers represent thermocouples installed in the lower PSL and red markers represent thermocouples which will be installed in the upper PSL during the DivIIo-Upgrade [HTZ+19]. Right: Poloidal cross-section of a full tungsten divertor target tile with the two thermocouples. The thermocouple probe-head is not installed on the rear side of the tile, but is fully placed into a drill hole (14 mm deep for this type of tile).

with the drill hole is common to all thermocouples in the AUG tokamak.

3.3.1 The underlying theory for the calorimetric evaluation of the thermocouples

The calorimetric evaluation of the AUG thermocouples is based on the approach described in Ref. [MEF+01] and revised in Ref. [MBD+17]. The idea is to measure the cooling down phase of the tiles between two discharges and to use the equilibriated temperature decay profile as fit reference in order to extrapolate the decay fit profile back to the beginning of the AUG pulse and to extrapolate the decay profile to the initial temperature before the temperature rise starts. As a consequence of this requirement, only time-integrated values are available. For this purpose, the time a tile needs to reach internal thermal equilibrium must be much smaller than the cooling time of thermal conduction or thermal radiation. By fulfilling this condition the effective tile temperature is obtained, which allows the thermal energy stored in the tile to be calculated. The underlying equation for thermal

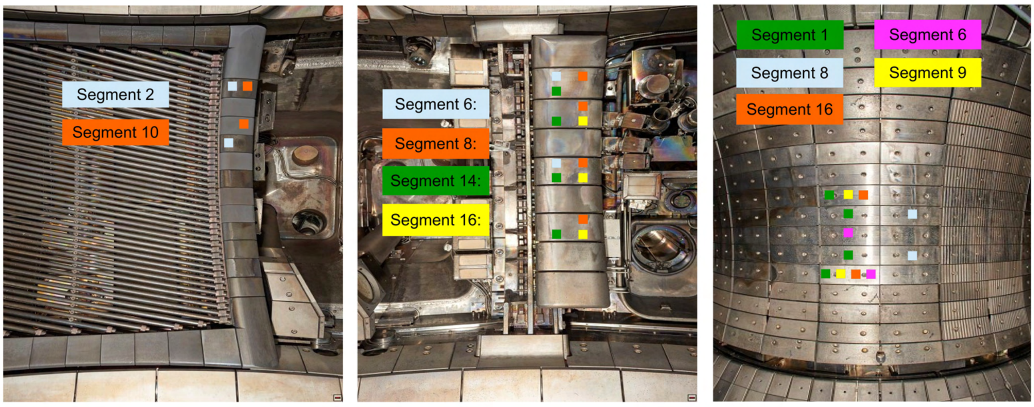

Figure 3.10: Overview of the thermocouple distribution at the ICRH antenna, auxiliary limiter and heat shield. The colored labels correspond to different segments. The colored squares are used to indicate a tile equipped with a thermocouple, but do not give the actual thermocouple position within a tile.

energy Q is:

$$Q = m_{\text{tile}} \int_{T_{\text{end}}}^{T_{\text{begin}}} c_{\text{p}}(T)dT, \tag{3.3}$$

where m_{tile} is the mass of the tile, $c_{\text{p}}(\text{T})$ is the temperature-dependent heat capacity and the boundaries (T_{end}, T_{begin}) of the integral define the temperature rise. The mass of each tile can be found in Ref. [RHE+23b]. On AUG, three different tile materials are in use:

graphite, **tungsten** and **P92 steel**

The majority of the tiles in AUG are tungsten coated graphite tiles [NBB+07]. The target tiles at the outer divertor are made of solid tungsten. In case of the heat shield, the central seven tile rows around the midplane level are equipped with P92 steel tiles. The required fit formulas of the temperature-dependent heat capacity for each tile material are visualized in Fig. 3.11. The temperature dependency of the heat capacity must be considered in the integration scheme, otherwise incorrect values of the deposited energy will occur as reported in Ref. [MBD+17]. The critical point is to find a suitable fit function in order to obtain the effective temperature. For this purpose, the general formula for thermal transfer is needed:

$$\frac{\partial T}{\partial t} = \alpha \frac{\partial^2 T}{\partial x^2} - \beta(T^4 - T_{\text{sur}}^4), \tag{3.4}$$

where the first term on the right-hand side describes thermal conduction and the second term describes thermal radiation. T_{sur} denotes the surrounding temperature, α and β are prefactors containing physical parameters and simplifying the formula. Any energy losses due to convective transport can be neglected in a vacuum chamber. As known from Refs.

[MBD+17, MEF+01], JET tiles are thermally insulated from the JET support structure and therefore thermal radiation is the dominant energy loss channel for such tiles. At AUG, the situation is different: standard AUG tiles are in good thermal contact with the AUG support structure (otherwise the cooling water calorimetry would not work). Thermal radiation only contributes, if $T_{\text{tile,max}} \gg T_{\text{sur}}$, since it correlates with $T^4 - T^4_{\text{sur}}$. Such conditions are not satisfied in AUG discharges [HtAUT01], therefore thermal conduction is the dominant energy loss channel for AUG tiles. Consequently, the second term in Equ. (3.4) can be neglected. Using the separation of variables the remaining equation can be separated into two components: one describing the temporal evolution and the other one the spatial evolution of the temperature within the tile. Since the approach of tile

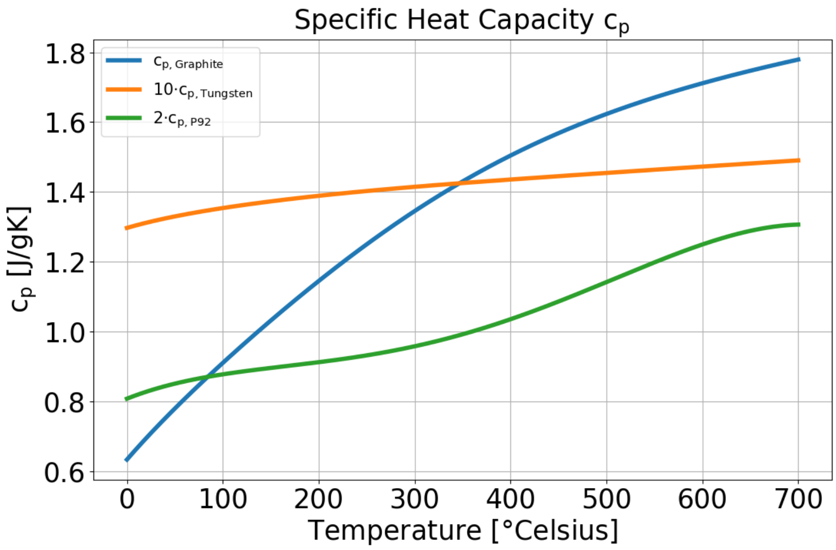

Figure 3.11: The temperature dependent heat capacities for graphite, tungsten and P92 steel. The heat capacity of tungsten and P92 are multiplied by a factor to fit on a common coordinate. The fit formulae are obtained from results in Refs. [BM73, DPM99, Heb23].

calorimetry requires internal thermal equilibrium, the component of the spatial evolution is set constant. The remaining temporal differential equation is solved to:

$$T(t) = (T_{\text{start}} - T_{\text{initial}}) \cdot \mathrm{e}^{-\kappa_{\text{cooling down}} \cdot (t - t_{\text{start}})} + T_{\text{initial}}, \tag{3.5}$$

T_{initial} is the initial temperature before the temperature rise, T_{start} the temperature at the starting point for the fit, t_{start} the time at the starting point and $\kappa_{\text{cooling down}}$ the cooling down coefficient. On AUG, the time and temperature parameters are taken from the experimental data and only the cooling down coefficient $\kappa_{\text{cooling down}}$ has to be fitted. Fig. 3.12 shows the temperature profile measured with a thermocouple (blue curve). The green curve represents the part of the temperature profile which is supposed to be thermally equilibriated. The starting point is set to 200 s for all thermocouples. It has been checked exploiting IR thermography that the divertor target tiles are in thermal equilibrium after

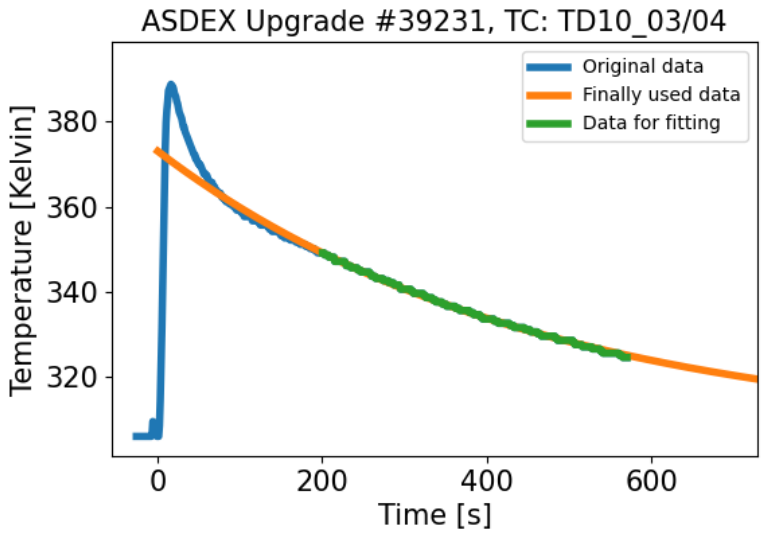

Figure 3.12: Plot of the mean decay profile of the thermocouples (TD10_03 and TD10_04) installed in the full tungsten tile in segment 10. The blue curve represents the acquired raw data, the green curve the part which is used as reference for the fit and the orange curve represents the fully extrapolated fit function.

$\sim$ 80 s. This boundary check will be discussed later in Section 3.3.2. Exploiting the green curve, the cooling down coefficient, required for Equ. (3.5), is determined. The orange curve represents the fit function extrapolated to the beginning of the pulse and to the end of the decay profile reaching the initial temperature before the rise. The obtained profile serves as input for the integral boundaries and the temperature-dependent heat capacity in Equ. (3.3) in order to determine the stored energy Q for each tile. Additionally, an uncertainty of the evaluation scheme can be estimated:

1) uncertainties in the fit formula of the heat capacity c_p for each tile material

2) uncertainties in measuring the mass of the tile.

3) the uncertainty in the acquired temperature profiles, here $\pm$ 0.5 K.

4) uncertainty in the back extrapolation due to the low temperature resolution

The fit formula of each heat capacity **1)** reveals intrinsic uncertainties by its nature, which can hardly be assessed. In case of the tile masses **2)** any mass weights were realized without the drill holes, so the tiles installed in the tokamak might be slightly lighter. A further impact is given by the low temperature resolution **3)**, 0.5 K, which causes a certain freedom in fitting the profile, particularly for tiles with low thermal energy loads. The last uncertainty **4)** is caused by the inaccuracy of the back extrapolation scheme due to the low temperature resolution. The temperature value at the starting point (first value of the fitted reference profile) has a significant impact on the temperature profile which is

extrapolated back to the beginning of the AUG pulse. Uncertainties **1)** and **4)** can only be guessed and are supposed to be at least ± 15 %. Uncertainties **2)** and **3)** are used as an additional input in the fitting routine for Equ. (3.5). The upper/lower error of the calculated energy for each thermocouple is obtained by increasing/decreasing the fit parameters and masses according to their respective uncertainty. This yields an overall estimated error of ± 17 % according to the presented evaluation scheme.
The availability of the tile-calorimetry enables the tile-resolved visualization of energy distributions. The poloidal tile-resolved energy distribution obtained by the thermocouples

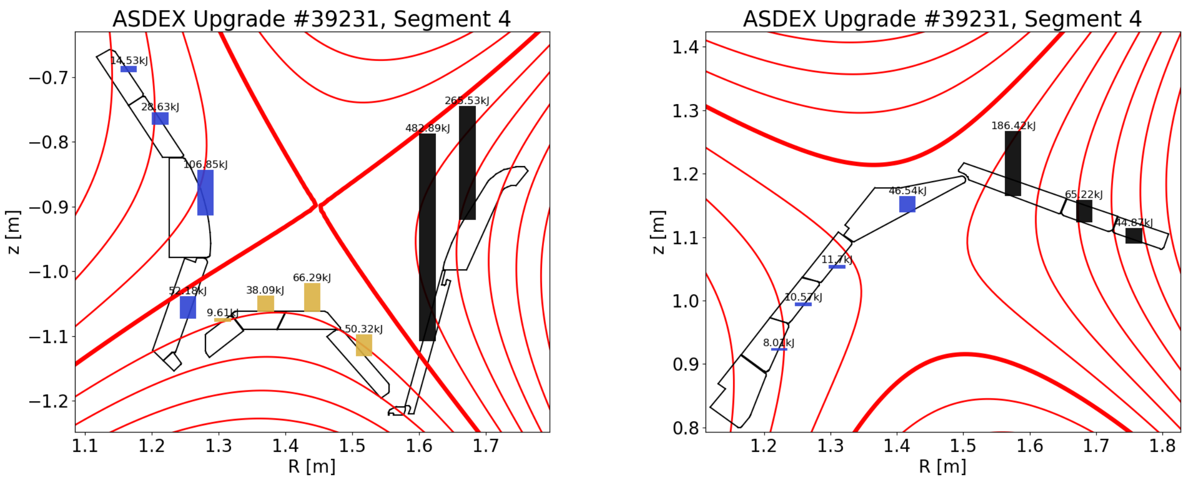

Figure 3.13: Overview of energy distribution in AUG calculated with the thermocouples in the upper and lower divertor in segment 4. The red contour represents the magnetic flux surfaces, the thicker one the last closed flux surface. The results are obtained for AUG shot #39231.

allows the impact on the inner and/or outer divertor energy loads to be precisely studied. Of particular interest can be the energy loads at the roof baffle, an area that is assumed to be only exposed to small thermal energy loads and which cannot be individually resolved by the cooling water calorimetry. An example of the distribution in the upper and lower divertors of segment 4 is shown in Fig. (3.13). The energy determined from the thermocouples was multiplied by the corresponding number of tiles per row of a segment.
At JET [MBD+17], extensive analyses were conducted to verify the tile-calorimetry approach. However, due to the lack of an alternative calorimetric measurements at JET, a simple cross-validation is not possible. Nevertheless, certain concerns regarding this approach have been eliminated by these JET-studies [GGC+24]. Recent results from the WEST tokamak [BAA+22], operated by CEA in Cadarache, have provided further proof for the tile-calorimetry approach. WEST is equipped with a cooling water calorimetry [BAA+22] similar to that of AUG and with a large number of thermocouples. The calorimetric results of the two independently performed calorimetric measurements are in agreement [GGC+24].

3.3.2 Studying the temperature distribution evolution of a full-tungsten tile with IR thermography

IR thermography is used to study the evolution of the temperature distribution of the tiles and to identify the initial value required to apply the tile-calorimetry approach on AUG tiles. To do this, the IR-camera labelled as *Sektor9Zeile* is used. This camera is located behind the outer target focused on an observation slit defined by a gap between two adjacent tiles of the divertor main target in segment 9. Through this slit the camera

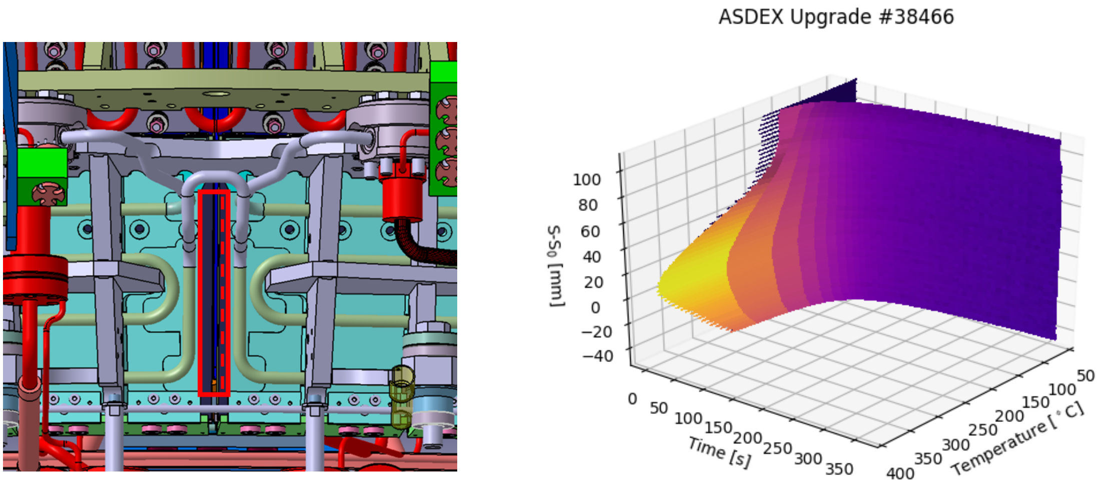

Figure 3.14: Left: Cutout of a CAD drawing focusing on the observation area of the IR-camera *Sektor9Zeile*. The red box indicates the actual observation area. The red dotted line denotes the LOS which is evaluated for studying the evolution of the temperature distribution. Right: Evaluated temperature distribution visualized in a 3D-contour plot covering the poloidal position, temperature and time.

can measure the surface temperature on the inner divertor or on the outer divertor by using a steerable mirror. The red box in Fig. 3.14 (left) denotes the observation area traceable by this IR-camera. As can be seen from the sketch, the observation area of the IR-camera covers parts of the rear side of the adjacent tiles defining the observation slit. This possibility is exploited to acquire the temporal evolution of the poloidal temperature distribution of the divertor target tile rear side. This tile pair defining the observation area is connected to the AUG cooling system. Consequently, the adjacent tiles have the same the boundary conditions as the one equipped with thermocouples which are used for tile-calorimetry. To study the temperature decay profile, the acquisition frequency of the IR-camera is strongly reduced to 20 Hz, extending the acquisition time from original 10 s to 360 s. The acquisition frequency of 20 Hz is sufficient to resolve the temperature evolution and the acquisition length of 360 s is sufficient to observe the phase of thermalisation within the tile. The red dotted line in Fig. 3.14 denotes the line of sight evaluated in AUG discharge #38466. For the data evaluation, an initial tile temperature of 25 °C and an emissivity ϵ of 0.3 are assumed. The evaluated temperature profile is shown in Fig. 3.14 (right) as a 3D-contour plot. The three axes denote the target location $S - S_0$ [mm] with S_0 the strikeline position, the temperature [°C] and the time [s]. The value of the temperature at a certain position and time is visualized by colored contours. One can clearly see that at the beginning of the discharge and shortly after the end the temperature is mainly located around the strikeline. The spikes appearing at the beginning of the shot are artifacts. With every time step after the end of the experiment the temperature is continuously distributed over the entire poloidal tile length. After $\sim$ 80 s, the entire temperature distribution is flattened over the whole poloidal tile length. The entire tile is in thermal equilibrium which represents the minimum starting time point in order to apply the tile-calorimetry approach. Since different tile materials and geometries are used in the AUG tokamak, the starting time point for the tile-calorimetry approach is set to 200 s in order to ensure that all tiles are equilibriated, when the tile-calorimetry approach is applied.

3.3.3 Correction of the calculated energy deposition by exploiting the inclination of the magnetic field line on the flat divertor tile surface

The divertor target tiles are vertically cut into two toroidally adjacent equally sized tile halves in order to reduce thermal stress reactions within the tile. This setup is henceforth referred to as a *tile-pair*. Except for two tiles in campaign 2020/2021, which are installed in segments 8 and 13, all divertor target tiles are arranged as tile-pairs. At the start of campaign 2021/2022 all tiles are halved. In Fig. 3.15 (left), a surface temperature measurement of a tile pair located in segment 10 by means of IR-thermography is plotted. The cut between the two halved tiles can be clearly seen. The asymmetry in the surface temperatures for each halved tile is also visible. In the recent setup, thermocouples are installed in the tile half which is exposed to the peak heat flux. Temperature measurements of the other tile half are not available. To determine the entire energy deposited in a tile pair, the inclination of the magnetic field line $\alpha(\vec{r}, \text{t})$ along the flat tile surface must be considered. Fig. 3.15 (middle) visualizes the inclination of the magnetic field over the entire flat tile surface [KBC+18]. The variation of the inclination of the entire tile surface is clearly visible. The cut, which halves the tile, is indicated with the solid black line, the position of the two thermocouples installed in such a tile are added as black circles, the hypothetical thermocouple location as black dot and the required position in order to correct the thermocouple results by a black filled square. The black dot represents the hypothetical position of the thermocouple whose profile is based on the mean of the two available thermocouple measurements. In Fig. 3.15 (right), the energy deposited in the unhalved tile in segment 8 is plotted against the energy deposited in the halved tile in segment 10. For this comparison, the tile mass of a halved tile is assumed to be identical to an unhalved tile. A colormap is added visualizing the fraction of energy found in the halved tile normalised against the energy found in an unhalved tile. A linear regression

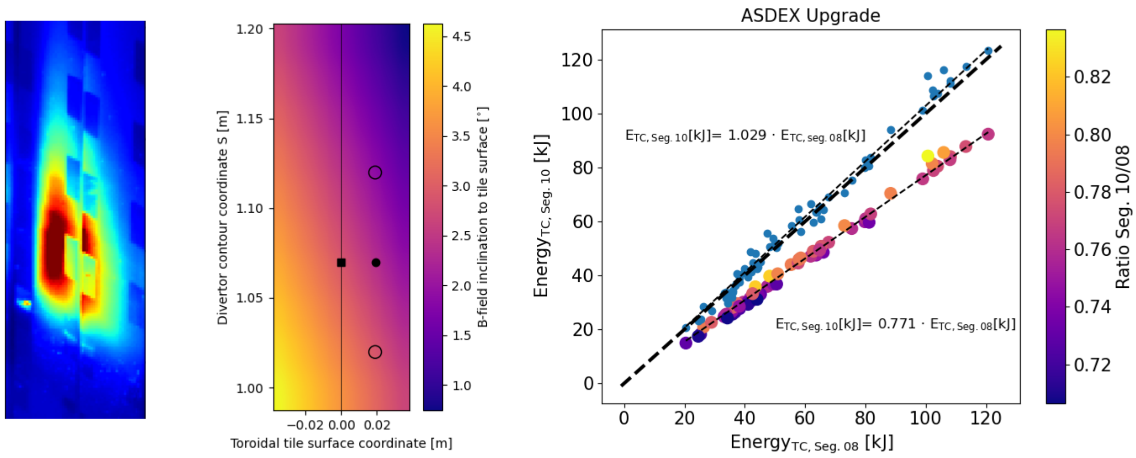

Figure 3.15: Left: Surface temperature measurements of a target tile pair. The asymmetry in the surface temperature is clearly visible. Middle: Map of the inclination of the field angle on the flat tile surface with the cut line of the divertor tile (solid black line), the contour of the thermocouple positions (black circles), the position of the hypothetical thermocouple generated from the mean value of the temperature profile of both thermocouples (black dot) and the required position in order to correct the thermocouple results (black square). Right: Deposited energy in an unhalved tile installed in segment 8 against the deposited energy in a halved tile installed in segment 1.

shows that a halved tile captures 77% of the energy of an unhalved tile. To adjust the measured energy in the halved tile, one calculates the inclination of the magnetic field $\alpha(\vec{r}, t)$ at the position of the hypothetical thermocouple and at the position of the square marker. With both values, the corrective ratio $\alpha_{\text{adjustment}} = \alpha_{\text{TC location}}/\alpha_{\text{shifted}}$ can be calculated. The energy obtained from a halved tile is divided by this ratio in order to obtain the correct energy value. Interestingly, to obtain a reasonable match between both halved and unhalved, tiles, α_{shifted} must be set to x = 0.0 cm of the toroidal tile position. The corrected tile values from segment 10 can be found in Fig. 3.15 (right). A linear regression is applied yielding an almost perfect match ($\sim$ 1.029) between corrected values and the reference values from an unhalved tile.

3.3.4 Comparison between thermocouples and IR-thermography

The capabilities of the thermocouples are compared with IR-measurements from the divertor target tile and extrapolated to the entire toroidal circumference. In the case of the thermocouples, the energy deposited for one tile must be multiplied by 128 in order to cover the full toroidal circumference. The heat flux density from the IR-thermography is normally calculated from the tile half with the higher surface temperature. The heat flux density obtained is then spatially integrated in the poloidal and toroidal directions and then temporally in order to determine the deposited energy. Since the heat flux density is obtained from the tile, which is exposed to the peak heat flux, the results obtained would significantly overestimate the energy loads one would expect. To adjust the overestimated heat flux density, the same correction factor is used as for the halved tiles, but instead of dividing, it is multiplied by this factor $\alpha_{\text{adjustment}}$. In Fig. 3.16, the results from both

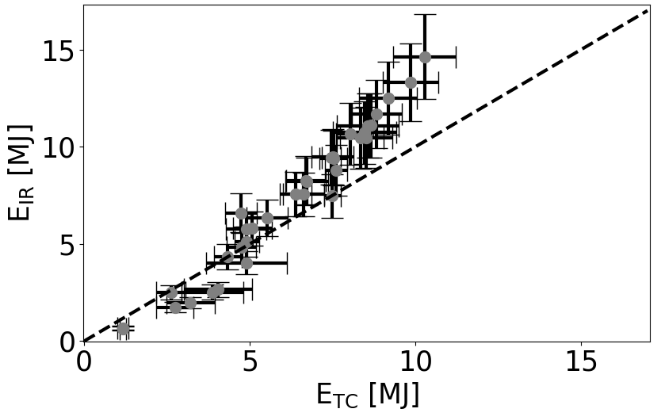

Figure 3.16: Energy at the outer target obtained with the IR-thermography and the thermocouples covering an energy deposition between 1 MJ and 11 MJ. Each marker denotes a single discharge. The black dashed diagonal represents 100 % match between IR and thermocouples.

diagnostics are visualized. A good agreement between both diagnostics within the error bars is evident and comparisons between both diagnostics seem reasonable.

3.3.5 Comparison between thermocouples and the cooling water calorimetry

As a last aspect, the agreement between thermocouple measurements and cooling water calorimetry should be checked. To do this, a small database of discharges has been created in which discharges in LSN configuration only are taken into account. Four areas are compared: outer/inner upper divertor and outer/inner lower divertor. These are the areas where the thermocouples have the best poloidal coverage. The toroidal coverage of thermocouple is sparse. Only one tile per tile row and segment which is equipped with one thermocouple (excluding the divertor target tile thermocouples). The comparison between both calorimetric diagnostics for all four areas is visualized in Fig. 3.17. There is a systematic underestimate of the energy obtained from thermocouples. On average, the thermocouples find only between 69 % (94 %) of the energy determined from cooling water calorimetry for the lower outer (inner) divertor. In case of the upper divertor, the thermocouples detect only 46 % of the inner divertor, which can be explained by the fact that the heat fluxes reaching these PFCs are not sufficient to apply the tile-calorimetry approach. At the same time, a reasonable agreement with $\sim 94\%$ has been achieved for the upper outer divertor. For most cases, this area of the vessel is only heated up by plasma

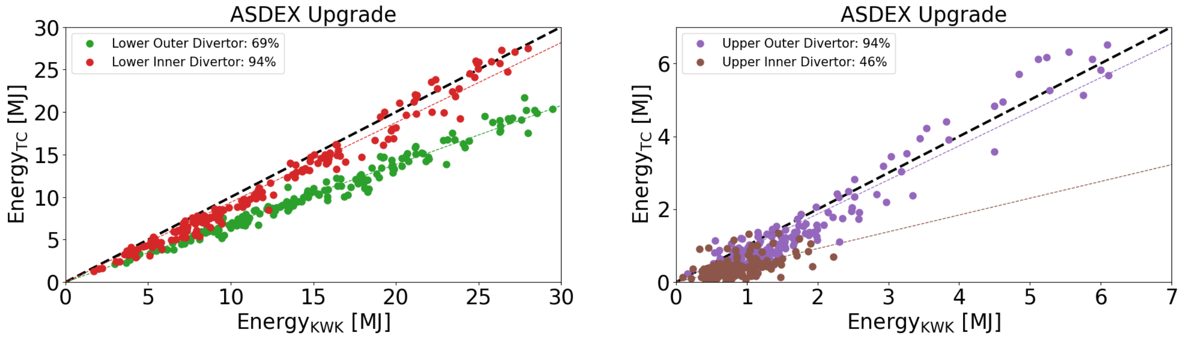

Figure 3.17: Comparison of energy loads between thermocouples and cooling water calorimetry for the four divertor areas. The black dashed diagonals represent 100 % match between cooling water calorimetry and thermocouples.

radiation, which propagates isotropically and explains the good agreement.
These results suggest the presence of toroidal asymmetries and might be connected with the observations summarized in Ref. [RBH+23], which reports on an uneven distribution of cracked and broken divertor target tiles within a segment of AUG. For a reasonable comparison between thermocouples and cooling water calorimetry, a substantial extension of toroidal coverage with thermocouples would be required.

Chapter 4

A new attempt to achieve the global energy balance in AUG

In this chapter, a new attempt is discussed to achieve global energy balance in the AUG tokamak using the revamped KWK. Providing a reasonable energy balance is a fundamental requirement for any trustworthy energy load studies. It is worth mentioning that the same exercise whenever is has been tried on different devices [HER+04, FEH+05, MBD+17, BEK+15] so far, proved to be particularly difficult. In the first section of this chapter, the energy balance equation for AUG is introduced and all required contributions are discussed. A linear regression study, following the example reported in Ref. [MBD+17], is added in order to identify possible systematic uncertainties in the input and output contributions. A further section is added in order to discuss the source of the energy loads for two areas of the AUG tokamak which cannot be properly accounted for by the KWK. Subsequently, the same task is repeated to achieve a reasonable global energy balance in the JET tokamak. This chapter is concluded with an implication for empirical scalings based on the observations deduced by achieving the global energy balance. Excerpts of this chapter are taken from Ref. [RHE+23a].

4.1 The global energy balance of the AUG tokamak

A proper energy balance requires the determination of all the possible energy sources and losses according to the following equation:

$$E_{\mathrm{OH}} + E_{\mathrm{NBI}} + E_{\mathrm{ECRH}} + E_{\mathrm{ICRH}} = E_{\mathrm{Calorimetry}} + E_{\mathrm{Rad,\ Limiter+PSL}} + E_{\mathrm{NBI\text{-}losses}}, \tag{4.1}$$

where the terms on the left-hand side (LHS) denote the energy input accounting for all possible heating possibilities available on AUG. The ohmic heating power is obtained from the plasma current and loop voltage measurements. For the NBI contribution, the total injected energy is used. In case of the ECRH and ICRH contributions, a 100 % coupling-efficiency is supposed.

The first contribution on the right-hand side (RHS) of Equ. (4.1) represents the sum of the energy loads on all in-vessel components obtained with the revised cooling water calorimetry. $E_{\text{Rad, Limiter+PSL}}$ denotes the part of radiation energy which cannot be acquired by the cooling water calorimetry and has to be simulated. Whereas most of the ions and electrons are collected by the limiters, the area in between is mostly heated by radiation. Since this area is used for the installation of diagnostics and the PSL, the cooling water calorimetry is strongly hindered. A short analysis supporting this assumption of dominating radiative heat loads will be discussed later in Section 4.2. The final contribution $E_{\text{NBI-losses}}$ summarizes the contributions of the NBI shine-through, NBI first-orbit and NBI charge-exchange (CX) losses, which individually may be small, but in sum may have an impact on the global energy balance. Recent studies on TCV [GKD+17] and more recently on JET [KSC+23] have shown that NBI losses can be significant. The NBI-losses are calculated with the RABBIT [WBD+18] code and the fraction of the shine-through reaching the PSL is estimated exploiting the Analytical Beamlet Code 3D ABC3D [dHROH20]. In the two subsequent sections, the determination of the two quantities $E_{\text{Rad, Limiter+PSL}} + E_{\text{NBI-losses}}$ is briefly summarized.

4.1.1 Determination of $E_{\text{Rad, Limiter+PSL}}$

In order to estimate the radiative energy loads for both areas (limiter shadow and PSL), the simulation framework CHERAB [GMC+18] is exploited. CHERAB is mainly used for spectroscopic plasma emission simulations, but is also able to simulate, given a prescribed radiative source, the radiative energy loads on any PFC. A previous study [MCD+21] simulating the distribution for DEMO PFCs illustrates the capabilities and supports its choice. Fig. 4.1 shows the setup realized for the AUG tokamak in CHERAB for a manually optimized experimental 2D emissivity profile determined from AUG bolometry (left column, upper) and the corresponding poloidal radiative heat load distribution of the AUG PFCs (Fig. 4.1 (left column, lower)) obtained for discharge #39231 at time = 7.5 s. The starting point and direction of the evaluation scheme for the poloidal distribution of the radiative heat loads is indicated in the upper plots, where the black lines represent the 2D-poloidal contour of the AUG vessel and in-vessel components. The blue line denotes the so-called *synthetic wall detectors*. These detectors are implemented for the determination of the radiative power reaching the respective areas.
To count the fraction of radiative power reaching each synthetic wall detector, CHERAB exploits the Python package raysect using the ray-tracing approach [CMB+18]. These wall detectors follow the entire contour of the AUG in-vessel components with a small offset (magnitude 1 mm) to ensure numerical stability.
To obtain the amount of radiative energy at any PFC for a large database, a systemic approach is required. The standard bolometry tomography method (an example is shown in Fig. 4.1 (left column)) used at AUG requires manual optimization of a set of parameters for each reconstruction and is therefore not suited for automatic computation of a large sample of data [DBP+21]. Instead, a recently developed Gaussian process tomography (GPT) model has been used [MBD+22]. This model uses a set of hyperparameters which is trained on a database of 214 profiles including 75 experimental emission distributions

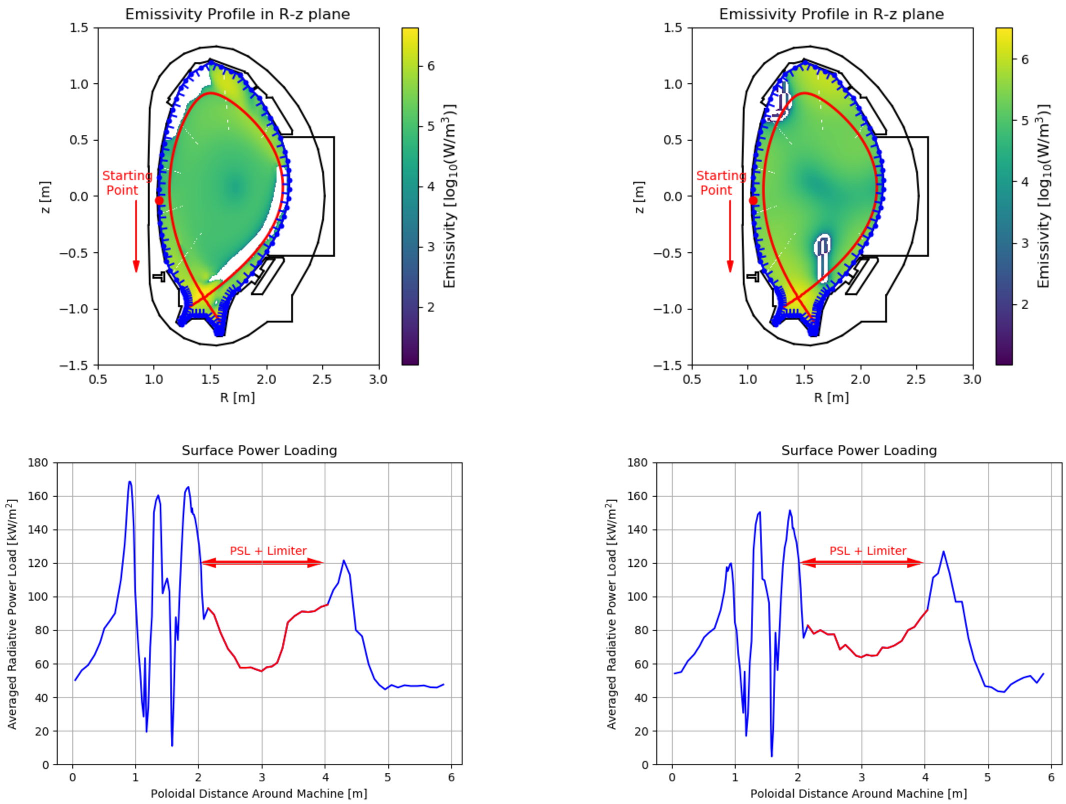

Figure 4.1: Overview of the setup used in CHERAB in order to assess the poloidal distribution of radiative heat loads for discharge #39231 at time = 7.5 s: left column with experimental 2D emissivity profile and the resulting poloidal radiative heat load distribution, right column with simplified synthetic 2D emissivity profile and the resulting poloidal radiative heat load distribution. The starting point and direction of the evaluation scheme is indicated in each upper plot. The area of interest *PSL + Limiter* is indicated in red in both poloidal distributions.

considering different AUG scenarios. For this study, the hyperparameters for the Cartesian kernel function have been used. For more details, in particular on its validation for AUG conditions, the reader is referred to [MBD$^+$22]. The bolometric input values are median averaged with a temporal resolution of 1 ms. The radiative contribution is temporally integrated with a time resolution of 2 ms.
The newly obtained emissivity profile and the poloidal distribution of the radiative heat loads can be found in Fig. 4.1 (right column). While the output of GPT differs from the manually optimized case, the differences are only minor in the LFS poloidal plane. The differences are, however, more substantial on the surface power loading outcome (compare Fig. 4.1 lower left and right), exhibiting the need for a reliable radiation computation and its error estimation, justifying the choice of the well benchmarked GPT method using 3D viewing cones. Even though the evaluation of the framework based on CHERAB and the

GPT model has certain uncertainties, it is presently the best compromise between evaluation time, model accuracy and flexibility. In the example showcased here, the largest discrepancies are in the inner divertor (poloidal distance ¡ 1 m), but otherwise agreement is good. To obtain the incident radiative energy at the PSL for the entire tokamak vessel surface, the values determined for the respective wall detector covering the PSL are extended to the full toroidal circumference, integrated in time and summed up. In the case of the limiter shadow, the same procedure is performed but excluding the fraction of the limiter area which is covered by the four ICRH antennas.

4.1.2 Determination of $E_{\text{NBI-losses}}$

AS mentioned earlier, the contribution $E_{\text{NBI-losses}}$ comprises the contributions of the NBI shine-through which reaches the PSL, the NBI first-orbit and the NBI CX losses. While the first contribution can be accurately determined with the aid of RABBIT and ABC3D, this does not apply to the two latter contributions [WBD+18, BGS+21, WBS+23].

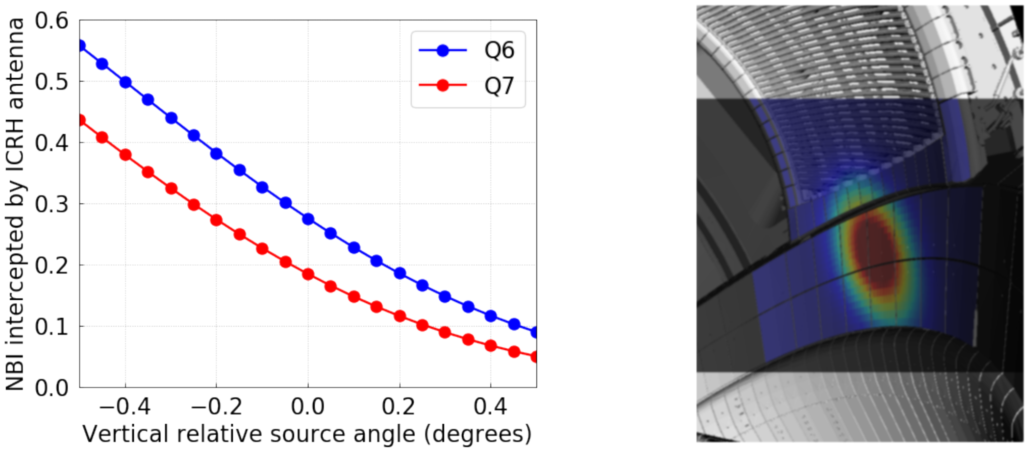

Figure 4.2: Left: relative fraction of the NBI shine-through beam intercepted by the ICRH antenna for both NBI sources (see Fig. 2.2) and for different values of vertical relative source angles with identical horizontal relative angle. Right: calculated power deposition of beam 7 reaching the PFCs of PSL and the ICRH antenna in segment 12 for discharge #34364. The gap in the power deposition which splits the power distribution between PSL and ICRH antenna is clearly visible. Taken from Ref. [dHROH20].

A minor correction is given by the consideration of the shine-through of the NBI sources 6 and 7, particularly for discharges at low separatrix density. The ASDEX Upgrade NBI heating system has two NBI boxes with a total number of 8 sources. of which 6 can hit the inner heat shield as shine-through. These shine-through losses are properly counted by the cooling water calorimetry. The beam sources 6 and 7 are tangentially oriented, since both are used for current drive (for illustration, it is referred to Fig. 2.2). Both beams focused on segment 12 impact the PSL and the ICRH antenna: Source 6 can hit the lower

PSL and the lower part of the ICRH antenna, whereas source 7 can hit the upper PSL and the upper part of the ICRH antenna. Any shine-through from both beams, which will partially reach the PSL, cannot be acquired by the calorimetric diagnostic. To calculate the fraction of the NBI shine-through of the NBI beam sources 6 and 7 intercepted by the ICRH antenna, results from RABBIT (providing the shine-through values) and ABC3D (providing the values of the area intercepted by the PSL) are used. The code ABC3D must be used, since both beam sources 6 and 7 are steerable in the horizontal and vertical directions.

The fraction deposited on the PSL and ICRH antenna depends mostly on the vertical angle. Fig. 4.2 (left) illustrates the integrated power density that is intercepted by the ICRH antenna for sources 6 and 7 as the fraction of the total beam power for different vertical relative source angles. Fig. 4.2 (right) visualizes the simulated power deposition on the PSL and the ICRH antenna in segment 12. The gap between the PSL and the ICRH antenna cuts the power deposition into two parts. The power density of the beam is given by the sum over the individual beamlets, which are parameterized as:

$$F_{\text{Shine-Through}}(l_{\parallel}, l_{\perp}) = \frac{E_{\text{Shine-Through}}}{2\pi\sigma_{\perp}^2} e^{-\frac{l_{\perp}^2}{2\sigma_{\perp}^2}}, \tag{4.2}$$

with

$$\sigma_{\perp} = \frac{l_{\parallel}\tan(\epsilon)}{\sqrt{2}}, \tag{4.3}$$

where $E_{\text{Shine-Through}}$ is the integrated NBI shine through power in time, ϵ is the divergence defined as the half opening angle of a cone with energy density at $1/e$ of the on-axis energy density, $l_{\parallel}$ the parallel and $l_{\perp}$ are the perpendicular distances with respect to the beam axis. The effects are only observable in low density discharges, where significant shine-through contributions can occur. This correction only plays a role for a minority of the database. In single cases, more than 6 MJ was found on the PSL due to the shine-through of source 6 and/or 7.

For the remaining two NBI-contributions (first-orbit and CX losses), certain assumptions have to be taken into account. It is assumed that most of these two losses are deposited on the LFS, where the revised calorimetry has the lowest coverage, resulting in a low acquisition of these losses. With the standard input profiles, RABBIT is able to determine first-orbit losses throughout the RABBIT orbit-averaging approach. The known coordinates of the PFCs are transformed into a flux radius ρ_{lim} and every guiding center orbit (+ its gyro-radius) which exceeds ρ_{lim}, is lost. Within the RABBIT-model, subsequent collision-induced orbit losses are not considered. The standard input profiles are sufficient to determine this contribution.

A robust calculation of CX losses [BGS+21, WBS+23] would require, next to the standard input profiles, the proper determination of the neutral particle density n_0. This input profile is hard to obtain for a single discharge and even more for a large database, because it is not directly measured. For this analysis, the same fit profile (illustrated in Fig. 4.3) for the neutral particle density is used for the entire database. In the extended Fokker-Planck

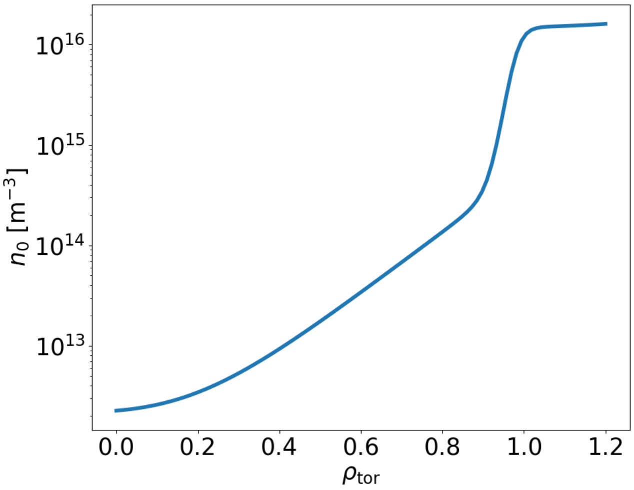

Figure 4.3: Visualization of the fit profile for the neutral particle density based on the fit introduced in Ref. [BGS+21]. The same fit profile is used for the entire database.

equation, CX losses can be expressed by:

$$-\frac{\tau_s}{\tau_{cx}(v)} f, \tag{4.4}$$

where f denotes the beam distribution function, τ_s the Spitzer slowing down time and $\tau_{cx}(v)$ the mean CX lifetime of a particle of velocity v. Ref. [Gaf76] suggests to write $\tau_{cx}(v)$ as:

$$\tau_{cx}(v)^{-1} = n_0 \cdot \sigma_{cx}(v) \cdot v, \tag{4.5}$$

where $\sigma_{cx}(v)$ denotes the velocity-dependent CX cross-section.

4.1.3 The AUG energy balance

Taking into account the information in the previous sections, terms on the RHS of Equ. (4.1) can be estimated. Estimated errors of the input energy and of the calculated energy loads on the PFCs can also be provided:

- NBI: ±7 %
- ECRH: ±5 %
- ICRH: ±5 %
- Ohmic Heating: ±5 %
- Calorimetry: ±6-7 %
- Radiation: ±12 %

Due to the complexity of the external heating methods, an exact determination of the uncertainties cannot be realized (see Ref. [MEF+01]). The uncertainty of the ohmic heating is based on the uncertainties of the measurement setup of the Rogowski coils and the toroidal conductor loop. In the case of the KWK, the uncertainty has been estimated in Section 3.2.1. For the uncertainty of bolometric measurements including the GPT-based reconstructions, see Ref. [DBP+21]. The uncertainty of the poloidal radiative distributions depends on a set of parameters in the CHERAB code. For this study, an uncertainty of $\sim 3\%$ for the radiative distribution can be estimated.
Fig. 4.4 (upper) presents the global energy balance of AUG realized with a database of almost 600 discharges from the second half of the 2020/2021 campaign and the full 2021/2022 campaign. The x- and y-axes of Fig. 4.4 (upper) represent the sum of the left and right sides of Equ. (4.1), respectively. The dashed bold bisector represents the goal of 100 % detection. A colormap is added visualizing the simulated radiation energy normalised against the injected energy. This database covers a large range of different scenarios (different equilibrium configurations, different seeding gases (N, Ne, Ar, He), heating schemes, fuelling levels including pellet fuelling and main gases (D, He)), which have been executed in the last two campaigns at AUG and a large range in injected energy, starting from $\sim$ 5 MJ up to $\sim$ 100 MJ.
The thin dashed line represents the detection rate obtained from a linear regression between input energy and detected energy. According to the applied linear regression the presented setup is able to find 95 % of the input energy on average for various, strongly different discharge scenarios and fractions of simulated radiated energy. Additionally, the mean error based on the sum of the individual uncertainties of each contribution is determined for the entire database. The mean error reveals a low scatter in both directions ($\pm$ 5.0 % and $\pm$ 9.4 % in the x- and y-directions, respectively) supporting the reliability of the AUG global energy balance.
Fig. 4.4 (middle) and (lower) visualize the individual contributions to the global energy balance according to Equ. (4.1), starting with the heating contributions (middle) of the LHS of Equ. (4.1). The lower plot illustrates the three contributions (the energy measured with the calorimetry, the fraction of simulated radiative energy reaching the limiter shadow and the PSL and contributions related to NBI losses), which can be found on the RHS of Equ. (4.1). According to the plots, one can identify that the simulated radiative fraction for the RHS of Equ. (4.1) is relevant due to its significance in the energy balance for any input energy. The entire radiation energy, $\mathrm{E_{Rad,tot}}$ is added in the lower plot as comparison to the simulated contribution.
As mentioned earlier, the contribution $E_{\text{NBI-losses}}$ includes the components of the NBI shine-through, which reaches the PSL, the NBI first-orbit and the NBI CX losses. While The first contribution can be accurately determined with the aid of the RABBIT and ABC3D codes, this does not apply to the two latter contributions [WBD+18, BGS+21, WBS+23]. In this study, for the entire database both contribute on average $\sim$ 3 % to the energy balance (see Fig. 4.4 (lower)). However, studies on TCV [GKD+17] and more recently on JET [KSC+23] have shown that NBI losses can be significant.
According the applied linear regression the mean discrepancy between input and detected

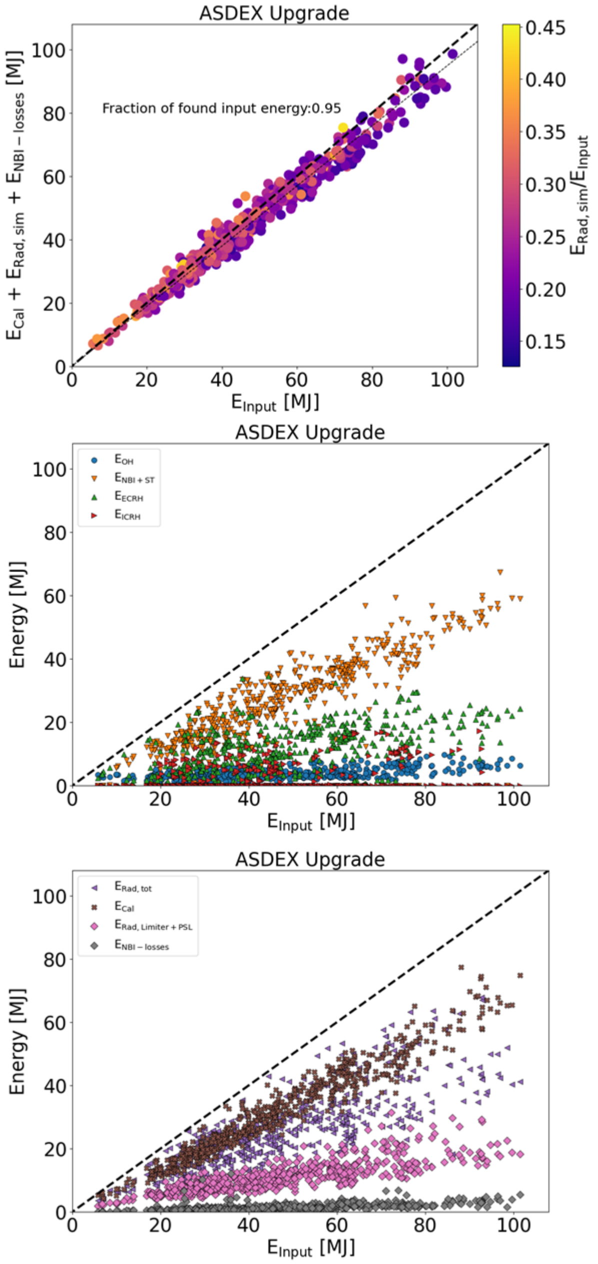

Figure 4.4: Upper: Visualization of the global energy balance obtained with the revised cooling water calorimetry on the AUG tokamak. The x- and y-axes represent LHS and RHS of Equ. 4.1. A colormap is added representing the fraction of simulated radiative energy normalised to the injected energy. Middle: Visualization of each contributor to the global energy balance of the LFS of Equ. 4.1. The four contributions represent the injected energy of each heating system. Lower: Visualization of each contributor to the global energy balance of the RHS of Equ. 4.1. The three contributions represent the calorimetrically captured energy, the simulated radiative energy reaching the limiter shadow and the PSL and contributions related to NBI losses. Additionally, the total radiative energy is added as comparison to the simulated contribution.

energy is $\sim$ 5 %. The large database demonstrates that the calorimetry can capture between 58 % and 83 % of the total injected energy for arbitrary plasma scenarios. The calorimetric diagnostic thus represents the main contributor to the RHS of Equ. (4.1). The great effort in improving the data resolution and maximizing the acquisition time [HRR+23], together with a reasonable extrapolation fit, is the basis for robust values for arbitrary plasma scenarios. The lower limit of the energy captured by the KWK is given by CRD scenarios, which have a dominating radiative fraction (> 90 %) [LBB+23]. The high radiation fraction for such discharges is also reflected by the high energy loads found with the limiter cooling units (purple bars) in Fig. 3.8 (third column, lower plot). At the same time, the radiative component provided by means of CHERAB and a GPT-model is key, since its contribution can vary between 13 % and 45 % (corresponding to the values in Fig. 4.4 (upper)), thus encompassing a significant range of the injected energy. This broad contribution to the energy balance strongly emphasizes the need for accurate and reliable calculations of radiative losses for the areas around the limiter and the PSL, which the AUG calorimetry, despite its very good coverage, cannot capture.
With the establishment of the energy balance using the revised KWK, a novel approach based on the code CHERAB and a simple GPT model for bolometric reconstruction in order to accurately determine the radiative fraction has been introduced. The results derived with both codes compare well with results based on bolometric reconstructions (see Fig. 4.1) and are suitable for a reasonable calculation of the key contribution for any plasma scenario. In previous studies at AUG [FEH+05, HER+04], JET [MEF+01] and EAST [ZMY+22] addressing the global energy balance challenge, appropriate determinations of radiative losses realised by means of bolometric measurements have not been realised. So far, simplifications, such as constant correction factors, were applied on databases in order to take into account radiative losses. The AUG results with the CHERAB framework show already that the radiation losses can vary widely for a large database and that radiative losses require a shot-by-shot assessment.
Despite the promising new energy balance, a small mismatch of $\sim$ 5 % has been identified. Using a linear regression study based on the data shown in Fig. 4.4 may provide further insights into systematic errors (e.g. the supposed 100 % wave heating absorption) which could explain the (small) mismatch in the energy balance [MBD+17]. Case (1) in Table 4.1 denotes the regression for the LHS of Equ. (4.1) assessing the respective energy inputs. The strongest drop is obtained for the ohmic contributions, which should be lowered to 70 % of the actual measured value. At the same time, ECRH and NBI are both close to unity, indicating no clear source of the mismatch for the dominating input contributions. The ICRH efficiency for this database is $\sim$ 91 %. There might be some systematic disagreements in estimating the absorbed ICRH energy. Repeating the analysis excluding the subset of ICRH-heated discharges in the database (case (2) in table 4.1) leads to similar prefactors as for case (1).
The calculations can now be repeated for the RHS of Equ. (4.1) in table 4.1 with (case (3)) and without the ICRH-contribution (case (4)). For case (3), the linear regression reveal that all three measured contributions are equally increased by 4 - 6 %. No clear source for the mismatch can be identified. In case (4), the prefactor for the NBI-losses is tripled.

$a \cdot E_{\text{OH}} + b \cdot E_{\text{NBI}} + c \cdot E_{\text{ECRH}} + d \cdot E_{\text{ICRH}} = e \cdot E_{\text{Calorimetry}} + f \cdot E_{\text{Rad,Limiter+PSL}} + g \cdot E_{\text{NBI-losses}}$								
Case	fitted	a	b	c	d	e	f	g
(1) LHS of Equ. (4.1)	a,b,c,d	0,7	0,97	0,98	0,91	**1**	**1**	**1**
(2) LHS of Equ. (4.1)	a,b,c	0,69	0,99	0,97	**0**	**1**	**1**	**1**
(3) RHS of Equ. (4.1)	e,f,g	**1**	**1**	**1**	**1**	1,05	1,05	1,06
(4) RHS of Equ. (4.1)	e,f,g	**1**	**1**	**1**	**0**	1,03	1,08	1,18

Table 4.1: Overview of different configurations of the AUG energy balance equation (Equ. (4.1). Bold prefactors are pre-set in regression studies.

However, the impact on the energy balance is small. The averaged contribution is ~ 3 % leading to ~ 3.6 % using the prefactor of case (4). The study suggests that the mismatch is caused by small uncertainties of all contributors.

4.2 Validation of the AUG global energy balance assumptions

In this section, the respective assumptions made for the limiter shadow and the PSL are cross-checked exploiting thermocouple measurements at the lower PSL and on the in-vessel piezoelectric valve, which is utilized for local gas injection of the Thermal Helium Beam (THB) diagnostic.

4.2.1 Analysis of the energy loads in the limiter shadow

To check what the energy loads in the limiter shadow depend on, a protection measurement of the THB diagnostic is exploited. The in-vessel piezo valves of the THB-diagnostic are installed in the limiter shadow. The THB-diagnostic [GWC$^+$18] has (status 2021) two valves for injecting helium puffs at the LFS midplane into the plasma, which are installed in segments 13 and 16. Each valve is equipped with a thermocouple measuring the temperature of the setup consisting of the valve, its protection tile and the connectors to the support structure. In Fig. 4.5, the valve system installed in segment 13 is highlighted in green. The temperature of each valve setup is acquired every minute. Fig. 4.6 (upper) shows the valve temperature profile obtained with the thermocouple for two days in 2017. The solid line represents the temperature measurement in segment 13 and the dashed line represents the measurement in segment 16. Each color represents the database of one THB-valve per day. The black vertical lines denote any discharge (technical, useful, not useful) executed in these two days. One can observe that the solid line (representing the segment 13 temperature profile) increases continuously during the entire experiment day with almost no decay, whereas the dashed curve (representing the temperature in segment 16) rises less during the same day. The reason is that the THB-valve in segment 16 is connected to the AUG cooling water system avoiding overheating due to its location next

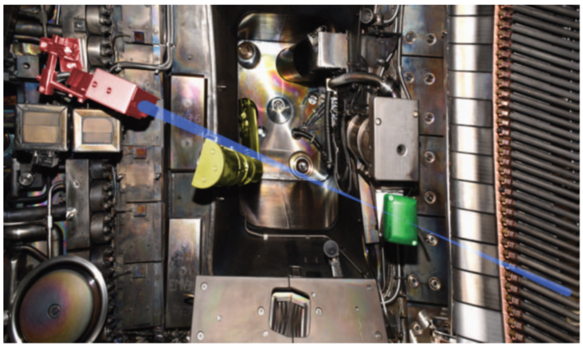

Figure 4.5: In-vessel components of the THB and the gas-puff imaging (GPI) system at the LFS in segment 13. One thermocouple used for this check is installed in the valve system which is indicated in green. Additionally, the optical head is indicated in red, the corresponding LOS distribution in blue and the GPI system in yellow. Taken from Ref. [Gri18].

to the NBI box 1 in segment 16, in contrast the valve setup in segment 13 was connected only to the support structure at the time of these experiments, thus the heat transfer of the valve setup is strongly damped. Following the tile-calorimetry approach, the amount of energy deposited for each executed discharge can be computed. The mass and the heat capacity of each component of the valve setup is taken from Ref. [Gri18]. The underlying equation for determining thermal energy is,

$$Q = \sum_{i=0}^{n} m_\mathrm{i} \int_{T_\mathrm{end}}^{T_\mathrm{begin}} c_\mathrm{p,i}(T) dT, \tag{4.6}$$

where m_i is the mass of the i-th component, $c_\mathrm{p,i}(T)$ is the temperature-dependent heat capacity of the i-th component and the boundaries of the integral defines the temperature rise. As this approach requires thermal equilibrium, one can suppose that each component of the valve setup has the same temperature at the starting point for the fit and a common decay behaviour. Normally, one would use a standard exponential decay function as followed. Due to the low temperature rise measured with both thermocouples, an exponential decay function is not suitable. Instead, the Taylor series until the first order of an exponential function yielding a linear fit function is implemented. The fit function finally used is defined as:

$$T(t) = (T_\mathrm{start} - T_\mathrm{initial}) \cdot \kappa_\mathrm{cooling\ down} \cdot (t - t_\mathrm{start}) + T_\mathrm{start}, \tag{4.7}$$

where T_initial is the initial temperature before the temperature rise, T_start is the temperature at the starting point for the fit, t_start is the time at the starting point for the fit and $\kappa_\mathrm{cooling\ down}$ is the cooling down coefficient. It must be mentioned, that due to the requirement for thermal equilibrium, the impact of any given scan cannot be resolved. This setup can only resolve trends of the deposited energy per discharge on each valve system and has

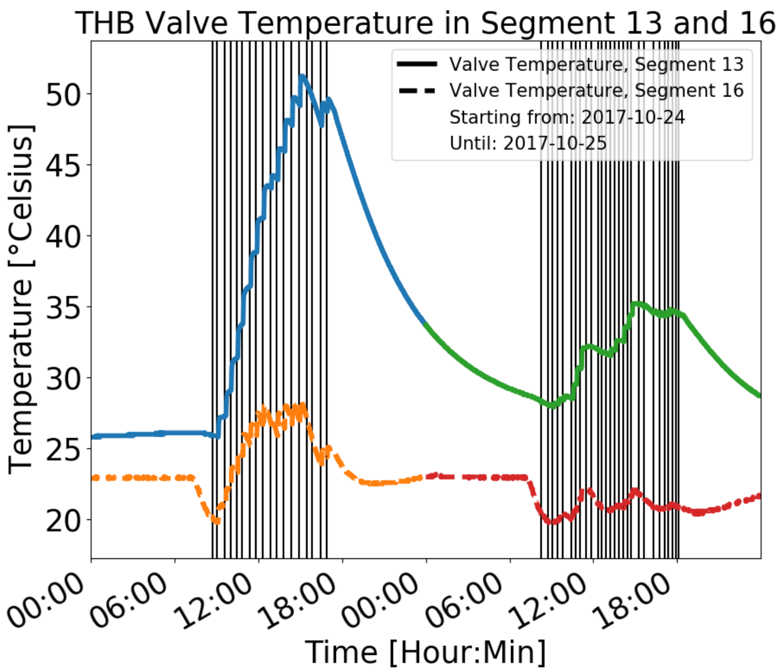

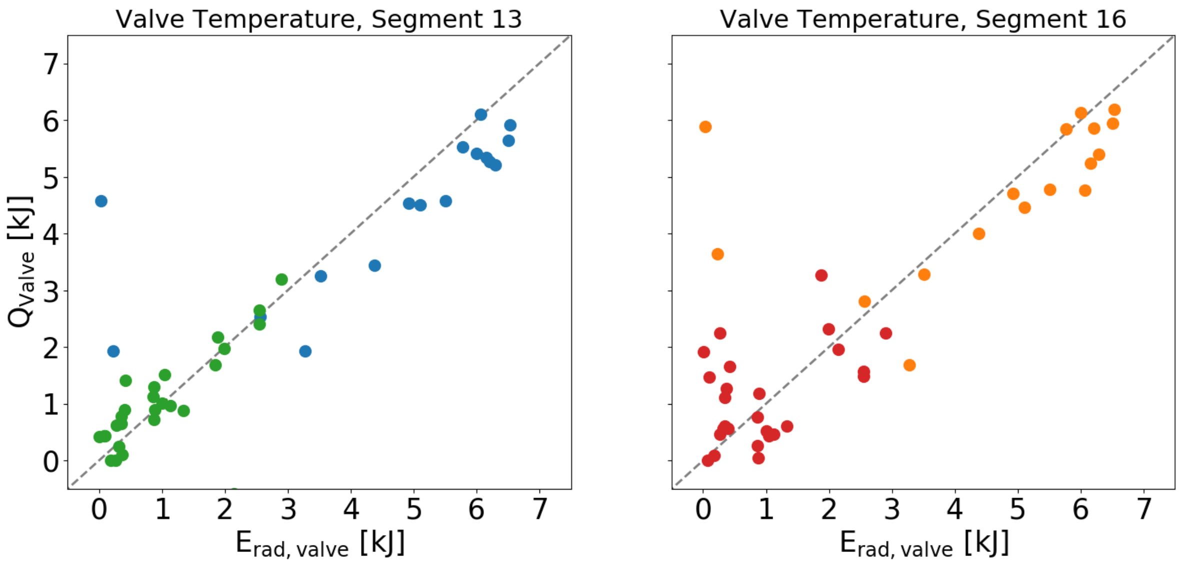

Figure 4.6: Upper: Traces of the valve temperature obtained with the thermocouple for two days in 2017. The solid and dashed lines represent the temperature measurements in segments 13 and 16, respectively. Each color represents a database of one THB-valve of one day. The black vertical lines denote any discharge (technical, useful, not useful) executed in those two days. Lower: The energy stored in the valve setups against the energy stored according to radiation heating up the respective protection tile surface. A good linear agreement between both parameters can be observed. The magnitude of both estimated energy parameters also match reasonably. Each color represents the database of one THB-valve per day.

been compared against several plasma parameters. A promising trend has been observed between the radiated energy and the energy measured for both valves. As a further check, the amount of radiation reaching each valve is estimated. The radiative energy is divided by the plasma surface taken at a certain time point and then multiplied by the area of the plasma-facing protection tile. The outcome is labelled as $E_{\mathrm{rad,valve}}$ and the deposited energy estimated for both valves can be found in Fig. 4.6 (lower). The x-axis denotes the amount of radiative energy reaching the protection tile, whereas the y-axis denotes the amount of energy deposited according to the thermocouples installed in the valve setups. An almost linear trend between the estimated amount of radiative energy reaching the valve and the energy deposited according to the thermocouples can be observed. The magnitude of both parameters is in good agreement as well. For both valves outliers can be observed. They may be caused by disrupted discharges, where the energy stored in the plasma hits the first wall in the region between segment 13 and 16 causing the strong rise in the deposited valve energy. With that observation it seems that radiation is the dominant source during normal plasma operation (no disruption) for energy deposition in the limiter shadow.

4.2.2 Analysis of the energy loads on the PSL

A similar study can be realised for the lower PSL. The thermocouple measurements of the PSL tiles *PSL Tile 1* and *PSL Tile 2* are compared against the radiative energy loads obtained from the CHERAB framework introduced previously in this chapter. For the upper PSL, such checks are not available yet. During the DivIIo-Upgrade, thermocouples will be installed in the upper PSL. For the lower PSL, reasonable thermocouple profiles are not available for the entire database, only for the AUG campaign 2021/2022. The thermocouple measurement of *PSL Tile 1* is compared against the radiative energy loads of the area highlighted in green and the thermocouple measurement of *PSL Tile 2* is compared against the radiative energy loads of the area highlighted in red in Fig. 4.7. The comparisons of both tiles can be seen in Fig. 4.8. Fig. 4.8 (left) illustrates the results of *PSL Tile 1*. The x-axis denotes the energy according to thermocouple measurements, the y-axis denotes the energy according to the CHERAB calculations. A dashed bisector illustrating perfect match is added. The comparison reveals a good agreement indicating that *PSL Tile 1* seems to be dominantly heated up by radiation. Single outliers can be observed, which might be related to disrupted plasma discharges or corrupted thermocouple evaluation. Fig. 4.8 (right) illustrates the results of *PSL Tile 2*. The description is identical to Fig. 4.8 (left). in contrast to *PSL Tile 1*, the thermocouple results of *PSL Tile 2* are below the results provided by the CHERAB calculations. It indicates that the energy (from radiation or particles) seems to be below the energy threshold being required for the use of the tile-calorimetry approach. The results from both tiles suggest that the energy loads reaching these two tiles are dominated by radiation. Further impacts from plasma-wall-interaction have not be resolved so far, but cannot entirely be excluded due to the lack of a sufficient toroidal coverage with thermocouples or of further diagnostics.

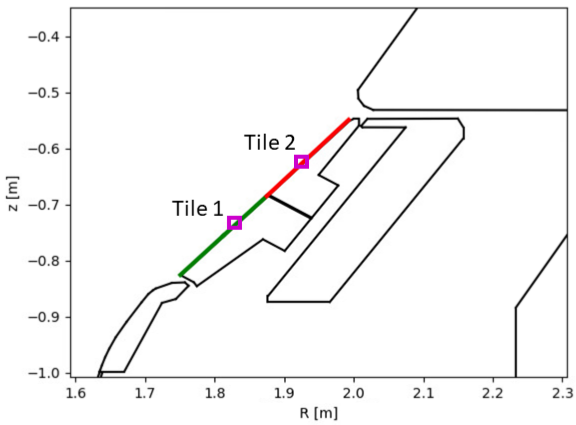

Figure 4.7: Cutout of the CHERAB setup shown in Fig. 4.1. The cutout shows the lower PSL. The two areas of the PSL used for this comparison are marked in green for *PSL Tile 1* and in red for *PSL Tile 2*. Available thermocouples are marked as purple markers.

4.3 The novel attempt on the JET global energy balance

The promising results and new findings based on the AUG energy balance motivate for a novel attempt on the energy balance challenge at JET. The latest energy balance results at JET indicate that only 75% of the injected energy can be detected [MBD+17]. Detailed analyses were carried out to identify potential sources of errors and, if possible, to eliminate them. Single assumptions of the extensive study [MBD+17] are used as a starting point. The JET energy balance equation following the definition from Ref. [MBD+17] can be expressed as:

$$E_{\mathrm{OH}} + E_{\mathrm{NBI}} + E_{\mathrm{ICRH}} = E_{\mathrm{TC,Div}} + E_{\mathrm{E,Lim}} + (E_{\mathrm{R}} - f_{\mathrm{B}} E_{\mathrm{RB}} - f_{\mathrm{Div}} E_{\mathrm{RDiv}}), \tag{4.8}$$

where $E_{\mathrm{TC,Div}}$ denotes the energy obtained by the divertor thermocouples and $E_{\mathrm{E,lim}}$ the energy obtained by the limiter thermocouples. E_{R} denotes totally radiated power, whereas E_{RB} the bulk plasma radiation and E_{RDiv} the divertor radiation. The radiation is divided into bulk and divertor radiation in order to assess double accounting (by f_{B} and f_{Div}, the fraction of radiation which is already accounted by the thermocouples [MBD+17]). For both adjusting parameters constant values for the entire database ($f_{\mathrm{B}} \sim 0.11$ and $f_{\mathrm{Div}} \sim 0.27$) are suggested. Due to the low data reliability, thermocouples from the 48 bulk tungsten tile modules placed in the center of the divertor are excluded from the analysis. Therefore, the database considers only discharges for which the strikeline is not put on this area. Furthermore, it is assumed that this area is only exposed to plasma radiation properly acquired by the bolometry [MBD+17]. To compensate the sparse poloidal coverage of the limiter thermocouples, the limiter results are multiplied by 1.6 in order to match with JET limiter discharges as benchmark test. For this setup, about 75% of the

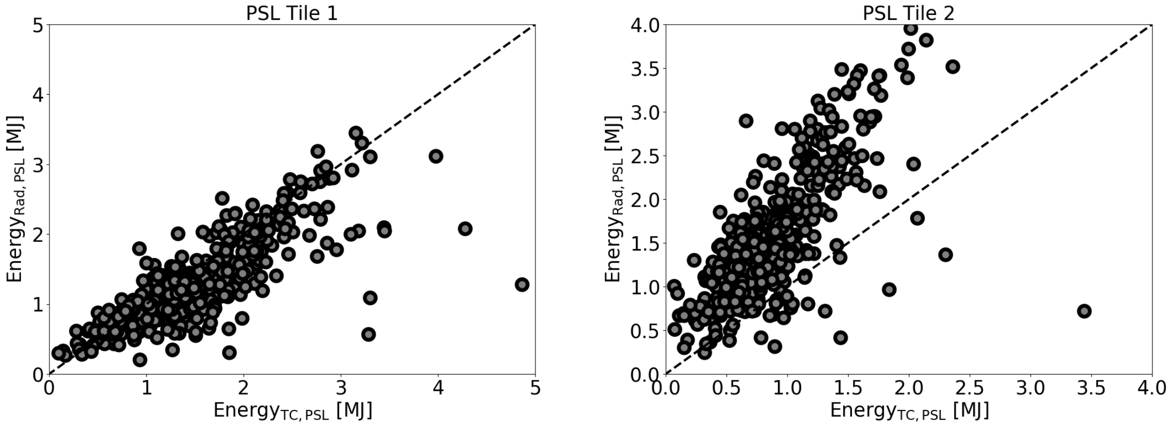

Figure 4.8: Left: Comparison of the deposited energy according to CHERAB calculations and thermocouple measurements of *PSL Tile 1* as defined in Fig. 4.7. A dashed bisector is added representing an ideal match between both quantities. A good agreement between both quantities for the entire range is observed. Right: Comparison of the deposited energy according to CHERAB calculations and thermocouple measurements of *PSL Tile 2* as defined in Fig. 4.7. A dashed bisector is added representing an ideal match between both quantities. The CHERAB results provide higher values than the thermocouple measurements.

injected energy have been found on average for a JET database of $\sim$ 350 discharges.
The results and the extensive analysis of potential uncertainties discussed in Ref. [MBD$^+$17] could not identify a single source causing the mismatch in energy balance. Latest calibration work [KSC$^+$23] on the JET NBI comparing D and T-beams reveal no mismatch on relative scales. It suggests that the mismatch is independent of the beam species. A simple check can be performed by exploiting the change of the time derivative of the plasma stored energy when the NBI power is switched off or on. The heating efficiency in its simplest form can be written as:

$$\eta = \frac{\Delta(\frac{dW}{dt})}{\Delta P_{\mathrm{in}}}, \tag{4.9}$$

where the numerator denotes the change in the time derivative of the stored plasma energy and the denominator the change in the injected heating power. The fits applied on the slope of both quantities suggest for JET L-modes that only about 80% of the NBI power is actually stored in the plasma [KSC$^+$23]. Further analysis with more sophisticated numerical codes like TRANSP/NUBEAM [Haw80, GMT$^+$81, PMA$^+$04] or ASCOT [HSP93] are required to investigate this observation. Any NBI losses (shine through, CX, orbit and re-ionization) have not been assessed in this analysis. The observations with respect to the newly obtained AUG global energy balance suggest to update Equ. (4.8) adapting the contribution assigned to radiation and NBI-losses. As shown for AUG, the fraction of missing radiation, which cannot be accounted by the AUG cooling water calorimetry varies strongly throughout the entire database which is in contrast to the assumptions presumed

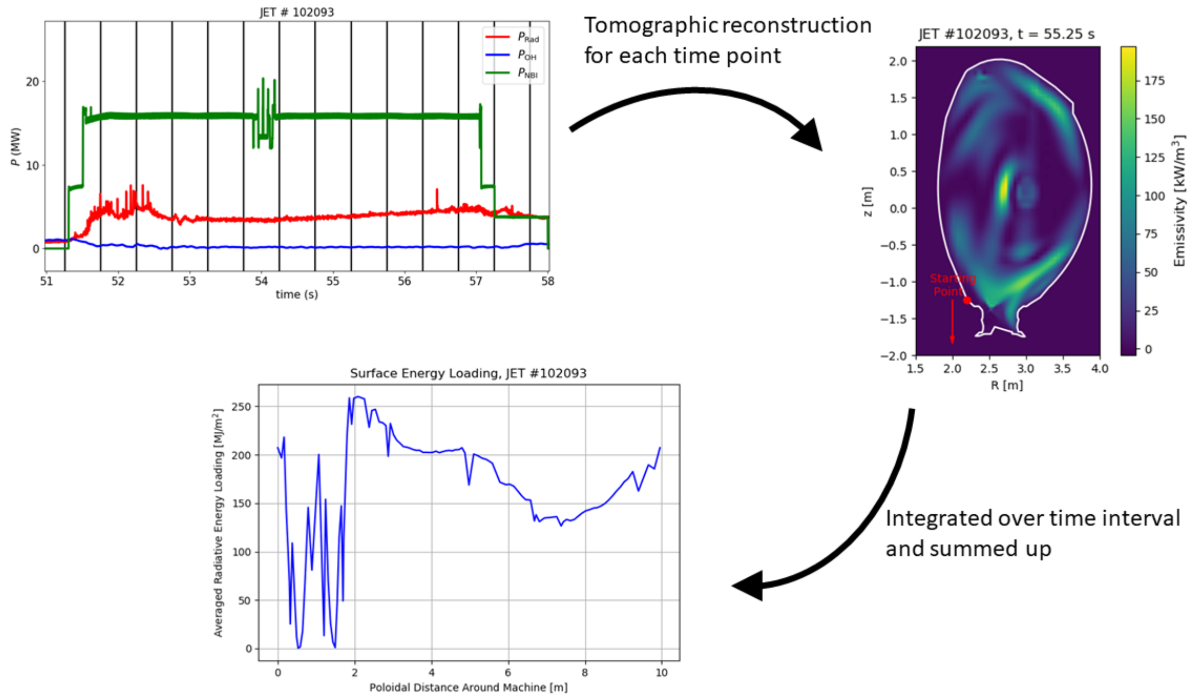

Figure 4.9: Workflow required at JET to determine the poloidal radiative energy distribution.

in Ref. [MBD⁺17] and requires adjustments.
In the updated analysis, the thermocouples of the divertor baffle tiles and the upper dump plates are additionally considered. Latest work with QCE H-mode discharges support the consideration of any available calorimetric measurements to acquire properly any particle energy loads on non-divertor PFCs. In order to assess the poloidal radiative distribution, a workflow similar to the one introduced for AUG is also available at JET. The AUG workflow exploits a novel GPT-model minimizing manual efforts, whereas the JET workflow requires several manually optimized tomographic reconstructions for a single discharge. Fig. 4.9 illustrates the work flow: A discharge has to be divided into sections (shown here as vertical black lines). These have longer intervals (2 s) in the L-mode phase and shorter intervals (0.5 s) in the H-mode phase. For each time a manually optimized tomographic reconstruction has to be generated. Exploiting the standard JET intershot analysis, the radiative heat loads for each time interval is determined. This is repeated for all time intervals. As last step, the poloidal radiative heat load distributions are temporally integrated to determine the poloidal radiative energy load distribution for the full discharge [MBD⁺17].
In contrast to AUG, the missing radiative fraction of dedicated areas is not added. Instead, the contributions of the whole divertor (including divertor baffle tiles and excluding *Tile 5*), the upper dump plates and the inner and outer limiter are subtracted from the total plasma

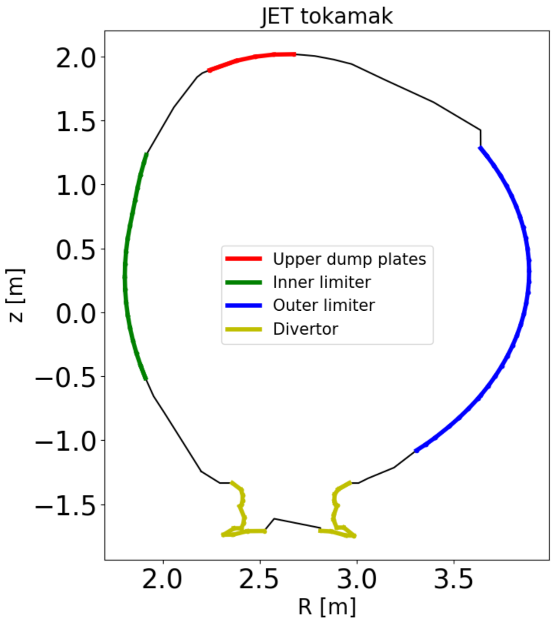

Figure 4.10: Poloidal contour of the JET tokamak. The radiative energy loads from areas, which are colored (yellow, blue, red, green), are subtracted from the total radiation in order to avoid double counting. The central part in the yellow contour corresponds to the 48 bulk tungsten modules or also called *Tile 5*

radiation. The coverage of the four areas is visualized in Fig. 4.10. Discharges with the strikeline on *Tile 5* are not considered in this database [MBD+17]. This newly introduced radiation contribution replaces the former radiation expression ($E_{\mathrm{R}} - f_{\mathrm{B}} E_{\mathrm{RB}} - f_{\mathrm{Div}} E_{\mathrm{RDiv}}$). The observations with respect to the NBI power stored in the plasma suggests to update Equ. (4.8) considering additionally NBI-losses on the output-side. As suggested by the AUG results, a term summarizing the NBI-losses seems to be demanded for an appropriate attempt in achieving a reasonable global energy balance (and supported by the observations in Ref. [KSC+23]). From previous experimental and numerical studies at TCV [GKD+17], it has been observed that the NBI-losses can dominate the NBI-power balance leading to a heating efficiency around ~ 17 %. This low NBI heating efficiency is known

$a \cdot E_{\mathrm{OH}} + b \cdot E_{\mathrm{NBI}} + c \cdot E_{\mathrm{ICRH}} = d \cdot E_{\mathrm{TC}} + e \cdot E_{\mathrm{Rad,adjusted}} + f \cdot E_{\mathrm{NBI-losses}}$								
case	fitted	match	a	b	c	d	e	f
(1) Benchmark Equ. (4.10)	none	75 %	**1**	**1**	**1**	**1**	**1**	**0**
(2) right side of Equ. (4.10)	d, e, f	100 %	**1**	**1**	**1**	0.97	1.02	0.36
(3) left side of Equ. (4.10)	a, b, c	100 %	0.89	1.04	0.95	**1**	**1**	**0.36**
(4) left side of Equ. (4.10) #2	a, b, c	100 %	0.89	0.68	0.95	**1**	**1**	**0**

Table 4.2: Overview of different configurations of the JET energy balance equation (Equ. (4.10). Bold prefactors are pre-set in regression studies.

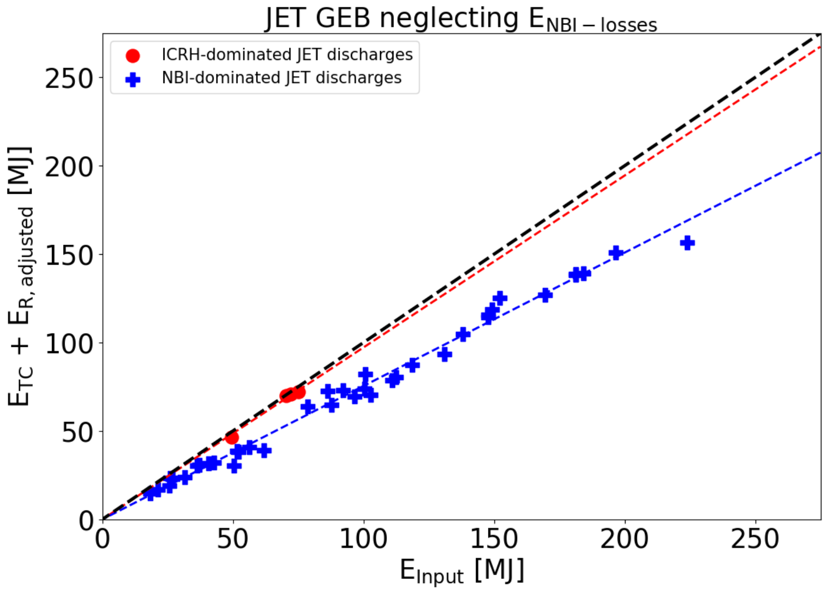

Figure 4.11: Global energy balance in JET setting the NBI-losses to 0 being consistent with studies at JET. For NBI-dominated JET-discharges only 75 % of the injected energy can be found, whereas for ICRH-dominated JET-discharges an almost perfect agreement can be achieved.

for smaller devices, but expected to be small for larger devices. Latest JET-results suggest the opposite and indicate a NBI heating-efficiency of ~ 80 % in L-modes [KSC+23]. The JET energy balance equation can be rewritten in the subsequent form:

$$E_{\mathrm{OH}} + E_{\mathrm{NBI}} + E_{\mathrm{ICRH}} = E_{\mathrm{TC}} + E_{\mathrm{Rad,adjusted}} + E_{\mathrm{NBI-losses}}. \tag{4.10}$$

The contribution $E_{\mathrm{NBI-losses}}$ summarizes for the JET analysis any possible NBI loss including shine through and re-ionization. In the first step, the contribution $E_{\mathrm{NBI-losses}}$ is set to 0, to benchmark the global energy balance obtained with the novel definition given Equ. (4.10) against the former regression results. The database utilized for this analysis, consists of 42 discharges (38 with dominating NBI-heating and 4 with dominating ICRH-heating ($E_{\mathrm{ICRH}} > 5 \cdot E_{\mathrm{NBI}}$)). The injected energy covers a range between 18 and 223 MJ and various H-mode scenarios. The main gases in this database are H, D and He. A small subset is with additional impurity seeding. Fig. 4.11 illustrate the energy balance results obtained with this setup. The blue markers denote JET discharges with dominating NBI-heating, whereas the red markers denote JET discharges with dominating ICRH-heating. In case of dominating NBI-heating a similar trend as given with the original Equ. (4.8) is observed. On average, only ~ 75 % of the injected energy can be found. At the same time, JET discharges with dominating ICRH-heating achieve an energy balance of ~ 97 %-agreement, which seems consistent with the observations in Refs. [MBD+17, GGC+24]. It was reported that for JET-discharges with lower input, where ICRH and OH become more important, the energy balance seems to improve. These discharges are located in an intermediate

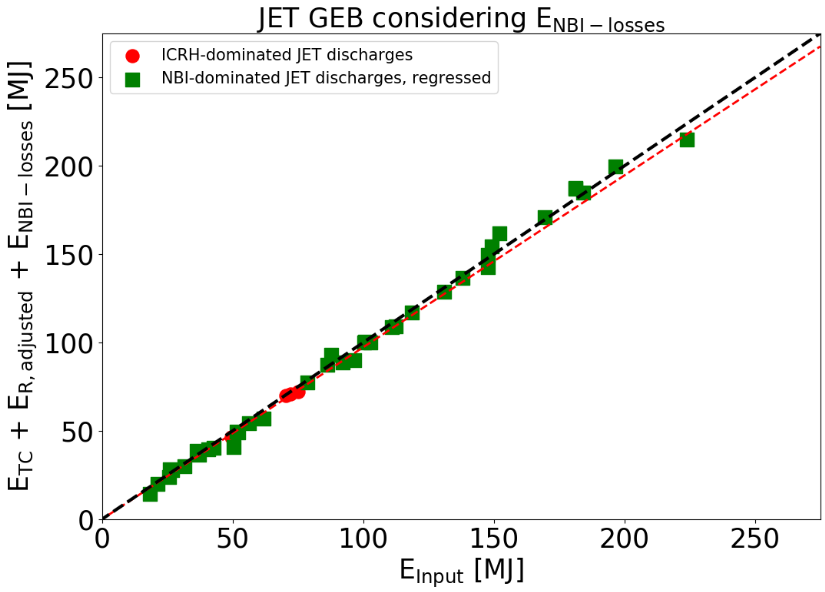

Figure 4.12: Global energy balance in JET considering NBI-losses on the output-side assuming 39 % obtained from the linear regression (green markers) corresponding to case (2) in table 4.2).

range of injected range in which trustworthy and robust results from tile-calorimetry can be expected. Latest energy balance studies conducted at the WEST tokamak report on a similar match for wave-heated discharges for a large representative database of about 600 experiments. It rather suggests that the treatment of NBI-losses was indeed incomplete in previous studies. The assumptions and results of this case with NBI-dominated JET-discharges are summarized in table 4.2 under the designation *(1) Benchmark Equ.* (4.10). As check, a linear regression is applied on both sides of Equ. (4.10) starting with the RHS and fixing the prefactors of the LHS to 1. The obtained weighting coefficient will correspond to the magnitude of NBI-losses with the respect to the totally injected NBI energy. The regressed energy balance is visualized in Fig. 4.12 and its results under the designation *(2) RHS of Equ.* (4.10). The same task is repeated with keeping fixed the RHS of Equ. (4.10) and regress the the prefactors of the input energy. The prefactor for the NBI-losses is set to 0.36. The regressed values are labelled *(3) left side of Equ.* (4.10) in the summarizing table. As final check, the regression is repeated, in which the prefactor of the NBI losses is set 0. This case is labelled as *(4) left side of Equ.* (4.10) *#2*.
For case (2), one can identify that the corrections for thermocouples and radiation remain around unity, whereas the corrections factor for NBI-losses is around ~ 36 % meaning that more than 1/3 of the NBI power leaving the duct is not stored in the plasma. As the limiter coverage with thermocouples is sparse on JET, localised re-ionization losses around the NBI ducts or the inner limiter may not be acquired and therefore they are not properly accounted in the energy balance. The regressed value seems high, but in Ref. [MBD+17]

it was already reported that the NBI-power has to be reduced to 65 - 80 % to match the energy balance, which seems not to be different to the prefactors presented here. The case (3) indicates similar results.
For case (4), the prefactor of the NBI-losses is set to 0 representing the setup introduced in Ref. [MBD+17]. The regression of the input contributions suggest the same prefactors for E_{OH} and E_{ICRH}, whereas the NBI contribution is reduced to 68 % being consistent with the results reported in Ref. [MBD+17]. The large drop in the NBI contribution underlines once again that NBI losses must indeed be taken into account in the energy balance.

4.4 Implications for empirical scaling laws

As shown with the energy balance analyses on AUG and on JET, a single calorimetric diagnostic covering the in-vessel components is not sufficient to establish a meaningful energy balance. A meaningful assessment of the radiation fraction reaching the in-vessel components disconnected from the calorimetry and the NBI losses have to be taken into account. The NBI losses at AUG are almost negligible, whereas they seem to be significant at JET. As mentioned earlier, so far it was only known that NBI losses can be significant on small experiments such as TCV [GKD+17].
However, these observations are of greater importance with respect to empirical scalings, which can depend on the absorbed heating power P. As discussed in Section 1.4, the regression formula (1.31) predicting the energy confinement time τ_{E} depends on P. The erroneous determination of the deposited power in NBI-dominated plasmas may lead to a systematic underestimation of this quantity making the predictions for ITER conditions more optimistic. It would be appropriate in future regression studies to consider the NBI-losses more correctly by splitting the absorbed power into its individual contributions (NBI, ECRH, ICRH and OH) in order to assess individually the performance of NBI-dominated or wave-heating-dominated plasmas:

$$\tau_{\mathrm{E}} \propto (P_{\mathrm{NBI}} - P_{\mathrm{NBI-losses}})^{\alpha} \cdot P_{\mathrm{ECRH}}^{\beta} \cdot P_{\mathrm{ICRH}}^{\gamma} \cdot P_{\mathrm{OH}}^{\delta} \tag{4.11}$$

It might be the case that the JET contributions to any empirical scaling, which depends on P, are erroneous due to possible incomplete accounting of the NBI losses. In Ref. [MBD+17], it has been reported that the ansatz to achieve the global energy balance has been repeated for JET discharges with carbon wall, which leads to a similar mismatch as with the ILW.

Chapter 5

An extensive analysis of SOL properties in high-δ H-mode discharges in the AUG tokamak

The impact of enhanced filamentary transport on the overall energy load distribution on divertor and non-divertor components is of exceptional importance. In the following chapter, the properties of the high-δ discharge database are firstly addressed. Due to the consideration of calorimetric diagnostics, certain constraints have to be taken into account. Subsequently, the coverage of the established database is discussed in terms of $T_{\mathrm{e,sep}} - n_{\mathrm{e,sep}}$-framework. The power exhaust capabilities of the discharges performed are evaluated using the calorimetric measurements. The evolution of the energy distribution are correlated with suitable parameters and generalized with an enlarged database. Furthermore, the evolution of the upstream and downstream SOL profiles are linked to separatrix quantities. As final aspect, the evolution of the filamentary properties in high-δ discharges is discussed. The filament heat flux contribution is assessed by setting up a limiter power balance. The gross erosion on limiter tiles in H-mode discharges is estimated exploiting dedicated limiter probe measurements. Excerpts of this chapter are taken from Refs. [REV$^+$24, REV$^+$23].

5.1 Setup of the high-δ discharge database

In order to cope with the aforementioned diagnostic constraints, including the capability of the calorimetric diagnostic to provide only time-integrated information, an appropriate shot plan has been conceived. The database consists of H-mode discharges in which the heating power combining NBI+ECRH or NBI only and the flattop fuelling in feed-forward using a high-δ, high-κ magnetic equilibrium is kept constant during the execution. Within this database, discharges have been executed at three different B_{tor}-values (-1.8 T, -2.45 T and -2.8 T) for a variation of q while keeping I_{p} fixed at 0.8 MA. The corresponding q_{95}-values are: -4.2, -5.5 and -6.4. Due to different B_{tor}-values, different heating schemes have to be used. The variations in heating, q and fuelling with a long flattop phase of about ~ 6 s in each discharge, allow to clearly correlate the calorimetric energy loads with different plasma quantities. Table 5.1 briefly summarizes the discharge setup characteristics. Fig. 5.1

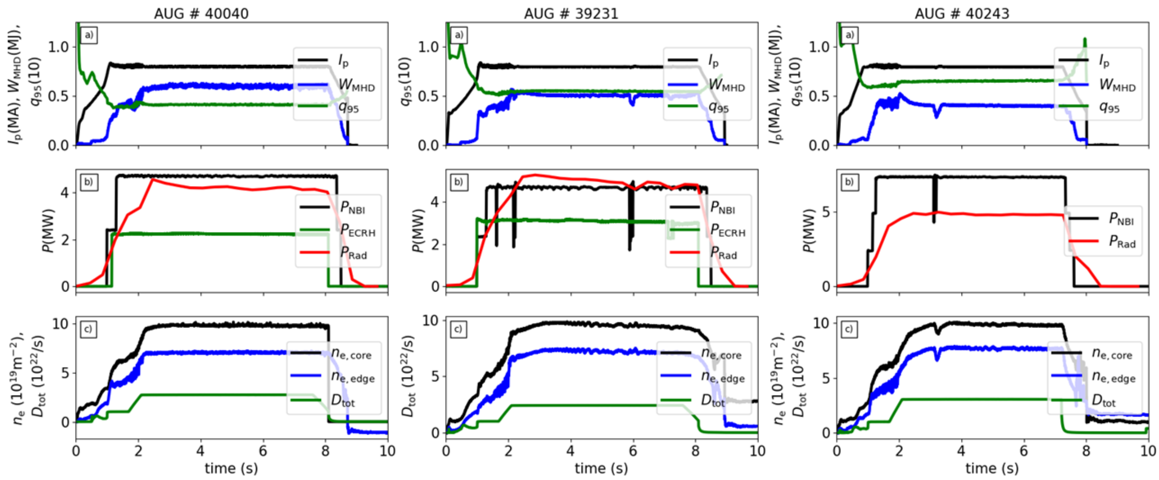

Figure 5.1: Experimental time traces of dedicated plasma parameters characterizing AUG discharges #40040, #39231 and #40243.

illustrates the time traces of dedicated plasma parameters for three discharge representing the discharge configuration considered in the database. In Fig. 5.1, panel b) shows the time traces of the heating scheme combining NBI (black) and ECRH in X2-mode (green) for #40040, #39231 and #40243. For #39231, two radially directed NBI sources and 4 ECRH gyrotrons directed as *central heating* are configured. For $B_{\rm tor}$=-2.8 T (#40243) the ECRH contribution is replaced by one additional NBI source, whereas for $B_{\rm tor}$=-1.8 T (#40040), the ECRH contribution is used in X3-mode (using 3 gyrotrons instead of 4). Radiative losses $P_{\rm rad}$ (red) are calculated by exploiting the novel bolometric calculation BPT [DBP$^+$21]. Using different heating schemes may change the $T_{\rm e}$-profile at the separatrix in order to support the conclusions drawn in Refs. [HWD$^+$18], [FEH$^+$21], [SVT$^+$22] that the separatrix emerges as key region to characterize the plasma performance. For the entire database, the same magnetic equilibrium is used with $\delta_{\rm u} \approx 0.28$ and $\kappa \approx 1.7$, leading to a CDN shaping. The shape is visualized in Fig. 2.3.

A significant range of the density operational space is covered by a variation of the flattop fuelling level on a shot-to-shot-basis. All discharges are fuelled from the divertor. Panel c) in Fig. 5.1 (middle) shows the fuelling level in the flattop phase for #39231 at 2.5e22/s. The database covers for this configuration a flattop fuelling between 0.1e22/s and 2.85e22/s. The highest fuelling level was limited by the ECRH cut-off density. With the continuous decrease of flattop fuelling, a gradual transition from the QCE regime to a Type-I ELMy H-mode occurs below 0.6e22/s. At $B_{\rm tor}$=-2.8 T, the fuelling covers the range between 1.75e22/s and 3.2e22/s and at $B_{\rm tor}$=-1.8 T the range between 1.0e22/s and 3.2e22/s is covered. Where the range of different $B_{\rm tor}$-values overlap each other, the same flattop fuelling levels have been used. For PFC energy distribution studies, only discharges are considered which are ended without the use of killergas. The use of killergas would falsify

$B_{\rm tor}$	NBI	ECRH	Fuelling range	# of successful
-1.8 T	2 radially directed NBI sources	3 *central heating* gyrotrons in X3-mode	1.0 - 3.2 e22/s	5
-2.45 T	2 radially directed NBI sources	4 *central heating* gyrotrons in X2-mode	0.1 - 2.85 e22/s	8 (+2 fuelling scans)
-2.8 T	3 radially directed NBI sources	0 gyrotrons	1.75 - 3.2 e22/s	4

Table 5.1: Overview of the heating scheme for the NBI+ECRH or NBI-only heated discharges ,fuelling range for the different $B_{\rm tor}$-values and number of successful discharges used in this study.

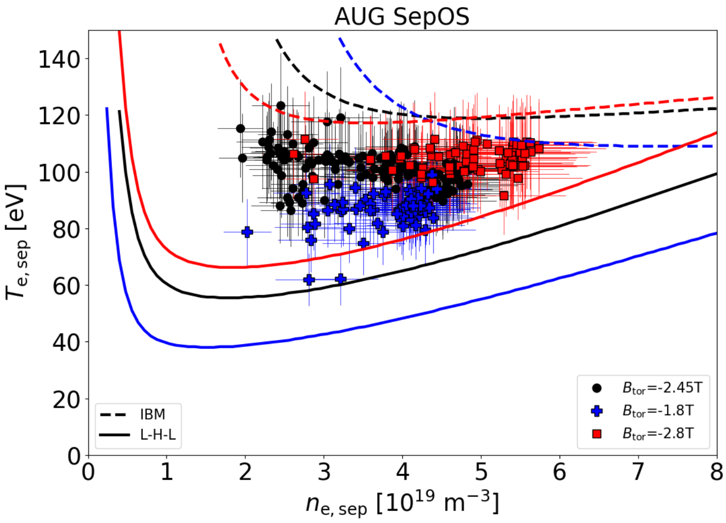

Figure 5.2: Coverage of the AUG operational space according to the SepOS-theory for the three different $B_{\rm tor}$-values of the database introduced before.

the energy distribution, which has to be avoided for this study. Due to technical issues with the data acquisition of the BPP system single discharges at $B_{\rm tor}$=-2.45 T had to be repeated to acquire the required limiter probe measurements.

5.1.1 Coverage of the AUG operational space

The database coverage in the AUG operational space is qualified by means of the SepOS-theory. In Fig. 5.2, the operational windows for all three configurations in $B_{\rm tor}$ are illustrated. Since $\alpha_{\rm MHD}$ (defined in Equ. (2.31)) and the H-L-H transition criterion (Equ. 8 in Ref. [EMG+20]) depend on $q_{\rm cyl}$ (defined in Equ. (2.24)), the present database cannot be visualized in a single $T_{\rm e,sep} - n_{\rm e,sep}$-plot. Due to the lack of a reasonable $Z_{\rm eff}$-estimate at the separatrix in AUG, the value is set to 1.24 for the entire database. The fuelling scan realized with the present database covers a significant range in the density operational

space without a substantial variation in $T_{\mathrm{e,sep}}$ for each B_{tor}. In terms of Greenwald density (for the database setup is $n_{\mathrm{GW}} = 1 \cdot 10^{20}/m^3$), the separatrix density spans the range of 0.2 - 0.6 n_{GW}.
Each marker color denotes a single discharge. For each discharge, the provided $T_{\mathrm{e,sep}} - n_{\mathrm{e,sep}}$-tuples are distributed close to each other and shows only slight variations for each discharge. The dedicated discharge boundaries have provided small variations within a discharge, which are demanded for conclusive calorimetric analyses. Since the SepOS-theory aims to correctly describe the power exhaust capabilities of a plasma, the evolution of the energy load distribution of this database is studied in the following section.

5.2 The distribution of energy loads on AUG in-vessel components

5.2.1 The global energy balance of the database as requirement for reliable energy load studies

Any energy loads studies require a consistent global energy balance in order to ensure reasonable conclusions. In Section 4.1.3, the AUG global energy balance has been achieved for a large, representative database considering 577 discharges. To obtain the global energy balance, the revamped cooling water calorimetry numerical codes, which are used to estimate the radiative and NBI-losses contributions for the right-hand side of Equ. (4.1), have been exploited. The global energy balance following Equ. (4.1) for the database introduced in Section 5.1 is shown in Fig. 5.3. The different marker colors denote the

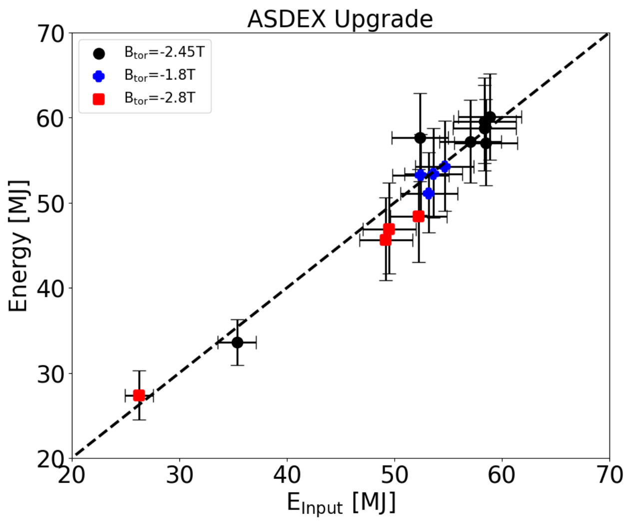

Figure 5.3: The plot presents the global energy balance obtained with the AUG cooling water calorimetry for the database introduced before.

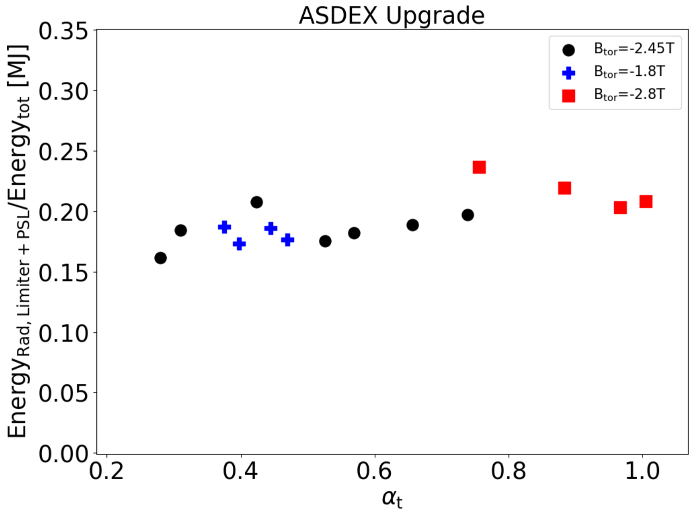

Figure 5.4: The quantity $E_{\text{Rad, Limiter+PSL}}$ from Equ. (4.1) normalized by the sum of the left hand-side of Equ. (4.1) is plotted against α_t. The increase of radiation is for the covered range marginal.

different B_{tor}-values considered in this database. For the entire database, the injected and measured energy match almost perfectly. For the subsequent energy load studies, only the first term ($E_{\text{Calorimetry}}$ in Equ. (4.1)) is considered. The term $E_{\text{NBI-losses}}$ contributes only slightly for AUG discharges. This has been discussed in Section 4.1.3. The evolution of $E_{\text{Rad, Limiter+PSL}}$ normalised to the total input energy is shown in Fig. 5.4. The fractions are plotted against α_t and varies marginally with α_t.
The focus in this analysis is on the change of energy distribution through the presence of enhanced filamentary transport. The areas assigned to the contribution $E_{\text{Rad, Limiter+PSL}}$ are not exposed to particle transport and are dominantly heated up by plasma radiation as shown in Section 4.2. Therefore, they are not of interest for the subsequent energy load analysis.

5.2.2 Evolution of the energy loads on AUG in-vessel components

In this section, the evolution of the energy loads on any PFCs in AUG is discussed. Here, the limiter, the lower/upper divertor (with inner/outer divertor together) and the heat shield are individually discussed.
To infer the evolution on the PFC heat loads whenever the plasma scenario moves from Type-I ELMy regimes to high density QCE regimes, all available cooling units of the AUG cooling water calorimetry are considered and cumulated to dedicated areas. Following the notation in Ref. [HER+04], the limiter in AUG is defined by the four ICRH antennas and the four auxiliary limiters (black highlighted areas and labels in Fig. 3.3 (left)). The

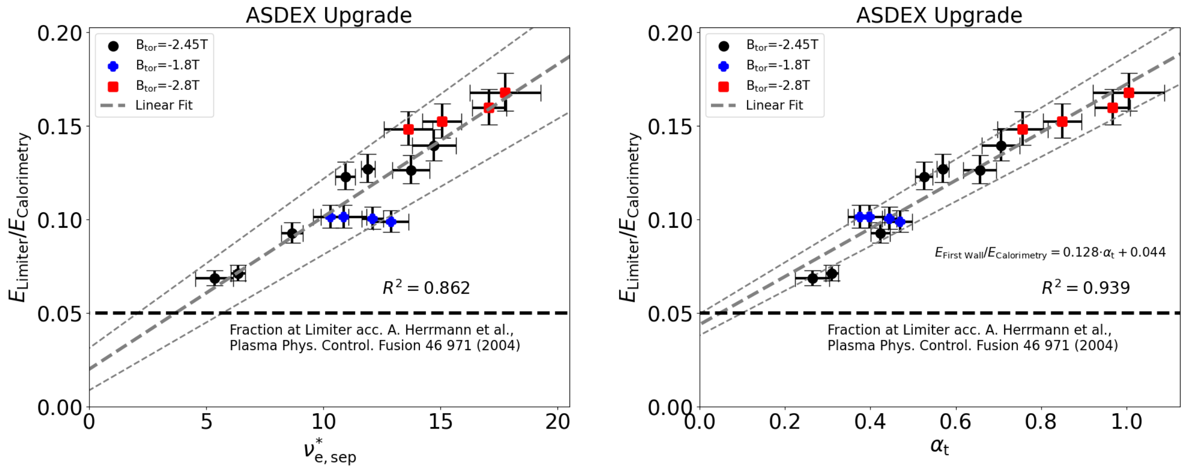

Figure 5.5: Scaling of the energy loads at the AUG limiter exploiting two separatrix parameters: the separatrix collisionality $\nu^*_{\mathrm{e,sep}}$ (left plot) and the turbulence control parameter α_{t} (right plot). One can see that using α_{t} provides a clear, almost linear trend over the entire H-mode range of α_{t} $(0.1 \leq \alpha_{\mathrm{t}} \leq 1.0)$

latter PFCs are installed on both sides (left and right) of each NBI duct. Following the observations in Ref. [HER+04], ELMs can reach the auxiliary limiters and emphasize the consideration of these PFCs. Each ICRH antenna and auxiliary limiter acts as an individual cooling unit. The cooling units of the inner and outer divertor of AUG (orange/blue highlighted areas and labels in Fig. 3.3 (left)) are in sum 32 cooling units and define the lower divertor. The *upper divertor* follows this scheme and combines the inner and outer divertor of AUG (red/green highlighted areas and labels in Fig. 3.3 (left)), which are in sum 32 cooling units. The *heat shield* is based on the cooling units highlighted in brown in Fig. 3.3 (left). This area consists of 16 cooling units. Each introduced dedicated area is normalised by the sum of all available cooling units.

In recent years, it has been experimentally shown at AUG [HWD+18], [FEH+23] and theoretically suggested [ELP+13], [EMG+20], [Sco97] that the region around the separatrix emerges as a key region to describe the entire plasma performance and underscores also the choice of the separatrix parameters to characterize the heat fluxes reaching the PFCs. As discussed in Refs. [FEH+21, HWD+18], the QCE regime may have a second drive affecting the SOL which seems to be in agreement with the reflections outlined in Ref. [Sco97] that at certain plasma conditions the bottom of the pedestal, close to the separatrix becomes strongly ballooning unstable, and this drives small scale turbulent structures, which are peeled of and travel through the SOL. In the following we will investigate the role of these instabilities, and of their non-linear evolution into plasma filaments, on the convective radial transport of heat and particles.

By comparing the normalized limiter energy loads with the separatrix collisionality $\nu^*_{\mathrm{e,sep}}$ (following the definition introduced in Equ. (2.38)) and with the turbulence control parameter α_{t} (following the definition introduced in Equ. (2.37)), it has been observed that the

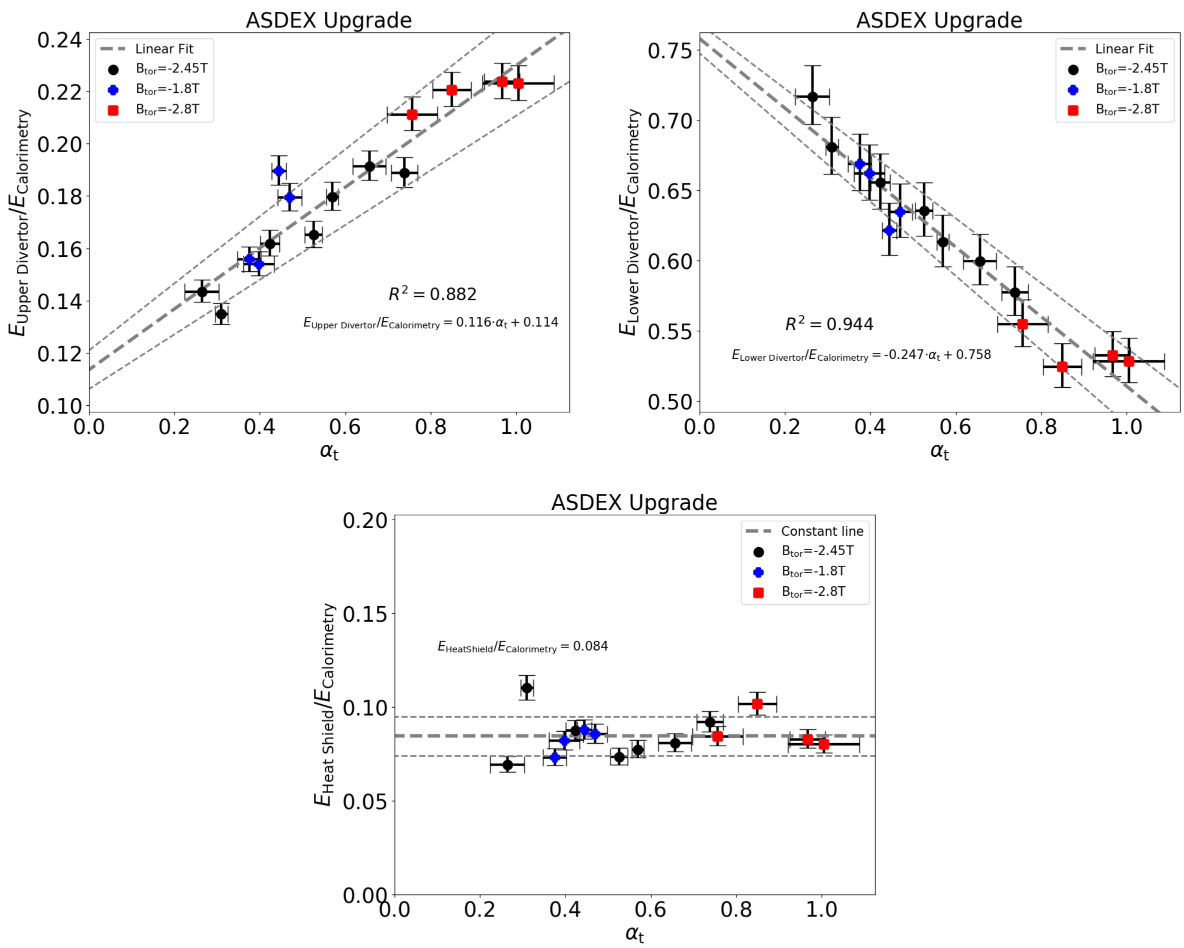

Figure 5.6: The evolution of the PFC heat loads at the upper divertor (upper left), the lower divertor (upper right) and the heat shield (lower). The regression formulae for the three cases and the correlation parameter R^2 (excluding the lower case) are added.

trend of the normalized limiter energy loads increases almost linearly with α_t. This trend is illustrated in Fig. 5.5. Additionally, the regression formula with respect to α_t is added. The energy load scaling covers the, so far, known range for H-mode discharges in α_t. The major difference between $\nu^*_{e,sep}$ and α_t ($\approx 100 * q_{cyl}\nu^*_{e,sep}$)) is the different dependence on q_{cyl}. The transition from QCE discharges at higher fuelling to Type-I ELMy H-modes with continuously decreased flattop fuelling seems to be gradual, which is consistent with observations of the gradual increase of λ_q and the co-existence of Type-I ELMs with smallish, filamentary ELMs as reported in Ref. [FEH+21]. The transition to Type-I ELMs dominating the transport behaviour occurs normally for $\alpha_t < 0.55$ at AUG [FEH+23].
Furthermore, the results for the limiter energy loads of a previous AUG study [HER+04] is added as dashed horizontal line. At that time, 5% of the energy loads have been found at the limiter of a low density ELMy H-mode in AUG with carbon walls and seems to be in

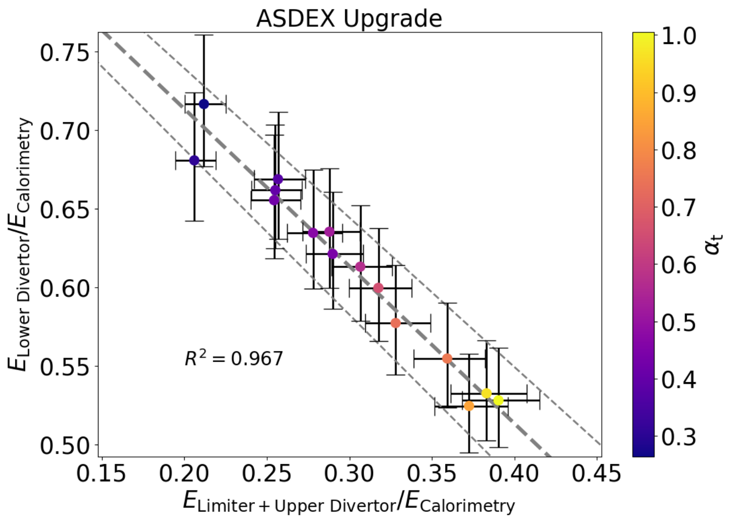

Figure 5.7: The evolution of the fraction of energy loads at the lower divertor is plotted against the evolution of the fraction of energy loads at the limiter and the upper divertor together. Both parameters are normalised by the total energy acquired by the revamped calorimetry. A colormap is added visualizing the α_t-value of each discharge.

good agreement with latest calorimetric observations in a full tungsten-device. Separatrix values are not available due to the data quality of the edge TS at that time together with the lack of a reasonable Z_eff-estimate at the separatrix, which is particularly important for carbon devices.

The increase of energy loads at the limiter is not related to an increase of radiative energy loads at the limiter. As reported in Ref. [FEH+21], the continuous increase of fuelling leads to a slight increase of radiation, which is consistent with the trend of the normalised quantity $E_\mathrm{Rad,sim}$ illustrated in Fig. 5.4. However, its impact on the energy load evolution at the limiter is small compared to energy loads originated by particle transport. The offset obtained from the regression and visualized in the plot is expected to be associated with radiative energy loads and will be picked up again later in Section 5.6.2.

This scaling is extended to all areas connected to the cooling water calorimetry. Fig. 5.6 illustrates the evolution of the energy loads at the upper divertor (upper left), at the lower divertor (upper right) and at the heat shield (lower). For both, the upper and lower divertor, the correlation parameter R^2 and the regression formula with respect to α_t are added. The regression coefficient R^2 show for both the areas a high value indicating a reasonable correlation and supporting the trend with respect to the limiter scaling. Interestingly, the slopes of both regressions, the upper divertor and the limiter, point out that the energy loads are equally transferred to both areas.

The comparison of the evolution of both, the limiter and the upper divertor together, with the lower divertor is shown in Fig. 5.7. Together with the observations from Figs. 5.3 and 5.4, this trend indicates that the energy distribution between divertor and non-divertor

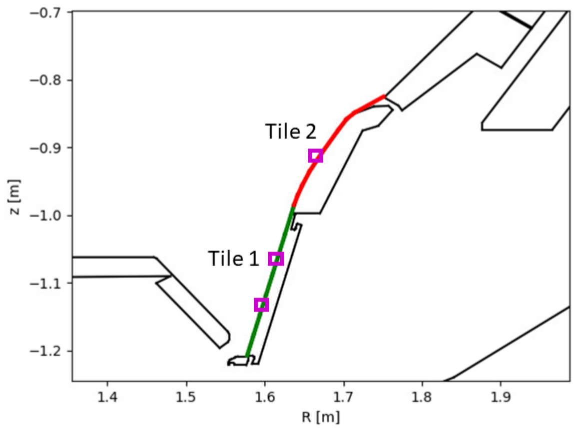

Figure 5.8: Close-Up of the lower outer divertor. The green highlighted range with label *Tile 1* denotes the target with the full tungsten tiles and the red highlighted area with label *Tile 2* the baffle tiles above the target.

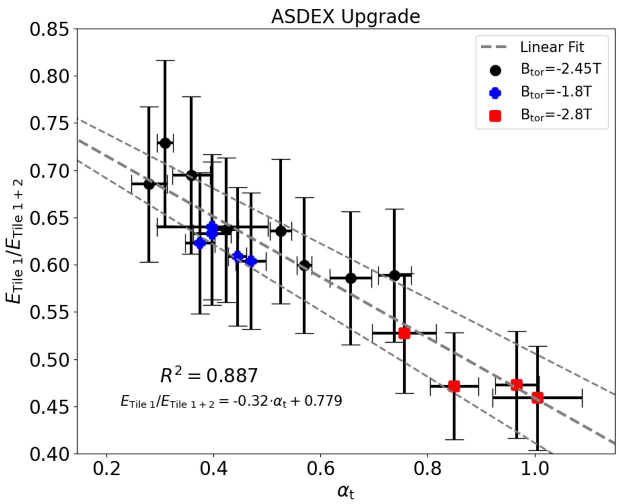

Figure 5.9: Evolution of the energy deposition at the outer target at *Tile 1* normalised against the sum of both tiles is plotted against α_t. With increasing α_t, the energy found on *Tile 1* decreases almost linearly from ~ 0.7 to ~ 0.45, corresponding to a decrease of the energy deposited on the target.

components have been changed without substantially modifying the overall energy loss. The reduction at the lower divertor may be linked with a reduction of the conductive SOL

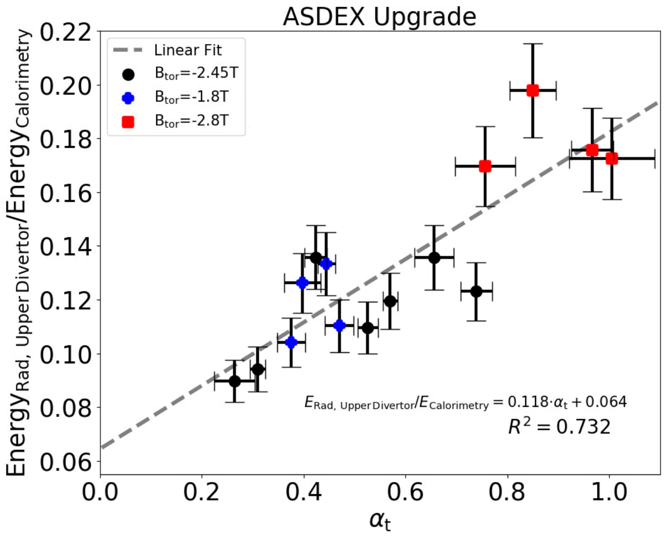

Figure 5.10: Evolution of the radiative heat loads reaching the upper divertor normalized by $E_{\mathrm{Calorimetry}}$ is plotted against α_t. A reasonable agreement between the radiation reaching the upper divertor and α_t is observed.

transport reaching the main target and a simultaneous energy transfer to non-divertor components through an additionally arising energy loss channel.

A reduction of the energy deposited at the main target would support the speculations of a further energy loss channel carried by turbulent structures/ballooning modes at the separatrix. To analyze the evolution of the energy loads at *Tile 1*, the energy loads acquired by thermocouple measurements on *Tile 1* are normalized by the sum of energy loads acquired by thermocouple measurements for *Tile 1* and *Tile 2*. The distribution of both areas, *Tile 1* and *Tile 2*, is illustrated in Fig. 5.8. This ratio is plotted against α_t and shown in Fig. 5.9. A clear linear trend with a significant reduction in energy loads at *Tile 1* is observed. R^2 derived from the linear regression reveals a reasonable value of 0.887. The tile-calorimetry approach has an intrinsic uncertainty of $\sim 17\%$, which can affect R^2. It is presumed that the energy loads on *Tile 2* are not subject to significant variations due to additionally occurring transport processes. Cross-checks with IR-, LP-measurements and radiative energy loads will be discussed in Section 5.3 in order to verify this presumption. So far, the trend supports the hypothesis that the reduction in the energy loads on *Tile 1* is caused by a reduction of the parallel conductive transport. This observation seems to be in line of a possible redistribution of the perpendicular/parallel energy load in favour of an increased radial heat flux and may be compatible with the broadening of downstream profiles.

As reported in Ref. [FEH$^+$21] by using IR-thermography, the energy loads in the upper divertor increases whenever the QCE-regime is achieved. Since the upper divertor is not

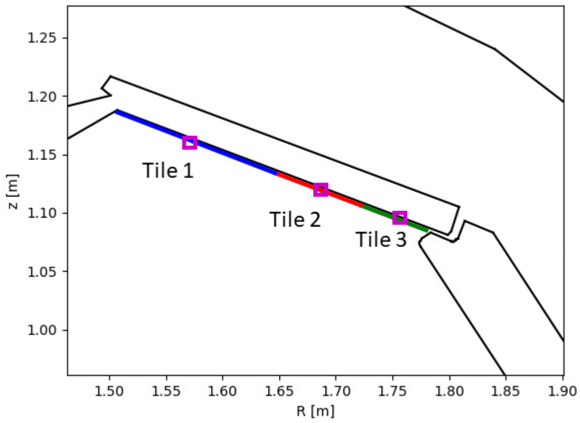

Figure 5.11: Distribution of the three relevant tiles in the upper outer divertor.

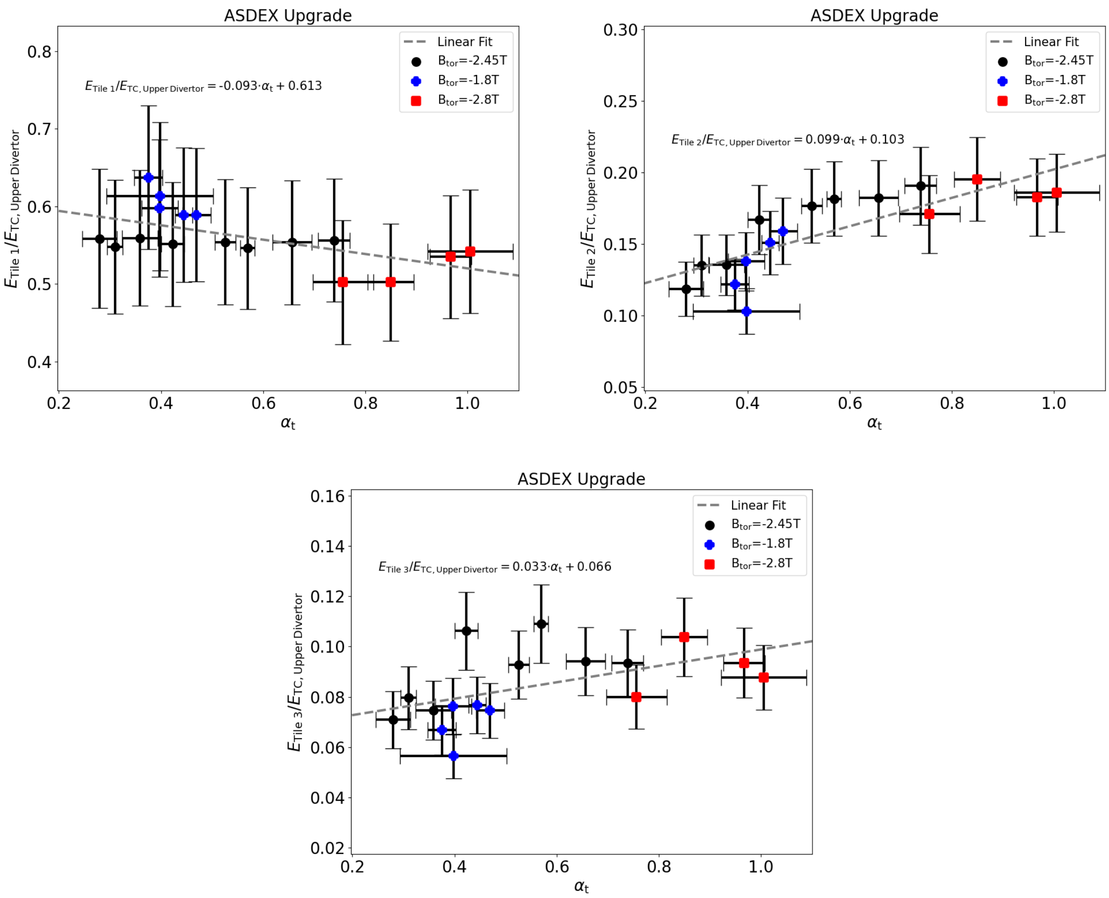

Figure 5.12: Evolution of the energy load distribution for the three tiles of the upper outer divertor normalized by $E_{\mathrm{TC,Upper\,Divertor}}$ is plotted against α_{t}.

connected with the main plasma, the increase of energy loads is associated with an increase of cross-field transport [FEH+21]. The tomographic reconstructions and poloidal radiative heat load distributions of QCE discharge #39231 in Fig. 4.1 in Section 4.1.1 indicate a strong localised radiation pattern between the upper X-point and the upper divertor plates.

As the calorimetric observations suggest that the increase of energy loads at the upper divertor are connected with the increase separatrix turbulence described by α_t, the evolution of this additional, localised radiation pattern may follow this trend as well. Also the magnitude of the radiative energy loads reaching the upper divertor is of interest. The connection between filamentary transport and this localised radiation pattern at the upper divertor plates is yet not clear and requires further investigations.

With the aid of the framework introduced in Section 4.1.1, the radiative energy loads reaching the upper divertor are estimated. In Fig. 5.10, the evolution of the radiative energy loads at the upper divertor normalised to the total energy load as inferred by the calorimetry $E_\mathrm{Calorimetry}$ is plotted against α_t. A reasonable trend between the normalised radiative energy loads and α_t can be observed. The regression formula and R^2 of this evolution is added. The slope of the radiative evolution matches well with the one from calorimetric measurements. Comparing Fig. 5.6 (upper right) with Fig. 5.10, we recognise that the radiation contribution to upper divertor energy loads is significant over the explored α_t-range, moving from about 56 % at lower α_t up to almost 80% at higher values. Following Ref. [FEH+21], a certain contribution from parallel conductive transport is expected to be deposited at the upper divertor. The results from *Tile 1* illustrated in Fig. 5.9 suggest that the conductive contribution is significant at low α_t and decreases with increasing α_t. Fig. 5.12 represents the evolution of the energy loads on *Tile 1*, *Tile 2* and *Tile 3* for the upper outer divertor following the labelling in Fig. 5.11. It is normalised by the total energy obtained from thermocouple measurements covering the entire upper divertor. The distributions of the inner divertor tiles reveal no substantial variations throughout the whole database and therefore they are not shown. *Tile 1* is the tile which is expected to be dominantly exposed to the parallel conductive transport. For lower α_t, a larger fraction of the total energy reaching the entire upper divertor is deposited at *Tile 1* than for higher α_t. At the same time, an increase of the fraction of deposited energy can be observed for *Tile 2* and *Tile 3*. The slope of both tiles matches to the slope of *Tile 1*. Following the conclusions previously drawn for the lower divertor, the reduction at *Tile 1* may be accompanied by a reduction of the parallel transport causing a change in the energy distribution of the upper divertor. It cannot be excluded that due to the λ_q-broadening reported in Ref. [FEH+21], a part of the parallel conductive transport reaches a neighboring tile in the upper divertor and thus (additionally) influences the energy distribution. The data quality of the LP measurements is not sufficient to draw further conclusions. This trend needs to be confirmed in future studies.

It can only be speculated, how this localised radiation pattern is connected with α_t. Further investigations on that phenomena are needed, in particular in further devices, in order to understand the link between the CDN-magnetic field configuration, first wall geometry and PFC material.

Plot label	I_p [MA]	$\|B_{tor}\|$ [T]	P_{tot} [MW]	D_{tot} [10^{22}/s]	δ_u	κ
QCE with $\|B_{tor}\| \leq 1.9$ T	0.8 - 0.94	1.9 - 1.5	NBI: 7.5 - 5.0 ICRH: 4.0 - 0.0	1.0 - 4.0	0.31	1.65 - 1.81
QCE with max. $n_{e,sep}$	0.8	2.5	NBI: 12.5 - 7.5 ICRH: 4	5.0 - 5.5 (with additional pellet fuelling)	0.31	1.66
L-H-L high density discharge	0.8	2.5	NBI: 7.5 - 5 ECRH: 1.5	0.15 - 10.6	0.075	1.64
Low density H-mode + pellet	0.8	2.5	NBI: 4 - 10 ECRH: 3.6	1.0 - 0.5 (with additional pellet fuelling)	0.1-0.3	1.68 - 1.60
HDL discharge	0.8	2.5	NBI: 2.5 - 5 ECRH: 0 - 3.2	0.9 - 3.0	0.29	1.66

Table 5.2: Overview of the selected discharges with their properties to extend the first wall energy load scaling in Fig. 5.13.

5.2.3 Generalization of limiter energy load scaling

It is of great interest, whether the observed limiter trend can be extended to further discharges. A selection of discharges with different plasma characteristics have been added to the database. Each discharge provides several separatrix data points. For each discharge, the mean value of the separatrix values from the flattop phase are used to determine α_t. The table 5.2 summarizes the characteristics of the database extension. Fig. 5.13 visualizes the extension of the first wall energy load scaling. The scaling shows an almost linear correlation with α_t indicated by a high R^2. It suggests that the different properties, at least for the limiter, do not have a large effect on the scaling. The main challenge at AUG is the narrow spatial operational space of the edge TS in which shaping dependencies can be investigated. A scan of the position of the separatrix would be of great interest to confirm or refute the hypothesis of a filament decay length. To investigate these aspects, similar studies need to be performed on other machines with ITER-like-wall to identify further geometry/shaping dependencies. The extension to further machines would be also demanded to identify the actual upper limit of α_t. For low-δ plasma, the upper limit seems to be 1 [EMG+20], whereas for high-δ plasmas values larger than 1 can be achieved [FEH+23].

5.3 The evolution of upstream and downstream SOL profiles

The evolution of energy loads on the PFCs in AUG discussed in the previous section reports on promising trends. A significant fraction of the energy can be deposited on non-divertor components, namely the limiter and the upper divertor. It is now of interest to investigate, how the SOL profiles change within this database.

Firstly, the evolution of the divertor heat flux profiles by means of IR-thermography is

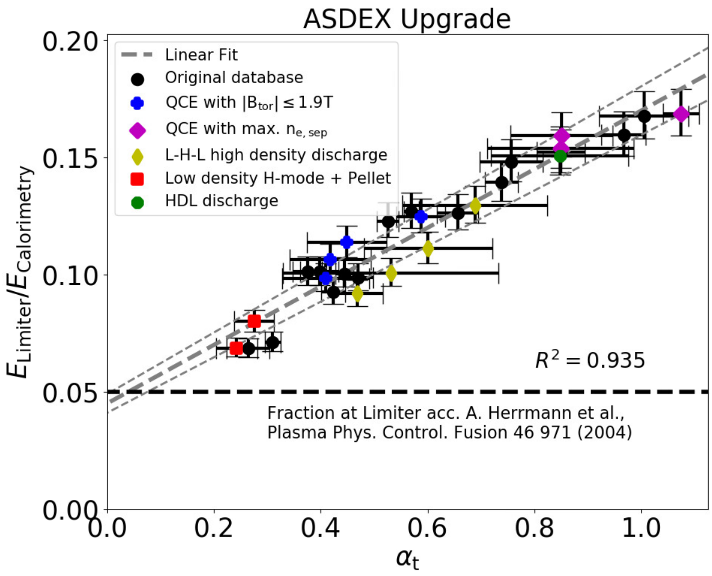

Figure 5.13: Evolution of the limiter energy loads considering further AUG discharges. The different color markers correspond to the entries in Table 5.2. The linear trend by using α_t is preserved, which is emphasized by the high value of R^2. The error-bars of the added discharges do not denote the uncertainty of the measurements, but the variation throughout the discharge.

discussed. Fig. 5.14 shows the divertor heat flux profiles for a set of AUG discharges conducted at $B_{tor} = -2.45$ T. In this analysis, f_x is set to 5.0. The legend denotes the different discharges with the respective quantities λ_q and S in descending ordering with respect to the normalised separatrix density in terms of n_{GW}. The two cases with lowest fuelling (#40240 and #39523) are ELM-filtered and illustrate only the Inter-ELM profiles. In the subsequent plots, the same color code is utilized for the B_{tor} = -2.45 T subset.
The background obtained from the Eich-fit is removed for this study in order to avoid discrepancies due to negative background values after Type-I ELM crashes caused by the implied energy conservation in THEODOR [HJG+95]. The background heat flux is for most discharges in the order of 0.5 MW/m^2. Since ELMs are not considered, only the profiles at higher fuelling represents the total power reaching the target. As reported in Ref. [FEH+21, FEH+23, SVT+22], a continuous increase of λ_q and S with increasing fuelling is witnessed. In case of #40240 and #40241, S does not perfectly match to this trend, as the T_e at the main target is slightly different as proven by the LP measurements shown in Fig. 5.15 [SFE+17]. Even though the low density cases represent only parts of the total power reaching the target, a reduction of the peak heat flux is still observed with increasing fuelling, which is beneficial for the ITER divertor peak heat flux limits. λ_q increases by a factor of 3, S by a factor of 2, whereas the peak heat flux is reduced from $\sim$ 8 MW/m^2 to below 3 MW/m^2 at maximum fuelling. Combining this observation with the trend illustrated in Fig. 5.9, one can conclude that an increase of α_t seems to

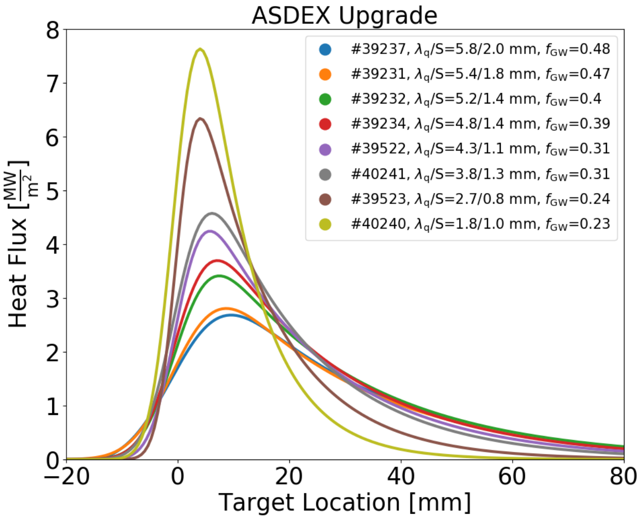

Figure 5.14: Heat flux profiles measured with the IR-thermography at the main target and remapped to the OMP. The strikeline position and the background heat flux (taken from the Eich-fit) are subtracted from all profiles. The legend illustrates the order of discharges by exploiting the achieved separatrix density, which is normalised by the Greenwald density n_{GW} ($\approx 10^{20}$ m^{-3}). In case of the two lowest flattop fuelling cases being in dominating Type-I ELM H-mode, only the Inter-ELM profiles are shown.

be associated with a reduction of the parallel conductive transport to the target together with a simultaneous reduction of the peak heat flux and a simultaneous increase of A_{Div}. The evolution of λ_q in QCE-phase follows the regression introduced in Ref. [FEH$^+$23], which suggests a correlation with $n_{\mathrm{e,sep}}$ or the separatrix pressure $p_{\mathrm{e,sep}}$. Recent studies from TCV [SVT$^+$22] suggest rather a reasonable trend λ_q with α_t. These diverse observations require an extension of the QCE scenario to further devices with ITER-like conditions, in order to provide further insights in the for ITER beneficial λ_q-broadening.
The corresponding LP-measurements are provided in Fig. 5.15. The LP profiles (ion saturation current density j_{sat} (upper), the electron density n_e (middle) and the electron temperature T_e (lower)) illustrate the evolution for B_{tor} = -2.45 T. The profiles are ELM-filtered and along the divertor coordinate each probe is median-averaged over a time interval of $\sim$ 1 s. The error-bars denote the standard deviation. The values from probes, which are close to the strikeline, might be negatively affected and have to be interpreted with care. The black vertical line denotes the separation between *Tile 1* (left side of the line) and *Tile 2* (right side of the line). For the first part of the discussion, the focus is on *Tile 1*. Starting with the lower panel, it can be observed that throughout the entire fuelling scan the target T_e remains mostly constant for each discharge configuration. At the same time, a gradual increase of the target n_e can be observed in the middle panel. The upper panel visualizing j_{sat} observe an increase of impinging particles, which is to be expected, when a density shoulder formation is aimed for.

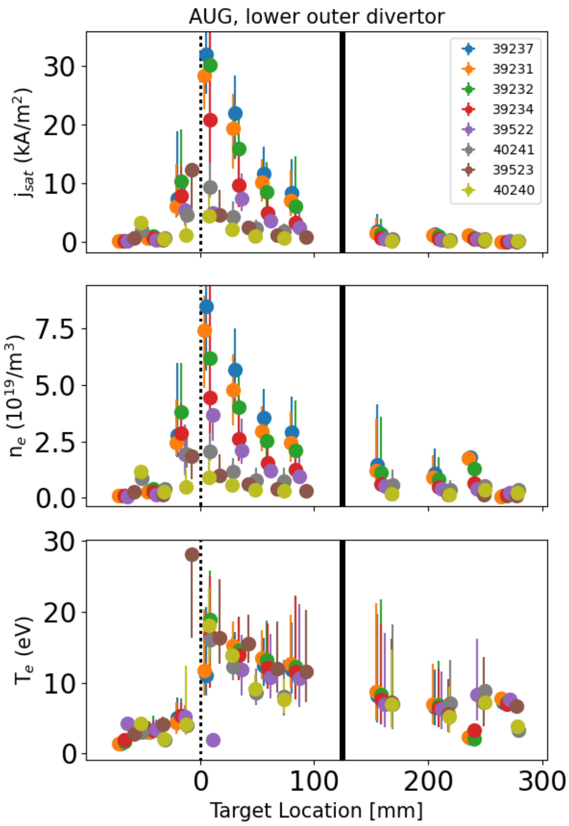

Figure 5.15: LP profiles for B_{tor} = -2.45 T are ELM-filtered and each probe along the divertor coordinate is median-averaged over a time interval of $\sim$ 1 s. The error-bars denote the standard deviation. The plots illustrate the ion saturation current density j_{sat} (upper), the electron density n_{e} (middle) and the electron temperature T_{e} (lower) at the main target (*Tile 1*, left side of black vertical line) and *Tile 2* (right side of black vertical line).

The observations concluded from IR and calorimetric measurements are in contradiction to the heat flux derived from LP measurements. As illustrated in Fig. 5.16, a continuous increase of $q_\perp$ with increasing fuelling can be observed. The general form [BLW+17, BSE+20] of the heat flux $q_\perp$ deduced from LP measurements can be written as:

$$q_\perp = q_{\text{kin,i}} + q_{\text{kin,e}} + q_{\text{ref}} + q_{\text{refl}}. \tag{5.1}$$

$q_\perp$ can be decomposed into four contributions: the ion/electron heat flux $q_{\text{kin,j}}$, the recombination heat flux q_{ref} and the reflected heat flux q_{refl}. The kinetic electron contribution $q_{\text{kin,e}}$ takes into account the impact of j_{net}, the electric current density to the target, following Ref. [BSE+20]. For most applications assuming $T_{\text{e}} = T_{\text{i}} = T$ and j_{net}=0, Equ. (5.1) can be simplified to:

$$q_\perp = (\gamma T + E_{\text{rec}})\Gamma, \tag{5.2}$$

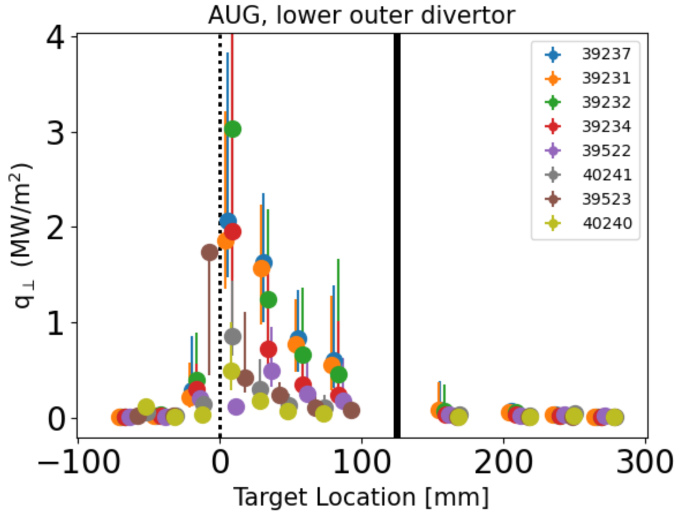

Figure 5.16: Evolution of $q_\perp$ from LP-measurements conducted at B_{tor} = -2.45 T. The same color code as in Fig. 5.2 is used.

where γ denotes the sheath heat transmission coefficient, E_{rec} the sum of the ionization energy and the Franck-Condon dissociation energy per recycled ion and Γ the ambipolar ion particle flux to the wall. γ can be expressed as:

$$\gamma = [4.85(1 - R_{\mathrm{E}}) + 2.15], \tag{5.3}$$

using the numerical values reported in Ref. [BLW+17] and R_{E} being the ion energy reflection coefficient. For most electron temperatures, R_{E} can be set to 0.5 leading to a $\gamma \approx 4.5$. The prefactor R_{N}, which describes the fraction of ions reflected from the target as neutrals and which may have a considerable impact on $q_\perp$ for high-recycling divertor conditions, depends like R_{E} strongly on T_{e} presuming $T_{\mathrm{e}} = T_{\mathrm{i}}$. This observation requires further dedicated investigations, which takes into account the proper values of T_{e} and T_{i} separately.

The thermocouple measurements at the outer divertor report on a reduction of the power reaching the divertor main target (*Tile 1*) presuming the energy loads on the baffle tile (*Tile 2*, right side of the black line Figs. 5.15 and 5.16) do not dramatically change. The proof of this presumption can barely be obtained, but checks with divertor LPs, IR and bolometry supporting the presumptions can be done.

Latest studies on AUG [FEH+23] have shown that also the link between λ_{t} and λ_{q} has changed for the QCE regime. Theoretically predicted [Sta00] and experimentally proven [SWE+15] at AUG the following relation holds in low-δ plasmas:

$$\lambda_{\mathrm{q}} = \frac{2}{7}\lambda_{\mathrm{t}}. \tag{5.4}$$

This ratio is considered in the *Two-Point Model*. The observations in the temperature profiles obtained with the AUG edge TS in Ref. [FEH+21] claims a change of the relation

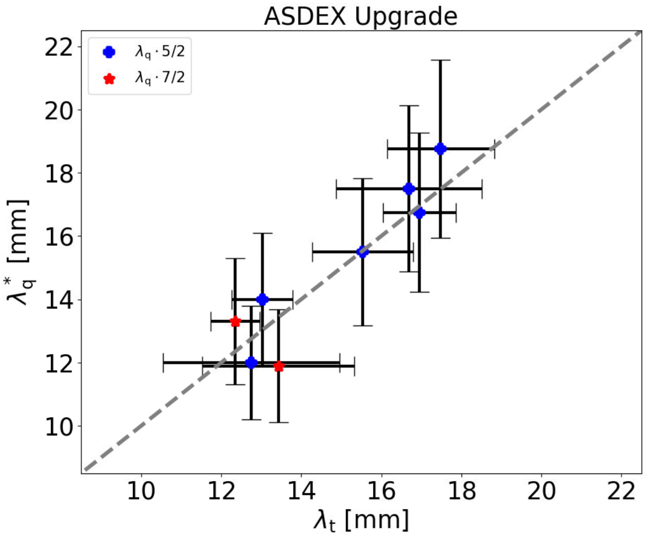

Figure 5.17: Comparison between λ_q^* and λ_t. The red markers denotes the values of λ_q which are multiplied by the ratio 7/2 and indicate discharges being Type-I ELMy H-modes. The blue markers denote the values of λ_q which are multiplied by the ratio 5/2. This value is in introduced in Ref. [FEH+23] and seems to be characteristic for the QCE regime taking into account kink in the temperature decay length between the confined region and the near SOL [FEH+21].

in Equ. (5.4) and is formalised in Ref. [FEH+23] to:

$$\lambda_q = \frac{2}{5}\lambda_t. \tag{5.5}$$

This novel ratio suggests to take into account the change in the electron temperature gradient between inside and outside the separatrix for the QCE regime. In Fig. 5.17, the relation between λ_q and λ_t is plotted. The classification of λ_q into QCE-Phase or Type-I ELMy H-mode is done manually. The red markers denote the values of λ_q taken from Type-I ELMy H-modes using the relation given in Equ. (5.4), whereas the blue ones denote the cases of QCE-discharges using the relation given in Equ. (5.5). It clearly illustrates that the connection between λ_q and λ_t has changed.
An explanation for the mechanism which regulates both, the inner and outer gradient, do not exist yet [FESC20, SEF+20]. Ref. [FEH+21] suggests that a second drive acts near the separatrix without affecting the pedestal top. This hypothesis picks up ideas from Ref. [Sco97] on which the SepOS-theory is based on.

Cross-checks for the validation of the energy load evolution on Tile 2

A comprehensive analysis using Langmuir Probes, IR and Bolometry has been performed to confirm the hypothesis on *Tile 2* energy deposition.
The LP measurements summarized in Fig. 5.15 indicate on the right-hand side of the

black vertical line only a small increase of j_{sat} (upper panel) and n_e (middle panel). j_{sat} is a simple proxy for impinging particles and remains on a low level throughout the entire database. This is also confirmed by the heat flux profiles derived from probes in Fig. 5.16 for B_{tor} = -2.45 T. By exploiting the Eich-fits obtained from IR-measurements, one

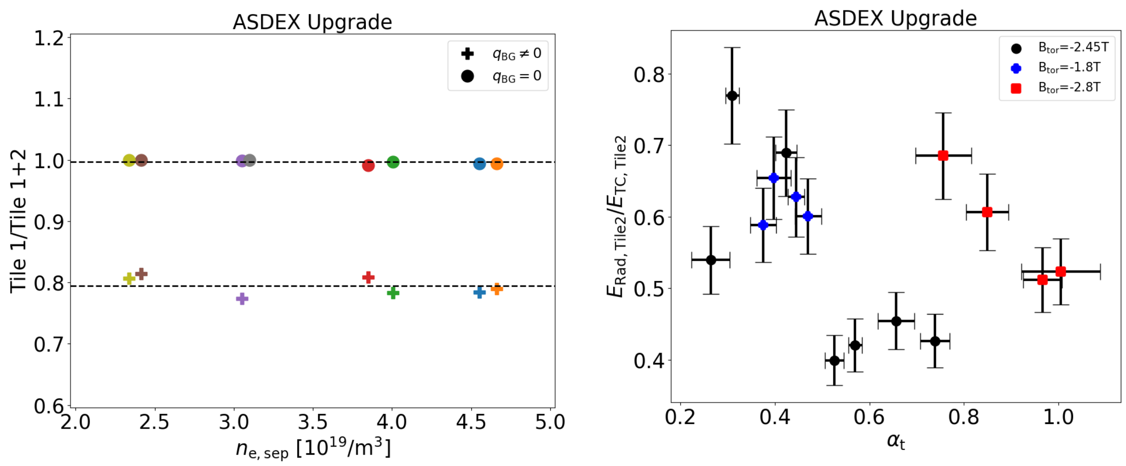

Figure 5.18: Left: Evolution of the heat flux deposition at *Tile 1* normalised against the sum of both tiles is plotted against $n_{e,sep}$. For both cases, with and without q_{BG}, the ratio reveals no variation indicating that no conductive transport is deposited on *Tile 2* through the λ_q-broadening. Right: Normalised radiative energy loads on *Tile 2* based on the framework exploiting CHERAB and the GPT model. No clear trend is observable.

can check, whether a fraction of the parallel SOL transport reaches *Tile 2* through the λ_q-broadening. The available Eich-fits are extrapolated to the full poloidal length of *Tile 1* and *Tile 2*. The integrated values for *Tile 2* are normalised against the sum of both tiles. The ratio is visualized in Fig. 5.18 (left). For both cases, with and without q_{BG}, the ratio reveals no variation suggesting that no conductive transport reaches *Tile 2* due to the λ_q-broadening.

Finally, the evolution of the deposited radiative energy on *Tile 2* can be checked. For this purpose, the results from the workflow using CHERAB and the GPT model are normalized by the results from the thermocouples for *Tile 2*. This ratio is shown in Fig. 5.18 (right). No clear trend is observable. The absolute values from thermocouple results reveal no significant variations.

So far, all checks support the picture that the reduction in the energy deposition is not caused by the λ_q-broadening or the density shoulder reaching *Tile 2*, but indeed by a reduction of the parallel transport down to the target due to an additional energy loss channel, which is localised upstream. It suggests that α_t describes well those turbulent structures. It further indicates that the reduction of energy loads measured with the thermocouples is not directly related to the λ_q-broadening and may be decoupled.

5.3.1 Qualification of the density shoulder amplitude in QCE H-modes

As reported in Ref. [SWE+15], achieving high $n_{e,sep}$ leads to a broadening of the e-folding temperature and density decay lengths λ_t and λ_n and to a formation of a density shoulder. The formation of a density shoulder is generally associated with an enhancement of filamentary activities in the far-SOL [FEH+21, VWD+21, SVT+22, WLC+18, SSC+22] and a common characteristics of the QCE-regime [FEH+21]. Fig. 5.19 illustrates the evolution of the density in the near- and far-SOL exploiting LIB-measurements for database discharges conducted at $B_{tor} = -2.45$ T for which most LIB-measurements are available. The density in the SOL is normalized by $n_{e,sep}$. The two vertical dashed lines denote the position of the separatrix ($\rho_{pol} = 1.0$) and the limiter tile surface ($\rho_{pol} = 1.1$) at the midplane. Throughout the discharge subset, a substantial variation of the SOL density can be observed. The change of density in the near- and far-SOL is solely caused by changing the flattop fuelling level. At the highest normalized SOL density, a saturation of the density amplitude appears.

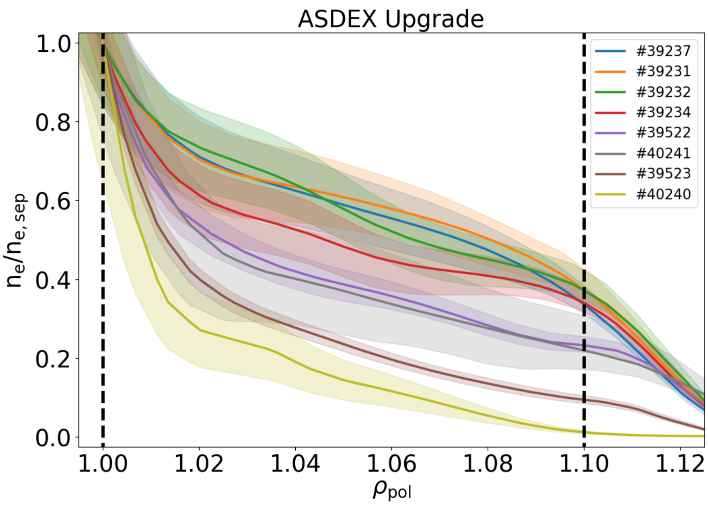

Figure 5.19: Evolution of the density shoulder for discharges conducted at B_{tor} = -2.45 T and measured by the LIB diagnostic.

To qualify the evolution of the density amplitude in the far-SOL, a qualifier is exploited, which has been introduced in Ref. [FTH+20]. This procedure characterize the shoulder across the near- and far- SOL range by the subsequent definition:

$$\tilde{n}_e = \frac{\int_{1.0}^{1.1} n_e \mathrm{d}\rho_{pol}}{n_{e,sep}\Delta\rho_{pol}} = \frac{\langle n_e \rangle_{SOL}}{n_{e,sep}}, \tag{5.6}$$

where n_e denotes the electron density in the SOL, ρ_{pol} denotes the normalized poloidal flux coordinate and $\Delta\rho_{pol}$ the integration range with the magnetic coordinate. LIB-measurements, which cover n_e in the near- and far-SOL, are available for most of the database discharges. The integration covers the range from 1.0 to 1.1 of ρ_{pol}. The values obtained with the qualifier defined in Equ. (5.6) are visualized in Fig. 5.20 as solid markers. It can be seen that the with increasing α_t, the density shoulder qualifier increases

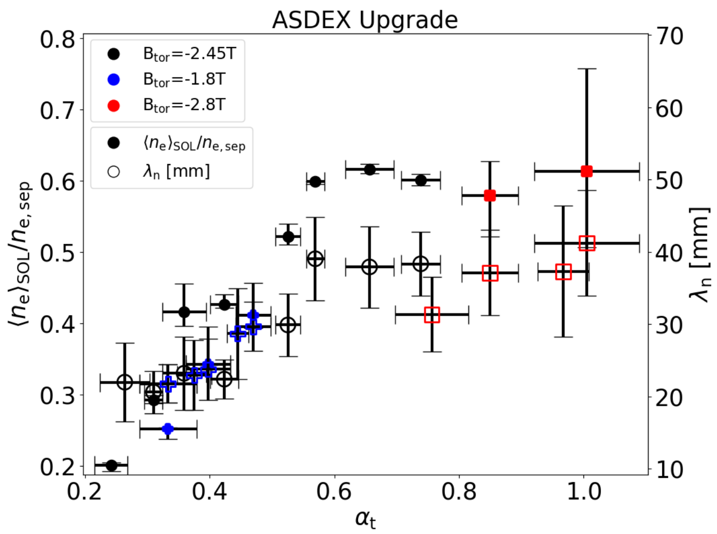

Figure 5.20: The density shoulder amplitude qualifier (solid markers) is plotted against α_t. Exceeding $\alpha_t \approx 0.55$, a saturation in the qualifier can be observed. The markers with no face-color visualize the evolution of e-folding density decay length λ_n obtained with the edge TS with respect to α_t.

continuously until α_t exceeds ~ 0.55. Exceeding $\alpha_t = 0.55$ leads to a saturation of the density shoulder amplitude. The saturation threshold in α_t is similar to the limit introduced in Ref. [FEH$^+$23] classifying a discharge into a Type-I ELMy H-mode and into a QCE H-mode. This observation suggests that a fully formed density shoulder might be connected with achieving a QCE H-mode. It is in agreement with the observations from TCV for QCE H-modes observing also a saturation in the density shoulder amplitude above a critical value in α_t [SVT$^+$22].
Additionally, the e-folding decay length λ_n obtained with the edge TS is plotted (markers with no face color) illustrating the behaviour of the near-SOL while forming the density shoulder. A similar trend as for the density shoulder qualifier is observed suggesting that the formation of the density shoulder is not only correlated with the properties in the far-SOL, but also still connected with the properties of the SOL near suspecting a dependence on separatrix quantities. It is also important to note from Fig. 5.20 that despite the increase of far SOL density, the general shape of the density SOL profile is not substantially changed with a break between near and far SOL approximately around $\rho_p \approx 1.015$. This is not actually an universal features since different profile evolution is observed as density is increasing on TCV [SVT$^+$22] or JET [WLC$^+$18] and clearly further multi-machine investigation is needed to address this question, but this topic is clearly beyond the present work.

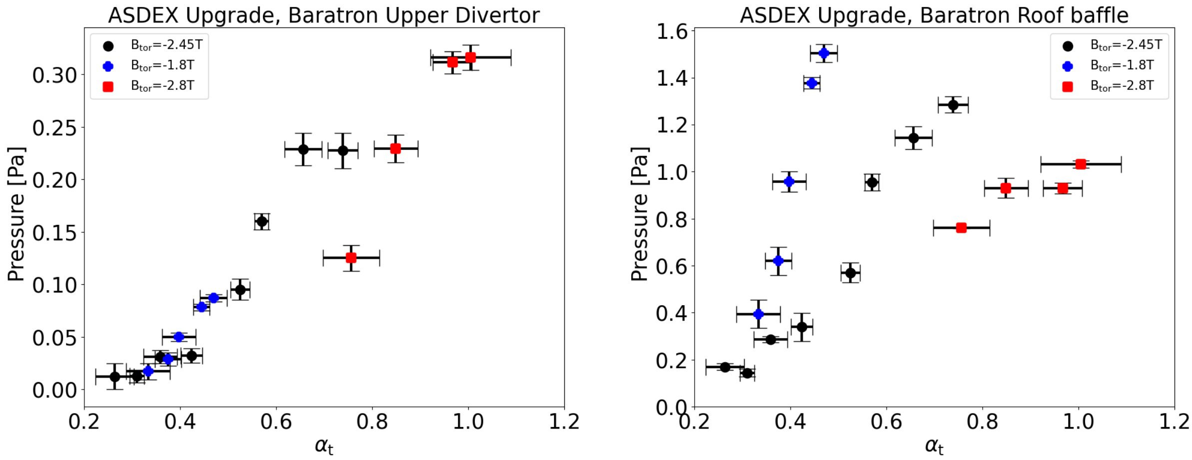

Figure 5.21: Left: The neutral pressure measured above the midplane is plotted against α_t. A reasonable agreement is observable indicating a connection between the turbulence activity at separatrix and the neutral pressure in the SOL. Right: The neutral pressure measured at the roof baffle is plotted against α_t. A correlation with a different dependence on q_{cyl}/B_{tor} is observed indicating a missing connection between separatrix and divertor conditions.

The formation of a density shoulder seems to be connected with an increase of the neutral pressure in the SOL. Previous studies at TCV [SVT+22, FTH+20] and AUG [VCT+20] and at JET [WLC+18, SSC+22] have suspected the requirement of increased neutral pressure in the divertor and/or high recycling states to achieve the formation of a density shoulder in the far-SOL. On the other side, investigations in L-modes at TCV [TBB+22] have suggested a major role by the midplane neutral pressure.

Fig. 5.21 illustrate the evolution of the neutral pressure close to the upper divertor (left) and in the lower divertor (right) being measured below the roof baffle. Both measurements are plotted against α_t. The left plot indicate a clear correlation between α_t and the upper divertor neutral pressure, whereas the divertor neutral pressure increases with α_t, but demands a different dependence on q_{cyl}/B_{tor} indicating a missing connection between separatrix and divertor conditions. The upper divertor baratron provides high neutral pressure values, which might be affected by its close position to the upper divertor and the localised radiation pattern in the upper divertor as discussed before.

The trends in the baratron measurements are cross-checked with manometer measurements. F03 and F13 operate at similar poloidal positions as their corresponding baratron pendants, whereas F14 is a manometer measuring the neutral flux density in the main chamber. The measurements of all three manometers are illustrated in Fig. 5.22. The divertor manometer (F03) reveals a similar trend as the corresponding divertor baratron in demanding a different dependence on q_{cyl}/B_{tor} when scaled against α_t. Both manometers operating in the main chamber and close to the upper divertor show a similar trend as the main chamber baratron.

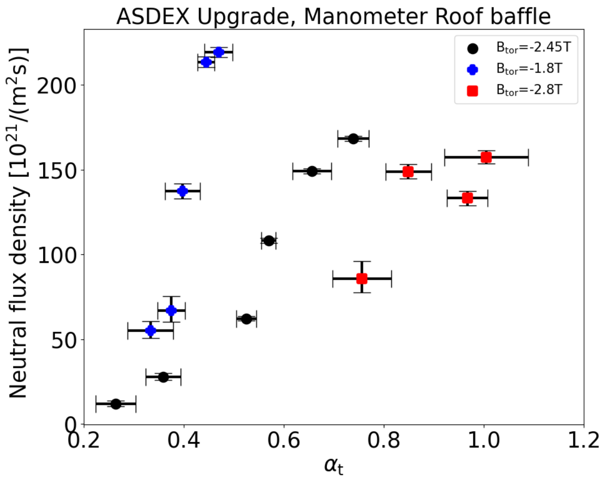

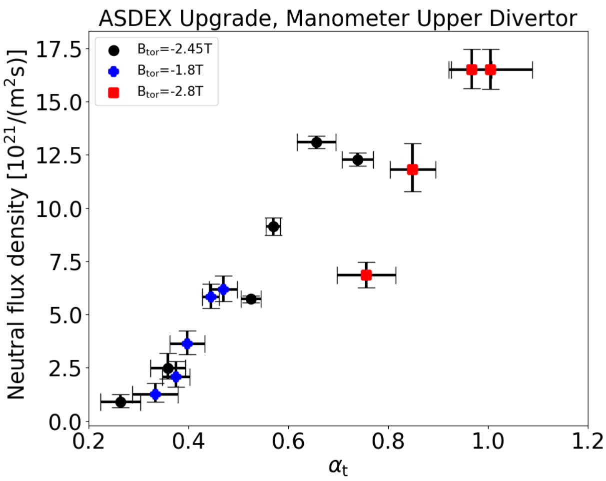

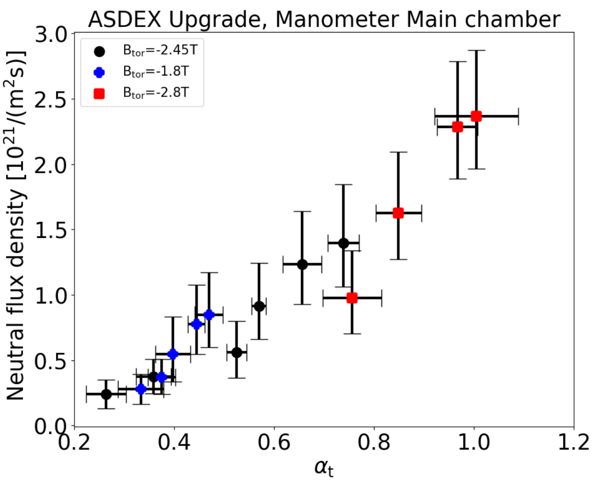

Figure 5.22: The neutral flux densities measured in the roof baffle (upper), close to the upper divertor (middle) and in the main chamber (lower) are plotted against α_t. The divertor manometer F03 reveals a similar trend as the divertor baratron requesting a different dependence on q_{cyl}/B_{tor}.

5.4 Evolution of the breaking point in the SOL density profile

The availability of LIB-profiles allows to investigate the evolution of the breaking point in the SOL density profile and and its connections, which might be relevant for a safe operation of ITER [BPS+21]. For this purpose, three discharges (#39523, #39522 and #39234) of the database are chosen to assess this aspect. These three discharges are conducted at B_{tor}= -2.45 T and cover the flattop fuelling levels at 0.2, 0.6 and 1.0e22/s. Additionally,

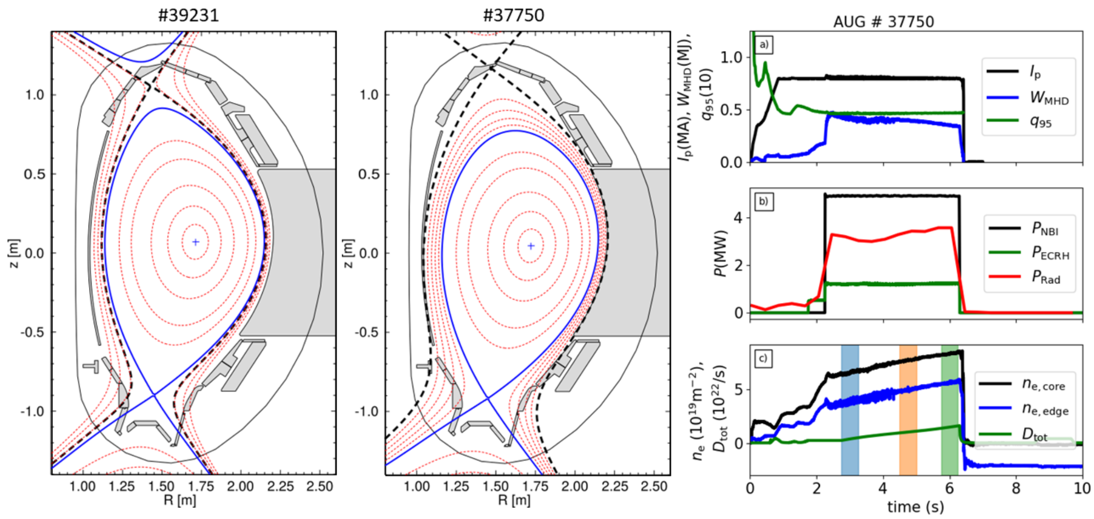

Figure 5.23: Left and middle: Poloidal cross-section of AUG discharges #39231 and #37750. The black dashed line indicates the position of the secondary separatrix. Right: Experimental time traces of #37750. The shaded areas in the lower panel indicate the time intervals evaluated for this analysis.

AUG discharge #37750, which features a fuelling ramp thus reaching comparable α_{t}-values as the three database discharges, is chosen. Furthermore, operating at lower δ_{u} and lower κ, discharge #37750 exhibit a different location of the secondary separatrix with respect to the rest of the database. For the database discharges, the secondary separatrix is placed close to the separatrix, whereas for #37750 the secondary separatrix is located outside the main chamber behind the restricting limiter (illustrated in Fig. 5.23). The latter configuration is known as *edge optimized configuration* (EOC). Further details on discharge #37550 are extensively discussed in Ref. [VWD+21].
To determine the range of the near-SOL, the power balance approach cannot be applied as for the edge TS. As reported in Ref. [SWG+12], the range between the extreme values of $\nabla^2 n_{\mathrm{e}}$-profile determine the near-SOL range and is exploited for this analysis. The outer boundary of the near-SOL range is also denoted as break point R_{break}. The far-SOL range is therefore defined between the outer boundary of the near-SOL range and the first wall PFC. The latter position is fixed at $R_{\mathrm{lim}} = 2.177$ m. To fit both ranges, near- and far-SOL,

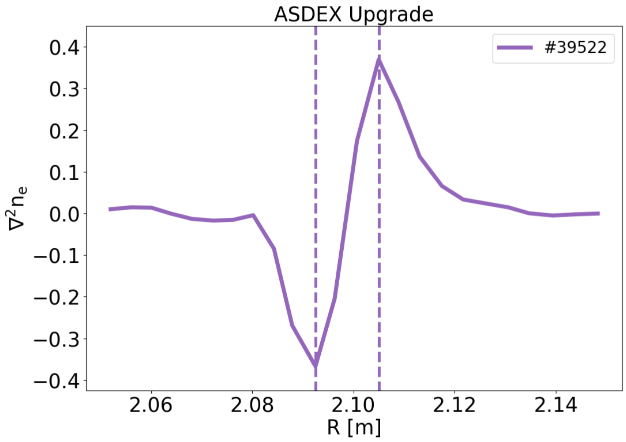

Figure 5.24: Illustration of the second derivative of the SOL density profile. The two vertical dashed lines denote the near-SOL range between the extreme values identified in the curvature profile.

an exponential fit function of the following form is used:

$$f(x) = a \cdot e^{-b\cdot(x-c)} + d \tag{5.7}$$

Fig. 5.25 illustrates the SOL density profiles with their respective fit functions for the near- and far-SOL for both secondary separatrix configurations. For both configurations,

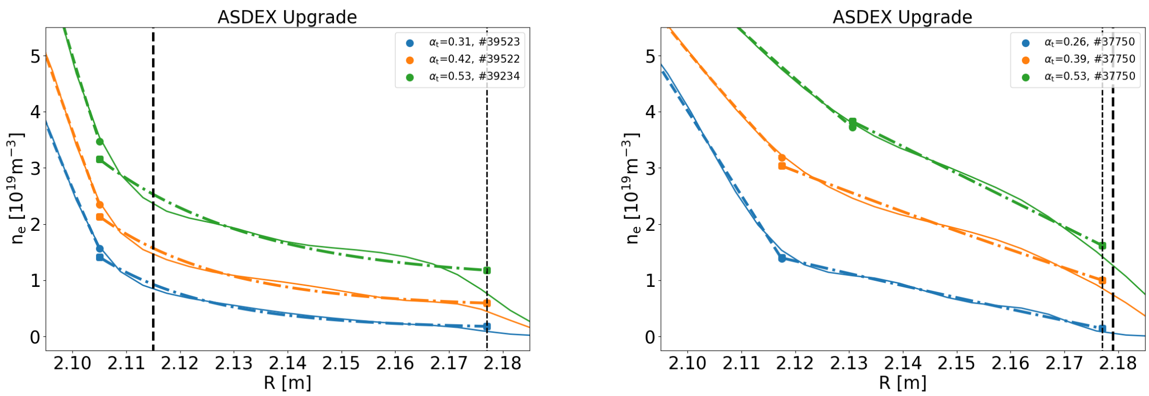

Figure 5.25: Illustration of the SOL density profiles for AUG discharges #39523, #39522 and #39524 (left) and for #37750 (right) with their respective fitting range: circle markers denote the near-SOL ranges, whereas the square markers denote the far-SOL range. The thick dashed line denotes the position of the secondary separatrix, whereas the thin dashed line denotes R_{lim}.

a simple exponential decay function seems sufficient to describe both SOL ranges.
Of rather importance is the evolution of the break point position. The break point, which

is defined as the maximum-peak in the $\nabla^2 n_\mathrm{e}$-profile is located between 1.3 and 1.7 cm in front of the separatrix in Fig. 5.25 (left), whereas it is located at 3.0 cm in front of the separatrix in Fig. 5.25 (right). At highest α_t, the breaking point is located at 4.2 cm. It seems that for both configurations the secondary separatrices, which are between 2.2 and 2.6 cm in front of the primary separatrix for the setup in Fig. 5.25 (left) and about 9.0 cm in front of primary separatrix beyond the restricting limiter for the setup in Fig. 5.25 (right), do not affect the position of the break point.

5.5 Estimation of the parallel conductive heat flux reaching the first wall PFCs

In order to determine the heat flux decay profile, the heat flux at the separatrix must firstly be calculated. The common expression is given by:

$$q_{\|,\mathrm{LCFS}} = \frac{F P_\mathrm{sep} B_\mathrm{tor,OMP}}{2\pi R_\mathrm{OMP} \lambda_\mathrm{q,near} B_\mathrm{pol,OMP}}. \tag{5.8}$$

$\lambda_\mathrm{q,near}$ is taken from the IR-measurements shown in Fig. 5.14. For #37750, no IR-evaluation is available and therefore is not considered in this analysis. F denotes ratio of the power deposition between inner and outer divertor. It is mostly presumed to 0.5. Exploiting thermocouple measurements, one can estimate this ratio for the set of discharges, which varies between 0.63 and 0.72. P_sep denotes the power crossing the separatrix ($P_\mathrm{injected} - P_\mathrm{radiation,core}$). This quantity varies between 5.0 and 5.5 MW. $B_\mathrm{tor,OMP}$, $B_\mathrm{pol,OMP}$ and R_OMP denote the toroidal, poloidal magnetic field strength and the major radius at the outer midplane.
The heat flux decay profile for the entire SOL can be described by two functions. The near-SOL profile is described by:

$$q_{\|,\mathrm{near}}(\Delta r) = q_{\|,\mathrm{LCFS}} \exp\left(-\frac{\Delta r}{\lambda_\mathrm{q,near}}\right), \text{ for } \Delta r < R_\mathrm{break}, \tag{5.9}$$

whereas the far-SOL decay profile can be expressed as:

$$q_{\|,\mathrm{far}}(\Delta r) = q_{\|,\mathrm{LCFS}} \exp\left(-\frac{\Delta r}{\lambda_\mathrm{q,far}} + \frac{R_\mathrm{break}}{\lambda_\mathrm{q,far}} - \frac{R_\mathrm{break}}{\lambda_\mathrm{q,near}}\right), \quad \text{for } \Delta r > R_\mathrm{break}. \tag{5.10}$$

The values for R_break are taken from the analysis discussed in Section 5.4. Since $\lambda_\mathrm{q,far}$-profiles cannot be obtained from the IR-measurements, the calorimetric heat flux values, which are introduced in Section 5.6.2, are exploited to constraint the predicted $q_{\|,\mathrm{far}}$ at the limiter and to estimate $\lambda_\mathrm{q,far}$. This ansatz yields to values between 11.5 and 16.1 mm for $\lambda_\mathrm{q,far}$. Since the calorimetric values cannot discriminate the different sources of heat

fluxes to the first wall, the estimated decay lengths might overestimate the experimental decay lengths. The results of both equations (5.9) and (5.10) are illustrated in Fig. 5.26. The two vertical dashed lines denote the radial position of the secondary separatrix (thick line) and the limiter (thin line). It can clearly be seen that R_{break} depends neither on the secondary separatrix position nor the far-SOL filament radial velocity $v_{\mathrm{r,fil}}$ illustrated in Fig. 5.28, which is in contrast to previous assumptions summarized in [PCE+11].
In the context of the present assumption, it is therefore assumed that the separatrix operating space determines the level of heat load on the first wall. Operation at higher normalized separatrix collision or α_t leads to an increase in the ratio $q_{\|,\mathrm{far}}/q_{\|,\mathrm{near}}$, which must be taken into account for the correct dimensioning of the thermal capabilities of the first wall.

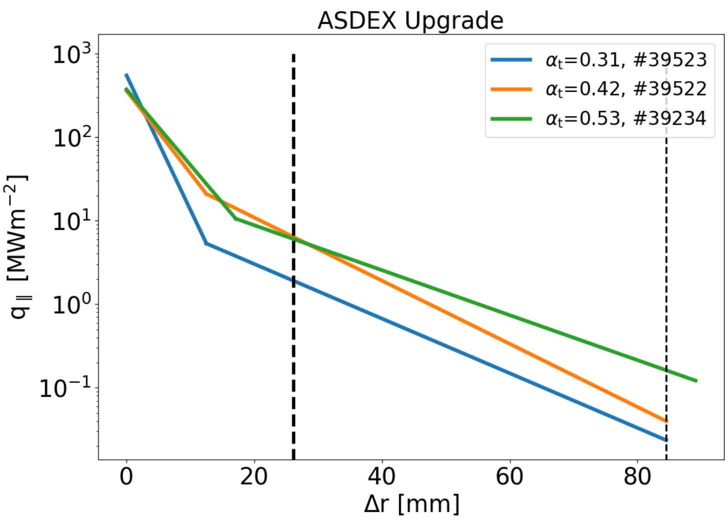

Figure 5.26: Illustration of the parallel conductive heat flux decay profile in the SOL. The two vertical dashed lines denote the radial position of the secondary separatrix (thick line) and the limiter (thin line).

5.6 The radial filamentary heat transport in high-δ discharges

5.6.1 Determination of the filamentary heat flux using probe measurements

Dedicated limiter probe measurements were executed in most discharges to derive the quantities describing the filament characteristics. The derived quantities from both probe-heads can also be used to determine the radial filamentary heat flux associated to filaments. The expression describing this radial convective transport, has been introduced in Ref.

[CAB+18] and applied on AUG high-density L-mode discharges:

$$q_{\mathrm{r,fil}}^{\mathrm{total}} = q_{\mathrm{r,fil}}^{\mathrm{electron}} + q_{\mathrm{r,fil}}^{\mathrm{ion}} = \frac{5}{2}\Gamma_{\mathrm{r,fil}} T_{\mathrm{e,fil}} + \frac{1}{2}\Gamma_{\mathrm{r,fil}}\left[5T_{\mathrm{i,fil}} + m_{\mathrm{i}}(c_{\mathrm{s}}M_{\parallel})^2\right]. \tag{5.11}$$

The radial filamentary heat transport consists of an electron $q_{\mathrm{r,fil}}^{\mathrm{electron}}$ and an ion contribution $q_{\mathrm{r,fil}}^{\mathrm{ion}}$. Contributions parallel and perpendicular to the magnetic fields contribute to the radial heat transport. The perpendicular contribution is given by $\frac{5}{2}\Gamma_{\mathrm{r,fil}} T_{\mathrm{j,fil}}$. The parallel contribution is deduced from the inertia term in the energy conservation and only its ion contribution is considered due to $m_{\mathrm{e}} << m_{\mathrm{i}}$. It is approximated by $\frac{1}{2}\Gamma_{\mathrm{r,fil}} m_{\mathrm{i}}(c_{\mathrm{s}}M_{\parallel})^2$.

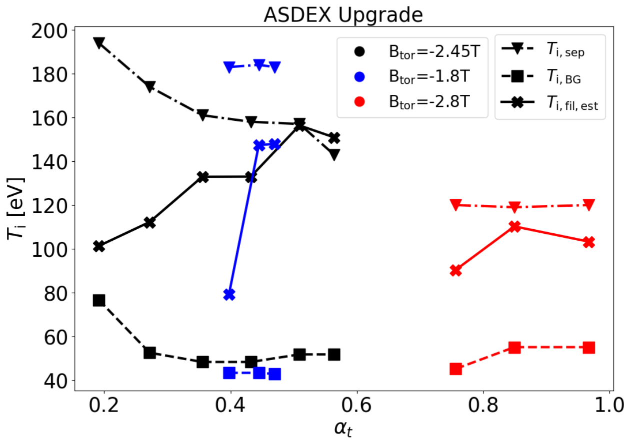

Figure 5.27: Illustration of the range of $T_{\mathrm{i,fil,est}}$ within its lower and upper boundary given by $T_{\mathrm{i,sep}}$ from CXRS and $T_{\mathrm{i,BG}}$ from RFA2.

As discussed in Section 2.2, the RFA2 sweeping frequency at 5 kHz was not sufficient to estimate $T_{\mathrm{i,fil}}$. The obtained values are averaged over filaments and represent the background ion temperature $T_{\mathrm{i,RFA2}} = T_{\mathrm{i,BG}}$. In Ref. [CAB+18], it is has been reported that in high-density L-mode discharges $T_{\mathrm{i,fil}}$ is in the range of $T_{\mathrm{i,BG}}$. Given the lack of similar information concerning H-mode, we are assuming that the ion temperature relative fluctuation scales similarly to the electron one, thus assuming:

$$\frac{T_{\mathrm{i,fil}}}{T_{\mathrm{i,BG}}} = \frac{T_{\mathrm{e,fil}}}{T_{\mathrm{e,BG}}}, \tag{5.12}$$

The values of the estimated filament ion temperature $T_{\mathrm{i,fil,est}}$ are illustrated in Fig. 5.27. The estimated values are within the boundaries given by the IDI-profiles, which are based on CXRS-measurements, at the separatrix and given by the RFA2. The magnitude at lowest α_{t} representing Inter-ELM $T_{\mathrm{i,fil}}$ are in agreement with previous studies conducted at AUG exploiting the RFA2 [KACC+12, KGK+12, KMN+13]. For higher α_{t}, $T_{\mathrm{i,fil,est}}$ tends to $T_{\mathrm{i,sep}}$. However, no references for QCE-$T_{\mathrm{i,fil}}$ are known to compare them with $T_{\mathrm{i,fil,est}}$.

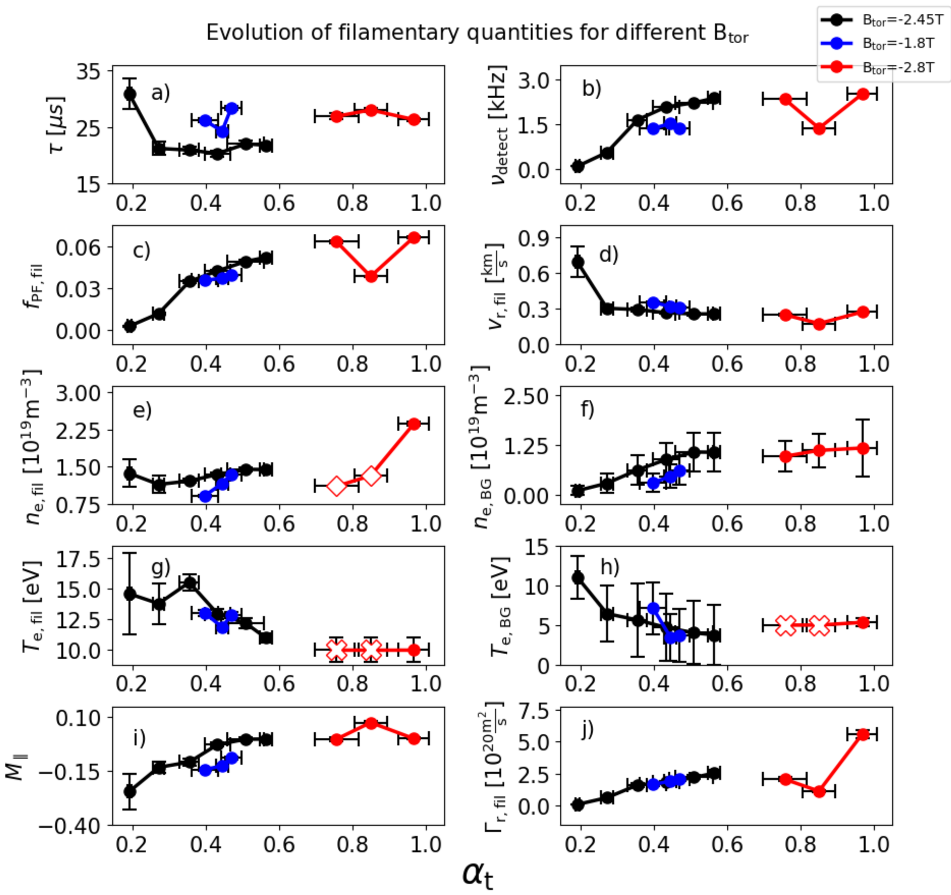

Figure 5.28: Overview of the filamentary quantities obtained with the BPP plotted against α_t: a) the filament correlation time, b) the filament detection frequency, c) filamentary packing fraction, d) the filamentary radial velocity, e) the filamentary electron density, f) the background electron density, g) the filamentary electron temperature, h) the background electron temperature, i) the filamentary parallel Mach number, j) the filamentary particle flux.

Fig. 5.28 provides an overview of the quantities derived from the BPP measurements. This analysis excludes the evaluation of ELMs, as the acquired profiles were not sufficient to deduce robust quantities from ELM-averaged I-V curves. All quantities are plotted against α_t. Furthermore, to estimate $n_{e,BG}$ and $n_{e,fil}$ following Equ. (2.13), the T_i-values of filaments and background plasma introduced before are utilized.

The filament packing fraction $f_{PF,fil}$, which has been introduced in Equ. (2.16), is illustrated in panel c) and depends on the quantities shown in panel a) and b). The continuous increase of $f_{PF,fil}$ is triggered only by the growth of ν_{detect}, which represents the number of detected filaments within a certain time interval, whereas at the same time the correlation time τ reveals no substantial variations when QCE-filaments start to dominate the SOL transport. Since τ is a proxy for the filament size (at least for the radial dimension assuming "frozen

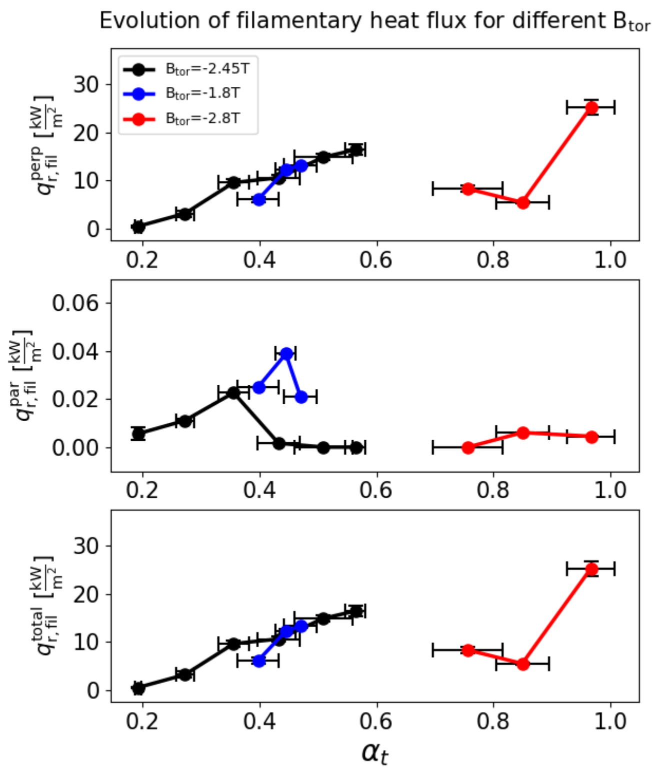

Figure 5.29: Contributions to radial filamentary heat flux: Upper: the filamentary perpendicular heat flux, middle: the filamentary parallel heat flux, lower: the filamentary total heat flux.

turbulence hypothesis"), it additionally suggests that Inter-ELM filaments are larger than QCE-filaments. Due to the lack of poloidal velocity measurements, further conclusions cannot be drawn.

Interestingly, the radial filament velocity $v_{\mathrm{r,fil}}$ close to the limiter shown in panel d) is lower for QCE filaments than for Inter-ELM filaments and also reveals only slight variations when the QCE-phase has been achieved. This seems to be in contradiction to previous studies conducted in AUG using the THB-diagnostic [Gri18] and at TCV using a reciprocating probe [SVT$^+$22]. With respect to the density shoulder observations discussed in Section 5.3.1, it can also be concluded that the mechanism behind the density shoulder formation seems not to be linked to the far-SOL filament radial velocity $v_{\mathrm{r,fil}}$, which is in contrast to previous assumptions [PCE$^+$11].

Together with the observations in panel e), g) and in Fig. 5.27 visualizing the filamentary electron density, electron temperature and ion temperature, one can conclude that the enhancement of convective transport is carried by more frequently generated and denser filaments and not by an increase of the ion or electron temperature. The two diamond red markers for $n_{\mathrm{e,fil}}$ denote results where the I_{sat} fluctuation went above the analog-to-digital converter resolution. As a consequence, $n_{\mathrm{e,fil}}$ are for those two cases likely underestimated.

The two red crosses for $T_{\text{e,fil}}$ and T_{BG} denotes cases, where ϕ_{f} was somehow corrupted and the corresponding temperature values are taken from the remaining discharge conducted at B_{tor} = -2.8 T. The evolution of $M_{\parallel}$ is shown in panel i). Its behaviour converging to 0 with increasing α_{t} seems to be in agreement with recent numerical GBS simulations at TCV [MRV+21] realised for high-density L-mode discharges. The sign of $M_{\parallel}$ is negative meaning the parallel contribution reaches the outer divertor.
Following the definition of $\Gamma_{\text{r,fil}}$ from Equ. (2.16) and illustrated in panel j), it can be concluded that the particle flux carries mostly the enhancement of filamentary transport in high-δ discharges.
Fig. 5.29 illustrate the evolution of the perpendicular, parallel and total heat flux associated with filaments. The trend of the perpendicular filamentary heat flux $q_{\text{r,fil}}^{\text{perp}}$ shown in upper

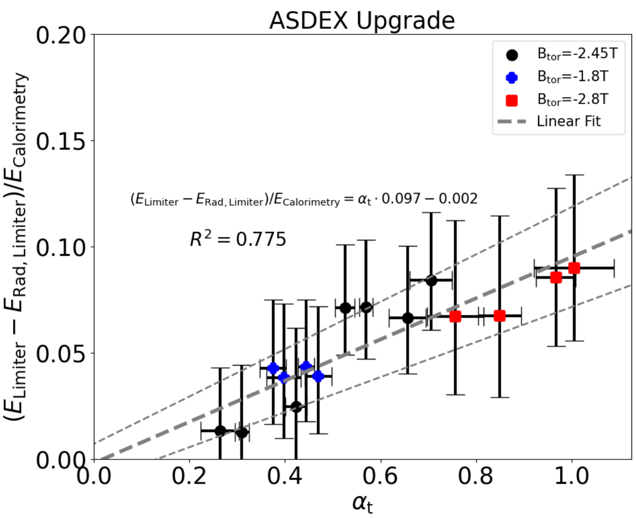

Figure 5.30: The energy loads of the limiter without the radiative energy loads are plotted against α_{t}.

plot is dominated by $\Gamma_{\text{r,fil}}$. The middle plot visualizes the parallel contribution. Over the entire range, this contribution is negligible. The lower plot illustrates $q_{\text{r,fil}}^{\text{total}}$ as defined in Equ. (5.11).

5.6.2 Comparison of $q_{\text{r,fil}}^{\text{total}}$ with $q_{\text{Calorimetry, Limiter}}$

In the previous section, the convective heat flux associated with filaments has been determined using probe measurements, which were performed close to the limiter surface. These results can now be compared with the calorimetric results to estimate the magnitude of the filamentary contribution to the total heat flux reaching the limiter caused by particle transport. The averaged heat flux reaching the limiter, $q_{\text{Calorimetry, Limiter}}$, can be estimated by:

$$q_{\text{Calorimetry, Limiter}} = \frac{E_{\text{Calorimetry, Limiter}} - E_{\text{Rad, Limiter}}}{t_{\text{Plasma}} \cdot A_{\text{Limiter}}}. \tag{5.13}$$

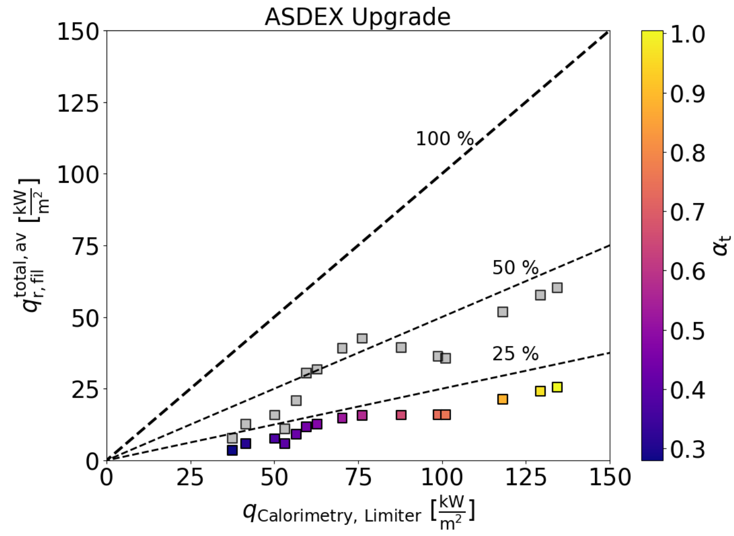

Figure 5.31: Comparison between the averaged heat flux reaching the limiter estimated by means of the AUG cooling water calorimetry and the filamentary heat flux based on probe measurements. The three dashed lines represent he case of 25 %-, 50 %-, 100%-contribution of $q_{\mathrm{r,conv}}$ with respect to $q_{\mathrm{Calorimetry,\,Limiter}}$. The colored markers indicate the filament heat flux for which $T_{\mathrm{i,BG}}$ and $T_{\mathrm{i,fil}}$ from the RFA2 has been utilized in Equ. (2.13), whereas the grey shaded markers illustrate the case, where $T_{\mathrm{e}} = T_{\mathrm{i}}$ has been assumed for Equ. 2.13.

$E_{\mathrm{Calorimetry,\,Limiter}}$ denotes the calorimetrically acquired energy of the 8 cooling units defining the Limiter, $E_{\mathrm{Rad,\,Limiter}}$ the radiative energy reaching the limiter, t_{Plasma} the duration of the flattop phase of the respective discharge, which is about ≈ 6 s, and A_{Limiter} the surface area of the AUG limiter, which consists of the 4 ICRH antennas and the 4 auxiliary limiters, is $\approx 4.6\ \mathrm{m}^2$. The calorimetry cannot differentiate the sources of energy loads on the PFCs. Therefore, the workflow based on CHERAB and the GPT model introduced in Ref. [REV+23] is exploited in order to determine the incident radiation energy on the limiter. The term $(E_{\mathrm{Calorimetry,\,Limiter}} - E_{\mathrm{Rad,\,Limiter}})$ summarizes the energy loads of the limiter, which are caused by all particle transport present in the SOL. The evolution of this quantity is shown in Fig. 5.30 Even after the subtraction of $E_{\mathrm{Rad,\,Limiter}}$, a reasonable trend is preserved covering the conclusion drawn in Fig. 5.5 (upper right). Remarkably, the regression matches almost perfectly with the origin supporting the picture that α_{t} may properly describe the turbulent activities close to the separatrix.
Additionally, an averaged $q_{\mathrm{r,fil}}^{\mathrm{total,av}}$ has to be determined. Since filaments are of ballooning origin, they occur only around LFS midplane, where the curvature of the plasma is unfavourable and t filamentary activity corresponds to the position, it can be assumed that the activities increase closer to the outer midplane at $z = 0.0$ m, where it reaches its maximum. $q_{\mathrm{r,fil}}^{\mathrm{total}}$ obtained at the MEM position is at the outer midplane increased by the factor $\cos(\pi/6)$ following the argumentation in Ref. [CAB+18]. Since $q_{\mathrm{Calorimetry,\,Limiter}}$ corresponds to a poloidally averaged heat flux, $q_{\mathrm{r,fil}}^{\mathrm{total,mid}}$ must also be poloidally averaged.

The maximum poloidal angle θ_{max} is assumed to be $\pi/3$ following Ref. [CAB+18] with respect to the poloidal angle at the outer midplane as $\theta_0 = 0°$. $q_{\mathrm{r,fil}}^{\mathrm{total,av}}$ is obtained by the expression:

$$q_{\mathrm{r,fil}}^{\mathrm{total,av}} = \frac{\int_{-\pi/3}^{\pi/3} q_{\mathrm{r,fil}}^{\mathrm{total,mid}} \cos(\theta) d\theta}{\int_{-\pi/3}^{\pi/3} d\theta} \tag{5.14}$$

The comparison between both heat fluxes are illustrated in Fig. 5.31. The results suggest that filaments contribute up to 25 % to the total particle-related heat flux reaching the limiter presuming $T_{\mathrm{i,fil,est}}$ is in a realistic magnitude. Even at lowest α_{t} corresponding to the filamentary activities of low density H-modes, the filamentary contribution is non-negligible. Furthermore, the case, where $T_{\mathrm{e}} = T_{\mathrm{i}}$ has been assumed for Equ. 2.13, is added as grey shaded markers, For this case, the filaments would contribute up to 50% to the total heat flux reaching the limiter emphasizing the need of reliable T_{i}-values for studies at the limiter.

5.6.3 Estimation of the gross erosion at the AUG first wall

The availability of limiter probe measurements allows to estimate the filament and background induced gross erosion at the AUG first wall. The estimation of the gross erosion presented here is based on a simplified model introduced in Refs. [Sta00, BMC+15] and does not cover all erosion processes (e.g. prompt redeposition is not considered). The deduced values for the first wall tile gross erosion represent the estimated gross erosion at the position, where they have been acquired. They do not represent the gross erosion for

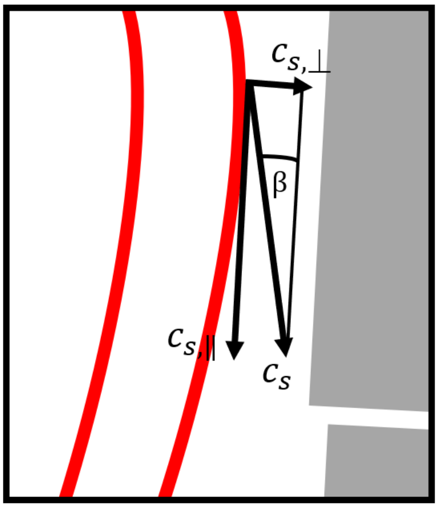

Figure 5.32: A sketch illustrating the estimate of the perpendicular contribution for the particle flux. The red lines represents magnetic field lines and the grey squares limiter tiles.

the entire first wall. Following Refs. [Sta00, BMC+15, Hut02], the gross erosion can be expressed by:

$$E_{\text{gross}} = \frac{1}{2} \cdot c_{\text{s},\perp} \cdot n_{\text{e}} \cdot Y_{\text{Yamamura}} \cdot f_{\text{PF}} \cdot \Delta t / n_{\text{PFC}}. \tag{5.15}$$

Y_{Yamamura} denotes the Yamamura sputtering yield[YYI83], n_{PFC} the PFC material density, $c_{\text{s},\perp}$ the perpendicular contribution of the sound speed with respect to the tile normal vector, Δt the exposure time and f_{PF} the packing fraction. In contrast to the study in Ref. [BMC+15], f_{PF} is considered for both, background plasma and filaments, induced gross erosion. The time period, which is not occupied by filaments, is associated to the background contribution and is simply obtained by subtracting f_{PF} from 1. The exposure

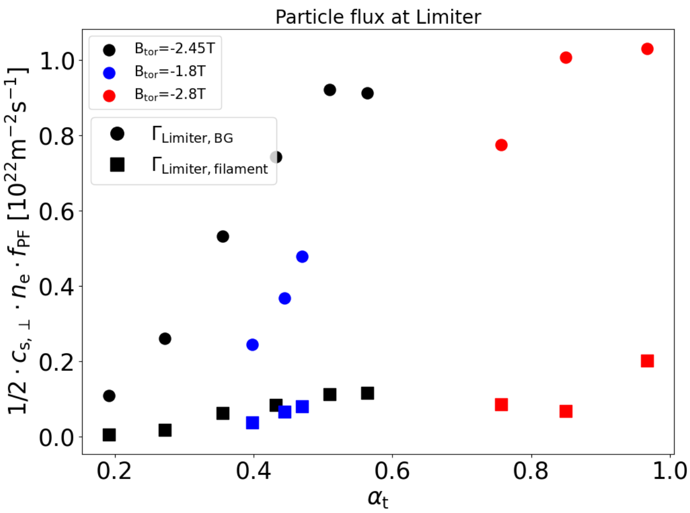

Figure 5.33: Illustration of the particle flux Γ_{Limiter} reaching the limiter.

time Δt is set to $31.5 \cdot 10^6$ s corresponding to a full year of plasma operation. For tungsten, n_{PFC} is set to $6.3 \cdot 10^{28}$ m^{-3}.
The term $\frac{1}{2} \cdot c_{\text{s},\perp} \cdot n_{\text{e}} \cdot f_{\text{PF}}$ denotes the perpendicular particle flux Γ_{Limiter}. The erosion on main chamber tiles is carried by the perpendicular projection $c_{\text{s},\perp}$ of the ion speed sound c_{s}, which can be approximated by:

$$c_{\text{s},\perp} \approx c_{\text{s}} \cdot \sin(\beta), \tag{5.16}$$

where β denotes the angle of the perpendicular velocity contribution with respect to the total velocity contribution. Refs. [CR95, Sta12] suggest that such cross-field transport arises at shallow field line inclinations. However, the inclination of the magnetic field lines along limiter tiles varies with its position and is therefore a non-constant parameter. For this simplified estimation, the corresponding angle β describing the perpendicular contribution is supposed to be 2°. Fig. 5.32 sketches the perpendicular projection of c_{s} on limiter tiles. Fig. 5.33 illustrates the evolution of Γ_{Limiter} for the available probe measurements. The background particle flux $\Gamma_{\text{Limiter,BG}}$ increases stronger than the filament particle flux $\Gamma_{\text{Limiter,filament}}$. A saturation of $\Gamma_{\text{Limiter,BG}}$ is observed, when α_{t} exceeds 0.55.

Structure of the sputtering yield Y_{Yamamura}

Y_{Yamamura} describes the sputtering yield (*number of PFC atoms expelled per incident ion from the plasma*) following the definition in Ref. [YYI83] and is a non-linear function of the electron and ion temperature. Y_{Yamamura} is based on the the revised Bohdansky formula [Boh84], which also takes into account the angle α between the trajectory vector of the incident ion and the PFC surface normal vector at the impact position. At AUG, α is

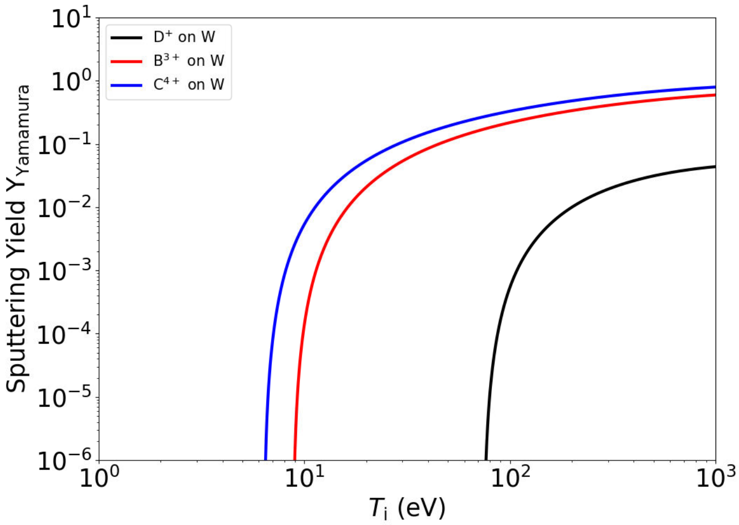

Figure 5.34: The sputtering yield Y on a tungsten surface for different incident ion species (D^+, B^{3+} and C^{4+}) is plotted against the ion temperatures assuming $T_\text{i} = 3 \cdot T_\text{e}$. X- and y-axis use logarithmic scale.

typically $\approx 60°$ for D$^+$ [SMA$^+$10]. The determination of Y is based on results summarized in Ref. [EGRRO93]. Starting from the revised Bohdansky formula, the sputtering yield for an incident angle of $\alpha = 0°$ is defined as:

$$Y_{\text{Bohdansky}}(E_0) = Q \cdot s_\text{n}^{\text{KrC}}(\epsilon) \left(1 - \left(\frac{E_\text{th}}{E_0}\right)^{2/3}\right) \left(1 - \frac{E_\text{th}}{E_0}\right)^2, \tag{5.17}$$

where E_0 denotes the projectile energy, $s_\text{n}^{\text{KrC}}(\epsilon)$ the nuclear stopping cross-section following the *Kr* - *C* potential and ϵ the reduced energy. Q, which represents the eroded atoms per incident ion, and E_th, which represents the threshold energy, are fitting parameters [Boh84]. ϵ is defined as:

$$\epsilon = E_0 \frac{M_2}{M_1 + M_2} \frac{a_\text{L}}{Z_1 Z_2 e^2} = \frac{E_0}{E_{\text{TF}}}, \tag{5.18}$$

where Z_1 and Z_2 denotes the respective nuclear charges and M_1 and M_2 the respective masses of the projectile and the target atom. a_L represents the Lindhard screening length, which is given by:

$$a_\text{L} = \left(\frac{9\pi^2}{128}\right)^{1/3} \cdot a_\text{B} \cdot \left(Z_1^{2/3} + Z^{2/3}\right)^{-1/2}, \tag{5.19}$$

Projectile	E_{TF} [eV]	E_{th} [eV]	Q [atoms/ion]
D^{+}	9925.0	209.37	0.07
B^{+3}	65241.0	46.37	0.8
C^{+4}	66517.0	41.20	1.02

Table 5.3: Overview of the input parameters required to determine Y_{Yamamura} for the three different projectile.

where a_{B} denotes the Bohr radius. The nuclear cross-section $s_{\text{n}}^{\text{KrC}}(\epsilon)$ is written as:

$$s_{\text{n}}^{\text{KrC}}(\epsilon) = \frac{0.5\ln(1+1.2288\epsilon}{\epsilon + 0.1728\sqrt{\epsilon} + 0.008\epsilon^{0.1504}}. \tag{5.20}$$

To obtain finally Y_{Yamamura}, $Y_{\text{Bohdansky}}$ must be corrected by a term which takes into account the angular dependence of the sputtering yield [YYI83]:

$$Y_{\text{Yamamura}}(E_0,\alpha) = Y_{\text{Bohdansky}}(E_0)\cdot\cos(\alpha)^{-f}\exp(f[1-\cos(\alpha)^{-1}]\cdot\cos(\alpha_{\text{opt}})), \tag{5.21}$$

$$\text{with } f = \sqrt{E_{\text{s}}}\left(0.94 - 1.33\cdot 10^{-3}\frac{M_2}{M_1}\right) \tag{5.22}$$

$$\alpha_{\text{opt}} = \frac{\pi}{2} - a_{\text{L}} n_{\text{PFC}}^{\frac{1}{3}}\left(2\epsilon\sqrt{\frac{E_{\text{s}}}{\gamma E_0}}\right)^{-\frac{1}{2}}. \tag{5.23}$$

α_{opt} denotes the angle of incidence, where Y_{Yamamura} has its maximum and E_{s} the surface binding energy. The fitting values for all three ion species considered in this estimate are summarized in table 5.3. For f and α_{opt} , the same values for all three species are used, 1.46 and 82.3°, respectively. The values correspond to the sputtering of H on W.

Determination of Y_{Yamamura}

To determine Y_{Yamamura}, it is assumed that the ions are Maxwellian distributed, which leads to the following expression for E_0:

$$E_0 = 2k_{\text{B}}T_{\text{i}} - ZeV_{\text{S}}, \tag{5.24}$$

where the first term denotes the approximated thermal energy of ions and the second one the energy of a single ion with charge Z gained at the sheath potential drop V_{S}. V_{S} is negative for floating conditions and can be written in terms of $k_{\text{B}}T_{\text{e}}$ as:

$$\frac{eV_{\text{S}}}{k_{\text{B}}T_{\text{e}}} = 0.5\cdot\ln\left[\left(2\pi\frac{m_{\text{e}}}{m_{\text{i}}}\right)\left(1+\frac{T_{\text{i}}}{T_{\text{e}}}\right)(1-\delta_{\text{SEE}})^{-2}\right], \tag{5.25}$$

where δ_{SEE} denotes the secondary electron emission coefficient. At $\delta_{\text{SEE}} = 0$, the ideal sheath potential is foreseen with $V_{\text{S}} \approx 2.5k_{\text{B}}T_{\text{e}}/e$, whereas at e.g $\delta_{\text{SEE}} = 0.775$ V_{s} can drop to $k_{\text{B}}T_{\text{e}}/e$ reducing the acceleration of the ions in the sheath and consequently reducing the induced gross erosion. Following Ref. [Tol14], the range of T_i suggests to set δ_SEE to 0. In Fig. 5.34, the sputtering yields Y on tungsten for 3 species assuming $T_\mathrm{i} = 3 \cdot T_\mathrm{e}$ are visualized: D^+, B^{3+} and C^{4+}. The latter impurity was used in Ref. [BMC+15]. Focusing on the case with deuterium only (black line), one can see that Y becomes only important for T_i above a threshold of 100 eV. This threshold can be exceeded by very hot filaments, which is given only for a small subset of the available measurements presupposing that $T_\mathrm{i,fil,est}$ is in a realistic magnitude. Sputtering yields of possible impurities, here B^{3+} and C^{4+}, becomes already important at lower T_i. For the presented cases, the threshold is around 10 eV. Just

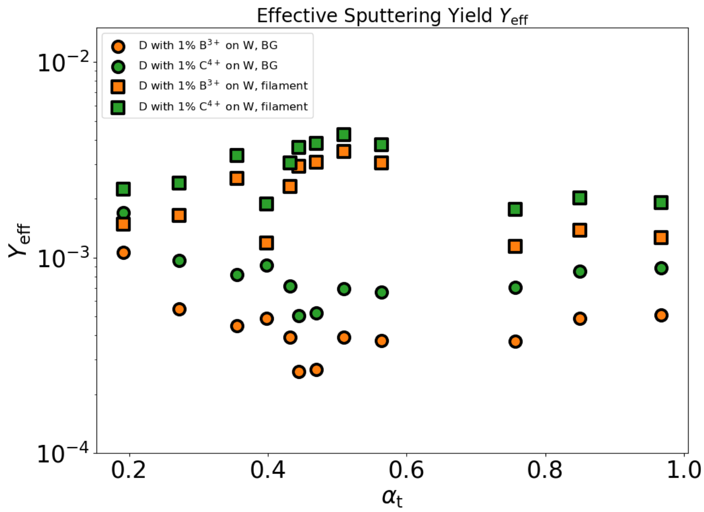

Figure 5.35: The effective sputtering yield Y_eff according to the definition in Equ. (5.26). Y_eff of background and of filaments are shown for two impurity species: B^{3+} and C^{4+}.

from the sputtering yields, one can conclude that neither a pure deuterium background plasma nor filaments (excluding extremely hot filaments) would cause any gross erosion on tungsten. Gross erosion would only become important by the presence of impurities in the far-SOL.

Estimation of the gross erosion in high-δ H-modes

To fill up Equ. (5.15) with both contributions, the values presented in Figs. 5.27, 5.28 and 5.34 are considered. To consider impurities, Y must be weighted accordingly to their assumed fractions in the plasma. The sputtering yield is weighted as followed:

$$Y_\mathrm{eff} = \frac{\sum_\mathrm{j} Y_\mathrm{j} \cdot n_\mathrm{j}}{n_\mathrm{e}}, \tag{5.26}$$

where Y_j denotes the sputtering yield and n_j the density of the jth-species. n_e represents the electron density of filaments or background. Fig. 5.35 illustrates Y_eff for background plasma (square markers) and filament (circle markers) for two impurity species as suggested before. The orange and green markers denote the case with 1% impurity concentration in the far-SOL. Overall, Y_{eff} of filaments are higher than of the background plasma. Fig. 5.36 illustrates the results for the gross erosion induced solely by the background (circle markers) and by both (square markers) for AUG operation conditions. The orange and green markers denote the case with 1% impurity concentration in the far-SOL. At lowest α_{t}, representing the inter-ELM phase of a Type-I ELMy H-mode, the estimated erosion yields a magnitude of between 0.7 and 1.2 mm depending on the impurity species. For this

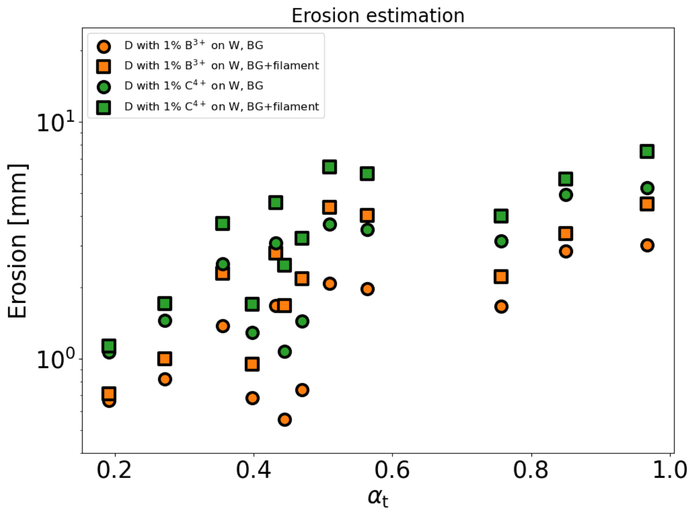

Figure 5.36: Estimated gross erosion for an exposure time $\Delta\, t$ of one burn year (24h/7d operation) for AUG H-modes. Above $\alpha_{\mathrm{t}} \approx 0.5$ achieving the QCE scenario, the gross erosion saturates. The gross erosion is dominated by the background plasma associated to the density shoulder. The contribution from filaments can be significant, but they never dominate the total gross erosion. The y-axis uses a logarithmic scale.

analysis only Inter-ELM profiles are considered. The impact of ELMs cannot be assessed, because at least 20-30 ELMs would be required to achieve a reasonable ELM-averaged value. Due to the short plunge duration, a sufficient number of ELMs was not acquired. The gross erosion at lowest α_{t} is dominated by the background plasma. Filaments would only cause a gross erosion below 0.1 mm. With increasing α_{t} the estimated erosion increases continuously until α_{t} exceeds 0.55, which is similar to the condition to distinguish Type-I ELMy H-modes from QCE H-modes as introduced in Ref. [FEH+23]. Exceeding this value, the gross erosion saturates. The estimated erosion varies between 3.0 mm and 7.5 mm depending on the impurity species. Even in this range of α_{t}, the erosion is still dominated by the background plasma, which is consistent with observations made in Ref. [BMC+15] for high-density L-modes AUG discharges. Replacing $T_{\mathrm{i,fil,est}}$ by $T_{\mathrm{i,sep}}$ or $T_{\mathrm{i,BG}}$, the contribution of filaments varies only slightly. The wetted area exposed to the gross erosion can be approximated by:

$$A_{\mathrm{wetted}} = \lambda_{\Gamma}^2 \cdot N/(\sin(\beta)\cos(\gamma)), \tag{5.27}$$

where λ_Γ denotes the particle flux decay length, N the number of ICRH limiter edges, which is 8, and γ the inclination between the parallel particle flux and the surface normal of the ICRH edge tile, which is about 15°. β has already been introduced describing the inclination of the particle flux along the tile surface and is about 2°. λ_Γ can be obtained from the MEM measurements, which suggests a decay length between 0.5 and 1.0 cm. Here, a value of 0.75 cm is considered. Inserting these values into the expression for A_{wetted} suggests a wetted area of about 0.13 m^2.

Possible impact of the prompt redeposition on the gross erosion

So far, any consequences of prompt redeposition are not considered and would impact the gross erosion. Detailed studies on the prompt tungsten redeposition in QCE H-modes, in particular with focus on the main chamber, do not yet exist. Therefore, it seems appropriate to simply scan the net erosion from 0% to 100% f_{redep} by defining E_{net} as:

$$E_{\text{net}} = (E_{\text{fil}} + E_{\text{BG}}) \cdot (1 - f_{\text{redep}}). \tag{5.28}$$

For both contributions (filament and background), the same f_{redep} is assumed. Fig. 5.36 (lower) illustrates the evolution of E_{net} with increasing f_{redep} for a subset with B^{3+} as impurity. A continuous decrease of E_{net} occurs with increasing f_{redep}. The area between

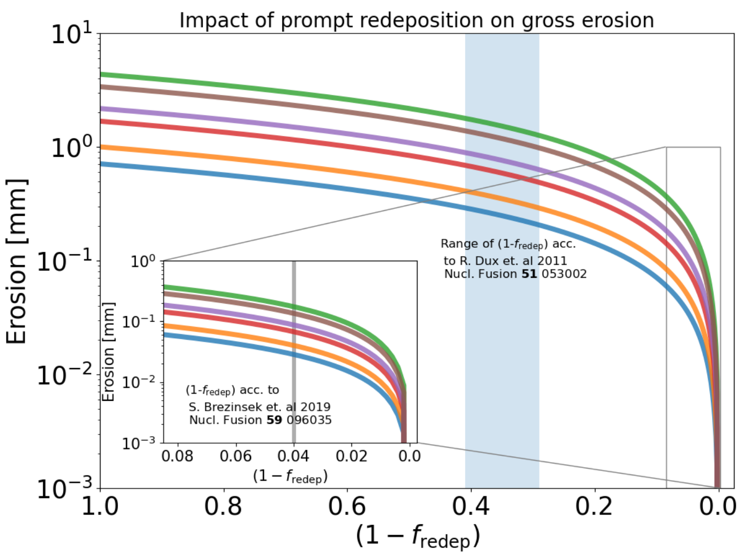

Figure 5.37: Lower: Evolution of the gross erosion for a subset with B^{3+} as impurity taken from Fig. 5.36 with increasing f_{red}. The y-axis uses a logarithmic scale.

0.09 and 0.0 is shown in a supplementary plot. Additionally, the possible range of (1-f_{redep}) from a previous AUG study for low density Type-I ELMy H-modes in full W-environment [DJPT11] is added. According to this study, the possible range of f_{redep} is within 0.59 - 0.71. This study includes also the impact of ELMs for different f_{ELM} in f_{redep}, which

worsens f_{redep}. The values from Ref. [DJPT11] are therefore the lower limit of f_{redep} and the actual values for QCE H-modes may be more optimistic. The estimated net erosion of the Inter-ELM phase would be about 0.2 - 0.3 mm within the possible range of f_{redep}. The estimated net erosion for QCE-phase at max. α_{t} would be about 1.2 - 1.8 mm.
The value for f_{redep} from a study assessing the Inter-ELM induced net erosion in the JET divertor is added as grey vertical line [BKM^{+}19] in the supplementary plot. The study on JET with the open divertor configuration reports on a prompt redeposition of about 96 % excluding ELMs. This would push the net erosion for the low density H-mode Inter-ELM to 0.03 mm and for the QCE at maximum α_{t} to 0.17 mm.
Further studies including high-precision measurements and sophisticated numerical codes [DLA^{+}17] with focus on f_{redep} in QCE are demanded, as the impact of high recycling state with increased neutral pressure in the main chamber together with an increased particle density near the first wall on f_{redep} are unknown.

Chapter 6

Summary

This thesis summarizes the investigations on energy loads of divertor and non-divertor components realized at the ASDEX Upgrade tokamak and the JET tokamak. A solution to the power exhaust challenge is the key requirement for the successful operation of future fusion power plants for electricity generation. Therefore, the heat transport from the confined plasma into the SOL and then to the PFCs has to be best understood. In next generation devices, like ITER, the heat flux limit for divertor components is limited to 10 MW/m^2 and for non-divertor components to 2 MW/m^2. The empirical ITPA multi-machine scaling describing the inter-ELM power fall-off length for low density H-modes in attached conditions predicts a power fall-off length of 1 mm for ITER conditions exceeding the divertor engineering limitations. Furthermore, periodically expelled Type-I ELMs would cause transient heat loads on both, divertor and non-divertor components, which will also significantly reduce their lifetimes and have therefore to be mitigated/suppressed in ITER and even totally avoided in future fusion reactors.

The focus of this thesis reports on the energy loads of divertor and non-divertor components for dedicated AUG H-mode discharges. For this purpose, the AUG calorimetry consisting of a cooling water calorimetry and a wall thermometry has been completely revamped and recommissioned. As a prerequisite for confident energy load studies, a reasonable global energy balance has been achieved in which 95 % of the injected energy has been found for a representative database of 577 discharges. In addition to the cooling water calorimetry, which covers almost the entire in-vessel components in poloidal and toroidal direction, a shot-to-shot assessment of the radiative energy contribution for areas, which are not covered by calorimetry, and an appropriate consideration of NBI-losses (first orbit, charge exchange and shine through losses) are fundamental. For this study, a framework based on the code CHERAB and a GPT-model trained on the AUG foil bolometry diagnostic has been introduced. NBI losses are determined by exploiting the codes RABBIT and ABC3D. These findings at AUG have been exploited to renew the attempt of the global energy balance at JET. The consideration of the NBI-losses on JET, which seems to be of 36 % of the injected NBI energy at JET, provides a possible explanation of the previous discrepancies between injected and measured energies in NBI-dominated plasmas at JET. A reasonable energy balance can be achieved with ICRH-dominated discharges at JET

without any further constraints.
A database optimized for calorimetric measurements has been acquired to analyze the evolution of the energy loads on almost all PFCs in AUG. The scenarios considered in this database are Type-I ELMy and QCE H-modes in a high-δ, high-κ magnetic equilibrium. The database covers a significant range in the density operational space of AUG (0.2 - 0.6 n_{GW}). A scan on edge safety factor has been obtained by changing the toroidal magnetic field B_{tor}, while the plasma current I_{p} is kept fixed. Due to the consideration of calorimetric diagnostics, the variations in this database are realized by changes in the flattop fuelling level and toroidal magnetic field on shot-to-shot basis. With the aid of this dedicated database, a reasonable correlation has been observed between the normalized energy loads on the AUG PFCs and the turbulence control parameter α_{t} with better agreement with respect to separatrix collisionality $\nu^*_{\mathrm{e,sep}}$. Interestingly, the increase of energy loads deposited at the first wall and the upper divertor is equally distributed which is consistent with the decrease of the energy loads of the lower divertor. Exploiting framework on CHERAB, it has been proven that a strong localized radiation pattern evolves between the plasma and the upper divertor when the QCE regime has been achieved. This radiation pattern can significantly contribute to the energy loads deposited on the upper divertor. Simultaneously, thermocouple and IR measurements from the divertor main target indicates a reduction of peak heat fluxes together with reduction of the energy loads from parallel conductive transport. Neither IR, LP nor bolometry measurements indicate an increase of heat fluxes on surrounding baffle tiles at the outer target. Interestingly, the heat fluxes derived from target LP measurements suggest an increase of the heat fluxes reaching the divertor main target. An extension of the database considering AUG discharges with different I_{p} and B_{tor} combinations, κ, δ and $n_{\mathrm{e}} - T_{\mathrm{e}}$ tuples suggest that the scaling of first wall energy loads seems to be generalizable.
The formation of the density shoulder in the far-SOL, which is generally associated with an enhancement of filamentary transport, has been assessed in terms of a density shoulder qualifier and the near-SOL density decay length. For this dedicated database, an increase of both quantities is observed with the turbulence control parameter α_{t} up to a saturation of the density shoulder amplitude when the QCE regime has been achieved. It may also suggest a stronger link between separatrix conditions and the formation of a density shoulder. Further checks regarding the break point separating near- and far-SOL suggest independence of this break point on the radial filament velocity and the secondary separatrix position. This observation is supported by the consideration of a discharge in the edge optimized configuration, where the secondary separatrix is sitting outside of the vacuum vessel.
The baratron and manometer measurements close to the upper divertor and the main chamber follow linearly α_{t}, whereas the divertor measurements of both diagnostics suggest a different dependency on $q_{\mathrm{cyl}}/B_{\mathrm{tor}}$. It may suggest that the requirement in achieving the high-recycling state are more linked to the main chamber conditions than to divertor conditions.
With the aid of dedicated probe measurements performed close to the limiter surface, it has been identified that the increase in filamentary transport is due to the increase of the

particle flux. This is primarily achieved by generating more, denser filaments. The ion and electron temperatures in QCE H-modes do not show significant variation. Also the radial velocity as well as their radial dimensions show only small variations whenever the QCE H-mode has been achieved. This is in contradiction to observations in high-density L-modes in AUG, which identified the increase in filament size as the trigger for the enhancement of filamentary transport. A comparison between the heat flux estimated from calorimetry and filament heat flux reaching the first wall reveals no increase of the filament contribution to the total one. The filament contribution remains constant, mostly below 25 %, throughout the entire scan.

Based on the limiter probe measurements, the gross erosion on limiter tiles has been determined using a simplified model. Gross erosion becomes only relevant in the presence of impurities in the far-SOL and is dominated by the background erosion regardless of the scenario, which is consistent with a previous study in high-density L-modes in AUG. The results indicate a saturation of the gross erosion above $\alpha_\mathrm{t} \approx 0.55$ predicting a maximum gross erosion of 7.5 mm for tungsten for a full year operation in AUG.

6.1 Outlook

The global energy balance studies at AUG and JET indicate that the impact of NBI losses on the energy balance has been misjudged so far. In future studies, such analyses should be repeated on further magnetically confining devices (WEST, W7-X, etc.). WEST would be a promising experiment for this purpose to confirm the observations in JET for purely ICRH-dominated as well as future NBI-dominated discharges. Furthermore, it would be great importance to identify and to understand the cause of the significant NBI-losses on JET by utilizing sophisticated numerical codes.
The most important observation drawn from global energy balance studies implies a erroneous consideration of the absorbed heating power in NBI-dominated discharges, at least for JET discharges in carbon wall and ILW, in any empirical scaling law so far. This observation for NBI-dominated discharges needs to be confirmed by studies on further experiments with a robust calorimetry encompassing the entire in-vessel components. At the same time, it would be beneficial to revise empirical scalings which depend on the absorbed heating power.
The evolution of the normalized energy loads at the PFCs show a reasonable correlation with α_{t}. This trend must be confirmed by including further fusion experiments. First results from JET should be available soon. Furthermore, the dominating radiation pattern at the upper divertor requires investigations in order to understand its dependence on the CDN-magnetic field configuration, first wall geometry and/or PFC material. The heat flux trend resolved by target LPs also requires further investigations. They are in contrast to IR, thermocouple and cooling water calorimetry results. With the DivIIo-Upgrade of the AUG upper divertor, novel capabilities will be available to investigate this localized radiation pattern. The availability of a cryopump in the new upper divertor may help to identify the cause of the radiation pattern. Furthermore, such a measurement can also may serve as a key input for numerical codes to provide further insights into this phenomenon.
The evolution of SOL properties at the outer midplane reveals that the density shoulder amplitude shows a saturation when the high density QCE regime is achieved in this database. In future studies, a variation of the heating scheme has to be performed in order to provide further insights behind the saturation of the density shoulder amplitude. The measurements of the baratrons and pressure gauges indicate different dependencies in the divertor and in the main chamber, which may also be linked to the density shoulder formation. The performance of high-powered QCE discharges in USN, which can be realised with the DivIIo-Upgrade, would provide important insights into the link between divertor and separatrix conditions in achieving a density shoulder. Furthermore, further effort should be put on the physics behind the break point, which separates the SOL into near and far. The proper physical understanding of any phenomena related to the power exhaust challenge may be of great importance for ITER and any future fusion reactors.
The results on gross erosion are a first indication that further in-depth analysis is needed. In future studies, a combined analysis of suitable probe and spectroscopic measurements should be carried out to obtain the most valuable experimental coverage and to complement previous measurements. A focus should also be placed on sophisticated numerical

codes to reliably predict the prompt redeposition for the QCE regime of present and future devices.

Bibliography

[AKP+08] J. Adamek, M. Kocan, R. Panek, J.P. Gunn, E. Martines, J. Stöckel, C. Ionita, G. Popa, C. Costin, J. Brotankova, R. Schrittwieser, and G. Van Oost. Simultaneous measurements of ion temperature by segmented tunnel and katsumata probe. *Contributions to Plasma Physics*, 48 (5-7):395–399, 2008.

[AMS+16] J. Adamek, H.W. Müller, C. Silva, R. Schrittwieser, C. Ionita, F. Mehlmann, S. Costea, J. Horacek, B. Kurzan, P. Bilkova, P. Böhm, M. Aftanas, P. Vondracek, J. Stöckel, R. Panek, H. Fernandes, and H. Figueiredo. Profile measurements of the electron temperature on the ASDEX Upgrade, COMPASS, and ISTTOK tokamak using Thomson scattering, triple, and ball-pen probes. *Review of Scientific Instruments*, 87:043510, 2016.

[BAA+22] J. Bucalossi, J. Achard, O. Agullo, T. Alarcon, L. Allegretti, H. Ancher, G. Antar, S. Antusch, V. Anzallo, C. Arnas, D. Arranger, J.F. Artaud, M.H. Aumeunier, S.G. Baek, X. Bai, J. Balbin, C. Balorin, T. Barbui, A. Barbuti, J. Barlerin, V. Basiuk, T. Batal, O. Baulaigue, A. Bec, M. Bécoulet, E. Benoit, E. Benard, J.M. Benard, N. Bertelli, E. Bertrand, P. Beyer, J. Bielecki, P. Bienvenu, R. Bisson, V. Bobkov, G. Bodner, C. Bottereau, C. Bouchand, F. Bouquey, C. Bourdelle, J. Bourg, S. Brezinsek, F. Brochard, C. Brun, V. Bruno, H. Bufferand, A. Bureau, S. Burles, Y. Camenen, B. Cantone, E. Caprin, S. Carpentier, G. Caulier, N. Chanet, O. Chellai, Y. Chen, M. Chernyshova, P. Chmielewski, W. Choe, A. Chomiczewska, G. Ciraolo, F. Clairet, J. Coenen, L. Colas, G. Colledani, J. Colnel, P. Coquillat, E. Corbel, Y. Corre, S. Costea, X. Courtois, T. Czarski, R. Daniel, J. Daumas, M. De Combarieu, G. De Temmerman, P. De Vries, C. Dechelle, F. Deguara, R. Dejarnac, J.M. Delaplanche, L.F. Delgado-Aparicio, E. Delmas, L. Delpech, C. Desgranges, P. Devynck, S. Di Genova, R. Diab, A. Diallo, M. Diez, G. Dif-Pradalier, M. Dimitrova, B. Ding, T. Dittmar, L. Doceul, M. Domenes, D. Douai, H. Dougnac, X. Duan, L. Dubus, N. Dumas, R. Dumont, F. Durand, A. Durif, A. Durocher, F. Durodié, A. Ekedahl, D. Elbeze, S. Ertmer, A. Escarguel, F. Escourbiac, K. Ezato, F. Faisse, N. Faure, N. Fedorczak, P. Fejoz, C. Fenzi-Bonizec, F. Ferlay, M. Firdaouss, L. Fleury, D. Flouquet, A. Gallo, Y. Gao, X. Garbet, J. Garcia, J.L. Gardarein, L. Gargiulo, P. Garibaldi, S. Garitta, J. Gaspar, E. Gauthier, P. Gavila, S. Gazzotti, F. Gely, M. Geynet, S. Gharafi, P. Ghendrih, I. Giacalone, C. Gil, S. Ginoux, S. Girard, E. Giroux, G. Giruzzi, C. Goletto, M. Goniche, T. Gray, E. Grelier, H. Greuner, E. Grigore, C. Grisolia, A. Grosjean, A. Grosman, D. Guibert, D. Guilhem, C. Guillemaut, B. Guillermin, R. Guirlet, J.P. Gunn, Y. Gunsu, T. Gyergyek, A. Hakola, J. Harris, J.C. Hatchressian, W. Helou, P. Hennequin, C. Hernandez, K. Hill, J. Hillairet, T. Hirai, G.T. Hoang, M. Houry, T. Hutter, F. Imbeaux, N. Imbert, I. Ivanova-Stanik, R. Jalageas, A. Jardin, L. Jaubert, G. Jiolat, A. Jonas, P. Joubert, A. Kirschner, C. Klepper, M. Komm, M. Koubiti, J. Kovacic, M. Kozeiha, K. Krieger, K. Krol, B. Lacroix, L. Laguardia, V. Lamaison, H. Laqua, C. Lau, Y. Lausenaz, R. Lé, M. Le Bohec, N. Lefevre, N. Lemoine, E. Lerche, M. Lewerentz, Y. Li, M. Li, A. Liang, P. Linczuk, C. Linsmeier, M. Lipa, X. Litaudon, X. Liu, J. Llorens, T. Loarer, A. Loarte, T. Loewenhoff, G. Lombard, J. Lore, P. Lorenzetto, P. Lotte, M. Lozano, B. Lu, R. Lunsford, G. Luo, P. Magaud, P. Maget, J.F. Mahieu, P. Maini, P. Malard, K. Malinowski, P. Manas, L. Manenc, Y. Marandet, J.L. Marechal, S. Marek, C. Martin, E. Martin, A. Martinez, P. Martino, D. Mazon, P. Messina, L. Meunier, D. Midou, Y. Mineo, M. Missilian, R. Mitteau, B. Mitu, P. Mollard, V. Moncada, T. Mondiere, J. Morales, M. Moreau, P. Moreau, Y Moudden, G. Moureau, D. Mouyon, M. Muraglia, A. Nagy, T. Nakano, E. Nardon, A. Neff, F. Nespoli, J. Nichols, S. Nicollet, R. Nouailletas, M. Ono, V. Ostuni, C. Parish, H. Park, H. Parrat, J.Y. Pascal, B. Pégourié, F.P. Pellissier, Y. Peneliau, M. Peret, Y. Peysson, E. Pignoly, G. Pintsuk, R. Pitts, C. Pocheau, C. Portafaix, M. Poulos, P. Prochet, A. Puig Sitjes, M. Rasinski, G. Raup, X. Regal-Mezin, C. Reux, B. Riccardi, J. Rice, M. Richou, F. Rigollet, H. Roche, J. Romazanov, C. Ruset, R. Sabot, A. Saille, R. Sakamoto, T. Salmon, F. Samaille, A. Santagiustina, B. Santraine, Y. Sarazin, E. Serre, H. Shin, S. Shiraiwai, Ja. Signoret, Je. Signoret, A. Simonin, O. Skalli Fettachi, Y. Song, A. Spring, P. Spuig, S. Sridhar, B. Stratton, C. Talatizi, P. Tamain, R. Tatali, M. Téna, A. Torre, L. Toulouse, J.M. Travère, W. Treutterer, E. Tsitrone, E. Unterberg, G. Urbanczyk, D. Van Eester, G. Van Rooij, S. Vartanian, J.M. Verger, L. Vermare, D. Vézinet, N. Vignal, B. Vincent, S. Vives, D. Volpe, G. Wallace, E. Wang, L. Wang, Yi. Wang, Yo. Wang, T. Wauters, B. Wirth, M. Wirtz, A. Wojenski, J. Wright, M. Xu, Q. Yang, H. Yang, B. Zago, Zagorski, B. Zhang, X. Zhang, and X. Zou. Operating a full tungsten actively cooled tokamak: overview of WEST first phase of operation. *Nuclear Fusion*, 62(4):042007, 2022.

[BBB+99] K. Behler, H. Blank, A. Buhler, R. Drube, H. Friedrich, K. Förster, K. Hallatschek, P. Heimann, F. Hertweck, J. Maier, R. Merkel, M.-G. Pacco-Düchs, G. Raupp, H. Reuter, U. Schneider-Maxon, R. Tisma, M. Zilker, the Computer ScienceDivision, the Garching Computer Centre, and the ASDEX Upgrade Team. Review of the ASDEX Upgrade data acquisition environment—present operation and future requirements. *Fusion Engineering and Design*, 43:247–258, 1999.

[BBB+14] K. Behler, H. Blank, A. Buhler, R. Drube, H. Eixenberger, K. Engelhardt, A. Lohs, R. Merkel, G. Raupp, W. Treutterer, the ASDEX Upgrade Team, and the Rechenzentrum Garching. Update on the ASDEX Upgrade data acquisition and data management environment. *Fusion Engineering and Design*, 89:702–706, 2014.

[BCC+16] G. Birkenmeier, M. Cavedon, G.D. Conway, P. Manz, U. Stroth, R. Fischer, G. Fuchert, T. Happel, F.M. Laggner, M. Maraschek, A. Medvedeva, V. Nikolaeva, D. Prisiazhniuk, T. Pütterich, F. Ryter, L.M. Shao, M. Willensdorfer, E. Wolfrum, H. Zohm, and the ASDEX Upgrade Team. Magnetic structure and frequency scaling of limit-cycle oscillations close to L- to H-mode transitions. *Nuclear Fusion*, 56(8):086009, 2016.

[BEK+15] M. Bernert, T. Eich, A. Kallenbach, D. Carralero, A. Huber, P. T. Lang, S. Potzel, F. Reimold, J. Schweinzer, E. Viezzer, H. Zohm, and the ASDEX Upgrade Team. The H-mode density limit in the full tungsten ASDEX Upgrade tokamak. *Plasma Physics and Controlled Fusion*, 57:014038, 2015.

[Ber13] M. Bernert. Analysis of the H-mode density limit in the ASDEX Upgrade tokamak using bolometry. *PhD Thesis, LMU*, 2013.

[BFF+17] A. Bock, E. Fable, R. Fischer, M. Reich, D. Rittich, J. Stober, M. Bernert, A. Burckhart, H. Doerk, M. Dunne, B. Geiger, L. Giannone, V. Igochine, A. Kappatou, R. McDermott, A. Mlynek, T. Odstrčil, G. Tardini, H. Zohm, and The ASDEX Upgrade Team. Non-inductive improved H-mode operation ASDEX Upgrade. *Nuclear Fusion*, 57:126041, 2017.

[BGS+21] K. Bogar, B. Geiger, P.A. Schneider, A. Jansen van Vuuren, O. Grover, the ASDEX Upgrade Team, and the EUROfusion MST1 Team. Direct determination of midplane background neutral density profiles from neutral particle analyzers. *Nuclear Fusion*, 61:036001, 2021.

[Big19] B. Bigot. Progress toward ITER's First Plasma. *Nuclear Fusion*, 59(11):112001, 2019.

[BJS+21] M. Bernert, F. Janky, B. Sieglin, A. Kallenbach, B. Lipschultz, F. Reimold, M. Wischmeier, M. Cavedon, P. David, M.G. Dunne, M. Griener, O. Kudlacek, R.M. McDermott, W. Treutterer, D. Brida, O. Fevrier, S. Henderson, M. Komm, the EUROfusion MST1 Team, and the ASDEX Upgrade Team. X-point radiation, its control and an ELM suppressed radiating regime at the ASDEX Upgrade tokamak. *Nuclear Fusion*, 61:024001, 2021.

[BKM+19] S. Brezinsek, A. Kirschner, M. Mayer, A. Baron-Wiechec, I. Borodkina, D. Borodin, I. Coffey, J. Coenen, N. den Harder, A. Eksaeva, C. Guillemaut, K. Heinola, A. Huber, V. Huber, M. Imrisek, S. Jachmich, E. Pawelec, M. Rubel, S. Krat, G. Sergienko, G.F. Matthews, A.G. Meigs, S. Wiesen, A. Widdowson, and JET contributors. Erosion, screening, and migration of tungsten in the jet divertor. *Nuclear Fusion*, 59(9):096035, 2019.

[BLOW13] D. Brunner, B. LaBombard, R. Ochoukov, and D. Whyte. Scanning retarding field analyzer for plasma profile measurements in the boundary of the Alcator C-Mod tokamak. *Review of Scientific Instruments*, 84(3), 2013.

[BLW+17] D. Brida, T. Lunt, M. Wischmeier, M. Bernert, D. Carralero, M. Faitsch, Y. Feng, T. Sehmer, B. Sieglin, W. Suttrop, E. Wolfrum, The ASDEX Upgrade Team, and The MST1 Team. Heat flux pattern in detached L-modes and ELM mitigated H-modes with rotating magnetic perturbations in ASDEX Upgrade. *Nuclear Fusion*, 57(11):116006, 2017.

[BM73] A.T.D. Butland and R.J. Maddison. The specific heat of graphite: an evaluation of measurements. *Journal of Nuclear Materials*, 49:45–56, 1973.

[BMC+15] G. Birkenmeier, P. Manz, D. Carralero, F.M. Laggner, G. Fuchert, K. Krieger, H. Maier, F. Reimold, K. Schmid, R. Dux, T. Pütterich, M. Willensdorfer, E. Wolfrum, and the ASDEX Upgrade Team. Filament transport, warm ions and erosion in ASDEX Upgrade L-modes. *Nuclear Fusion*, 55:033018, 2015.

[Boh84] J. Bohdansky. A universal relation for the sputtering yield of monatomic solids at normal ion incidence. *Nuclear Instruments and Methods in Physics Research B2*, 2:587–591, 1984.

[bpb23] bpb. *https://www.bpb.de/nachschlagen/zahlen-und-fakten/globalisierung/52741/primaerenergie-versorgung*. last viewed on 05.01.2023.

[BPS+21] M. Brank, R.A. Pitts, G. Simič, P. Lamalle, M. Kocan, F. Köchl, Y. Gribov, V. Polli, and L. Kos. Assessment of plasma power deposition on the ITER ICRH antennas. *Nuclear Materials and Energy*, 27:101021, 2021.

[Bra65] S.I. Braginskii. Transport processes in a plasma. *Reviews of Plasma Physics*, 1:205, 1965.

[BSE+20] D. Brida, D. Silvagni, T. Eich, M. Faitsch, P. McCarthy, the ASDEX Upgrade Team, and the MST1 Team. Role of electric currents for the SOL and divertor target heat fluxes in ASDEX Upgrade. *Plasma Physics and Controlled Fusion*, 62(10):105014, 2020.

[BWH+17] M. Bernert, M. Wischmeier, A. Huber, F. Reimold, B. Lipschultz, C. Lowry, S. Brezinsek, R. Dux, T. Eich, A. Kallenbach, A. Lebschy, C. Maggi, R. McDermott, T. Pütterich, and S. Wiesen. Power exhaust by SOL and pedestal radiation at ASDEX Upgrade and JET. *Nuclear Materials and Energy*, 12:111–118, 2017. Proceedings of the 22nd International Conference on Plasma Surface Interactions 2016, 22nd PSI.

[BWS+15] J.E. Barton, W.P. Wehner, E. Schuster, F. Felici, and O. Sauter. Simultaneous Closed-loop Control of the Current Profile and the Electron Temperature Profile in the TCV Tokamak. *American Control Conference*, 2015.

[CAB+18] D. Carralero, S. Artene, M. Bernert, G. Birkenmeier, M. Faitsch, P. Manz, P. de Marne, U. Stroth, M. Wischmeier, E. Wolfrum, the ASDEX Upgrade Team, and the EURO-fusion MST1 Team. On the role of filaments in perpendicular heat transport at the scrape-off layer. *Nuclear Fusion*, 58:096015, 2018.

[CGH+17] M.A. Chilenski, M.J. Greenwald, A.E. Hubbard, J.W. Hughes, J.P. Lee, Y.M. Marzouk, J.E. Rice, and A.E. White. Experimentally testing the dependence of momentum transport on second derivatives using Gaussian process regression. *Nuclear Fusion*, 57:126013, 2017.

[CHH+22] A. Cathey, M. Hoelzl, G. Harrer, M.G. Dunne, G.T.A. Huijsmans, K. Lackner, S.J.P. Pamela, E. Wolfrum, S. Günter, the JOREK Team, the ASDEX Upgrade Team, and the EUROfusion MST1 Team. MHD simulations of small ELMs at low triangularity in ASDEX Upgrade. *Plasma Physics and Controlled Fusion*, 64(5):054011, 2022.

[CMB+18] M. Carr, A. Meakins, M. Bernert, P. David, C. Giroud, J. Harrison, S. Henderson, B. Lipschultz, F. Reimold, the EUROfusion MST1 Team, and the ASDEX Upgrade Team. Description of complex viewing geometries of fusion tomography diagnostics by ray-tracing. *Review of Scientific Instruments*, 89:083506, 2018.

[Con98] J.W. Connor. A review of models for ELMs. *Plasma Physics and Controlled Fusion*, 40(2):191, 1998.

[CR95] R.H. Cohen and D.D. Ryutov. Plasma sheath in a tilted magnetic field: Closing of the diamagnetic currents; effect on plasma convection. *Physics of Plasmas*, 2(6):2011–2019, 1995.

[DBP+21] P. David, M. Bernert, T. Pütterich, C. Fuchs, S. Glöggler, T. Eich, and the ASDEX Upgrade Team. Optimization of the computation of total and local radiated power at ASDEX Upgrade. *Nuclear Fusion*, 61:066025, 2021.

[dHROH20] N. den Harder, D. Rittich, G. Orozco, and C. Hopf. Analytical Beamlet Code 3D for neutral beam injectors. *Plasma Physics and Controlled Fusion*, 62:025023, 2020.

[DJPT11] R. Dux, A. Janzer, T. Pütterich, and ASDEX Upgrade Team. Main chamber sources and edge transport of tungsten in H-mode plasmas at ASDEX Upgrade. *Nuclear Fusion*, 51:053002, 2011.

[DLA+17] R. Dux, A. Loarte, C. Angioni, D. Coster, E. Fable, and A. Kallenbach. The interplay of controlling the power exhaust and the tungsten content in ITER. *Nuclear Materials and Energy*, 12:28–35, 2017.

[dlLCR+15] E. de la Luna, I.T. Chapman, F. Rimini, P.J. Lomas, G. Saibene, F. Koechl, R. Sartori, S. Saarelma, R. Albanese, J. Flanagan, F. Maviglia, V. Parail, A.C.C. Sips, E.R. Solano, and JET contributors. Understanding the physics of ELM pacing via vertical kicks in JET in view of ITER. *Nuclear Fusion*, 56(2):026001, 2015.

[DML+03] A.W. Degeling, Y.R. Martin, J.B. Lister, L. Villard, V.N. Dokouka, V.E. Lukash, and R.R. Khayrutdinov. Magnetic triggering of ELMs in TCV. *Plasma Physics and Controlled Fusion*, 45(9):1637, 2003.

[DMZ11] D.A. D'Ippolito, J.R. Myra, and S.J. Zweben. Convective transport by intermittent blob-filaments: Comparison of theory and experiment. *Physics of Plasmas*, 18:060501, 2011.

[DPM99] P.I. Dorogokupets, E.M. Ponomarev, and E.A. Melekhova. Optimization of experimental data on the heat capacity, volume, and bulk moduli of minerals. *Petrology*, 7:574–591, 1999.

[DRXH09] M. Dreval, D. Rohraff, C. Xiao, and A. Hirose. Retarding field energy analyzer for the Saskatchewan Torus–Modified plasma boundary. *Review of Scientific Instruments*, 80(10), 2009. 103505.

[EAH+07] T. Eich, P. Andrew, A. Herrmann, W. Fundamenski, A. Loarte, R.A. Pitts, and the JET-EFDA contributors. ELM resolved energy distribution studies in the JET MKII Gas-Box divertor using infra-red thermography. *Plasma Physics and Controlled Fusion*, 49:573–604, 2007.

[Edd20] A. Eddington. The Internal Constitution of the Stars. *Nature*, 106:14–20, 1920.

[EGK+18] T. Eich, R.J. Goldston, A. Kallenbach, B. Sieglin, H.J. Sun, ASDEX Upgrade Team, and JET Contributors. Correlation of the tokamak H-mode density limit with ballooning stability at the separatrix. *Nuclear Fusion*, 58:034001, 2018.

[EGRRO93] W. Eckstein, C. Garcià-Rosales, J. Roth, and W. Ottenberger. Sputtering Data. *IPP Report*, IPP 9/82, 1993.

[ELP+13] T. Eich, A.W. Leonard, R.A. Pitts, W. Fundamenski, R.J. Goldston, T.K. Gray, A. Herrmann, A. Kirk, A. Kallenbach, O. Kardaun, A.S. Kukushkin, B. LaBombard, R. Maingi, M.A. Makowski, A. Scarabosio, B. Sieglin, J. Terry, A. Thornton, the ASDEX Upgrade Team, and the JET EFDA Contributors. Scaling of the tokamak near the scrape-off layer H-mode power width and implications for ITER. *Nuclear Fusion*, 53:093031, 2013.

[EMG+20] T. Eich, P. Manz, R.J. Goldston, P. Hennequin, P. David, M. Faitsch, B. Kurzan, B. Sieglin, E. Wolfrum, the ASDEX Upgrade team, and the EUROfusion MST1 team. The separatrix operational space of ASDEX Upgrade due to interchange-drift-Alfvén turbulence. *Nuclear Fusion*, 60:056016, 2020.

[EMtAUt21] T. Eich, P. Manz, and the ASDEX Upgrade team. Turbulence driven widening of the near-SOL power width in ASDEX Upgrade H-Mode discharges. *Nuclear Fusion*, 61:086017, 2021.

[ESS+11] T. Eich, B. Sieglin, A. Scarabosio, W. Fundamenski, R.J. Goldston, A. Herrmann, and ASDEX Upgrade Team. Inter-ELM Power Decay Length for JET and ASDEX Upgrade: Measurement and Comparison with Heuristic Drift-Based Model. *Physical Review Letters*, 107:215001, 2011.

[EUR23] EUROfusion. *https://www.euro-fusion.org/index.php?id=237.* last viewed on 12.01.2023.

[FBB+99] S. Fiedler, R. Brandenburg, J. Baldzuhn, K. McCormick, F. Aumayr, J. Schweinzer, H.P. Winter, W7-AS, and ASDEX-Upgrade Team. Edge plasma diagnostics on W7-AS and ASDEX-Upgrade using fast Li beams. *Journal of Nuclear Materials*, 266 - 269:1279–1284, 1999.

[FBB+19] G. Federici, C. Bachmann, L. Barucca, C. Baylard, W. Biel, L.V. Boccaccini, C. Bustreo, S. Ciattaglia, F. Cismondi, V. Corato, C. Day, E. Diegele, T. Franke, E. Gaio, C. Gliss, T. Haertl, A. Ibarra, J. Holden, G. Keech,

R. Kembleton, A. Loving, F. Maviglia, J. Morris, B. Meszaros, I. Moscato, G. Pintsuk, M. Siccinio, N. Taylor, M.Q. Tran, C. Vorpahl, H. Walden, and J.H. You. Overview of the DEMO staged design approach in Europe. *Nuclear Fusion Fusion*, 59:066013, 2019.

[FEH+05] J. C. Fuchs, T. Eich, A. Herrmann, K.F. Mast, and the ASDEX Upgrade Team. Radiation distribution and energy balance during type-I ELMs in ASDEX Upgrade. *Journal of Nuclear Materials*, 337–339:756–760, 2005.

[FEH+21] M. Faitsch, T. Eich, G. F. Harrer, E. Wolfrum, D. Brida, P. David, M. Griener, U. Stroth, the ASDEX Upgrade Team, and the EUROfusion MST1 Team. Broadening of the power fall-off length in a high density, high confinement H-mode regime in ASDEX Upgrade. *Nuclear Materials and Energy*, 26:100890, 2021.

[FEH+23] M. Faitsch, T. Eich, G.F. Harrer, E. Wolfrum, D. Brida, P. David, M. Dunne, L. Gil, B. Labit, U. Stroth, the ASDEX Upgrade Team, and the EUROfusion MST1 Team. Analysis and expansion of the quasi-continuous exhaust (QCE) regime in ASDEX Upgrade. *Nuclear Fusion*, 63(7):076013, 2023.

[FESC20] M. Faitsch, T. Eich, B. Sieglin, and JET Contributors. Correlation between near scrape-off layer power fall-off length and confinement properties in JET operated with carbon and ITER-like wall. *Plasma Physics and Controlled Fusion*, 62(8):085004, 2020.

[FGI+20] R. Fischer, L. Giannone, J. Illerhaus, P.J. McCarthy, R.M. McDermott, and ASDEX Upgrade Team. Estimation and Uncertainties of Profiles and Equilibria for Fusion Modeling Codes. *Fusion Science and Technology*, 76:879–893, 2020.

[FKW+14] G. Federici, G. Kemp, D. Ward, C. Bachmann, T. Franke, S. Gonzalez, C. Lowry, M. Gadomska, J. Harman, B. Meszaros, C. Morlock, F. Romanelli, and R. Wenninger. Overview of EU DEMO design and R & D activities. *Plasma Physics and Controlled Fusion*, 89:882, 2014.

[FLS03] G. Federici, A. Loarte, and G. Strohmayer. Assessment of erosion of the ITER divertor targets during type I ELMs. *Plasma Physics and Controlled Fusion*, 45:1523, 2003.

[FMH+94] J.C. Fuchs, K.F. Mast, A. Herrmann, K. Lackner, and ASDEX Upgrade Team. Twodimensional reconstruction of the radiation power density in ASDEX upgrade. *Europhysics Conference Abstracts (Proc. of the 21th EPS Conference on Controlled Fusion and Plasma Physics*, 18B:1308–1311, 1994.

[FTH+20] O. Février, C. Theiler, J. R. Harrison, C. K. Tsui, K. Verhaegh, C. Wüthrich, J. A. Boedo, H. De Oliveira, B. P. Duval, B. Labit, B. Lipschultz, R. Maurizio, H. Reimerdes, the TCV Team, and the EUROfusion MST1 Team. Nitrogen-seeded divertor detachment in TCV L-mode plasmas. *Plasma Physics and Controlled Fusion*, 62(3):035017, 2020.

[FWStAUT08] R Fischer, E Wolfrum, J Schweinzer, and the ASDEX Upgrade Team. Probabilistic lithium beam data analysis. *Plasma Physics and Controlled Fusion*, 50(8):085009, 2008.

[Gaf76] J. Gaffey. Energetic ion distribution resulting from neutral beam injection in tokamaks. *Journal of Plasma Physics*, 16(2):149–169, 1976.

[GAK+22] G. Grenfell, J. Adamek, M. Komm, D. Brida, G.D. Conway, P. Manz, P. Tolias, T. Eich, D. Sestak, A. Herrmann, T. Nishizawa, U. Stroth, and ASDEX Upgrade Team. High-heat flux ball-pen probe head in ASDEX-Upgrade. *Review of Scientific Instruments*, 93:023507, 2022.

[GBB+00] M. Greenwald, R. Boivin, P. Bonoli, C. Fiore, J. Goetz, R. Granetz, A. Hubbard, I. Hutchinson, J. Irby, Y. Lin, E. Marmar, A. Mazurenko, D. Mossessian, T. Sunn Pedersen, J. Rice, J. Snipes, G. Schilling, G. Taylor, M. Greenwald, R. Boivin, P. Bonoli, C. Fiore, J. Goetz, R. Granetz, A. Hubbard, I. Hutchinson, J. Irby, Y. Lin, E. Marmar, A. Mazurenko, D. Mossessian, T. Sunn Pedersen, J. Rice, J. Snipes, J. Terry, S. Wolfe, and S. Wukitch. Studies of EDA H-mode in Alcator C-Mod. *Plasma Physics and Controlled Fusion*, 42(5A):A263, 2000.

[GGC+24] J. Gaspar, J. Gerardin, Y. Corre, J. Daumas, N. Fedorczak, V. Lamaison, C. Bourdelle, G. Ciraolo, A. Ekedahl, A. Gallo, N. Rivals, E. Tsitrone, and the WEST Team. Calorimetry measurement for energy balance and energy distribution in west for l-mode plasmas. *Nuclear Fusion*, 64(3):036018, 2024.

[GGGH11] N. Ghahramany, Sh. Gharaati, M. Ghanaatian, and M. Hora. New scheme of nuclide and nuclear binding energy from quark-like model. *Iranian Journal of Science & Technology*, A3:201–208, 2011.

[GKD+17] B. Geiger, A.N. Karpushov, B.P. Duval, C. Marini, O. Sauter, Y. Andrebe, D. Testa, M. Marascheck, M. Salewski, P.A. Schneider, the TCV Team, and the EUROfusion MST1 Team. Fast-ion transport in low density L-mode plasmas at TCV using FIDA spectroscopy and the TRANSP code. *Plasma Physics and Controlled Fusion*, 59:115002, 2017.

[GMC+18] C. Giroud, A. Meakins, M. Carr, A. Baciero, and C. Bertrand. CHERAB Spectroscopy Modelling Framework (Version v0.1.0). *Zenodo*, http://doi.org/10.5281/zenodo.1206142, 2018.

[GML+88] P. Gohil, M. Ali Mahdavi, L. Lao, K.H. Burrell, M.S. Chu, J.C. DeBoo, C.L. Hsieh, N. Ohyabu, R.T. Snider, R.D. Stambaugh, and R.E. Stockdale. Study of Giant Edge-Localized Modes in DIII-D and Comparison with Ballooning Theory. *Physical Review Letters*, 61:1603–1606, 1988.

[GMS02] L. Giannone, K. Mast, and M. Schubert. Derivation of bolometer equations relevant to operation in fusion experiments. *Review of Scientific Instruments*, 73:3205–3214, 2002.

[GMT+81] R.J Goldston, D.C McCune, H.H Towner, S.L Davis, R.J Hawryluk, and G.L Schmidt. New techniques for calculating heat and particle source rates due to neutral beam injection in axisymmetric tokamaks. *Journal of Computational Physics*, 43(1):61–78, 1981.

[GR58] H. Grad and H. Rubin. Hydromagnetic Equilibria and Force-Free Fields. *Proceedings of the 2nd UN Conference on the Peaceful Uses of Atomic Energy*, 31:P/386, 1958.

[Gre02] M. Greenwald. Density limits in toroidal plasmas. *Plasma Physics and Controlled Fusion*, 44:R27, 2002.

[Gri18] M. Griener. Active Line Ratio Spectroscopy on Thermal Helium at ASDEX Upgrade. *PhD Thesis, TUM*, 2018.

[GRS17] R.J. Goldston, M.L. Reinke, and J.A. Schwartz. A new scaling for divertor detachment. *Plasma Physics and Controlled Fusion*, 59:055015, 2017.

[GSH+20] L. Gil, C. Silva, T. Happel, G. Birkenmeier, G.D. Conway, L. Guimarais, A. Kallenbach, T. Pütterich, J. Santos, P.A. Schneider, M. Schubert, E. Seliunin, A. Silva, J. Stober, U. Stroth, E. Trier, E. Wolfrum, the ASDEX Upgrade team, and the EUROfusion MST1 team. Stationary ELM-free H-mode in ASDEX Upgrade. *Nuclear Fusion*, 60(5):054003, 2020.

[GWC+18] M. Griener, E. Wolfrum, M. Cavedon, R. Dux, V. Rohde, M. Sochor, J.M. Muñoz Burgos, O. Schmitz, U. Stroth, , and ASDEX Upgrade Team. Helium line ratio spectroscopy for high spatiotemporal resolution plasma edge profile measurements at ASDEX Upgrade (invited). *Review of Scientific Instruments*, 89.10:10D102, 2018.

[Haw80] R.J. Hawryluk. An Empirical Approach to Tokamak Transport. *Physics of Plasmas Close to Thermonuclear Conditions, ed. by B. Coppi, et al.*, 1:19–46, (CEC, Brussels), 1980.

[HB98] G. Haas and H.-S. Bosch. In vessel pressure measurement in nuclear fusion experiments with ASDEX gauges. *Vacuum*, 51.1:39–46, 1998.

[Heb23] Hebei. http://www.metalspiping.com/typical-physical-properties-of-p92-t92-steel.html, last viewed on 22.01.2023.

[HER+04] A. Herrmann, T. Eich, V. Rohde, C. J. Fuchs, J. Neuhauser, and the ASDEX Upgrade Team. Power deposition outside the divertor in ASDEX Upgrade. *Plasma Physics and Controlled Fusion*, 46:971, 2004.

[HFR+22] G.F. Harrer, M. Faitsch, L. Radovanovic, E. Wolfrum, C. Albert, A. Cathey, M. Cavedon, M. Dunne, T. Eich, R. Fischer, M. Griener, M. Hoelzl, B. Labit, H. Meyer, F. Aumayr, The ASDEX Upgrade Team, and The EUROfusion MST1 Team. Quasicontinuous Exhaust Scenario for a Fusion Reactor: The Renaissance of Small Edge Localized Modes. *Physical Review Letters*, 129:165001, 2022.

[HGK91] G.T.A Huysmans, J.P. Goedbloed, and W. Kerner. Isoparametric Bicubic Hermite Elements for Solution of the Grad-Shafranov Equation. *International Journal of Modern Physics C*, 02(01):371–376, 1991.

[HJG+95] A. Herrmann, W. Junker, K. Gunther, S. Bosch, M. Kaufmann, J. Neuhauser, G. Pautasso, T. Richter, and R. Schneider. Energy Flux to the ASDEX-Upgrade Divertor Plates Determined by Thermography and Calorimetry. *Plasma Physics and Controlled Fusion*, 37:17, 1995.

[HMA+07] A. Huber, K. McCormick, P. Andrew, P. Beaumont, S. Dalley, J. Fink, J.C. Fuchs, K. Fullard, W. Fundamenski, L.C. Ingesson, F. Mast, S. Jachmich, G.F. Matthews, Ph. Mertens, V. Philipps, R.A. Pitts, S. Sanders, W. Zeidner, and JET-EFDA Contributors. Upgraded bolometer system on JET for improved radiation measurements. *Fusion Engineering and Design*, 82:1327–1334, 2007.

[HRR+23] T. Hohmann, A. Redl, V. Rohde, G. Schall, M. Schandrul, and the ASDEX Upgrade Team. The revised calorimetry of the ASDEX Upgrade tokamak. *Fusion Engineering and Design*, 187:113365, 2023.

[HS39] O. Hahn and F. Strassmann. Über den Nachweis und das Verhalten der bei der Bestrahlung des Urans mittels Neutronen entstehenden Erdalkalimetalle. *Naturwissenschaften, 27*, 27:11–15, 1939.

[HSP93] J.A. Heikkinen, S.K. Sipilä, and T.J.H. Pättikangas. Monte Carlo simulation of runaway electrons in a toroidal geometry. *Computer Physics Communications*, 76(2):215–230, 1993.

[HtAUT01] A. Herrmann and the ASDEX Upgrade Team. Limitations for divertor heat flux calculations of fast events in tokamaks. *in: C. Silva, C. Varandas, D. Campbell (Eds.), 28th EPS Conference on Controlled Fusion and Plasma Physics. Contributed Paper, in: ECA*, 25A:2109–2112, 2001.

[HTZ+19] A. Herrmann, M. Teschke, I. Zammuto, M. Cuevas, M. Dibon, A. Kallenbach, T. Lunt, V. Rohde, G. Schall, T. Vierle, S. Vorbrugg, M. Weißgerber, H. Zohm, and the ASDEX Upgrade Team. A new upper divertor with internal coils for ASDEX upgrade – Status of the project. *Fusion Engineering and Design*, 146, Part A:920–923, 2019.

[Hut02] I.H. Hutchinson. Principles of plasma diagnostics. *Plasma Physics and Controlled Fusion*, 44:2603, 2002.

[HWD+18] G.F. Harrer, E. Wolfrum, M.G. Dunne, P. Manz, M. Cavedon, P.T. Lang, B. Kurzan, T. Eich, B. Labit, J. Stober, H. Meyer, M. Bernert, F.M. Laggner, F. Aumayr, the EUROfusion MST1 Team, and the ASDEX Upgrade Team. Parameter dependences of small edge localized modes (ELMs). *Nuclear Fusion*, 58:112001, 2018.

[IPP23a] IPP. *https://www.aug.ipp.mpg.de/aug/local/aug_only/AUG_Aufbau/Drawing_Gallery/ipage00002.htm.* last viewed on 05.01.2023.

[IPP23b] IPP. *https://www.ipp.mpg.de/15144/zuendbedingungen.* last viewed on 05.01.2023.

[IToCM+99] ITER Physics Expert Group on Confinement ITER, Transport, ITER Physics Expert Group on Confinement Modelling, Database, and ITER Physics Basis Editors. Chapter 2: Plasma confinement and transport. *Nuclear Fusion*, 39:2175, 1999.

[KACC+12] M. Kocan, S.Y. Allan, S. Carpentier-Chouchana, P. de Marne, S. Elmore, T. Franke, J.P. Gunn, A. Herrmann, A. Kirk, M. Kubic, T. Lunt, H.W. Müller, R.A. Pitts, V. Rohde, and the ASDEX Upgrade Team. Ion energies and currents of type I and mitigated ELMs in the ASDEX Upgrade far scrape-off layer. *Nuclear Fusion*, 52:023016, 2012.

[KBB+84] M. Keilhacker, G. Becker, K. Bernhardi, A. Eberhagen, M. ElShaer, G. FuBmann, O. Gehre, J. Gernhardt, G. v. Gierke, E. Glock, G. Haas, F. Karger, S. Kissel, O. Kluber, K. Kornherr, K. Lackner, G. Lisitano, G.G. Lister, J. Massig, H.M. Mayer, K. McCormick, D. Meisel, E. Meservey, E.R. Muller, H. Murmann, H. Niedermeyer, W. Poschenrieder, H. Rapp, B. Richter, H. Rohr, F. Ryter, F. Schneider, S. Siller, P. Smeulders, F. Soldner, E. Speth, A. Stabler, K. Steinmetz, K.-H. Steuer, Z. Szymanski, G. Venus, O. Vollmer, and F. Wagner. Confinement studies in L and H-type Asdex discharges. *Plasma Physics and Controlled Fusion*, 26:49, 1984.

[KBC+18] K. Krieger, M. Balden, J.W. Coenen, F. Laggner, G.F. Matthews, D. Nille, V. Rohde, B. Sieglin, L. Giannone, B. Göths, A. Herrmann, P. de Marne, R.A. Pitts, S. Potzel, P. Vondracek, ASDEX-Upgrade Team, and EUROfusion MST1 Team. Experiments on transient melting of tungsten by ELMs in ASDEX Upgrade. *Nuclear Fusion*, 58:026024, 2018.

[KCP+01a] A. Kallenbach, A. Carlson, G. Pautasso, A. Peeters, U. Seidel, H.-P. Zehrfeld, and ASDEX Upgrade Team. Electric currents in the scrape-off layer in ASDEX Upgrade. *Journal of Nuclear Materials*, 290-293:639–643, 2001.

[KCP+01b] A. Kallenbach, A. Carlson, G. Pautasso, A. Peeters, U. Seidel, H.-P. Zehrfeld, and ASDEX Upgrade Team. Electric currents in the scrape-off layer in ASDEX Upgrade. *Journal of Nuclear Materials*, 290293:639, 2001.

[KGK+12] M. Kocan, F.P. Gennrich, A. Kendl, H.W. Müller, and the ASDEX Upgrade Team. Ion temperature fluctuations in the asdex upgrade scrape-off layer. *Plasma Physics and Controlled Fusion*, 54(8):085009, 2012.

[KGM+98] T. Kass, S. Günter, M. Maraschek, W. Suttrop, H. Zohm, and ASDEX Upgrade Team. Characteristics of type I and type III ELM precursors in ASDEX upgrade. *Nuclear Fusion*, 38(1):111, 1998.

[KM11] B. Kurzan and H.D. Murmann. Edge and core Thomson scattering systems and their calibration on the ASDEX Upgrade tokamak. *Review of Scientific Instruments*, 82 103501, 2011.

[KMN+13] M. Kocan, H.W. Müller, Nold, T. Lunt, J. Adamek, S.Y. Allan, M. Bernert, G.D. Conway, P. de Marne, T. Eich, S. Elmore, F.P Gennrich, A. Herrmann, J. Horacek, Z. Huang, A. Kallenbach, M. Komm, M. Maraschek, F. Mehlmann, S. Müller, T.T. Ribeiro, V. Rohde, R. Schrittwieser, B. Scott, U. Stroth, W. Suttrop, E. Wolfrum, and the ASDEX Upgrade Team. Intermittent transport across the scrape-off layer: latest results from ASDEX Upgrade. *Nuclear Fusion*, 53:073047, 2013.

[KOS+09] A. Kirk, T. O'Gorman, S. Saarelma, R. Scannell, H.R. Wilson, and the MAST team. A comparison of H-mode pedestal characteristics in MAST as a function of magnetic configuration and ELM type. *Plasma Physics and Controlled Fusion*, 51(6):065016, 2009.

[KPP+13] A.S. Kukushkin, H.D. Pacher, G.W. Pacher, V. Kotov, R.A. Pitts, and D. Reiter. Consequences of a reduction of the upstream power SOL width in ITER. *Journal of Nuclear Materials*, 438:S203–S207, 2013.

[KSC+23] D.B. King, R. Sharma, C.D. Challis, A. Bleasdale, E.G. Delabie, D. Douai, D. Keeling, E. Lerche, M. Lennholm, J. Mailloux, G. Matthews, M. Nicassio, Ž. Štancar, T. Wilson, and JET Contributors. Tritium neutral beam injection on JET: calibration and plasma measurements of stored energy. *Nuclear Fusion*, 63(11):112005, 2023.

[Law57] J.D. Lawson. Some Criteria for a Power Producing Thermonuclear Reactor. *Proceedings of the Physical Society B*, 70:6, 1957.

[LBB+23] T. Lunt, M. Bernert, D. Brida, P. David, M. Faitsch, O. Pan, D. Stieglitz, U. Stroth, A. Redl, and the ASDEX Upgrade Team. Compact Radiative Divertor Experiments at ASDEX Upgrade and Their Consequences for a Reactor. *Physical Review Letters*, 130:145102, 2023.

[LBC+99] A. Loarte, S. Bosch, A. Chankin, S. Clement, A. Herrmann, D. Hill, K. Itami, J. Lingertat, B. Lipschultz, K. McCormick, R. Monk, G.D. Porter, M. Shimada, and M. Sugihara. Multi-machine scaling of the divertor peak heat flux and width for L-mode and H-mode discharges. *Journal of Nuclear Materials*, 266-269:587–592, 1999.

[LCE+04] P.T. Lang, G.D. Conway, T. Eich, L. Fattorini, O. Gruber, S. Günter, L.D. Horton, S. Kalvin, A. Kallenbach, M. Kaufmann, G. Kocsis, A. Lorenz, M.E. Manso, M. Maraschek, V. Mertens, J. Neuhauser, I. Nunes, W. Schneider, W. Suttrop, H. Urano, and the ASDEX Upgrade Team. ELM pace making and mitigation by pellet injection in ASDEX Upgrade. *Nuclear Fusion*, 44(5):665, 2004.

[Leb18] A. Lebschy. Experimental characterization of the core plasma flow at the ASDEX Upgrade tokamak. *PhD Thesis, LMU*, 2018.

[LEH+19] B. Labit, T. Eich, G.F. Harrer, E. Wolfrum, M. Bernert, M.G. Dunne, L. Frassinetti, P. Hennequin, R. Maurizio, A. Merle, H. Meyer, S. Saarelma, U. Sheikh, J. Adamek, M. Agostini, D. Aguiam, R. Akers, R. Albanese, C. Albert, E. Alessi, R. Ambrosino, Y. Andrèbe, C. Angioni, G. Apruzzese, M. Aradi, H. Arnichand, F. Auriemma, G. Avdeeva, J.M. Ayllon-Guerola, F. Bagnato, V.K. Bandaru, M. Barnes, L. Barrera-Orte, P. Bettini, R. Bilato, O. Biletskyi, P. Bilkova, W. Bin, P. Blanchard, T. Blanken, V. Bobkov, A. Bock, D. Boeyaert, K. Bogar, O. Bogar, P. Bohm, T. Bolzonella, F. Bombarda, L. Boncagni, F. Bouquey, C. Bowman, S. Brezinsek, D. Brida, D. Brunetti, J. Bucalossi, J. Buchanan, J. Buermans, H. Bufferand, S. Buller, P. Buratti, A. Burckhart, G. Calabrò, L. Calacci, Y. Camenen, B. Cannas, P. Cano Megías, D. Carnevale, F. Carpanese, M. Carr, D. Carralero, L. Carraro, A. Casolari, A. Cathey, F. Causa, M. Cavedon, M. Cecconello, S. Ceccuzzi, J. Cerovsky, S. Chapman, P. Chmielewski, D. Choi, C. Cianfarani, G. Ciraolo, S. Coda, R. Coelho, L. Colas, D. Colette, L. Cordaro, F. Cordella, S. Costea, D. Coster, D.J. Cruz Zabala, G. Cseh, A. Czarnecka, I. Cziegler, O. D'Arcangelo, A. Dal Molin, P. David,

G. De Carolis, H. De Oliveira, J. Decker, R. Dejarnac, R. Delogu, N. den Harder, M. Dimitrova, F. Dolizy, J.J. Domínguez-Palacios Durán, D. Douai, A. Drenik, M. Dreval, B. Dudson, D. Dunai, B.P. Duval, R. Dux, S. Elmore, O. Embréus, B. Erdõs, E. Fable, M. Faitsch, A. Fanni, M. Farnik, I. Faust, J. Faustin, N. Fedorczak, F. Felici, S. Feng, X. Feng, J. Ferreira, G. Ferrò, O. Février, O. Ficker, L. Figini, A. Figueiredo, A. Fil, M. Fontana, M. Francesco, C. Fuchs, S. Futatani, L. Gabellieri, D. Gadariya, D. Gahle, D. Galassi, K. Galazka, J. Galdon-Quiroga, S. Galeani, D. Gallart, A. Gallo, C. Galperti, S. Garavaglia, J. Garcia, J. Garcia-Lopez, M. Garcia-Muñoz, L. Garzotti, J. Gath, B. Geiger, L. Giacomelli, L. Giannone, S. Gibson, L. Gil, E. Giovannozzi, G. Giruzzi, M. Gobbin, J. Gonzalez-Martin, T.P. Goodman, G. Gorini, M. Gospodarczyk, G. Granucci, D. Grekov, G. Grenfell, M. Griener, M. Groth, O. Grover, M. Gruca, A. Gude, L. Guimarais, T. Gyergyek, P. Hacek, A. Hakola, C. Ham, T. Happel, J. Harrison, A. Havranek, J. Hawke, S. Henderson, L. Hesslow, F. Hitzler, B. Hnat, J. Hobirk, M. Hoelzl, D. Hogeweij, C. Hopf, M. Hoppe, J. Horacek, M. Hron, Z. Huang, A. Iantchenko, D. Iglesias, V. Igochine, P. Innocente, C. Ionita-Schrittwieser, H. Isliker, I. Ivanova-Stanik, A. Jacobsen, M. Jakubowski, F. Janky, A. Jardin, F. Jaulmes, T. Jensen, T. Jonsson, A. Kallenbach, A. Kappatou, A. Karpushov, S. Kasilov, Y. Kazakov, P.V. Kazantzidis, D. Keeling, M. Kelemen, A. Kendl, W. Kernbichler, A. Kirk, G. Kocsis, M. Komm, M. Kong, V. Korovin, M. Koubiti, J. Kovacic, N. Krawczyk, K. Krieger, L. Kripner, A. Křivská, O. Kudlacek, Y. Kulyk, T. Kurki-Suonio, R. Kwiatkowski, F. Laggner, L. Laguardia, A. Lahtinen, P. Lang, J. Likonen, B. Lipschultz, F. Liu, R. Lombroni, R. Lorenzini, V.P. Loschiavo, T. Lunt, E. Macusova, J. Madsen, R. Maggiora, B. Maljaars, P. Manas, P. Mantica, M.J. Mantsinen, P. Manz, M. Maraschek, V. Marchenko, C. Marchetto, A. Mariani, C. Marini, T. Markovic, L. Marrelli, P. Martin, J.R. Martín Solís, A. Martitsch, S. Mastrostefano, F. Matos, G. Matthews, M.-L. Mayoral, D. Mazon, C. Mazzotta, P. Mc Carthy, K. McClements, R. McDermott, B. Mcmillan, C. Meineri, V. Menkovski, D. Meshcheriakov, M. Messmer, D. Micheletti, D. Milanesio, F. Militello, I.G. Miron, J. Mlynar, V. Moiseenko, P.A. Molina Cabrera, J. Morales, J.-M. Moret, A. Moro, D. Moulton, F. Nabais, V. Naulin, D. Naydenkova, R.D. Nem, F. Nespoli, S. Newton, A.H. Nielsen, S.K. Nielsen, V. Nikolaeva, M. Nocente, S. Nowak, M. Oberkofler, R. Ochoukov, P. Ollus, J. Olsen, J. Omotani, J. Ongena, F. Orain, F.P. Orsitto, R. Paccagnella, A. Palha, L. Panaccione, R. Panek, M. Panjan, G. Papp, I. Paradela Perez, F. Parra, M. Passeri, A. Pau, G. Pautasso, R. Pavlichenko, A. Perek, V. Pericoli Radolfini, F. Pesamosca, M. Peterka, V. Petrzilka, V. Piergotti, L. Pigatto, P. Piovesan, C. Piron, L. Piron, V. Plyusnin, G. Pokol, E. Poli, P. Pölöskei, T. Popov,

Z. Popovic, G. Pór, L. Porte, G. Pucella, M.E. Puiatti, T. Pütterich, M. Rabinski, J. Juul Rasmussen, J. Rasmussen, G.A. Rattá, S. Ratynskaia, T. Ravensbergen, D. Réfy, M. Reich, H. Reimerdes, F. Reimold, D. Reiser, C. Reux, S. Reznik, D. Ricci, N. Rispoli, J.F. Rivero-Rodriguez, G. Rocchi, M. Rodriguez-Ramos, A. Romano, J. Rosato, G. Rubinacci, G. Rubino, D.A. Ryan, M. Salewski, A. Salmi, D. Samaddar, L. Sanchis-Sanchez, J. Santos, K. Särkimäki, M. Sassano, O. Sauter, R. Scannell, M. Scheffer, B.S. Schneider, P. Schneider, R. Schrittwieser, M. Schubert, J. Seidl, E. Seliunin, S. Sharapov, R.R. Sheeba, G. Sias, B. Sieglin, C. Silva, S. Sipilä, S. Smith, A. Snicker, E.R. Solano, S.K. Hansen, C. Soria-Hoyo, E. Sorokovoy, C. Sozzi, A. Sperduti, G. Spizzo, M. Spolaore, M. Stejner, L. Stipani, J. Stober, P. Strand, H. Sun, W. Suttrop, D. Sytnykov, T. Szepesi, B. Tál, T. Tala, G. Tardini, M. Tardocchi, A. Teplukhina, D. Terranova, D. Testa, C. Theiler, E. Thorén, A. Thornton, B. Tilia, P. Tolias, M. Tomes, M. Toscano-Jimenez, C. Tsironis, C. Tsui, O. Tudisco, J. Urban, M. Valisa, M. Vallar, P. Vallejos Olivares, M. Valovic, D. Van Vugt, B. Vanovac, J. Varje, J. Varju, S. Varoutis, S. Vartanian, O. Vasilovici, J. Vega, G. Verdoolaege, K. Verhaegh, L. Vermare, N. Vianello, J. Vicente, E. Viezzer, F. Villone, I. Voitsekhovitch, D. Voltolina, P. Vondracek, N.M.T. Vu, N. Walkden, T. Wauters, M. Weiland, V. Weinzettl, M. Wensing, S. Wiesen, M. Wiesenberger, G. Wilkie, M. Willensdorfer, M. Wischmeier, K. Wu, L. Xiang, R. Zagorski, D. Zaloga, P. Zanca, R. Zaplotnik, J. Zebrowski, W. Zhang, A. Zisis, S. Zoletnik, and M. Zuin. Dependence on plasma shape and plasma fueling for small edge-localized mode regimes in TCV and ASDEX Upgrade. *Nuclear Fusion*, 59(8):086020, 2019.

[LHF+14] A. Loarte, G. Huijsmans, S. Futatani, L.R. Baylor, T.E. Evans, D. M. Orlov, O. Schmitz, M. Becoulet, P. Cahyna, Y. Gribov, A. Kavin, A. Sashala Naik, D.J. Campbell, T. Casper, E. Daly, H. Frerichs, A. Kischner, R. Laengner, S. Lisgo, R.A. Pitts, G. Saibene, and A. Wingen. Progress on the application of ELM control schemes to ITER scenarios from the non-active phase to DT operation. *Nuclear Fusion*, 54:033007, 2014.

[LKG+17] F.M. Laggner, S. Keerl, J. Gnilsen, E. Wolfrum, M. Bernert, D. Carralero, L. Guimarais, V. Nikolaeva, S. Potzel, M. Cavedon, F. Mink, M.G. Dunne, G. Birkenmeier, R. Fischer, E. Viezzer, M. Willensdorfer, M. Wischmeier, F. Aumayr, the EUROfusion MST1 Team, and the ASDEX Upgrade Team. Divertor, scrape-off layer and pedestal particle dynamics in the ELM cycle on ASDEX Upgrade. *Plasma Physics and Controlled Fusion*, 60(2):025002, 2017.

[LSS+03] A. Loarte, G. Saibene, R. Sartori, M. Becoulet, L. Horton, T. Eich, A. Herrmann, M. Laux, G. Matthews, S. Jachmich, N. Asakura, A. Chankin, A. Leonard, G. Porter, G. Federici, M. Shimada, M. Sugihara, and G. Janeschitz. ELM energy and particle losses and their extrapolation to burning plasma experiments. *Journal of Nuclear Materials*, 313-316:962–966, 2003. Plasma-Surface Interactions in Controlled Fusion Devices 15.

[MBD+17] G.F. Matthews, P. Bunting, S. Devaux, P. Drewelow, C. Guillemaut, D.B. King, E. Lerche, S. Silburn, G. Szepesi, V. Riccardo, V. Thompson, and JET Contributors. Energy balance in JET. *Nuclear Materials and Energy*, 12:227–233, 2017.

[MBD+22] K. Moser, A. Bock, P. David, M. Bernert, R. Fischer, and ASDEX Upgrade Team. Gaussian Process Tomography at ASDEX Upgrade with Magnetic Equilibrium Information and Nonstationary Kernels. *Fusion Science and Technology*, 78:607–616, 2022.

[MCD+21] M. Moscheni, M. Carr, S. Dulla, F. Maviglia, A. Meakins, G.F. Nallo, F. Subba, and R. Zanino. Parametric study of the radiative load distribution on the EU-DEMO first wall due to SPI-mitigated disruptions. *Fusion Engineering and Design*, 172:112917, 2021.

[MEF+01] G.F. Matthews, S.K. Erents, W. Fundamenski, C. Ingesson, R.D. Monk, and V. Riccardo. Divertor energy distribution in JET H-modes. *Journal of Nuclear Materials*, 290-293:668–672, 2001.

[MEG+12] M.A. Makowski, D. Elder, T.K. Gray, B. LaBombard, C.J. Lasnier, A.W. Leonard, R. Maingi, T.H. Osborne, P.C. Stangeby, J.L. Terry, and J. Watkins. Analysis of a multi-machine database on divertor heat fluxes. *Physics of Plasmas*, 19(5), 2012.

[MF39] L. Meitner and O.R. Fischer. Disintegration of Uranium by Neutrons: a New Type of Nuclear Reaction. *Nature*, 143:239–240, 1939.

[MMS99] P.J. McCarthy, P. Martin, and W. Schneider. The CLISTE interpretive equilibrium code. *Technical Report IPP*, 5/85, 1999.

[MRV+21] D. Mancini, P. Ricci, N. Vianello, M. Giacomin, and A. Coroado. Investigation of the density shoulder formation by using self-consistent simulations of plasma turbulence and neutral kinetic dynamics. *Nuclear Fusion*, 61(12):126029, 2021.

[MSE+10] A. Mlynek, G. Schramm, H. Eixenberger, G. Sips, K. McCormick, M. Zilker, K. Behler, J. Eheberg, and ASDEX Upgrade Team. Design of a digital multiradian phase detector and its application in fusion plasma interferometry. *Review of Scientific Instruments*, 81:033507, 2010.

[MTI74] G.H. Miley, H. Towner, and N. Ivich. *Fusion cross sections and reactivities.* Technical Report, University of Illinois, 1974.

[NBB+07] R. Neu, M. Balden, V. Bobkov, R. Dux, O. Gruber, A. Herrmann, A. Kallenbach, M. Kaufmann, C.F. Maggi, H. Maier, H.W. Müller, T. Pütterich, R. Pugno, V. Rohde, A.C.C Sips, J. Stober, W. Suttrop, C. Angioni, C.V. Atanasiu, W. Becker, K. Behler, K. Behringer, A. Bergmann, T. Bertoncelli, R. Bilato, A. Bottino, M. Brambilla, F. Braun, A. Buhler, A. Chankin and. G. Conway, D.P. Coster, P. de Marné, S. Dietrich, K. Dimova, R. Drube, T. Eich, K. Engelhardt, H.-U. Fahrbach, U. Fantz, L. Fattorini, J. Fink, R. Fischer, A. Flaws, P. Franzen, J.C. Fuchs, K. Gál, M. García Muñoz, M. Gemisic-Adamov, L. Giannone, S. Gori, S. da Graca, H. Greuner, A. Gude, S. Günter, G. Haas, J. Harhausen, B. Heinemann, N. Hicks, J. Hobirk, D. Holtum, C. Hopf, L. Horton, M. Huart, V. Igochine, S. Kálvin, O. Kardaun, M. Kick, G. Kocsis, H. Kollotzek, C. Konz, K. Krieger, T. Kurki-Suonio, B. Kurzan, K. Lackner, P.T. Lang, P. Lauber, M. Laux, J. Likonen, L. Liu, A. Lohs, K. Mank, A. Manini, M.-E. Manso, M. Maraschek, P. Martin, Y. Martin, M. Mayer, P. McCarthy, K. McCormick, H. Meister, F. Meo, P. Merkel, R. Merkel, V. Mertens, F. Merz, H. Meyer, M. Mlynek, F. Monaco, H. Murmann, G. Neu, J. Neuhauser, B. Nold, J.-M. Noterdaeme, G. Pautasso, G. Pereverzev, E. Poli, M. Püschel, G. Raupp, M. Reich, B. Reiter, T. Ribeiro, R. Riedl, J. Roth, M. Rott, F. Ryter, W. Sandmann, J. Santos, K. Sassenberg, A. Scarabosio, G. Schall, J. Schirmer, A. Schmid, W. Schneider, G. Schramm, R. Schrittwieser, W. Schustereder, J. Schweinzer, S. Schweizer, B. Scott, U. Seidel, F. Serra, M. Sertoli, A. Sigalov, A. Silva, E. Speth, A. Stäbler, K.-H. Steuer, E. Strumberger, G. Tardini, C. Tichmann, W. Treutterer, C. Tröster, L. Urso, E. Vainonen-Ahlgren, P. Varela, L. Vermare, D. Wagner, M. Wischmeier, E. Wolfrum, E. Würsching, D. Yadikin, Q. Yu, D. Zasche, T. Zehetbauer, M. Zilker, and H. Zohm. Plasma wall interaction and its implication in an all tungsten divertor tokamak. *Plasma Physics and Controlled*, 49:B59, 2007.

[NPSC+15] R. Nazikian., C. Paz-Soldan, J.D. Callen, J.S. deGrassie, D. Eldon, T.E. Evans, N.M. Ferraro, B.A. Grierson, R.J. Groebner, S.R. Haskey, C.C. Hegna, J.D. King, N.C. Logan, G.R. McKee, R.A. Moyer, M. Okabayashi, D.M. Orlov, T.H. Osborne, J-K. Park, T.L. Rhodes, M.W. Shafer, P.B. Snyder, W.M. Solomon, E.J. Strait, and M.R. Wade. Pedestal Bifurcation and Resonant Field Penetration at the Threshold of Edge-Localized Mode Suppression in the DIII-D Tokamak. *Physical Review Letters*, 114:105002, 2015.

[NRSStAUT12] D. Neuwirth, V. Rohde, T. Schwarz-Selinger, and the ASDEX Upgrade Team. Formation of ammonia during nitrogen-seeded discharges at ASDEX Upgrade. *Plasma Physics and Controlled Fusion*, 54:085008, 2012.

[NvTSF18] D. Nille, U. von Toussaint, B. Sieglin, and M. Faitsch. Probabilistic Inference of Surface Heat Flux Densities from Infrared Thermography. *Bayesian Inference and Maximum Entropy Methods in Science and Engineering*, 55–64, 2018.

[OA90] T. Ozeki and M. Azumi. Access to the Second Stability Regime near the Plasma Surface in a High-q, Low-Shear Tokamak Plasma. *Journal of the Physical Society of Japan*, 59(3):927–933, 1990.

[OCL+90] T. Ozeki, M.S. Chu, L.L. Lao, T.S. Taylor, M.S. Chance, S. Kinoshita, K.H. Burrell, and R.D. Stambaugh. Plasma shaping, edge ballooning stability and ELM behaviour in DIII-D. *Nuclear Fusion*, 30(8):1425, 1990.

[ODB+20] R. Ochoukov, M. Dreval, V. Bobkov, H. Faugel, A. Herrmann, L. Kammerloher, P. Leitenstern, ASDEX Upgrade Team, and EUROfusion MST1 Team. Ion temperature measurement techniques using fast sweeping retarding field analyzer (RFA) in strongly intermittent ASDEX Upgrade tokamak plasmas. *Review of Scientific Instruments*, 91:063506, 2020.

[PBP06] R. Pitts, R. Buttery, and S. Pinches. Fusion: the way ahead. *Physics World*, 19(3):20, mar 2006.

[PCE+11] R.A. Pitts, S. Carpentier, F. Escourbiac, T. Hirai, V. Komarov, A.S. Kukushkin, S. Lisgo, A. Loarte, M. Merola, R. Mitteau, A.R. Raffray, M. Shimada, and P.C. Stangeby. Physics basis and design of the ITER plasma-facing components. *Journal of Nuclear Materials*, 415(1, Supplement):S957–S964, 2011. Proceedings of the 19th International Conference on Plasma-Surface Interactions in Controlled Fusion.

[PMA+04] A. Pankin, D. McCune, R. Andre, G. Bateman, and A. Kritz. The tokamak monte carlo fast ion module nubeam in the national transport code collaboration library. *Computer Physics Communications*, 159(3):157–184, 2004.

[RBH+23] V. Rohde, M. Balden, K. Hunger, I. Zammuto, A. Herrmann, and R. Neu. Surface features of strongly heated bulk tungsten divertor plates at asdex upgrade. *Nuclear Materials and Energy*, 34:101320, 2023.

[RDM+19] T. Reichbauer, A. Drenik, R. McDermott, V. Rohde, and the ASDEX Upgrade Team. Assessment o nitrogen fluence from the divertor plasma in nitrogen seeded discharges. *Fusion and Engineering and Design*, 149:111325, 2019.

[RDW+22] L. Radovanovic, M. Dunne, E. Wolfrum, G. Harrer, M. Faitsch, R. Fischer, F. Aumayr, the ASDEX Upgrade Team, and the EUROfusion MST1 Team. Developing a physics understanding of the quasi-continuous exhaust regime: pedestal profile and ballooning stability analysis. *Nuclear Fusion*, 62(8):086004, 2022.

[RDZ98] B.N. Rogers, J.F. Drake, and A. Zeiler. Phase Space of Tokamak Edge Turbulence, the L-H Transition, and the Formation of the Edge Pedestal. *Physcial Review Letters*, 81:4396, 1998.

[REV+23] A. Redl, T. Eich, N. Vianello, P. David, the ASDEX Upgrade Team, and the EUROfusion MST1 Team. Energy load on first wall components in high density, small ELM regimes in ASDEX Upgrade. *Nuclear Materials and Energy*, 34:101319, 2023.

[REV+24] A. Redl, T. Eich, N. Vianello, J. Adamek, M. Bernert, G. Birkenmeier, D. Brida, P. David, M. Faitsch, R. Fischer, G. Grenfell, R. Ochoukov, V. Rohde, B. Tal, M. Dreval, the ASDEX Upgrade Team, and the EUROfusion Tokamak Exploitation Team. An extensive analysis of sol properties in high-δ plasmas in asdex upgrade. *Nuclear Fusion*, 64(8):086064, 2024.

[RHE+23a] A. Redl, T. Hohmann, T. Eich, N. Vianello, M. Bernert, P. David, N. den Harder, A. Herrmann, V. Rohde, M. Weiland, the ASDEX Upgrade Team, and the EUROfusion MST1 Team. The global energy balance of the ASDEX Upgrade tokamak determined with the revised cooling water calorimetry. *Plasma Physics and Controlled Fusion*, 65(11):115003, 2023.

[RHE+23b] A. Redl, T. Hohmann, T. Eich, N. Vianello, M. Bernert, P. David, N. den Harder, A. Herrmann, V. Rohde, M. Weiland, the ASDEX Upgrade Team, and the EUROfusion MST1 Team. The global energy balance of the ASDEX Upgrade tokamak determined with the revised cooling water calorimetry. *Zenodo*, https://doi.org/10.5281/zenodo.6368069, 2023.

[RN10] C.E. Rasmussen and H. Nickisch. Gaussian processes for machine learning (GPML) toolbox. *Journal of Machine Learning Research*, 11:3011–3015, 2010.

[Rut19] E. Rutherford. Collision of α particles with light atoms. IV. An anomalous effect in nitrogen. *Philosophical Magazine Series*, 37:581–587, 1919.

[RV92] T. Richter and H. Vernickel. Beschreibung der Kühlwasserkalorimetrie - und der Wandthermotriediagnostik am Tokamak ASDEX Upgrade. *IPP Report*, 5/46, 1992.

[RV94] T. Richter and H. Vernickel. The cooling water calorimetry system at ASDEX upgrade tokamak. *Review of Scientific Instruments*, 65, 1994.

[Sak58] A.D. Sakharov. Teoriya magnitnogo termoyadernogo reaktora (The theory of magnetic thermonuclear reactor). *Plasma Physics and Problems of Controlled Thermonuclear Reactions*, 1:20, 1958.

[SALL99] O. Sauter, C. Angioni, and Y. R. Lin-Liu. Neoclassical conductivity and bootstrap current formulas for general axisymmetric equilibria and arbitrary collisionality regime. *Physics of Plasmas*, 6(7):2834–2839, 1999.

[Sau16] O. Sauter. Geometric formulas for system codes including the effect of negative triangularity. *Fusion Engineering and Design*, 112:633–645, 2016.

[Sco97] B.D. Scott. Three-dimensional computation of drift Alfvén turbulence. *Plasma Physics and Controlled Fusion*, 39(10):1635, 1997.

[Sco98a] B. Scott. Computation of Warm-Ion Drift Alfvén Turbulence. *Contributions to Plasma Physics*, 38:171, 1998.

[Sco98b] B. Scott. Warm-ion drift Alfvén turbulence and the L-H transition. *Plasma Physics and Controlled Fusion*, 40:823, 1998.

[Sco02] B.D. Scott. The nonlinear drift wave instability and its role in tokamak edge turbulence. *New Journal of Physics*, 4:52, 2002.

[Sco05a] B.D. Scott. Drift wave versus interchange turbulence in tokamak geometry: Linear versus nonlinear mode structure. *Physics of Plasmas*, 12:062314, 2005.

[Sco05b] B.D. Scott. Energetics of the interaction between electromagnetic ExB turbulence and zonal flows. *New Journal of Physics*, 7:92, 2005.

[Sco07] B.D. Scott. Tokamak edge turbulence: background theory and computation. *Plasma Physics and Controlled Fusion*, 49:S25, 2007.

[SEF$^+$16] B. Sieglin, T. Eich, M. Faitsch, A. Herrmann, A. Scarabosio, and the ASDEX Upgrade Team. Investigation of scrape-off layer and divertor heat transport in ASDEX Upgrade L-mode. *Plasma Physics and Controlled Fusion*, 58(5):055015, 2016.

[SEF$^+$20] D. Silvagni, T. Eich, M. Faitsch, T. Happel, B. Sieglin, P. David, D. Nille, L. Gil, U. Stroth, the ASDEX Upgrade team, and the EUROfusion MST1 team. Scrape-off layer (SOL) power width scaling and correlation between SOL and pedestal gradients across L, I and H-mode plasmas at ASDEX Upgrade. *Plasma Physics and Controlled Fusion*, 62(4):045015, 2020.

[SFE+17] B. Sieglin, M. Faitsch, T. Eich, A. Herrmann, W. Suttrop, JET Collaborators, the MST1 Team, and the ASDEX Upgrade Team. Progress in extrapolating divertor heat fluxes towards large fusion devices. *Physica Scripta*, 2017(T170):014071, 2017.

[SFH+15] B. Sieglin, M. Faitsch, A. Herrmann, B. Brucker, T. Eich, L. Kammerloher, and S. Martinov. Real time capable infrared thermography for ASDEX Upgrade. *Review of Scientific Instruments*, 86:113502, 2015.

[Sha66] V.D. Shafranov. Plasma Equilibrium in a Magnetic Field. *Reviews of Plasma Physics*, 2:103, 1966.

[Sie21a] Siemens. https://new.siemens.com/de/de/produkte/automatisierung/systeme/industrie/io-systeme/simatic-et-200m.html, last viewed on 22.08.2021.

[Sie21b] Siemens. https://new.siemens.com/de/de/produkte/automatisierung/systeme/industrie/sps/simatic-s7-400.html, last viewed on 22.08.2021.

[SKB+18] W. Suttrop, A. Kirk, V. Bobkov, M. Cavedon, M. Dunne, R.M. McDermott, H. Meyer, R. Nazikian, C. Paz-Soldan, D.A. Ryan, E. Viezzer, M. Willensdorfer, The ASDEX Upgrade, and MST1 Teams. Experimental conditions to suppress edge localised modes by magnetic perturbations in the ASDEX Upgrade tokamak. *Nuclear Fusion*, 58(9):096031, 2018.

[SLL+03] B. Streibl, P. T. Lang, F. Leuterer, J.-M. Noterdaeme, and A. Stäbler. Chapter 2: Machine Design, Fueling, and Heating in ASDEX Upgrade. *Fusion Science and Technology*, 44:578–592, 2003.

[SLS+05a] G. Saibene, P.J. Lomas, R. Sartori, A. Loarte, J. Stober, Y. Andrew, S.A. Arshad, G.D. Conway, E. de la Luna, K. Günther, L.C. Ingesson, M.A.H. Kempenaars, A. Korotkov, H.R. Koslowski, J.S. Lönnroth, D.C. McDonald, A. Meigs, P. Monier-Garbet, V. Parail, C.P. Perez, F.G. Rimini, S. Sharapov, and P.R. Thomas. Characterization of small ELM experiments in highly shaped single null and quasi-double-null plasmas in JET. *Nuclear Fusion*, 45(5):297, 2005.

[SLS+05b] J. Stober, P.J. Lomas, G. Saibene, Y. Andrew, P. Belo, G.D. Conway, A. Herrmann, L.D. Horton, M. Kempenaars, H.-R. Koslowski, A. Loarte, G.P. Maddison, M. Maraschek, D.C. McDonald, A.G. Meigs, P. Monier-Garbet, D.A. Mossessian, M.F.F. Nave, N. Oyama, V. Parail, Ch.P. Perez, F. Rimini, R. Sartori, A.C.C. Sips, P.R. Thomas, Contributors to the EFDA-JET workprogramme, and the ASDEX Upgrade Team. Small ELM regimes with good confinement on JET and comparison to those on ASDEX Upgrade, Alcator C-mod and JT-60U. *Nuclear Fusion*, 45(11):1213, 2005.

[SMA+10] K. Schmid, M. Mayer, C. Adelhelm, M. Balden, S. Lindig, and the ASDEX Upgrade team. Impact of gyro-motion and sheath acceleration on the flux distribution on rough surfaces. *Nuclear Fusion*, 50:105004, 2010.

[SML+00] W. Schneider, P.J. McCarthy, K. Lackner, O. Gruber, K. Behler, P. Martin, and R. Merkel. ASDEX Upgrade MHD equilibria reconstruction on distributed workstations. *Fusion Engineering and Design*, 48:127–134, 2000.

[Spi51] L. Spitzer. A proposed stellarator. *US Atomic Energy Commission Report*, 1951.

[SSC+22] H.J. Sun, S.A. Silburn, I.S. Carvalho, D.B. King, C. Giroud, G. Fishpool, G.F. Matthews, R.B. Henriques, D.L. Keeling, F.G. Rimini, L. Garzotti, D. Frigione, D. Van Eester, M. Groth, J. Flanagan, D. Kos, B. Viola, A. Boboc, P. Shi, M.-L. Mayoral, J. Mailloux, C. Maggi, A. Huber, D. Douai, N. Vianello, P.J. Lomas, M. Lennholm, M. Maslov, K. Kirov, P. Jacquet, C.G. Lowry, M. Baruzzo, C. Stuart, J. Mitchell, L. Horvath, D.C. McDonald, and JET Contributors. The broadening of SOL profiles in JET tritium plasma and its impact on machine operation. *Nuclear Fusion*, 63(1):016021, 2022.

[Sta00] P.C. Stangeby. *The plasma boundary of magnetic fusion devices.* Boca Raton, FL: CRC Press, 2000.

[Sta12] P.C. Stangeby. The chodura sheath for angles of a few degrees between the magnetic field and the surface of divertor targets and limiters. *Nuclear Fusion*, 52(8):083012, 2012.

[Str18] U. Stroth. *Plasmaphyik: Phänomene, Grundlagen und Anwendungen.* Springer Spektrum, 2018.

[SVT+22] A. Stagni, N. Vianello, C.K. Tsui, C. Colandrea, S. Gorno, M. Bernert, J.A. Boedo, D. Brida, G. Falchetto, A. Hakola, G. Harrer, H. Reimerdes, C. Theiler, E. Tsitrone, N. Walkden, the TCV Team, and the EUROfusion MST1 Team. Dependence of scrape-off layer profiles and turbulence on gas fuelling in high density H-mode regimes in TCV. *Nuclear Fusion*, 62:9, 2022.

[SWE+15] H.J. Sun, E. Wolfrum, T. Eich, B. Kurzan, S. Potzel, U. Stroth, and the ASDEX Upgrade Team. Study of near scrape-off layer (SOL) temperature and density gradient lengths with Thomson scattering. *Plasma Physics and Controlled Fusion*, 57:125011, 2015.

[SWF+02] P.B. Snyder, H.R. Wilson, J.R. Ferron, L.L. Lao, A.W. Leonard, T.H. Osborne, A.D. Turnbull, D. Mossessian, M. Murakami, and X.Q. Xu.

Edge localized modes and the pedestal: A model based on coupled peeling–ballooning modes. *Physics of Plasmas*, 9(5):2037–2043, 2002.

[SWG+12] P.A. Schneider, E. Wolfrum, R.J. Groebner, T.H. Osborne, M.N.A. Beurskens, M.G. Dunne, J.R. Ferron, S. Günter, B. Kurzan, K. Lackner, P.B. Snyder, H. Zohm, the ASDEX Upgrade Team, the DIII-D Team, and JET EFDA Contributors. Differences in the H-mode pedestal width of temperature and density. *Plasma Physics and Controlled Fusion*, 54(10):105009, 2012.

[TBB+22] C.K. Tsui, J.A. Boedo, D. Brida, O. Février, G.F. Harrer, A. Perek, H. Reimerdes, B.P. Duval, S. Gorno, U.A. Sheikh, C. Theiler, N. Vianello, N. Walkden, M. Wensing, M. Baquero-Ruiz, the TCV Team, and the EUROfusion MSTI Team. Evidence on the effects of main-chamber neutrals on density shoulder broadening. *Physics of Plasmas*, 29:062507, 2022.

[TBM+18] C.K. Tsui, J.A. Boedo, J.R. Myra, B. Duval, B. Labit, C. Theiler, N. Vianello, W.A.J. Vijvers, H. Reimerdes, S. Coda, O. Fevrier, J.R. Harrison, J. Horacek, B. Lipschultz, R. Maurizio, F. Nespoli, U. Sheikh, K. Verhaegh, N. Walkden, TCV Team, and EUROfusion MST1 Team. Filamentary velocity scaling validation in the TCV tokamak. *Physics of Plasmas*, 25:072506, 2018.

[TBPG07] I. Teliban, D. Block, A. Piel, and F. Greiner. Improved conditional averaging technique for plasma fluctuation diagnostics. *Plasma Physics and Controlled Fusion*, 49:485, 2007.

[Tol14] P. Tolias. On secondary electron emission and its semi-empirical description. *Plasma Physics and Controlled Fusion*, 56(12):123002, 2014.

[VCT+20] N. Vianello, D. Carralero, C.K. Tsui, V. Naulinand M. Agostini, I. Cziegler, B. Labit, C. Theiler, E. Wolfrum, D. Aguiam, S. Allan, M. Bernert, J. Boedo, S. Costea, H. De Oliveira, O. Fevrier, J. Galdon-Quiroga, G. Grenfell, A. Hakola, C. Ionita, H. Isliker, A. Karpushov, J. Kovacic, B. Lipschultz, R. Maurizio, K. McClements, F. Militello, A.H. Nielsen, J. Olsen, J.J. Rasmussen, T. Ravensbergen, H. Reimerdes, B. Schneider, R. Schrittwieser, E. Seliunin, M. Spolaore, K. Verhaegh, J. Vicente, N. Walkden, W. Zhang, the ASDEX Upgrade Team, the TCV Team, and the EUROfusion MST1 Team. Scrape-off layer transport and filament characteristics in high-density tokamak regimes. *Nuclear Fusion*, 60:016001, 2020.

[Vie18] E. Viezzer. Access and sustainment of naturally ELM-free and small-ELM regimes. *Nuclear Fusion*, 58(11):115002, 2018.

[VKR+21] Irina Veselova, Elizaveta Kaveeva, Vladimir Rozhansky, Ilya Senichenkov, Anastasia Poletaeva, Richard A. Pitts, and Xavier Bonnin. Solps-iter drift modelling of iter burning plasmas with narrow near-sol heat flux channels. *Nuclear Materials and Energy*, 26:100870, 2021.

[VPC+13] E. Viezzer, T. Pütterich, G.D. Conway, R. Dux, T. Happel, J.C. Fuchs, R.M. McDermott, F. Ryter, B. Sieglin, W. Suttrop, M. Willensdorfer, E. Wolfrum, and the ASDEX Upgrade Team. High-accuracy characterization of the edge radial electric field at ASDEX Upgrade. *Nuclear Fusion*, 53:053005, 2013.

[VSE+13] C. Vorpahl, W. Suttrop, M. Ebner, B. Streibl, H. Zohm, and the ASDEX Upgrade Team. Deformation measurement of internal components of ASDEX Upgrade using optical strain sensors. *Fusion Engineering and Design*, 88:537–540, 2013.

[VWD+21] N. Vianello, N. Walkden, M. Dunne, B. Lomanowski, E. Wolfrum, C. Tsui, A. Stagni, M. Griener, B. Tal, T. Eich, D. Refy, D. Brida, O. Fèvrier, M. Agostini, H. De Oliveira, S. Aleiferis, M. Bernert, J. Boedo M. Brix, D. Carralero, I. Carvalho, G. Falchetto, L. Frassinetti, C. Giroud, A. Hakola, A. Huber, J. Karhunen, A. Karpushov, B. Labit, A. Meigs, V. Naulin, T. Pereira, C. Perez von Thun, H. Reimerdes, S. Gorno, C. Theiler, the ASDEX Upgrade Team, the TCV team, the EUROfusion MST1 Team, and the JET Contributors. SOL profile and fluctuations in different divertor recycling conditions in H-mode plasmas. *2020 IAEA Fusion Energy Conference (Nice) [EX/P3-14]*, https://nucleus.iaea.org/sites/fusionportal/Shared%20Documents/FEC%202020/fec2020-preprints/preprint1051.pdf, 2021.

[WAA+17] R. Wenninger, R. Albanese, R. Ambrosino, F. Arbeiter, J. Aubert, C. Bachmann, L. Barbato, T. Barrett, M. Beckers, W. Biel, L. Boccaccini, D. Carralero, D. Coster, T. Eich, A. Fasoli, G. Federici, M. Firdaouss, J. Graves, J. Horacek, M. Kovari, S. Lanthaler, V. Loschiavo, C. Lowry, H. Lux, G. Maddaluno, F. Maviglia, R. Mitteau, R. Neu, D. Pfefferle, K. Schmid, M. Siccinio, B. Sieglin, C. Silva, A. Snicker, F. Subba, J. Varje, and H. Zohm. The DEMO wall load challenge. *Nuclear Fusion*, 57(4):046002, 2017.

[WAW+93] E. Wolfrum, F. Aumayr, D. Wutte, , H.P. Winter, E. Hintz, D. Rusbüldt, and P. Schorn. Fast lithium-beam spectroscopy of tokamak edge plasmas. *Review of Scientific Instruments*, 64:2285–2292, 1993.

[WBB+82] F. Wagner, G. Becker, K. Behringer, D. Campbell, A. Eberhagen, W. Engelhardt, G. Fussmann, 0. Gehre, J. Gernhardt, G. v. Gierke, G. Haas, M. Huang, F. Karger, M. Keilhacker, Q. Kluber, M. Kornherr, K. Lackner,

G. Lisitano, G.G. Lister, H.M. Mayer, D. Meisel, E.R. Müller, H. Murmann, H. Niedermeyer, W. Poschenrieder, H. Rapp, H. Bohr, F. Schneider, G. Siller, E. Speth, A. Stäbler, K.H. Steuer, G. Venus, O. Vollmer, and Z. Yü. Regime of Improved Confinement and High Beta in Neutral-Beam-Heated Divertor Discharges of the ASDEX Tokamak. *Physical Review Letters*, 49:1408, 1982.

[WBB+85] F. Wagner, R. Bartiromo, G. Becker, H.S. Bosch, A. Eberhagen, G. Fussmann, O. Gehre, J. Gernhardt, G.V. Gierke, E. Clock, O. Gruber, G. Haas, G. Janeschitz, F. Karger, M. Keilhacker, A. Kislyakov, O. Klüber, M. Kornherr, P.B. Kotzé, K. Lackner, M. Lenoci, G. Lisitano, A. Mahdavi, H.-M. Mayer, K. McCormick, D. Meisel, V. Mertens, E.R. Müller, H. Murmann, H. Niedermeyer, W. Poschenrieder, H. Rapp, F. Ryter, J. Roth, F. Schneider, G. Siller, P. Smeulders, F. Söldner, E. Speth, K. Steinmetz, K.-H. Steuer, and O. Vollmer. Experimental evidence for neoclassical ion transport effects in the H-transition of ASDEX. *Nuclear Fusion*, 25:1408, 1985.

[WBB+11] E. Wolfrum, M. Bernert, J.E. Boom, A. Burckhart, I.G.J. Classen, G.D. Conway, T. Eich, R. Fischer, A. Gude, A. Herrmann, N.C. Luhmann, M. Maraschek, R. McDermott, H.K. Park, T. Pütterich, J. Vicente, B. Wieland, M. Willensdorfer, and the ASDEX Upgrade Team. Characterization of edge profiles and fluctuations in discharges with type-II and nitrogen-mitigated edge localized modes in ASDEX Upgrade. *Plasma Physics and Controlled Fusion*, 53(8):085026, 2011.

[WBD+18] M. Weiland, R. Bilato, R. Dux, B. Geiger, A. Lebschy, F. Felici, R. Fischer, D. Rittich, M. van Zeeland, the ASDEX Upgrade Team, and the Eurofusion MST1 Team. RABBIT: Real-time simulation of the NBI fast ion distribution. *Nuclear Fusion*, 58:082032, 2018.

[WBS+23] M. Weiland, R. Bilato, B. Sieglin, F. Felici, L. Giannone, O. Kudlacek, M. Rampp, M. Scheffer, W. Treutterer, T. Zehetbauer, the ASDEX Upgrade Team, and the EUROfusion MST1 Team. Real-time implementation of the high-fidelity NBI code RABBIT into the discharge control system of ASDEX Upgrade. *Nuclear Fusion*, 63(6):066013, 2023.

[WC96] M. Weinlich and A. Carlson. Flush mounted probes in ASDEX Upgrade - can they be operated as triple probes? *Contributions to Plasma Physics*, 36 S1:53–59, 1996.

[WFG+84] F. Wagner, G. Fussmann, T. Grave, M. Keilhacker, M. Kornherr, K. Lackner, K. McCormick, E. R. Müller, A. Stäbler, G. Becker, K. Bernhardi, U. Ditte, A. Eberhagen, O. Gehre, J. Gernhardt, G. v. Gierke, E. Glock, O. Gruber, G. Haas, M. Hesse, G. Janeschitz, F. Karger, S. Kissel,

O. Klüber, G. Lisitano, H. M. Mayer, D. Meisel, V. Mertens, H. Murmann, W. Poschenrieder, H. Rapp, H. Röhr, F. Ryter, F. Schneider, G. Siller, P. Smeulders, F. Söldner, E. Speth, K.-H. Steuer, Z. Szymanski, and O. Vollmer. Development of an Edge Transport Barrier at the H Mode Transition of ASDEX. *Physical Review Letters*, 53:1415, 1984.

[WLC+18] A. Wynn, B. Lipschultz, I. Cziegler, J. Harrison, A. Jaervinen, G. F. Matthews, J. Schmitz, B. Tal, M. Brix, C. Guillemaut, D. Frigione, A. Huber, E. Joffrin, U. Kruzei, F. Militello, A. Nielsen, N.R. Walkden, S. Wiesen, and JET Contributors. Investigation into the formation of the scrape-off layer density shoulder in JET ITER-like wall L-mode and H-mode plasmas. *Nuclear Fusion*, 58(5):056001, 2018.

[WWF+12] M. Willensdorfer, E. Wolfrum, R. Fischer, J. Schweinzer, M. Sertoli, B. Sieglin, G. Veres, F. Aumayr, and the ASDEX Upgrade Team. Improved chopping of a lithium beam for plasma edge diagnostic at ASDEX Upgrade. *Review of Scientific Instruments*, 83:023501, 2012.

[YYI83] Y. Itikawa Y. Yamamura and N. Itoh. Angular dependence of sputtering yields of monatomic solds. *IPPJ-AM-26, Nagoya*, 1983.

[ZMY+22] Q. Zhuang, T. Ming, Y. Yu, Y. Liu, L. Yang, F. Long, Q. Shi, B. Li, S. Liu, H. Liu, G. Li, and X. Gao. Calorimetry system for heat load in long-pulse discharges on EAST tokamak. *Physica Scripta*, 97:095602, 2022.

[Zoh96] H. Zohm. Edge localized modes (ELMs). *Plasma Physics and Controlled Fusion*, 38:105, 1996.

[Zoh10] H. Zohm. On the Minimum Size of DEMO. *Fusion Science and Technology*, 58:2:613–624, 2010.

Acknowledgement

1012 days, that's how long it took me to finish the first draft of my thesis. It took me more time than I expected. As I write these lines, this version of the dissertation is not yet the final version, but already close. And with that, another adventure of my life is slowly coming to an end. An adventure from which I have learned and taken away a lot and also matured.

In order for this adventure to take place, I would first like to thank **Guiseppe Calabrò** and **Thomas Eich**, who made this promotion possible. Thomas has consistently steered me through the shoals of plasma physics and is a motivator unlike any other. I wish you nothing but the best in your new chapter at SPARC.

I would also like to thank my second supervisor **Nicola Vianello**, who always had a small window of time open for me in his busy schedule and guided me through the shoals of EUROfusion.

An experimental PhD thesis is not the work of an individual, but the work of a large team, whom I would like to thank. My deepest thanks goes to **Tim Hohmann**, the best technician at AUG. Together, we have been full of energy to bring AUG's old calorimetry back up to speed and have gotten phenomenal results because of it. It has always been a pleasure to work with you and together we have built the best diagnostics at AUG.

The work to revise calorimetry has required the knowledge of many and an open exchange. So my thanks go to **Anton Dollenbacher**, **Gerd Schall** and **Stefan Vorbrugg** for the great cooperation and any feedback. A big thanks also goes to **Volker Rohde** and **Albrecht Herrmann**, whose knowledge and suggestions on calorimetry were invaluable. Thanks also go to **Roland Merkel**, **Helmut Blank** and **Giovanni Tardini** for their support in embedding diagnostics into the IT structure.

I would also like to thank **Michael Faitsch** for the countless discussions on understanding the QCE regime. These discussions have generated many an idea and have been an important basis for considering whether the methodology of some approaches makes any sense at all.

My thanks also go to the master probes **Dominik Brida**, **Gustavo Grenfell**, **Roman Ochoukov**, **Mykola Dreval**, and **Jiri Adamek**. I learned a lot about probe measurements from this collaboration and I am still amazed at the quantities that can be derived from a slope like this. I would like to thank **Gustavo** for the countless discussions on the BPP probes. My biggest thanks go to **Mykola**, who did the evaluation of the RFA2 in Kharkov.

I would also like to thank **Matthias Bernert** and **Pierre David** for their great collaboration. Without the support from bolometry this promising energy balance could not have been achieved.

My thanks also go to the modelers **Markus Weiland**, **Dirk Stieglitz** and **Niek den Harder**. The discussion on RABBIT, THEODOR and ABC3D were always helpful and instructive for me.

Thanks to the suggestions of **Gustavo** I might also have the pleasure to work with **Gregor Birkenmeier**, **Ralph Dux**, **Rudi Neu** and **Klaus Schmid**. However, the way to the right fomel has caused more stir than expected.

Thanks also go to **Arne Kallenbach** for his suggestions and discussions on shot planning or the implementation of some ideas for testing calorimetry diagnostics.

Many a long day in the control room became much more entertaining thanks to debauched conversations of many colleagues (**Daniel Wendler**, **Joey Kalis**, **Benedikt Zimmermann**, **Balazs Tal** and many more).

The **IPP footballers** during my time at IPP must not be forgotten. Football was a nice balance to many a busy week.

Through my time at Consorzio RFX in Padua, I had the great pleasure of meeting many new faces and aspects of fusion research. A big thanks goes to **Adriano Stagni**, with whom I did many of my travels around Europe. I would like to thank all the colleagues at the Consorzio for my great Italian time. My thanks also go to **Marco di Narda**, **Tommaso Patton**, **Nicholas Vivenzi**, **Stefano Ciufo**, **Francesco Cani**, **Andrea Belpane**, **Yoana Nekova**, **Matteo Gambrioli** and countless others.

I had the pleasure to meet many colleagues from the European and the international community during my PhD. The discussions with **Guy Matthews** and **Scott Silburn** on their experiences energy balances at JET was invaluable to this work. I would also like to thank **Yann Corre** and **Jonathan Gaspar** for the insightful meetings on calorimetry at WEST Tokamak, which were the piece of the puzzle for important confirmations.

Thanks also go to all those colleagues I should have forgotten in this listing. I apologize to everyone for that.

Last but not least, I would like to thank **my family** who has always supported me in my adventure.

Tausend Dank! Thousand thanks! Grazie mille!

Ringraziamento

1012 giorni: è il tempo che ho impiegato per finire la prima stesura della mia tesi di dottorato. Mi ci è voluto più tempo di quanto mi aspettassi. Mentre scrivo queste righe, questa versione della tesi non è ancora la versione finale, ma è già vicina. E con ciò, un'altra avventura della mia vita sta lentamente volgendo al termine. Un'avventura dalla quale ho imparato e portato via molto, oltre che maturato.
Affinché questa avventura abbia luogo, vorrei innanzitutto ringraziare **Guiseppe Calabrò** e **Thomas Eich**, che hanno reso possibile questa promozione. Thomas mi ha costantemente guidato attraverso le secche della fisica del plasma ed è un motivatore unico. Vi auguro il meglio per il vostro nuovo capitolo alla SPARC.
Vorrei anche ringraziare il mio secondo supervisore, **Nicola Vianello**, che ha sempre avuto una piccola finestra di tempo per me nella sua fitta agenda e mi ha guidato attraverso le secche di EUROfusion.
Una tesi di dottorato sperimentale non è il lavoro di un singolo, ma di un grande team, che desidero ringraziare. Ringrazio di cuore **Tim Hohmann**, il miglior tecnico dell'AUG. Insieme, abbiamo fatto il pieno di energia per riportare la vecchia calorimetria di AUG al passo con i tempi e abbiamo ottenuto risultati fenomenali. È sempre stato un piacere lavorare con voi e insieme abbiamo costruito la migliore diagnostica di AUG.
Il lavoro di revisione della calorimetria ha richiesto la conoscenza di molti e uno scambio aperto. Ringrazio quindi **Anton Dollenbacher**, **Gerd Schall** e **Stefan Vorbrugg** per la grande collaborazione e per il feedback. Un grande ringraziamento va anche a **Volker Rohde** e **Albrecht Herrmann**, le cui conoscenze e suggerimenti sulla calorimetria sono stati preziosi. Si ringraziano inoltre **Roland Merkel**, **Helmut Blank** e **Giovanni Tardini** per il loro supporto nell'inserimento della diagnostica nella struttura informatica.
Vorrei anche ringraziare **Michael Faitsch** per le innumerevoli discussioni sulla comprensione del regime QCE. Queste discussioni hanno generato molte idee e sono state una base importante per valutare se la metodologia di alcuni approcci ha un senso.
I miei ringraziamenti vanno anche ai master probe **Dominik Brida**, **Gustavo Grenfell**, **Roman Ochoukov**, **Mykola Dreval** e **Jiri Adamek**. Grazie a questa collaborazione ho imparato molto sulla misurazione delle sonde e sono ancora stupito dalle quantità che si possono ricavare da una pendenza come questa. Vorrei ringraziare **Gustavo** per le innumerevoli discussioni sulle sonde BPP. Il mio più grande ringraziamento va a **Mykola**, che ha fatto la valutazione dell'RFA2 a Kharkov.
Vorrei anche ringraziare **Matthias Bernert** e **Pierre David** per la loro grande collabo-

razione. Senza il supporto della bolometria non sarebbe stato possibile realizzare questo promettente bilancio energetico.

I miei ringraziamenti vanno anche ai modellisti **Markus Weiland** e **Dirk Stieglitz**. Le discussioni su RABBIT e THEODOR sono sempre state utili e istruttive per me.

Grazie ai suggerimenti di **Gustavo** ho avuto il piacere di lavorare anche con **Gregor Birkenmeier**, **Ralph Dux**, **Rudi Neu** e **Klaus Schmid**. Tuttavia, la strada verso il fomel giusto ha suscitato più scalpore del previsto.

Si ringrazia anche **Arne Kallenbach** per i suggerimenti e le discussioni sulla pianificazione dei tiri o sull'implementazione di alcune idee per testare la diagnostica calorimetrica.

Molte lunghe giornate in sala di controllo sono diventate molto più divertenti grazie alle conversazioni dissolute di molti colleghi (**Daniel Wendler**, **Joey Kalis**, **Benedikt Zimmermann**, **Balazs Tal** e molti altri).

Non bisogna dimenticare i calciatori dell'IPP durante il mio periodo di lavoro. Il calcio è stato un piacevole equilibrio per molte settimane impegnative.

Durante il periodo trascorso al Consorzio RFX di Padova, ho avuto il grande piacere di conoscere molti volti e aspetti nuovi della ricerca sulla fusione. Un grande ringraziamento va a **Adriano Stagni**, con cui ho fatto molti dei miei viaggi in Europa. Vorrei ringraziare tutti i colleghi del Consorzio per il grande tempo trascorso in Italia. Ringrazio anche **Marco di Narda**, **Tommaso Patton**, **Nicholas Vivenzi**, **Stefano Ciufo**, **Francesco Cani**, **Andrea Belpane**, **Yoana Nekova**, **Matteo Gambrioli** e innumerevoli altri.

Durante il mio dottorato ho avuto il piacere di incontrare molti colleghi della comunità europea e internazionale. Le discussioni con **Guy Matthews** e **Scott Silburn** sulle loro esperienze di bilanci energetici al JET sono state preziose per questo lavoro. Desidero inoltre ringraziare **Yann Corre** e **Jonathan Gaspar** per gli approfonditi incontri sulla calorimetria al Tokamak WEST, che hanno rappresentato il tassello per importanti conferme.

Un ringraziamento va anche a tutti i colleghi che avrei dovuto dimenticare in questo elenco. Mi scuso con tutti per questo.

Infine, ma non per questo meno importante, vorrei ringraziare la mia famiglia che mi ha sempre sostenuto in questa avventura.

Tausend Dank! Thousand thanks! Grazie mille!

Danksagung

1012 Tage, so lange habe ich benötigt, um den ersten Entwurf meiner Doktorarbeit fertigzustellen. Ich habe damit mehr Zeit benötigt als ich erwartet habe. Wenn ich diese Zeilen schreibe, ist diese Version der Doktorarbeit noch nicht die finale Version, aber schon nahe dran. Und damit geht ein weiteres Abenteuer meines Lebens langsam dem Ende entgegen. Ein Abenteuer, aus dem ich ich viel gelernt habe und auch gereift bin.

Damit dieses Abenteuer erst stattfinden konnte, möchte ich mich zuallerst bei **Guiseppe Calabrò** und **Thomas Eich**, die diese Promotion erst ermöglicht haben. Thomas hat mich beständig durch die Untiefen der Plasmaphysik gelotst und ist ein Motivator, den es kein zweites Mal gibt. Ich wünsche dir bei deinem neuen Abschnitt bei SPARC nur das beste.

Ich möchte auch meinen zweiten Betreuer **Nicola Vianello** danken, der für mich stets ein kleines Zeitfenster in seinem engen Terminkalender offen hatte und mich durch die Untiefen von EUROfusion geführt hat.

Eine experimentelle Doktorarbeit ist keine Arbeit eines einzelnen, sondern die Arbeit eines großen Teams, dem ich danken möchte. Mein allergrößter Dank geht an **Tim Hohmann**, dem besten Techniker an AUG. Zusammen haben wir mit vollem Tatendrang die alte Kalorimetrie von AUG wieder auf Vordermann gebracht hat und deswegen phänomenale Ergebnisse erhalten. Es war mir stets eine Freude mit dir zusammenzuarbeiten und wir haben gemeinsam die beste Diagnostik an AUG aufgebaut.

Die Arbeit zur Ueberarbeitung der Kalorimetrie hat das Wissen vieler und einen offenen Austausch benötigt. Mein Dank gilt daher **Anton Dollenbacher**, **Gerd Schall** und **Stefan Vorbrugg** für die tolle Zusammenarbeit und jegliches Feedback. Ein großer Dank geht auch an **Volker Rohde** und **Albrecht Herrmann**, deren Wissen und Anregungen zur Kalorimetrie von unschätzbaren Wert waren. Ein Dank geht auch an **Roland Merkel**, **Helmut Blank** und **Giovanni Tardini** fuer die Unterstuetzung zur Einbettung der Diagnostik in die IT-Struktur.

Ich möchte mich auch bei **Michael Faitsch** bedanken für die unzähligen Gespräche zum Verständnis des QCE-Regimes. Diese Diskussionen haben so manche Ideen hervorgebracht und waren eine wichtige Grundlage zu prüfen, ob die Methodik manches Ansatzes überhaupt Sinn ergibt.

Meinem Dank gelten auch den Meistern der Sonden **Dominik Brida**, **Gustavo Grenfell**, **Roman Ochoukov**, **Mykola Dreval** und **Jiri Adamek**. Ich habe aus dieser Zusammenarbeit viel über Sondenmessungen gelernt und ich bin noch immer erstaunt, welche

Größen man so aus einer Steigung ableiten kann. Ich möchte **Gustavo** für die unzähligen Diskussionen zur BPP-Sonden danken. Mein Dank gilt auch **Mykola**, der die Auswertung des RFA2 von aus Charkow durchgeführt hat.
Für die großartige Zusammenarbeit möchte ich auch **Matthias Bernert** und **Pierre David** danken. Ohne die Unterstützung aus der Bolometrie hätte diese vielversprechende Energiebilanz nicht erreicht werden können.
Mein Dank gilt auch den Modellierern **Markus Weiland**, **Dirk Stieglitz** und **Niek den Harder**. Die Diskussionen über RABBIT, THEODOR und ABC3D waren für mich stets hilfreich und lehrreich.
Dank den Anregungen von **Gustavo** dürfte ich auch in den Genuss kommen mit **Gregor Birkenmeier**, **Ralph Dux**, **Rudi Neu** und **Klaus Schmid** zusammenzuarbeiten. Der Weg zur richtigen Fomel hat jedoch mehr Aufsehen erregt als erwartet.
Ein Dank geht auch an **Arne Kallenbach** für seine Anregungen und Diskussionen zur Schussplanung oder der Umsetzung mancher Idee zum Testen der Kalorimetrie-Diagnostik.
So manch langer Tag im Kontrollraum wurde dank ausschweifender Unterhaltungen vieler Kollegen (**Daniel Wendler**, **Joey Kalis**, **Benedikt Zimmermann**, **Balazs Tal** und viele mehr) wesentlich unterhaltsamer.
Die **IPP-Fußballer** während meine Zeit am IPP dürfen nicht vergessen werden. Der Fussball war ein schöner Ausgleich für manch anstrengende Woche.
Durch meine Zeit am Consorzio RFX in Padua, hatte ich das große Vergnügen viele neue Gesichter und Aspekte der Fusionsforschung kennenlernen zu dürfen. Ein großer Dank geht an **Adriano Stagni**, mit dem ich viele meiner Reisen durch Europa bestritten habe. Ich möchte all den Kollegen am Consorzio für meine großartige, italienische Zeit danken. Mein Dank geht an **Marco di Narda**, **Tommaso Patton**, **Nicholas Vivenzi**, **Stefano Ciufo**, **Francesco Cani**, **Andrea Belpane**, **Yoana Nekova**, **Matteo Gambrioli** und vielen weiteren.
Ich hatte das Vergnügen im Rahmen meiner Promotion viele Kollegen der europäischen und der internationalen Community kennenlernen zu dürfen. Die Diskussionen mit **Guy Matthews** und **Scott Silburn** zu ihren Erfahrungen zu Energiebilanzen an JET war von unschätzbarem Wert für diese Arbeit. Ich möchte mich auch bei **Yann Corre** und **Jonathan Gaspar** für die aufschlussreichen Meetings zur Kalorimetrie am WEST Tokamak bedanken, welche das Puzzleteil für wichtige Bestätigungen waren.
Ein Dank geht auch an alldiejenigen Kollegen, die ich in dieser Auflistung vergessen haben sollte. Ich entschuldige mich bei jedem dafür.
Zum guter Letzt möchte ich **meiner Familie** danken, die mich bei meinem Abenteuer stets unterstützt hat.
Tausend Dank! Thousand thanks! Grazie mille!